Randomised Measurements with Strings of Trapped Ions

Thesis submitted to the
FACULTY OF
MATHEMATICS, COMPUTER SCIENCE AND PHYSICS,
OF THE LEOPOLD-FRANZENS UNIVERSITY OF INNSBRUCK,

in partial fulfillment
of the requirements for the degree of

DOCTOR OF PHILOSOPHY
(PHYSICS)

carried out at the Institute of Experimental Physics
under the guidance of Rainer Blatt

presented by
TIFF BRYDGES

JUNE 2021

This work was undertaken at the:

Institute for Quantum Optics and Quantum Information (IQOQI)
Austrian Academy of Sciences
Technikerstraße 21a
6020 Innsbruck
Austria

Supervised by:

o. Univ.-Prof. Dr. Rainer Blatt and
Dr. Christian F. Roos

Abstract

The recent progress that has been made in quantum information science, with regards to moving towards realising quantum computers and simulators which can provide an advantage over classical computers and simulators, is without question remarkable. This thesis reports on several experiments and improvements/extensions to a pre-existing quantum simulation experiment in order to help further move towards the end goal of achieving such a ‘quantum advantage’. This thesis is based on the use of a pre-existing, trapped ion experiment which uses an optical transition in singly ionised calcium-40, $^{40}\mathrm{Ca}^{+}$, to encode a qubit and implement coherent quantum interactions.

Three experiments which are detailed in this thesis use *randomised measurements* in order to characterise such quantum dynamics. The experiments involve (i) determining the presence of bipartite entanglement in the system (on 10 ion partitions of strings of up to 20 ions) (ii) looking at the spread of quantum information in chains of 10 ions (iii) performing a proof-of-principle verification experiment on chains of 10 ions between two, ideally identical, states prepared sequentially on the experimental platform. The ability to perform such characterisation measurements is becoming of increasing importance as quantum simulators and computers move into regimes which are too computationally intensive to be classically simulated.

The final section of the thesis describes the implementation and characterisation of a new extension to the existing setup – the Raman setup. This new extension allows quantum information to be encoded in the ground states of $^{40}\mathrm{Ca}^{+}$, leading to significant increases in both the coherence time of the system as well as the speed of the entangling interactions which are generated.

The thesis concludes with a brief summary and discussion of the major avenues of future work which can be undertaken in the near future.

Kurzfassung

Der Fortschritt, der in den letzten Jahren im Gebiet der Quanteninformationsforschung im Bezug auf die Realisierung von Quantencomputern und -simulatoren, welche einen Vorteil gegenüber klassischen Computern und Simulatoren haben, gemacht wurde, ist ausser Frage beträchtlich. Diese Arbeit umfasst neue Experimente sowie Fortschritte und Erweiterungen von schon existierenden Experimenten zur Quantensimulation mit dem Ziel dem 'Quanten-Vorteil' näher zu kommen. Diese Arbeit basiert auf einem schon exisiterendem Experiment mit Ionenfallen, welches einen optischen Übergang in einfach ionisierten Kalzium-40 (^{40}Ca^{+}) benutzt, um ein Quantenbit zu kodieren und um kohärente Wechselwirkungen zu erzeugen.

Drei der in dieser Arbeit beschriebenen Experimente machen Gebrauch von *randomisierten Messungen*, um die Dynamik solcher Quantensysteme zu charakterisieren. Diese Experimente umfassen: (i) Die Bestätigung bipartiter Verschränkung in einem System (zwischen 10 Ionen die Teil einer Kette von 20 Ionen sind). (ii) Die Betrachtung der Verteilung von Quanteninformation in Ketten von 10 Ionen. (iii) Die Durchführung eines Proof-of-Principle Experiments zur Verifikation mit Ketten von 10 Ionen zwischen zwei, idealerweise identischen, Zuständen, welche sequenziell präpariert werden. Die Fähigkeit solche Experimente durchführen zu können wird je länger je wichtiger da Quantensimulatoren und Quantencomputer sich Bereichen nähern, in welchen klassische Simulationen zu rechenintensiv sind.

Der letzte Abschnitt der Arbeit befasst sich mit der Implementierung und Charakterisation von neuen Erweiterungen zu einem existierenden Aufbau - dem Raman Aufbau. Diese Erweiterung ermöglicht die Kodierung von Quanteninformation in Grundzuständen von ^{40}Ca^{+}. Dies ermöglicht eine signifikante Steigerung der Kohärenzzeit des Systems und der Geschwindigkeit mit der Verschränkung generiert wird.

Dieses Werk endet mit einer kurzen Zusammenfassung und Diskussion der wichtigen Forschungsrichtungen auf diesem Gebiet, welche in naher Zukunft erschlossen werden können.

Contents

Acknowledgements

There are always a huge number of people to thank for any thesis, and not nearly enough space to mention them all. Unending thanks must first be given to my wonderful parents, Helena and Chris, and fantastic sister and brother-in-law Beki and Phil, who are the ones who have always supported me in realising my dream of becoming a scientist. Thank you for always believing in me and not being too disturbed when I started dissecting ants in the kitchen.

Huge thanks must of course go to my supervisors Rainer Blatt and Christian Roos, who offered me this wonderful opportunity to complete my PhD with them. It has been a true privilege to work under the guidance of the best physicists in the field, and an experience I am truly glad to have had. Thanks to my predecessors Christine, Petar, and Ben, who taught me much of the experiment, put up with my many questions without becoming (visibly) frustrated, and were a great support to me throughout my time here. It's been fantastic to be able to work with all three of you, and I hope to have as much fun in my future work as I did in the lab with you. In addition, although only here for a short period, I had the most wonderful time in the lab with Aurélien, who is one of the most brilliant people I've had the good fortune to meet and work with. Allons-y!

Thanks must also go to my successors Johannes and Florian who have both shown themselves to be great people to work with, as well as being extremely competent. It is a wonderful feeling to know that the experiment will be left in safe hands under their future guidance.

Many thanks to Philipp Schindler who helped with a very large number of elements in this thesis, and volunteered a significant amount of his time in helping out; he is a rare gem. Huge thanks also to the wonderful administrative staff at IQOQI, including Elisabeth, Klaus, Valentin, and Mr Knabl, who always managed to smoothly resolve even the most headache-inducing administrative problems.

Finally, the true driver of this work has been my incredible husband James. He has been the biggest support one could imagine, keeping me going through the dark times and celebrating with me in the good times. To be able to have a partner and best friend who you can discuss physics with is a true privilege, and not more so when they are as insightful and brilliant as James is. I dedicate this work to you, and to all our future adventures together.

List of Abbreviations

AC Alternating Current

AOD Acousto-Optic Deflector

AOM Acousto-Optic Modulator

COM Centre of Mass

CP Complete Positivity

CUE Circular Unitary Ensemble

DC Direct Current

DDS Direct Digital Synthesiser

EMCCD Electron Multiplying Charged Coupled Device

GST Gate Set Tomography

IR Infrared

LBO Lithium Triborate

LGST Linear Inversion Gate Set Tomography

MLE Maximum Likelihood Estimation

MBL Many-Body Localisation

MS Mølmer-Sørensen (gate operation)

NISQ Noisy Intermediate-Scale Quantum (devices)

OTOC	Out-of-Time-Ordered Correlator
PBS	Polarising Beam Splitter
PD	Photodiode
PI	Photoionisation
PMT	Photomultiplier Tube
QPT	Quantum Process Tomography
QST	Quantum State Tomography
RWA	Rotating Wave Approximation
SPAM	State Preparation and Measurement (gates/errors)
TP	Trace Preservation
RF	Radio Frequency

Chapter 1

Introduction

Since their conceptualisation and primitive invention by Charles Babbage in the early 19th century, computers have without doubt revolutionised the modern world, ushering in a new age of information and technology. Moore's Law – a well-known trend in computer science – states that, through the miniaturisation of transistors, the number of transistors in a computer, and thus its computing power, doubles roughly every two years [1]. This has enabled computers to become smaller and faster at an almost exponential rate. However, at some point the miniaturisation of computers will reach a limit where effects from quantum physics need to be taken into account. Although at first the feature of quantum physics appears to be a limitation, in reality it opens up new possibilities for information processing through a different kind of computing – quantum computing. The 1980s were where it all kicked off for quantum computing, with Benioff [2], Feynman [3], and Deutsch [4] all making historic contributions to the development not only of the notion of quantum computing, but also to the quantum theory of computation [5].

Later on in the 1990s, Shor proposed a 'quantum algorithm' which, when implemented on a quantum device, allows the factorisation of large numbers [6, 7]. The ground-breaking part of this algorithm is that it outperforms even the most efficient classical algorithms that are currently known. Shor's algorithm, and its related extensions, have already been experimentally demonstrated many times and on multiple different platforms [8–11]. However, these demonstrations are still only 'proof-of-principle' – that is, they have only been demonstrated in regimes which are still easily accessible to classical computers, such as in factoring the number 15 [11]. As such, extensive further research is required in the area of quantum computing in order to develop this technology into a regime which classical computers cannot reach.

Feynman noticed that quantum computers also have the potential to simulate quantum systems whose properties are too complex to be calculated with a classical computer – so-called quantum simulators [3]. Simulation of large quantum systems is problematic for classical computers as the computation time grows exponentially with the size of the system [12]. Instead, quantum simulators, which manipulate a well-controlled quantum system such that properties of a different quantum system of interest can be emulated, are predicted to be of great importance [3, 13]. Quantum simulators, unlike quantum computers, are analogue quantum devices which evolve under controlled, engineered dynamics. As such, they cannot solve general problems (being non-universal), but are instead tailored to efficiently solve a particular set of physical problems of interest [14, 15].

Quantum simulation with trapped ions in particular is one of the most promising platforms for quantum technology so far, offering almost unrivalled control at the single-particle level [14, 16, 17]. It is of particular interest in the near-future with the development of *noisy intermediate-scale quantum (NISQ) devices* [18]. These are quantum devices comprised of 50-100 qubits, however are 'noisy' in that they will be limited by noise from imperfect control over the qubits. In fact, experiments using such devices (implemented, however, on a superconducting platform) have already been announced by Google [19] and IBM [20]. NISQ devices are interesting as they are predicted to operate in a regime which is beyond the simulation/calculation capabilities of even the most powerful classical computers [21]. While opening up a world of possibilities, this regime also presents problems when it comes to verifying that a quantum device is performing as expected – that is, confirming that the result from a 'computation' on such a machine is correct when it can no longer be verified through direct comparison to classical simulations.

The experiments presented in this thesis are performed on a pre-existing trapped-ion quantum simulation platform. Laser-driven interactions implement the transverse field Ising Hamiltonian and XY-model of interacting bosons with tunable-range interactions [22, 23] on chains of up to 20 ions. A major component of the experiments presented in this thesis is the use of randomised measurements to characterise the many-body dynamics resulting from evolution of the ion chains under these Hamiltonians. In particular, the experiments perform measurements of the Rényi entropy, indicating the presence of bipartite entanglement in the system [24], measurements of out-of-time-ordered correlators (OTOCs) in order to probe information scrambling in the system [25], and 'proof-of-principle' cross-platform verification of a prepared quantum state [26]. These experiments aim to help in the above-mentioned problem of characterising NISQ devices; they provide ways to characterise quantities of interest in quantum many-body systems comprised of tens of ions, as well as in performing a direct comparison between a state prepared on one quantum device and a state prepared on a separate device at potentially very different points in time and space. Such protocols will become of ever-increasing importance in the NISQ regime. In parallel to these experiments, a significant amount of technical work was carried out on the experimental system, with the aim of upgrading the system in order to move towards the NISQ regime. The upgrades detailed in this thesis will allow the laser-driven dynamics to proceed at significantly increased speeds, so allowing the potential for interesting, many-body states on up to 50 qubits to be realised in the near future.

This thesis is organised as follows:

Chapter 2 introduces the core theoretical concepts underpinning quantum information, ion trapping, and quantum optics, upon which the remainder of the thesis is based.

Chapter 3 gives an overview of the major components of the experimental setup relevant to this thesis. It goes on to describe two major experimental upgrades implemented during the course of this thesis: the Raman laser and optical setup to implement Raman transitions (Sections 3.2 & 3.3), and installation of permanent magnets to replace the magnetic field coils (Section 3.4).

Chapter 4 introduces the theoretical background to gate set tomography and its subsequent implementation, providing a characteristion of the single-qubit operations implemented in the experimental system. In addition, the stability of two of the major beam paths used for qubit manipulation is investigated.

Chapter 5 introduces three theoretical protocols using statistical correlations between randomised measurements to obtain quantities of interest. The first of these allows a measurement of the Rényi entanglement entropy, with the second investigating scrambling in chains of ions. The final protocol looks at performing cross-platform verification between two quantum devices. These three protocols are subsequently experimentally implemented in Chapters 6 & 7.

Chapter 6 reports on the experimental implementation of the first of the random measurement protocols to measure the Rényi entanglement entropy on 10-ion partitions of strings of up to 20 ions.

Chapter 7 describes the implementation of the second and third random measurement protocols on strings of 10 ions. The third protocol is a 'proof-of-principle' demonstration of cross-platform verification between quantum devices, demonstrated using only a single experimental system.

Chapter 8 details the implementation of the new Raman setup, including characterisation measurements of the setup as well as the implementation of entangling gates.

Chapter 9 concludes by summarising the work presented in this thesis, and outlining the next major avenues of future work to be looked at.

Chapter 2

Background Theory

This Chapter will introduce the basic theoretical concepts upon which the remainder of this thesis is based. It will cover topics in quantum information, ion trapping, and quantum optics that are used throughout the thesis to explain the various experiments described therein. As such, this Chapter aims to create a solid basis upon which to build an understanding of the remaining Chapters.

2.1 Quantum Information

The first of these concepts to be introduced is the field of quantum information. This term includes a broad range of topics, however this Section will focus in particular on introducing the quanta of information used for quantum computing and simulation. It will look at how these quanta can (and are) used to perform computations and simulations, and the various problems such as error processes which arise during practical implementation of these technologies.

2.1.1 Quantum Bits

In classical information science, information is encoded in fundamental units of information known as bits which can take the values ‘0’ or ‘1’. There is a quantum-mechanical analogue to classical binary bits termed the quantum bit, or *qubit.* In contrast to classical bits, qubits can take on values between 0 and 1 – they can be in what are known as coherent superpositions of both states, an infinite number of which exist. Mathematically, a general, pure-state qubit can be expressed as:

$$|\psi\rangle = \alpha|0\rangle + \beta|1\rangle, \tag{2.1}$$

where α and β are two complex numbers such that $|\alpha|^2 + |\beta|^2 = 1$. Equation 2.1 represents that, upon asking the question *“is $|\psi\rangle$ in the state 0 or 1?"*, the probability for the answer to be 0 is $|\alpha|^2$, and to find the the answer to be 1 is $|\beta|^2$. Here, the short form notation for a vector, known as Dirac-notation or 'Bra-ket' notation, has been used where $|0\rangle = \begin{pmatrix}1\\0\end{pmatrix}$ and $\langle 0| = \begin{pmatrix}1 & 0\end{pmatrix}$, $|1\rangle = \begin{pmatrix}0\\1\end{pmatrix}$ and $\langle 1| = \begin{pmatrix}0 & 1\end{pmatrix}$.

Equation 2.1 can also be written in terms of spherical coordinates, where it takes the form:

$$|\psi\rangle = e^{-i\alpha}\left[\sin(\theta/2)|0\rangle + e^{-i\phi}\cos(\theta/2)|1\rangle\right], \tag{2.2}$$

where α, θ and ϕ are real numbers. α is a global phase which has no absolute reference point and so can be set to any arbitrary value. Normally, the most straightforward value to assign to the global phase is $\alpha = 0$. Equation 2.2 is a very useful way of expressing a qubit as it can be shown visually on a sphere. The sphere which contains all possible single-qubit $|\psi\rangle$s is termed the ***Bloch sphere***, and provides a simple, yet extremely powerful, way to visualise single-qubit behaviour. Figure 2.1 shows an example of the Bloch sphere, where the basis states $|0\rangle$ and $|1\rangle$ are here defined as being at the poles of the sphere. A qubit can occupy all states on the surface of the sphere (the pure states), as well as inside the sphere (so-called mixed states). Shown on the surface of the sphere in Figure 2.1 is an example of a pure state, $|\psi\rangle$. Each state has an associated ***Bloch vector***, which is a vector pointing to the state in question, shown in the Figure as a black arrow pointing to $|\psi\rangle$. The Bloch vector is defined as:

$$\vec{r} = r_x\sigma_x + r_y\sigma_y + r_z\sigma_z, \tag{2.3}$$

where σ_i are the Pauli matrices, a set of matrices forming an orthogonal basis and spanning the Hilbert space $\mathscr{H}$, defined as

$$\mathbb{I} = \begin{pmatrix} 1 & 0 \\ 0 & 1 \end{pmatrix}, \quad \sigma_x = \begin{pmatrix} 0 & 1 \\ 1 & 0 \end{pmatrix}, \quad \sigma_y = \begin{pmatrix} 0 & -i \\ i & 0 \end{pmatrix}, \quad \sigma_z = \begin{pmatrix} 1 & 0 \\ 0 & -1 \end{pmatrix}. \tag{2.4}$$

For a pure state, the length of the Bloch vector is 1 – i.e. $|\vec{r}|^2 = r_x^2 + r_y^2 + r_z^2 = 1$. Thus, for single-qubit states, a pure state will always lie on the surface of the Bloch sphere.

A convenient way of describing quantum states is through the ***density matrix***. This representation is particularly useful when considering states which are not pure, known as mixed states, as well as for multi-qubit states. The density matrix for a pure quantum state, $|\psi\rangle$, can be expressed as:

$$\rho = |\psi\rangle\langle\psi|. \tag{2.5}$$

Mixed states are statistical mixtures of pure states, such that:

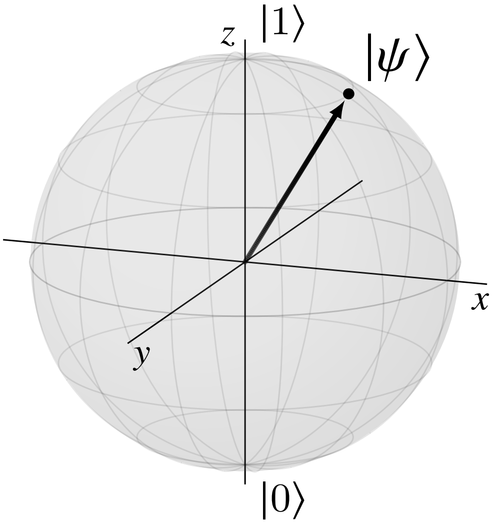

Figure 2.1: **The Bloch Sphere**. The Bloch sphere graphically represents all possible states a single qubit can occupy. The qubit can occupy states on the surface of the sphere (pure states) as well as inside the sphere (mixed states). The black dot signifies a pure state, $|\psi\rangle$, on the surface of the Bloch sphere, with its associated Bloch vector (shown by the black arrow).

$$\rho_{\text{mix}} = \sum_i P_i |\psi_i\rangle\langle\psi_i|, \tag{2.6}$$

where $P_i|\psi_i\rangle\langle\psi_i|$ is the contribution of the i^{th} pure state to the mixture (equivalent to the probability of that particular pure state being present in the mixture), and $\sum_i P_i = 1$. Mixed states have a Bloch vector whose length is less than one, $|\vec{r}|^2 < 1$ – that is, mixed states lie inside the Bloch sphere.

The ***purity*** of a state is a useful quantity which will come up often throughout this thesis. It gives a measure of how much the state is mixed and is defined, for a single qubit state ρ, by:

$$P(\rho) = \mathrm{Tr}(\rho^2) = \frac{1}{2}(1 + |\vec{r}|^2), \tag{2.7}$$

where Tr is the trace and $|\vec{r}|^2$ is the single-qubit Bloch-vector length. If a single-qubit state is completely pure, its purity is equal to 1. Conversely, if it is completely mixed (so lying at the centre of the Bloch sphere), its purity is equal to $1/2$.

For multiple qubits, the total Hilbert space expands as the tensor product of all the individual Hilbert spaces. For example, take N qubits; the total Hilbert space, $\mathscr{H}_N$, is given by:

$$\mathcal{H}_N = \mathcal{H}_n^{\otimes N} = \mathcal{H}_n \otimes \mathcal{H}_{n-1} \otimes \ldots \otimes \mathcal{H}_1, \tag{2.8}$$

where $\mathcal{H}_i$ are the Hilbert spaces of the individual qubits. The purity of a multiqubit state is likewise found from $P(\rho) = \mathrm{Tr}(\rho^2)$, with the purity for a completely mixed state given by $1/2^N$ (i.e. $P(\rho) \in \left[1, \frac{1}{2^N}\right]$).

Quantum Operations, Gates, and Hamiltonians

A quantum operation is a linear map which takes an arbitrary initial state ρ to another output state $\Lambda(\rho)$, where both ρ and $\Lambda(\rho)$ belong to the same Hilbert space, $\mathcal{H}$. In the context presented here, these maps will represent physical processes that can be performed in the experimental system. In order to represent physical processes, these maps have two requirements: (i) for any initial state ρ, the end state $\Lambda(\rho)$ must always be positive semi-definite (i.e. the eigenstate of any observable must have a non-negative probability) such that $\Lambda(\rho)$ is a valid density operator for any initial state ρ. These properties should remain true even if the operation is applied only to a subsystem of the total system, a requirement known as Complete Positivity, CP (ii) the total probability must be conserved such that, for a quantum operation E_i, $\sum_i E_i^\dagger E_i = \mathbb{I}$ (Trace Preservation, TP) [12]. The combination of these two requirements is that the map must be CPTP.

A quantum gate is an example of such a linear map acting on a quantum system. Some of the most famous quantum gates are the Pauli operators introduced in Equation 2.4. These operators are unitary operators, and can be used to rotate a qubit to different points on the Bloch sphere. For example, consider a qubit prepared in the initial state $|\psi_0\rangle = |0\rangle$. Application of a σ_x gate will rotate the state of this qubit around the Bloch sphere to the final state $|\psi_f\rangle = |1\rangle$. Combinations of all the Pauli operators allow an arbitrary initial pure state to be rotated to any other arbitrary pure state on the surface of the Bloch sphere.

An interesting question to now consider is how to describe the evolution of a single-qubit state in time. Imagine a simple example of a state, $|\psi\rangle$, described by a two level system with states labelled $|0\rangle$ and $|1\rangle$. One of the most important properties to know about a quantum system is its energy, which is described by its Hamiltonian, H. The Hamiltonian of this two-level system can be described by:

$$H = \frac{\hbar\omega}{2}\sigma_z, \tag{2.9}$$

where $\hbar\omega$ is the energy splitting between the two states $|0\rangle$ and $|1\rangle$. The evolution of the state under the influence of a Hamiltonian can be subsequently described by a ***propagator***. In general, a propagator can be expressed as:

$$U = e^{-iHt/\hbar}. \tag{2.10}$$

As H is Hermitian, the propagator must be unitary, which has interesting consequences for quantum systems: namely, unitarity shows that the propagator must have an inverse, and so every quantum evolution is reversible.

Therefore, using the propagator $U = e^{-i\omega t\sigma_z/2}$, at a later time t an initial state $|\psi_0\rangle = \alpha|0\rangle + \beta|1\rangle$ will have evolved into:

$$|\psi(t)\rangle = U|\psi_0\rangle = \alpha|0\rangle e^{-i\omega t/2} + \beta|1\rangle e^{i\omega t/2}. \tag{2.11}$$

2.1.2 Quantum Correlations, Entanglement, & Noise

Quantum computers and simulators are predicted to be able to solve some problems with an exponential speed-up compared to their classical counterparts [7, 27, 28]. However, it has been shown that pure product states, as well as those systems which generate only a small amount of entanglement, can still be efficiently simulated using a classical computer [29]. As such, quantum computers and simulators must generate large amounts of entanglement between their parts in order to achieve this fabled exponential speed-up. However, it seems that entanglement alone may not be entirely responsible for this speed-up, with general quantum correlations theorised to be necessary [30, 31]. This Section will now look at quantum correlations and entanglement, as well as noise processes which can interfere with the performance of such computations and simulations.

Entropy, Information, and Quantum Correlations

As quantum systems can be in both pure and mixed states, the question can be asked as to how to quantify the amount of information contained in such a state. Both entropy and correlations are frequently encountered in a classical setting, which will be considered first here before being generalised to the quantum setting. A famous example is that of the Shannon entropy [32, 33], which expresses the amount of information known about a certain event. Take a random variable X which has n possible outcomes, $x_1, \ldots, x_n$. If each of these possible outcomes occurs with probability $p(x_i)$, then the Shannon entropy is given by [33]:

$$S(X) = S(p(x)) = -\sum_i^n p(x_i) \log_2 p(x_i). \tag{2.12}$$

The Shannon entropy provides a quantification of the amount of uncertainty in X. The amount of correlation between X and a second random variable Y – that is the amount of relation there is between X and Y – can then be quantified using their joint distribution [33]:

$$S(X,Y) = S(p(x,y)) = -\sum_{i,j} p(x_i, y_j) \log_2 p(x_i, y_j), \tag{2.13}$$

where $p(x_i, y_j)$ is the probability of obtaining outcomes x_i and y_j . Further intuition as to the degree of correlation between X and Y can then be obtained from a quantity known as the *mutual information.* This is defined as:

$$I(X : Y) = S(p(x)) + S(p(y)) - S(p(x, y)), \tag{2.14}$$

where $I(X : Y) \geq 0$. What this equation shows is that the sum of the uncertainties of $p(x)$ and $p(y)$ is always equal to, or larger than, the uncertainty of their joint distribution [33]. For classical information, the maximum value the mutual information can take is $\log_2(2)$.

Analogous concepts to both of these quantities exist with regards to quantum states. The first of these is the quantum analogy to the Shannon entropy, and is termed the von Neumann entropy. The von Neumann entropy of a state ρ is defined to be [34]:

$$S(\rho) = -\mathrm{Tr}(\rho \log_2(\rho)) = -\sum_{i}^{n} \lambda_i \log(\lambda_i), \tag{2.15}$$

where λ_i are the eigenvalues of ρ. From comparing these two expressions it can be seen that density operators take the role of probability distributions in the Shannon entropy. The von Neumann entropy is zero for pure states, and greater than zero for mixed states. The maximum value the entropy can take is when a state is completely mixed – i.e. $\rho = \mathbb{I}/d$, where d is the dimension of the Hilbert space – in which case $S(\rho) = \log_2(d)$.

The concept of mutual information can also be extended to the quantum setting. Consider a bipartite state ρ_{AB}; that is, a state comprised of two parts A and B, where the state of A is represented by $\rho_A = \mathrm{Tr}_A(\rho_{AB})$ and the state of B is represented by $\rho_B = \mathrm{Tr}_B(\rho_{AB})$. The information content between the two subsystems can be expressed in terms of the von Neumann mutual information. The von Neumann mutual information between ρ_A and ρ_B is defined as:

$$I(\rho_A : \rho_B) = S(\rho_A) + S(\rho_B) - S(\rho_{AB}). \tag{2.16}$$

This mutual information quantifies the correlation between the subsystems ρ_A and ρ_B.

Entanglement

Entanglement is one of the most interesting features of quantum information. In order for quantum computers and quantum simulators to provide advantages over their classical analogues, large amounts of entanglement must be generated within their constituent parts [29].

Entanglement is a fascinating phenomenon, whereby multiple particles cannot be described independently of one another. That is, in a system comprised of two particles, say A and B, the state of the combined system, AB, cannot be described by the states of the two individual particles – i.e. $\rho_{AB} \neq \rho_A \otimes \rho_B$ [35, 36]. Such a state is known as non-separable.

A simple example which can demonstrate this is one of the well-known Bell states:

$$|\Psi\rangle = \frac{1}{\sqrt{2}} \left(|00\rangle + |11\rangle \right) . \tag{2.17}$$

Here it can be seen that it is not possible to write Equation 2.17 as a product of the two individual qubits. For a pure quantum state such as the one in Equation 2.17, the amount of entanglement can be quantified using the von Neumann entropy. To understand this relation, again consider a bipartite system containing two qubits, labelled A and B, with the total system described by the density matrix ρ_{AB}. The state of qubit A can be represented as ρ_A and the state of qubit B as ρ_B. If ρ_{AB} is a pure, separable state, then $S(\rho_{AB}) = S(\rho_A) = S(\rho_B) = 0$. However, if instead ρ_{AB} is an entangled state, then a measurement of ρ_A will not contain the whole information of the system. As such, this effective 'loss of information' can be seen as an increase in the entropy of the subsystem, and so $S(\rho_{AB}) < S(\rho_A) = S(\rho_B)$. As such, *if the subsystems of a bipartite system ρ_{AB} have greater entropy than the entropy of the whole system, then entanglement exists between ρ_A and ρ_B* [36]. The entanglement can be viewed as the lack of information of the reduced states, when compared to that of the whole state ρ_{AB}. The more entanglement contained in ρ_{AB}, the less information it is possible to have about the system from measurements of the states of ρ_A and ρ_B [33]. For a maximally entangled pure state, $S(\rho_{AB}) = 0$, however the subsystems will be maximally mixed, with $S(\rho_A) = S(\rho_B) = \mathbb{I}/2$.

The distinction between classical and quantum correlations can be highlighted by looking at the mutual information of a classical and entangled state. For a classical state, the maximum possible Shannon mutual information between two random variables is $\log_2(2)$. Conversely, the von Neumann mutual information for a maximally entangled state has a value of $2\log_2(2)$ (although for more weakly entangled states this value is reduced) [33]. It is this potential for the existence of stronger correlations in certain quantum systems than classical systems which are generally considered to be the crucial resource for quantum information processing, and its associated predicted speed-up compared to classical systems.

Coherent & Incoherent Errors

Practically, operations on qubits are subject to many different error processes. For example, crosstalk between qubits and environmental noise, to name many others, can cause the single qubit Bloch sphere to appear to shrink along one or more of its axes. In working towards fully realising quantum computation and simulation, it is therefore important to identify and, if possible, to eliminate such errors in order to implement better qubit operations.

One type of error which can arise in quantum systems are so-called coherent errors. These are errors which preserve the purity of the initial state and so are unitary operations, leaving the Bloch sphere of the qubit unchanged. A common example of a coherent error is an over/under rotation of an implemented gate – e.g. where, rather than implementing a π rotation on a state on the Bloch sphere, a $\pi \pm \delta$ rotation is instead implemented. Other examples of such coherent errors are cross-talk between qubits and unwanted qubit-qubit interactions [37].

In a perfect world, all the quantum gates and evolution dynamics discussed so far would be unitary – i.e. the Bloch vector length would remain unchanged throughout all gate processes and evolution of the system. However, unwanted interactions of the system with the environment can cause this evolution to not be truly unitary, a process which is collectively termed *decoherence*. When decoherence affects a system, the state of the system, $|\psi\rangle$, is known only probabilistically and the system becomes mixed, with the Bloch vector length correspondingly being less than one. Decoherence can be a major problem in the realisation of quantum computers and simulators as the errors which arise from it can cause information to be lost. As such, the understanding and control of decoherence is crucial in being able to utilise the full potential of these technologies.

As incoherent errors cannot be described by unitary operations, instead the evolution must be considered in terms of density matrices. Consider an initial state, ρ, which undergoes an incoherent error operation such that $\rho \rightarrow \Lambda(\rho)$. A general CPTP map (see Section 2.1.1) representing this process can be written as [38]:

$$\Lambda(\rho) = \sum_{j=1}^{n} K_j \rho K_j^{\dagger}. \tag{2.18}$$

Here, the operators $K_1, \ldots, K_n$ are the *Kraus operators* which model quantum operations, and $n \leq d^2$ for a system of Hilbert space dimension d. To ensure Equation 2.18 fulfils the trace-preserving condition, the Kraus operators must satisfy $\sum_i K_i^{\dagger} K_i = \mathbb{I}$.

A common example of such incoherent noise processes is known as *dephasing*, where the environment induces random phase changes in the state of the qubit. It is caused when the energy splitting of a qubit changes as a function of time, for example due to environmental influences such as laser frequency fluctuations and changes in the magnetic field. Dephasing can be represented by a phase-flip channel [12], where phase information is lost with a probability p, with the identity operation performed with probability $1 - p$. In this situation, the phase, ϕ, of the state becomes more uncertain with time and phase coherence is lost. Figure 2.2 a) shows a graphical representation of this process. The Bloch sphere effectively shrinks around the equator, being projected onto the Z-axis of the Bloch sphere, while remaining unchanged at the poles.

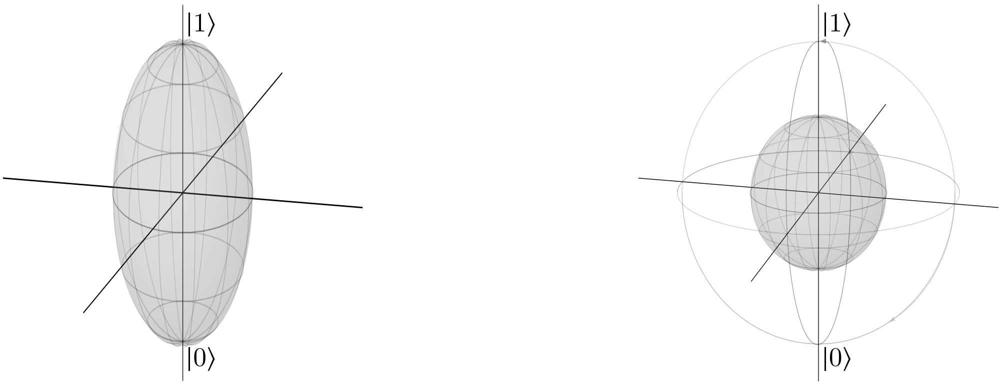

(a) Dephasing (b) Depolarisation

Figure 2.2: **Noise Processes affecting the Bloch Sphere**. a) The effect of dephasing on the Bloch Sphere. The sphere shrinks uniformly about the equator, with the Z-axis remaining unaffected. b) The effect of depolarisation on the Bloch Sphere. The sphere shrinks uniformly around all three axes. Shown in light grey is an outline of the shape of the un-deformed Bloch sphere for comparison.

Dephasing can be described by a quantum map given by [38]:

$$\Lambda_{\text{deph}}(\rho) = \left(1 - \frac{p}{2}\right)\rho + \frac{p}{2}\sigma_z\rho\sigma_z, \tag{2.19}$$

which takes the initial state ρ to $\Lambda_{\text{deph}}(\rho)$. The Kraus operators for this operation are:

$$K_0 = \sqrt{1 - \frac{p}{2}}\mathbb{I} \qquad \text{and} \qquad K_1 = \sqrt{\frac{p}{2}}\sigma_z. \tag{2.20}$$

Another common source of noise in such systems is *depolarisation*, which can be modelled by an associated depolarising noise channel. Depolarisation is a process where information is completely lost with some probability p, remaining unchanged with probability $1 - p$. This is a quantum operation which replaces the initial input state, ρ, with the maximally mixed state with probability p, implementing the identity operation with probability $1 - p$ [12]. Figure 2.2 b) shows the effect of this operation on the Bloch sphere, where the depolarising noise can be seen to cause a uniform shrinking of the Bloch sphere. The quantum map which represents this process is given by [12]:

$$\Lambda_{\text{dep}}(\rho) = \left(1 - \frac{3}{4}p\right)\rho + \frac{p}{4}(\sigma_x\rho\sigma_x + \sigma_y\rho\sigma_y + \sigma_z\rho\sigma_z). \tag{2.21}$$

For this operation, the Kraus operators are:

$$K_0 = \sqrt{1 - \frac{3p}{4}}\mathbb{I}, \qquad K_1 = \frac{\sqrt{p}}{2}\sigma_x, \qquad K_2 = \frac{\sqrt{p}}{2}\sigma_y, \qquad \text{and} \qquad K_3 = \frac{\sqrt{p}}{2}\sigma_z. \tag{2.22}$$

The final noise process discussed here is that of spontaneous emission (also known as amplitude damping). It effectively describes a loss of energy from a quantum system, with a common example of spontaneous emission being the transition of an atom from its excited state to its ground state with the emission of a photon [12]. Spontaneous emission occurs at a random point in time, however at a rate which can be determined, and is unique to the species of ion as well as the excited state in question. For spontaneous emission, the Kraus operators are given by:

$$K_0 = \begin{pmatrix} 1 & 0 \\ 0 & \sqrt{1-p} \end{pmatrix} \qquad \text{and} \qquad K_1 = \begin{pmatrix} 0 & \sqrt{p} \\ 0 & 0 \end{pmatrix}. \tag{2.23}$$

This Section has given an overview of some of the most important aspects of quantum information which are necessary for understanding the remainder of this thesis. The next Section will now go on to look at trapped ions, which are one of the many platforms available for encoding quantum information, and which are the platform of choice for the work presented in this thesis.

2.2 Trapped Ions

Trapped ions are one of the most attractive platforms for quantum information processing. Their charge enables them to be effectively confined and spatially manipulated, allowing almost unrivalled control at the single-particle level. There are two main types of trap which are typically used for low-energy applications – the radio frequency (RF) trap and the Penning trap [39]. Penning traps use a combination of electric and magnetic fields to confine charged particles, and were first pioneered by Hans Dehmelt in the 1960s [40]. RF-traps, in contrast, use a combination of static and time-dependent electric fields, with one of the most famous of such traps being the Paul trap, developed by Wolfgang Paul [41, 42]. As ion trapping, including in linear Paul traps, has been treated in great detail in references such as [39, 42, 43], only a brief overview of the major points will be given in the following Section.

2.2.1 Paul Traps

To be confined in three dimensions, charged particles require there to be a potential energy minimum at some region in space. This ensures that the corresponding restoring force on the particle is directed towards that region in all three dimensions. As such, if the particle makes an excursion away from the minimum point, it experiences a force which pushes it back towards the minimum once more. A convenient form for this binding potential is that of a harmonic well, where the restoring force increases linearly with the particle's excursion away from the minimum:

$$F_u = -k_u u, \qquad \text{for } u = x, y, z\ , \tag{2.24}$$

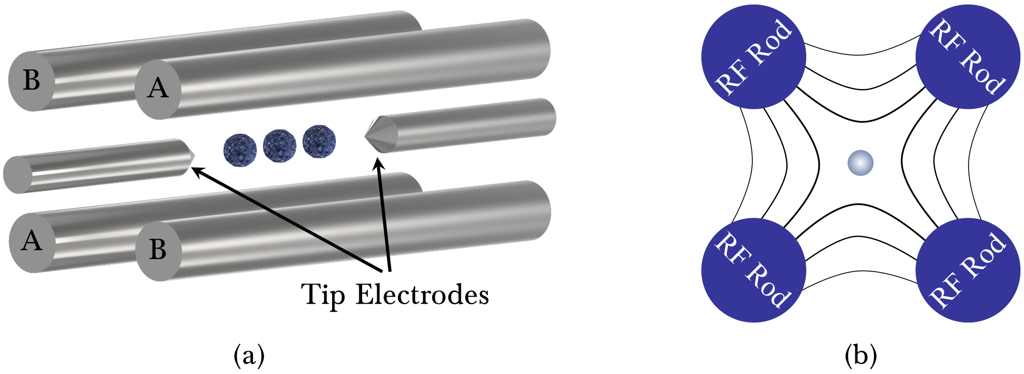

(a) (b)

Figure 2.3: **Linear Paul Trap** a) Schematic representation of a standard linear Paul trap. The electrodes labelled 'A' are at the same potential (e.g. ϕ_+), and those labelled 'B' are likewise at the same potential with opposite sign to the A electrodes (e.g. ϕ_-). These voltages then oscillate between ϕ_+ and ϕ_- at an RF frequency. This creates a time-dependent saddle potential where the ion is confined. The two tip electrodes, held at a constant DC voltage, provide confinement along the axial direction. b) RF-potential formed by the RF electrodes as viewed along the axial direction. The saddle potential formed by this arrangement provides a stable minimum at the centre where trapping can occur.

with k_u the force constant. As $\vec{F} = -\vec{\nabla}\Phi$, the general potential Φ associated with this force has a harmonic form such that:

$$\Phi(x, y, z) = \Phi_0(\alpha x^2 + \beta y^2 + \gamma z^2), \tag{2.25}$$

where α, β and γ are constant coefficients, and Φ_0 can be a time-dependent function. In free space, where no electric charges are present, Laplace's equation $\vec{\nabla}^2\Phi = 0$ must be satisfied. In order to satisfy Laplace's equation, this implies that the coefficients of Equation 2.25 must themselves then satisfy $\alpha + \beta + \gamma = 0$, and so at least one coefficient must be negative, implying the potential has a metastable saddle point. A stable trapping potential can then be generated in two main ways: Firstly, by using a combination of electric and magnetic fields, as with the Penning trap [40]. Secondly, and more importantly for this work, by using electric fields where Φ_0 is time-varying in one or more directions, forming a 'time-dependent saddle potential', as is the case with the Paul trap.

Figure 2.3 a) shows a schematic of a common design for linear Paul traps. In such a Paul trap, the time-varying electric field is generated by applying voltages oscillating at RF frequencies to the four rod electrodes labelled A and B. The electrodes labelled A have the same voltage, which is opposite in sign to those labelled B. The tip electrodes provide a constant confinement in the axial direction. The potential, Φ, can be correspondingly divided into a time-dependent radial part, Φ_r, and a static axial part, Φ_a, such that [43]:

$$\Phi_{\rm r}(x,y,z,t) = \frac{U_{\rm RF} + V_{\rm RF}\cos(\Omega t)}{2}\left(\alpha_x x^2 + \alpha_y y^2 + \alpha_z z^2\right) \tag{2.26}$$

$$\Phi_{\rm a}(x,y,z) = \frac{U_{\rm DC}}{2}\left(\beta_x x^2 + \beta_y y^2 + \beta_z z^2\right). \tag{2.27}$$

Here, $U_{\rm RF}$ and $V_{\rm RF}$ are a static splitting voltage and peak amplitude of an alternating voltage respectively, both of which are applied to the rod electrodes. Ω is the frequency at which the RF field oscillates, and $U_{\rm DC}$ is the static voltage applied to the tip electrodes to provide axial confinement. Figure 2.3 b) shows the radial potential formed by such an arrangement of RF rod electrodes: A stable minimum is formed at the centre of this time-dependent saddle-potential, allowing confinement of a charged particle at the centre.

The oscillation of the time-dependent potential must be made rapid enough such that the charged particle undergoes an oscillatory motion between the electrodes, without ever making contact with them [44]. The motion of a particle in such a confinement is then given by a differential equation of the form:

$$\frac{d^2u}{dt^2} + \frac{\Omega^2}{4}(a_u - 2q_u\cos\Omega t)u = 0, \quad \text{where} \quad u = x, y, z. \tag{2.28}$$

a_u and q_u are determined solely by the experimental parameters. Assuming the potential is rotationally invariant about the axial direction, then these parameters can be expressed as [45]:

$$a_x = a_y = -\frac{1}{2}a_z = -\frac{8QU_{\rm DC}}{m(r_0^2 + 2z_0^2)\Omega^2}, \tag{2.29}$$

$$q_x = q_y = -\frac{1}{2}q_z = \frac{4QV_{\rm RF}}{m(r_0^2 + 2z_0^2)\Omega^2}, \tag{2.30}$$

where Q is the charge of the particle to be confined. Equation 2.28 has very well-known, stable solutions [46], determined solely by the parameters a_u and q_u. In the limit of $0 < a_u < q_u < 1$, these solutions can be approximated as:

$$u(t) = A_u\cos(\omega_u t + \phi_u)\left(1 + \frac{q_u}{2}\cos(\Omega t)\right), \tag{2.31}$$

where A_u is a constant and $\omega_u = \beta_u\Omega/2$ is the secular frequency, with $\beta_u = \sqrt{(a_u + \frac{q_u^2}{2})}$.

The motion of a single particle under this potential can be understood as being comprised of two motions. The first of these is a harmonic motion at the secular frequency, ω_u, which is known as the secular motion. The second is a fast, driven motion at the trapping frequency Ω, and is known as micromotion. The amplitude of this micromotion is proportional to the distance of the particle from the RF-null (i.e. from the centre of the trap).

Paul traps are often used for confinement of multiple ions. For a linear string of ions to be formed, the confinement in the radial direction must be sufficiently higher than in the axial direction, corresponding to the radial secular centre-of-mass (COM) frequency being significantly higher than the axial COM frequency [47].

2.2.2 Quantum Harmonic Oscillators and Coherent States of Motion

The previous Section has introduced the functionality of the linear Paul trap, including its 3-dimensional confinement using a radial harmonic pseudo-potential, and an axial harmonic potential. Paul traps often have excellent optical access, which allows laser cooling of ions to be performed [48]. Due to the low temperature regime resulting from such cooling (on the order of 0.5 K for Doppler cooling, and even to the ground state for sideband cooling [49]), a quantum description of the ion motional energy is therefore needed.

One of the most well-known classical harmonic oscillators is the example of a particle of mass m oscillating in a quadratic potential of the form $V(x) = m\omega^2x^2/2$, with x the spatial coordinate and ω the oscillation frequency of the particle in the potential. This motion can also be represented in phase space, where the oscillator traces out a circle. Figure 2.4 a) shows an example of this situation, with the particle following the relation $\alpha(t) = |\alpha|e^{i\omega t}$, where $\alpha = x + ip$ and p is the momentum.

The quantum harmonic oscillator is the quantum analogue to the classical harmonic oscillator, an excellent treatment of which is given in [50]. In the regime where the kinetic energy of a harmonically confined particle becomes comparable to $\hbar\omega$, its motion becomes quantised. The Hamiltonian describing the motion of the particle is then a sum of its kinetic and potential energy, with the position and momentum operators, $\hat{x}$ and $\hat{p}$, replacing their classical counterparts:

$$H = \frac{1}{2}m\omega^2\hat{x}^2 + \frac{1}{2m}\hat{p}^2, \tag{2.32}$$

where m is the mass of the particle and ω the frequency of oscillation. By introducing the well-known creation and annihilation operators:

$$a^\dagger = \frac{1}{\sqrt{2m\hbar\omega}}(m\omega\hat{x} - i\hat{p}), \qquad a = \frac{1}{\sqrt{2m\hbar\omega}}(m\omega\hat{x} + i\hat{p}), \tag{2.33}$$

the position and momentum operators can be re-expressed as:

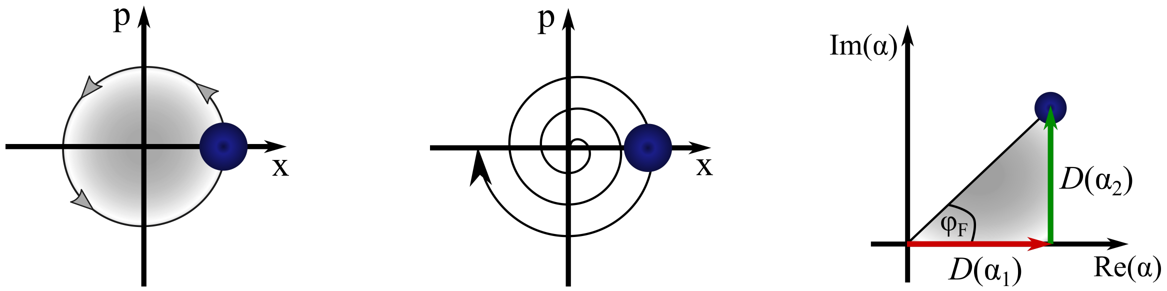

(a) Classical Simple Harmonic Oscillator

(b) Driven Harmonic Oscillator

(c) Displacement Operator

Figure 2.4: **Phase Space Representations** a) Trajectory of the classical simple harmonic oscillator. For a non-driven system, the particle follows a circular trajectory, with a complete circle corresponding to a single period of oscillation. b) The resonantly driven harmonic oscillator follows a path in phase space which spirals outwards with time, due to the constantly increasing amplitude. c) In moving to a frame which rotates at the drive frequency, ω_F, displacements of the initial motional ground state, $|0\rangle$, create a coherent state, $|\alpha\rangle$. The angle of this displacement is determined by the phase of the driving force, ϕ_F.

$$\hat{x} = (a + a^\dagger)x_0 \qquad \text{and} \qquad \hat{p} = i\frac{\hbar}{2x_0}(a^\dagger - a), \tag{2.34}$$

with $x_0 = \sqrt{\hbar/(2m\omega)}$. x_0 represents a characteristic length scale which, for the case of a trapped ion, corresponds to the root-mean-square extent of the ion's ground-state wavefunction. Equation 2.32 can then be expressed as:

$$H_{\text{qho}} = \hbar\omega\left(a^\dagger a + \frac{1}{2}\right) = \hbar\omega\left(\hat{n} + \frac{1}{2}\right), \tag{2.35}$$

with $\hat{n} = a^\dagger a$ the number operator. This Hamiltonian has a distinctive ladder-like energy spectrum with the eigenstates, $|n\rangle$ (also known as Fock states or number states), separated by an amount $\hbar\omega$. The application of the creation and annihilation operators (defined in Equation 2.33) to a given eigenstate, $|n\rangle$, raises or lowers the energy of the harmonic oscillator by one phonon respectively [50]:

$$a^\dagger|n\rangle = \sqrt{n+1}|n+1\rangle, \qquad a|n\rangle = \sqrt{n}|n-1\rangle \;\; \text{with} \;\; a|0\rangle = 0. \tag{2.36}$$

By applying the creation operator $a^\dagger$ n-times to the ground state $|0\rangle$, any Fock state $|n\rangle$ can be created via:

$$|n\rangle = \frac{1}{\sqrt{n!}}(a^\dagger)^n|0\rangle. \tag{2.37}$$

Driven Quantum Harmonic Oscillator

States which will be shown to be of significant interest later in this Chapter can be formed by considering the action of time-dependent forces on the quantum harmonic oscillator. Consider an external, time-dependent (classical) force of the form:

$$F(t) = A\sin(\omega_F t + \phi_F) = \frac{A}{2i}\left(e^{i(\omega_F t+\phi_F)} - e^{-i(\omega_F t+\phi_F)}\right), \tag{2.38}$$

with amplitude A, drive frequency ω_F, and phase ϕ_F. When this force is applied to a quantum harmonic oscillator, the Hamiltonian of Equation 2.35 needs to be extended such that $H = H_{\text{qho}} + H_F(t)$, where $H_F(t) = \hat{x}F(t)$. If the frequency of the driving force is made equal to the oscillation frequency of the particle, i.e. $\omega_F = \omega$, then the particle follows a spiral trajectory in phase space, as shown in Figure 2.4 b).

The effect of this force can best be seen by moving to the interaction picture using the transformation $U = e^{-iH_{\text{qho}}t/\hbar}$, such that $U|\psi\rangle = |\psi'\rangle$. Transformations into the interaction picture are explained and explicitly derived in Appendix B.1. The Hamiltonian in the interaction picture is then given by:

$$H_{\text{int}} = U^\dagger H U = \left(a e^{-i\omega t} + a^\dagger e^{i\omega t}\right) x_0 F(t). \tag{2.39}$$

For $\omega_F = \omega$, the rotating wave approximation (RWA) – where rapidly rotating terms are neglected – can subsequently be used to simplify Equation 2.39 to:

$$H_{\text{int}} = -\frac{A x_0}{2i}\left(a e^{-i\phi_F} + a^\dagger e^{i\phi_F}\right). \tag{2.40}$$

The time-evolution of a state under this Hamiltonian, given by $U = e^{-iH_{\text{int}}t/\hbar}$, can then be expressed by the unitary operator:

$$D(\alpha) = e^{\alpha a^\dagger - \alpha^* a} \qquad \text{where} \qquad \alpha = -\frac{A x_0 t}{2\hbar} e^{-i\phi_F}. \tag{2.41}$$

This propagator is known as the *displacement operator.* When this displacement operator is applied to the ground state of motion, $|0\rangle$, the result is a displaced coherent state [50]:

$$|\alpha\rangle = D(\alpha)|0\rangle = e^{-|\alpha|^2/2} \sum_n \frac{\alpha^n}{\sqrt{n!}}|n\rangle. \tag{2.42}$$

If such a state is viewed in the frame which rotates at the same frequency as that of the drive frequency, as shown in Figure 2.4, then the displacement operator can be seen to act such that it displaces the state linearly in phase space, with the direction of displacement dependent on the phase of the driving force ϕ_F.

Coherent states are the closest 'quantum' analogy to the classical states of a harmonic oscillator [50]. The creation and annihilation operators act on them such that:

$$a|\alpha\rangle = \alpha|\alpha\rangle, \qquad \text{and} \qquad \langle\alpha|a^\dagger = \alpha^*\langle\alpha|. \tag{2.43}$$

This Section has described how the motion of particles in low temperature regimes, such as those achieved through laser cooling of an ion in a linear Paul trap, requires a quantum description. The motion of such a particle can be described (approximately) using the quantum harmonic oscillator, with coherent states of motion created through application of a resonant driving force to the particle. The following Section will now give an overview of the ion used to encode quantum information in this thesis, detailing the relevant atomic structure and properties which make it an ideal candidate for use in quantum simulation.

2.2.3 ^{40}Ca$^+$ as a qubit

The experiments presented in this thesis use singly-ionised calcium-40, ^{40}Ca$^+$, to encode quantum information. ^{40}Ca$^+$ has a hydrogen-like electronic energy structure, and is ideal for use as a qubit for multiple reasons, such as its relatively simple level structure, easily accessible optical transitions, and metastable levels. It has a nuclear spin of zero, meaning it has no hyperfine structure. ^{40}Ca$^+$ is formed by a two-step ionisation process of neutral calcium, using lasers at wavelengths of 422 nm and 375 nm.

Figure 2.5 shows a simplified level structure of ^{40}Ca$^+$, containing the most relevant electronic energy levels and transitions for this thesis. The four main levels of importance to this thesis are the $|\mathrm{S}_{1/2}\rangle$, $|\mathrm{D}_{5/2}\rangle$, $|\mathrm{P}_{1/2}\rangle$, and $|\mathrm{P}_{3/2}\rangle$ levels. Each of these levels are split into Zeeman levels by application of an external magnetic field. As the lifetime of the $|\mathrm{P}_{1/2}\rangle$ and $|\mathrm{P}_{3/2}\rangle$ levels is extremely short (~7 ns), the splitting between the Zeeman levels of these levels is smaller than the width of the level itself, and so the Zeeman substructure is not shown in the Figure. In contrast, the $|\mathrm{D}_{5/2}\rangle$ level is a so-called 'metastable state', with a lifetime on the order of 1 s. This state is ideal for use in quantum information due to its long-lifetime. As such, an optical qubit can be encoded in ^{40}Ca$^+$ using the electronic ground state $|\mathrm{S}_{1/2}\rangle$ as $|0\rangle$ and the metastable $|\mathrm{D}_{5/2}\rangle$ state as $|1\rangle$, coupled using a narrow linewidth laser at 729 nm. Lasers at 866 nm and 854 nm optically pump population out of the $|\mathrm{D}_{3/2}\rangle$ and $|\mathrm{D}_{5/2}\rangle$ respectively to allow initialisation of the optical qubit in $|\mathrm{S}_{1/2}\rangle$. This optical qubit will form a major part of the following Chapters in this thesis.

A qubit can also be encoded in ^{40}Ca$^+$ using the Zeeman levels of the ground state $|\mathrm{S}_{1/2}\rangle$. It will be seen in Chapter 8 that the two Zeeman levels, given by $|\mathrm{S}_{1/2}, \mathrm{m_j} = -1/2\rangle$ and $|\mathrm{S}_{1/2}, \mathrm{m_j} = +1/2\rangle$, can be coupled using two lasers at ~393 nm.

The three main transitions of importance to this work are from these ground state Zeeman levels to the $|\mathrm{P}_{1/2}\rangle$ level (via the 397 nm transition), to the $|\mathrm{P}_{3/2}\rangle$ level (via the 393 nm transition), and to the $|\mathrm{D}_{5/2}\rangle$ manifold of Zeeman levels, through the 729 nm transition.

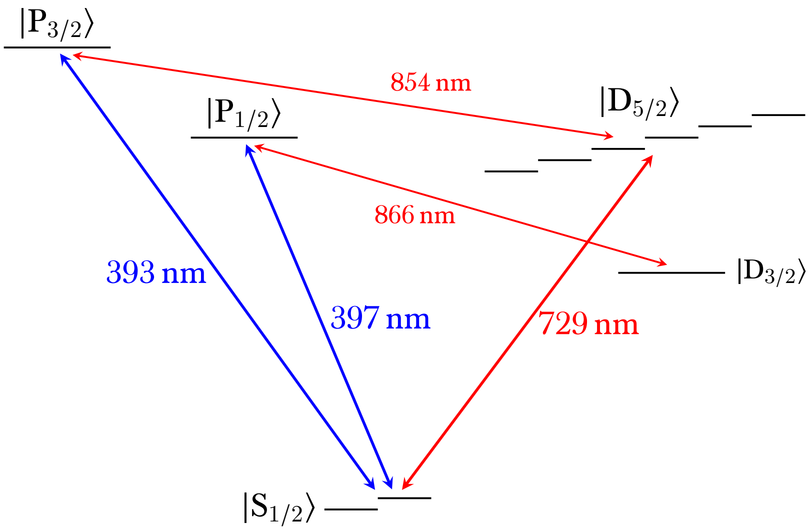

Figure 2.5: **^{40}Ca^{+} Level Structure**. Shown is a simplified diagram of the level structure of ^{40}Ca^{+}, with only the most relevant transitions for this thesis shown. Of particular importance is the $|S_{1/2}\rangle$ to $|D_{5/2}\rangle$ transition at 729 nm. The metastable nature of the $|D_{5/2}\rangle$ state means an optical qubit can be encoded using these two states. The 866 nm and 854 nm transitions optically pump population from the $|D_{3/2}\rangle$ and $|D_{5/2}\rangle$ respectively to allow initialisation of the qubit in $|S_{1/2}\rangle$.

Both the 393 nm and 397 nm transitions are dipole transitions, with the 729 nm transition being a ‘forbidden’ quadrupole transition. For further details see [49, 51–54].

Having now introduced ion-trapping in linear Paul traps and how ^{40}Ca^{+} can be used to encode quantum information, the following Section will look at the interaction between a generic atom with an incident laser beam. This interaction will reveal interesting dynamics which can subsequently be used to implement quantum gates on single and multiple ions.

2.3 Laser-Ion Interaction

The following Section will detail the interaction between a two-level atom, held in a fixed location in space, and a monochromatic laser field. It will closely follow the derivation given in sources such as [47, 49, 55]. The atom’s ground state is labelled $|\downarrow\rangle \equiv |0\rangle$ and its excited state $|\uparrow\rangle \equiv |1\rangle$, and it is assumed spontaneous emission can be neglected for the time-scales of interest here. It will be shown that the effect of the incident light field is to cause transitions between the two different energy levels in the atom, however these transitions will occur only when the frequency of the light is tuned to closely match the energy gap between the levels.

The first of these Sections will look at the general interaction of a laser field with a free atom. The second Section will extend this case to interaction of a laser field with a two-level *trapped* atom.

2.3.1 Interaction of a Two-Level Atom with a Laser Field

Consider a two-level atom (a quantum mechanical system), described by the Hamiltonian H_0, which is subjected to the oscillating electric field of a laser. The field is a time-varying perturbation which perturbs the eigenstates of H_0. The full Hamiltonian of this system can be written as the sum of a time-independent and time-dependent part, such that $H = H_0 + H_1(t)$.

If the zero point of energy is chosen to be halfway between the two states of the system, then the free evolution of the unperturbed two level system is described by the Hamiltonian:

$$H_0 = \frac{\hbar\omega_0}{2}\sigma_z = \frac{\hbar\omega_0}{2}\begin{pmatrix} 1 & 0 \\ 0 & -1 \end{pmatrix}, \tag{2.44}$$

where $\hbar\omega_0$ is the energy difference between the two states. The time-dependent term representing the oscillating electric field of the laser can be written as:

$$H_1 = \hbar\Omega\cos(\omega_{\mathrm{L}}t + \phi_{\mathrm{L}})\sigma_x = \hbar\Omega\begin{pmatrix} 0 & \cos(\omega_{\mathrm{L}}t + \phi_{\mathrm{L}}) \\ \cos(\omega_{\mathrm{L}}t + \phi_{\mathrm{L}}) & 0 \end{pmatrix}, \tag{2.45}$$

where ω_{L} is the frequency of the incident light field. Therefore, the total Hamiltonian is given by

$$H = H_0 + H_1 = \begin{pmatrix} \frac{\hbar\omega_0}{2} & \hbar\Omega\cos(\omega_{\mathrm{L}}t + \phi_{\mathrm{L}}) \\ \hbar\Omega\cos(\omega_{\mathrm{L}}t + \phi_{\mathrm{L}}) & -\frac{\hbar\omega_0}{2} \end{pmatrix}. \tag{2.46}$$

It is useful to consider the transitions between the two states of this system using an approach based on transforming the problem into a rotating frame, covered explicitly in Appendix B.1, where the transformation is chosen such that the new basis states rotate in synchrony with the splitting between the two energy states. Such a transformation into a frame rotating at ω_0 takes the form:

$$U = e^{-iH_0t\hbar} = e^{-i\omega_0 t\sigma_z/2} = \cos(\omega_0 t/2)\mathbb{I} - i\sin(\omega_0 t/2)\sigma_z, \tag{2.47}$$

where the final step uses the well-known relation $e^{i\theta\sigma_\alpha} = \cos(\theta)\mathbb{I} + i\sin(\theta)\sigma_\alpha$ for $\sigma_\alpha = \{\sigma_x, \sigma_y, \sigma_z, \mathbb{I}\}$. The so-called 'interaction Hamiltonian' associated with this is found from:

$$H_{\mathrm{int}} = U^\dagger H U + i\hbar\left(\frac{\partial U^\dagger}{\partial t}\right)U = \frac{\hbar\Omega}{2}(\cos(\delta t + \phi_L)\sigma_x + \sin(\delta t + \phi_L)\sigma_y), \tag{2.48}$$

where $\delta = \omega_\text{L} - \omega_0$, with this derivation shown explicitly in Appendix B.2. This Hamiltonian can be understood from a more physical perspective by considering two different cases: the resonant case where $\delta = 0$ and the off-resonant case where $\delta \neq 0$.

Resonant Transitions

The first case, where $\delta = 0$, is the case when the applied laser field is at the same frequency as the energy gap between the two eigenstates – i.e. $\omega_L = \omega_0$. For this case, the Hamiltonian of the system in the rotating basis simplifies to:

$$H_\text{int} = \frac{\hbar\Omega}{2}(\cos(\phi_L)\sigma_x + \sin(\phi_L)\sigma_y). \tag{2.49}$$

A natural question to ask is how a general state, $|\psi\rangle$, evolves under this Hamiltonian. Using the method of propagators (see Section 2.1.1) the (unitary) evolution under this Hamiltonian is:

$$U = e^{-iH_\text{int}t/\hbar} = \begin{pmatrix} \cos(\Omega t/2) & -ie^{-i\phi_\text{L}}\sin(\Omega t/2) \\ -ie^{i\phi_\text{L}}\sin(\Omega t/2) & \cos(\Omega t/2) \end{pmatrix}, \tag{2.50}$$

where this evaluation is shown explicitly in Appendix B.3. Therefore, the effect of such a Hamiltonian on the ground state $|\downarrow\rangle$ is:

$$|\psi(t)\rangle = U|\downarrow\rangle = \begin{pmatrix} \cos(\Omega t/2) \\ -ie^{-i\phi_\text{L}}\sin(\Omega t/2) \end{pmatrix}. \tag{2.51}$$

Therefore, the state dynamically evolves from $|\downarrow\rangle$ into $|\uparrow\rangle$ through a σ_x rotation (when $\phi_\text{L} = 0$). When $t = \pi/\Omega$, the state has rotated completely to $|\uparrow\rangle$. This process of dynamically evolving from the ground to excited state and back again in a sinusoidal manner is a process known as resonant *Rabi flopping*. In a similar manner, a σ_y rotation can instead be implemented by altering the phase ϕ_L.

Off-resonant Transitions

To see the effect for when the laser beam is off-resonant with respect to the splitting between the two energy levels, it is useful to move to a frame rotating in synchrony with one of the components of the light field – i.e. a frame rotating at speed $\omega_\text{L} = \omega_0 + \delta$. The interaction Hamiltonian in this frame is found to be:

$$H_\text{int} = \begin{pmatrix} -\frac{1}{2}\hbar\delta & \frac{1}{2}\hbar\Omega \\ \frac{1}{2}\hbar\Omega & \frac{1}{2}\hbar\delta \end{pmatrix} = -\frac{\hbar\delta}{2}\sigma_z + \frac{\hbar\Omega}{2}\sigma_x, \tag{2.52}$$

with $\delta = \omega_\text{L} - \omega_0$, and where this derivation is shown explicitly in Appendix B.4. The propagator for this Hamiltonian is then given by:

$$U = \begin{pmatrix} \cos(\Omega_{\text{eff}}t/2) + i\frac{\delta}{\Omega_{\text{eff}}}\sin(\Omega_{\text{eff}}t/2) & -i\frac{\Omega}{\Omega_{\text{eff}}}\sin(\Omega_{\text{eff}}t/2) \\ -i\frac{\Omega}{\Omega_{\text{eff}}}\sin(\Omega_{\text{eff}}t/2) & \cos(\Omega_{\text{eff}}t/2) - i\frac{\delta}{\Omega_{\text{eff}}}\sin(\Omega_{\text{eff}}t/2) \end{pmatrix}, \tag{2.53}$$

where $\Omega_{\text{eff}} = \sqrt{\delta^2 + \Omega^2}$ is the 'off-resonant Rabi frequency'. To again understand the effect of this propagator, apply it once more to the ground state $|\downarrow\rangle$:

$$|\psi(t)\rangle = U \begin{pmatrix} 1 \\ 0 \end{pmatrix} = \begin{pmatrix} \cos(\Omega_{\text{eff}}t/2) + i\frac{\delta}{\Omega_{\text{eff}}}\sin(\Omega_{\text{eff}}t/2) \\ -i\frac{\Omega}{\Omega_{\text{eff}}}\sin(\Omega_{\text{eff}}t/2) \end{pmatrix}. \tag{2.54}$$

From the form of Eq. 2.54, it can be seen that 'off-resonant Rabi flops' occur at a rate of Ω_{eff}. In the off-resonant case, $\Omega_{\text{eff}} > \Omega$, and so the frequency of these off-resonant Rabi flops is increased with respect to the resonant flops. However, due to the presence of the $i\frac{\delta}{\Omega_{\text{eff}}}\sin(\Omega_{\text{eff}}t/2)$ term, it can be seen that the oscillations will never fully reach $|\uparrow\rangle$ when starting from the initial state $|\downarrow\rangle$, being reduced in efficiency by a factor of $1/\Omega_{\text{eff}}$.

The AC-Stark Effect

The application of such a non-resonant perturbing field leads to a shift in the atomic energy levels due to the AC-Stark effect. To see how such a shift arises, first consider the eigenvalues of the interaction Hamiltonian in Equation 2.52. The equation for the eigenvalues, λ, of this equation is given by:

$$\begin{vmatrix} -\delta/2 - \lambda & \Omega/2 \\ \Omega/2 & \delta/2 - \lambda \end{vmatrix} = \lambda^2 - \left(\frac{\delta}{2}\right)^2 - \left(\frac{\Omega}{2}\right)^2 = 0. \tag{2.55}$$

The solutions to this equation are $\lambda = \pm(\delta^2 + \Omega^2)^{1/2}/2$. Often, such perturbing fields are of relevance when they are significantly detuned from resonance, i.e. when $|\delta| \gg \Omega$. In this limit, the eigenvalues simplify to:

$$\lambda = \pm\left(\frac{\delta}{2} + \frac{\Omega^2}{4\delta}\right). \tag{2.56}$$

The unperturbed eigenvalues are $\delta/2$, and so the applied light field shifts the states from their unperturbed frequencies by an amount $\pm\Omega^2/4\delta$. As such, a single energy level experiences a frequency shift from an applied perturbing light field of:

$$\Delta\omega_{\text{EL}} = \pm\frac{\Omega^2}{4\delta}. \tag{2.57}$$

As both the lower and upper energy levels of the transition will be shifted by $\pm\Omega^2/4\delta$, then the change in the transition frequency is twice this amount, and so the total shift in the atomic transition is subsequently:

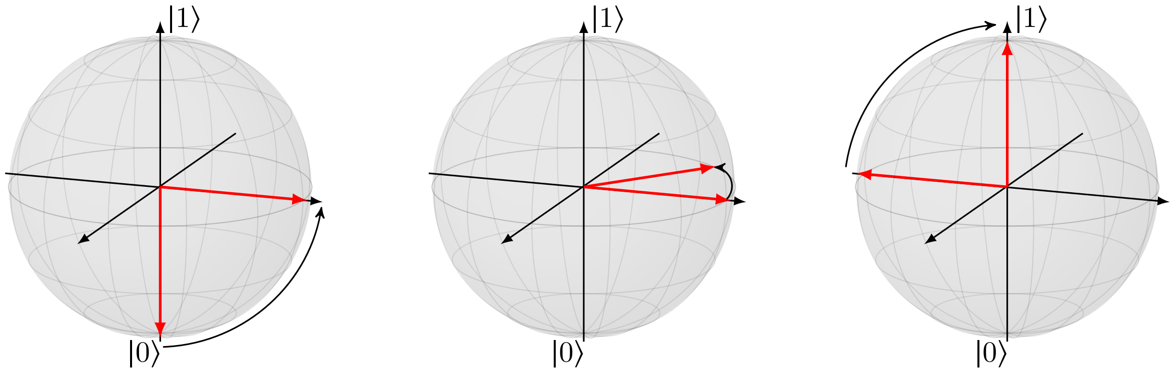

(a) $\pi/2$ pulse rotates the qubit into the equatorial plane

(b) The state evolves freely for a time τ

(c) A final pulse $\pi/2$ with variable phase ϕ

Figure 2.6: **Ramsey experiments** Shown is an illustration of a Ramsey-type experiment. a) The qubit, initialised in $|0\rangle$, is rotated into the equatorial plane by a $\pi/2$ pulse. b) The qubit is allowed to evolve freely for a time τ. If the first $\pi/2$ pulse was off-resonant with respect to the energy splitting of the levels – i.e. if $\omega_L \neq \omega_0$ – the qubit will precess around the equator of the Bloch sphere. c) A final $\pi/2$ is applied, the phase of which is often varied for a fixed free-evolution time τ.

$$\Delta\omega_{\mathrm{ac}} = 2\Delta\omega_{\mathrm{EL}} = \pm\frac{\Omega^2}{2\delta}. \tag{2.58}$$

Ramsey Experiments

This understanding of an atom in a laser field is extremely useful when using trapped ions for quantum information, not least for identifying noise processes. With so many different types and sources of noise as discussed in Section 2.1.2, it is important to have techniques in order to detect and characterise them. The atom-laser interaction can provide a straightforward method to investigate such noise process through the use of Ramsey experiments [56]. Ramsey experiments not only give key insights into the lifetime of an ion-qubit (quantified by the *coherence time* of the system), but can also provide information into the type and strength of noise processes which may be present. Ramsey fringes occur when two pulses with different phases are applied to a qubit, separated by a time period during which the system is allowed to evolve freely. Figure 2.6 illustrates this process: a qubit, initially prepared in $|0\rangle$, is rotated by a $\pi/2$ pulse into the equatorial plane of the Bloch sphere. This state is allowed to evolve freely for a period of time, τ, before a final $\pi/2$ pulse with variable phase is applied.

To best see the effect of this sequence, it is useful to consider this situation again in the rotating frame. From Equation 2.52, the Hamiltonian of the free evolution part is given by:

$$H = \begin{pmatrix} -\frac{1}{2}\hbar\delta & 0 \\ 0 & \frac{1}{2}\hbar\delta \end{pmatrix} = -\hbar\delta\sigma_z/2, \tag{2.59}$$

where $\delta = \omega_{\rm L} - \omega_0$ is the detuning of the first pulse from the resonance frequency of the atom. The evolution of the atom under this Hamiltonian is then:

$$U = \exp(-iHt/\hbar) = \exp(i\delta t\sigma_z/2) = \cos(\delta t/2)\mathbb{I} + i\sin(\delta t/2)\sigma_z. \tag{2.60}$$

Therefore, applying an initial $\pi/2$ pulse, followed by a free evolution for a time τ, and a final $\pi/2$ pulse which is, for example, 90° out of phase with the initial one, gives a combined unitary of:

$$U = e^{-i\pi\sigma_x/4}e^{i\delta\tau\sigma_z/2}e^{-i\pi\sigma_y/4}. \tag{2.61}$$

Assuming the state initially begins in $|\psi_0\rangle = |\downarrow\rangle$, the probability of the ion being found in $|\uparrow\rangle$, when a detuning of δ is present, is then given by:

$$P_\uparrow = |\langle\uparrow|U\psi_0\rangle|^2 = \frac{1}{2}(1 - \sin(\delta\tau)). \tag{2.62}$$

Therefore, if the probability for the ion to be found in $|\uparrow\rangle$ is measured as a function of the free-evolution time τ, then sinusoidal oscillations will occur at a frequency given by the detuning δ. Such a technique can be used to detect detunings caused by instabilities in the incident laser frequency as well as from ambient magnetic fields, as shown in Chapters 3 and 8.

This Section has introduced the interaction of an atom, which can be described as an ideal two-level system, with an incident laser beam. So far, only a free atom has been considered, where effects from confinement of the atom – such as from using an ion trap – have no effect. This treatment will now be extended in the following Section to include the effect of such a trap on this system.

2.3.2 Interaction of a Trapped Atom in a Laser Field

So far, the interaction of a bare atom with a laser field has been derived. In the following Section, the added complexity of placing the atom in a harmonic trapping potential, such as a linear Paul trap as discussed in Section 2.2.2, will be considered. When a bare atom is placed in a harmonic trapping potential as described in Equation 2.35, the resulting unperturbed Hamiltonian can be written as the combination of the two systems:

$$H_0 = \hbar\frac{\omega_0}{2}\sigma_z + \hbar\omega(a^\dagger a + \frac{1}{2}), \tag{2.63}$$

where ω_0 is the transition frequency of the atom and ω is the motional frequency of the atom. This additional oscillation from the motion of the trapped atom leads to a frequency modulation of ω_0, generating motional sidebands either side of the atomic transition at $\omega_0 \pm \omega$.

A simple physical understanding of why these sidebands occur can be gained from considering an atom confined in a one-dimensional well, which can radiate in all directions with electric field $E = E_0 e^{i(kx-\omega_0 t)}$. If the atom moves at a speed v between the confines of the trap, then x becomes a function of time, and the wave emitted by the atom is frequency modulated due to this motion. As such, x can be replaced by a function representing the ion motion: $x \longrightarrow x_0 + u\sin(vt)$. The radiated electric field therefore becomes: $E = E_0 e^{ikx_0} e^{-i\omega_0 t} e^{iku\sin(vt)}$. As terms of the form $e^{ik\sin(\theta)}$ can be expressed in terms of a Fourier series, with Bessel functions as the coefficients, so the electric field can subsequently be expressed as: $E = E_0 e^{ikx_0} e^{-i\omega_0 t} \sum_{n=-\infty}^{\infty} J_n(\beta) e^{invt}$, where n is an integer and $\beta = ku$. This expression is a discrete Fourier spectrum, consisting of a central line (the unmodulated transition frequency at ω_0) with sidebands consisting of equally spaced lines, extending with diminishing amplitude to infinity. These sidebands occur at the transition frequency, plus or minus integer multiples of the oscillation frequency. A more rigorous treatment of this situation will now be given in the following Section.

Interaction of a Trapped Ion with a Light Field

With the addition of a light field, a perturbation of the form $H_1 = \hbar\Omega\cos(\omega_{\mathrm{L}} t + k\hat{x} + \phi_{\mathrm{L}})\sigma_x$ is added (note the similarity to the perturbation in the previous section, however with the addition of $k\hat{x}$, as now the motional state must be taken into account). The Hamiltonian of the system is therefore:

$$H = H_0 + H_1 = \frac{\hbar\omega_0}{2}\sigma_z + \hbar\omega(a^\dagger a + \frac{1}{2}) + \hbar\Omega\cos(\omega_{\mathrm{L}} t + k\hat{x} + \phi_{\mathrm{L}})\sigma_x, \tag{2.64}$$

where now the perturbation includes the position-dependent term $k\hat{x}$. It is again useful to move into the frame rotating at the same frequency as the free evolution of the atom in order to understand the interesting interactions which arise from such a Hamiltonian. When moving into the interaction picture rotating at H_0, this part of the Hamiltonian drops out (see Section 2.3.1), and so only H_1 needs be considered. Therefore, by using the transformation $U = e^{-iH_0 t/\hbar}$, the interaction Hamiltonian is given by:

$$H_{\mathrm{int}} = U^\dagger H_1 U = \hbar\Omega e^{i(H_{0e}^\dagger + H_{0m}^\dagger)t/\hbar}\cos(\omega_{\mathrm{L}} t + \eta(a + a^\dagger) + \phi_{\mathrm{L}})\sigma_x e^{-i(H_{0e}+H_{0m})t/\hbar}, \tag{2.65}$$

where H_{0e} is the Hamiltonian for the electronic state of the bare atom, H_{0m} the Hamiltonian for the trapping potential (i.e. the Hamiltonian for the motional state of the ion), and the relations $\hat{x} = x_0(a + a^\dagger)$ and $\eta = kx_0$ have been used. η is of particular importance and will be discussed in more detail below. By expressing the cosine in terms of exponentials, this Hamiltonian can be written as:

$$H_{\text{int}} = \frac{\hbar\Omega}{2} e^{i(H_{0e}^{\dagger}+H_{0m}^{\dagger})t/\hbar} [e^{i(\omega_{\text{L}}t+\eta(a+a^{\dagger})+\phi_{\text{L}})} + e^{-i(\omega_{\text{L}}t+\eta(a+a^{\dagger})+\phi_{\text{L}})}] \sigma_x e^{-i(H_{0e}+H_{0m})t/\hbar}. \tag{2.66}$$

As the electronic and motional parts of the bare Hamiltonian commute with each other, these terms can be separated out. The subsequent evaluation of these parts is given explicitly in Appendix B.5, with the final Hamiltonian simplifying to:

$$H_{\text{int}} = \frac{\hbar\Omega}{2} \left(e^{-i(\delta t-\phi_{\text{L}})} \sigma_{+} e^{i\eta(ae^{-i\omega t}+a^{\dagger}e^{i\omega t})} \; + \; h.c. \right), \tag{2.67}$$

where $\delta = \omega_{\text{L}} - \omega_0$. The off-diagonal terms of this expression represent coupling between the ground and excited states, with the form of this expression showing that the internal state and the motional state are coupled.

The Lamb-Dicke Regime

Equation 2.67 can be simplified further when the atom is in what is known as the *Lamb-Dicke regime*. This is a regime where the spatial extent of the ground-state wavefunction, x_0, is much smaller than the wavelength of the transition frequency ω_0. A useful parameter to characterise such a regime is the so-called Lamb-Dicke parameter, η, which is defined as $\eta = \vec{k} \cdot \vec{x}$ for a single ion, with $\vec{k}$ the wavevector of the incident light field, and $\vec{x} = x_0\sqrt{\hbar/2m\omega}\;\vec{r}$. ω is the trap frequency, m the mass of the ion, and $\vec{r}$ the direction of the ion's motion in cartesian coordinates. The Lamb-Dicke regime is then defined such that $\eta^2(2n+1) \ll 1$. As η is very small in such a regime, then the exponential terms in η in Equation 2.67 can be Taylor expanded to first order, giving:

$$H_{\text{int}} = \frac{\hbar\Omega}{2} \left(e^{-i(\delta t-\phi_{\text{L}})} \sigma_{+} (1 + i\eta(ae^{-i\omega t} + a^{\dagger}e^{i\omega t})) \; + \; h.c. \right). \tag{2.68}$$

Therefore, processes which alter the motional state of the qubit by more than one phonon are strongly suppressed.

There are three interesting regimes which can be investigated using Equation 2.68 in the limit of $\omega \gg \Omega$: those of the carrier transition ($\delta = 0$), the blue sideband transition ($\delta = \omega$), and the red sideband transition ($\delta = -\omega$).

Carrier transition

The carrier transition occurs when the exciting radiation is resonant with the transition frequency of the ion – that is, $\delta = 0$. In this case, the Hamiltonian reduces to:

$$H_{\text{carr}} = \frac{\hbar\Omega_n}{2} \left(\sigma_{+} e^{i\phi_{\text{L}}} + \sigma_{-} e^{-i\phi_{\text{L}}} \right). \tag{2.69}$$

This Hamiltonian couples $|\downarrow, n\rangle \leftrightarrow |\uparrow, n\rangle$. The strength of this coupling is given by $\Omega_n \approx \Omega(1-\eta^2 n)$, where the reduction in coupling strength arises from higher order terms in Equation 2.68.

Blue Sideband Transition

The blue sideband transition occurs when the exciting radiation is positively detuned from the carrier frequency by the ion motional frequency – i.e. $\delta = \omega$ and so $\omega_\mathrm{L} = \omega_0 + \delta$. For this case, Equation 2.68 simplifies to:

$$\begin{aligned} H_\mathrm{b} = \frac{\hbar\Omega_{n,n+1}}{2}\Big(&\sigma_+[e^{-i(\omega t-\phi_\mathrm{L})} + i\eta(ae^{-i(2\omega t-\phi_\mathrm{L})} + a^\dagger e^{i\phi_\mathrm{L}})] \\ &+\sigma_-[e^{i(\omega t-\phi_\mathrm{L})} - i\eta(ae^{-i\phi_\mathrm{L}} + a^\dagger e^{i(2\omega t-\phi_\mathrm{L})})]\Big). \end{aligned} \tag{2.70}$$

If $\omega \gg \Omega$ (the so-called *resolved sideband limit*), then a second rotating wave approximation can be made, where terms oscillating at frequencies of order ω can be neglected. In this situation, the above Equation reduces to:

$$H_\mathrm{b} = i\eta\hbar\frac{\Omega_{n,n+1}}{2}\left(\sigma_+ a^\dagger e^{i\phi_\mathrm{L}} - \sigma_- a e^{-i\phi_\mathrm{L}}\right). \tag{2.71}$$

From this, it can be seen that an excitation of the ion to the upper electronic state also increases the vibrational quantum number by one; that is, this Hamiltonian couples $|\downarrow, n\rangle \leftrightarrow |\uparrow, n+1\rangle$ with strength $\Omega_{n,n+1} = \eta\sqrt{n+1}\Omega$.

Red Sideband Transition

Similarly, the red sideband transition occurs when the exciting radiation is negatively detuned from the carrier frequency by an amount equal to the motional frequency of the ion – i.e. $\delta = -\omega$. In this situation, after again the second rotating wave approximation, the Hamiltonian is of the form:

$$H_\mathrm{r} = i\eta\hbar\frac{\Omega_{n,n-1}}{2}\left(\sigma_+ a e^{i\phi_\mathrm{L}} - \sigma_- a^\dagger e^{-i\phi_\mathrm{L}}\right). \tag{2.72}$$

When the ion is excited to the upper electronic state, the vibrational quantum number decreases by one quantum of motion, that is this Hamiltonian couples $|\downarrow, n\rangle \leftrightarrow |\uparrow, n-1\rangle$ with strength $\Omega_{n,n-1} = \eta\sqrt{n}\Omega$.

This Section has introduced the interaction between a trapped atom with an incident light field, leading to coupling between the electronic and motional modes. This will be of particular importance in Section 2.5, where such interactions are shown to have the potential to implement entangling interactions between multiple ions.

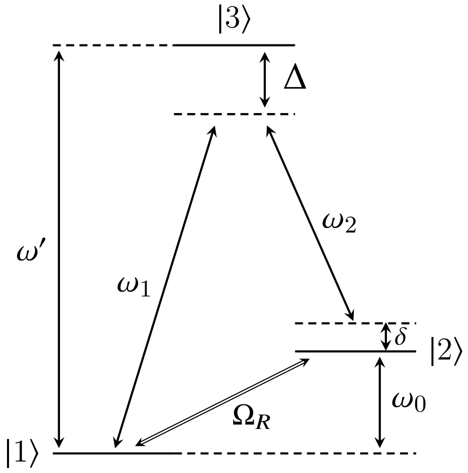

Figure 2.7: **Raman Transitions**. Schematic of an ideal Raman transition between two ground state levels, $|1\rangle$ and $|2\rangle$, mediated by an auxiliary level $|3\rangle$, where the phonon number is unchanged. Effective Rabi flops between $|1\rangle$ and $|2\rangle$ can be driven at a rate of Ω_R using two beams, detuned from the auxiliary level by an amount Δ.

2.4 Stimulated Raman Transitions for an Ideal Atom

The following Section will now present a theoretical discussion of an ideal stimulated Raman transition in a three-level system. A stimulated Raman transition is a two photon process involving three levels, as shown in Figure 2.7. The first Raman beam (Raman beam 1) has frequency ω_1 and drives the $|1\rangle \leftrightarrow |3\rangle$ transition with Rabi frequency Ω_1. The second beam (Raman beam 2), with frequency ω_2, drives the $|2\rangle \leftrightarrow |3\rangle$ transition with Rabi frequency Ω_2. The Raman transition involves population transfer between states $|1\rangle$ and $|2\rangle$ using the auxiliary level, $|3\rangle$, to mediate the process. It is important to note that this auxiliary level contains (in the ideal case) a negligible amount of population[1].

For an ideal Raman transition, an atom will interact with an electric field comprised of two components, with the Hamiltonian of this perturbation given by:

$$H_{\mathrm{P}} = \hbar\Omega_1 \cos(\omega_1 t)(|1\rangle\langle 3| + |3\rangle\langle 1|) + \hbar\Omega_2 \cos(\omega_2 t)(|2\rangle\langle 3| + |3\rangle\langle 2|). \tag{2.73}$$

Therefore, writing the cosine in terms of exponentials, the total Hamiltonian for the bare atom as well as this perturbation is:

---

[1] In a real ion, each Raman beam couples the two ground state levels to the multiple Zeeman levels of the auxiliary level. This is discussed in more detail in Chapter 8.

$$H = H_{\text{Atom}} + H_{\text{P}} = \frac{\hbar}{2}\begin{pmatrix} 0 & 0 & \Omega_1(e^{i\omega_1 t} + e^{-i\omega_1 t}) \\ 0 & 2\omega_0 & \Omega_2(e^{i\omega_2 t} + e^{-i\omega_2 t}) \\ \Omega_1(e^{i\omega_1 t} + e^{-i\omega_1 t}) & \Omega_2(e^{i\omega_2 t} + e^{-i\omega_2 t}) & 2\omega' \end{pmatrix}, \quad (2.74)$$

where the zero-energy level has been set at the $|1\rangle$ state. The interaction picture can now be moved to by using a suitable splitting of H_{Atom}, such that H_0 is given by [57]:

$$H_0 = \hbar\begin{pmatrix} \delta_1 & 0 & 0 \\ 0 & \omega_0 + \delta & 0 \\ 0 & 0 & \omega' - \Delta \end{pmatrix}. \quad (2.75)$$

The interaction Hamiltonian between the fields and ion is then found from:

$$\begin{aligned} H_{\text{int}} &= e^{iH_0 t/\hbar}(H - H_0)e^{-iH_0 t/\hbar}, \\ \implies H_{\text{int}} &= \frac{\hbar}{2}e^{iH_0 t/\hbar}\begin{pmatrix} -2\delta_1 & 0 & \Omega_1(e^{i\omega_1 t} + e^{-i\omega_1 t}) \\ 0 & -2\delta & \Omega_2(e^{i\omega_2 t} + e^{-i\omega_2 t}) \\ \Omega_1(e^{i\omega_1 t} + e^{-i\omega_1 t}) & \Omega_2(e^{i\omega_2 t} + e^{-i\omega_2 t}) & 2\Delta \end{pmatrix} e^{-iH_0 t/\hbar}, \\ \implies H_{\text{int}} &= \frac{\hbar}{2}\left(\Omega_1(|1\rangle\langle 3| + |3\rangle\langle 1|) + \Omega_2(|2\rangle\langle 3| + |3\rangle\langle 2|) - 2\delta_1|1\rangle\langle 1| - 2\delta|2\rangle\langle 2| + 2\Delta|3\rangle\langle 3|\right), \end{aligned}$$

where in the final step the rotating wave approximation has been applied. However, as Δ is free to be chosen, it can be set such that $\delta_1 = 0$, and so the interaction Hamiltonian correspondingly simplifies to:

$$H_{\text{int}} = \frac{\hbar}{2}\left(\Omega_1(|1\rangle\langle 3| + |3\rangle\langle 1|) + \Omega_2(|2\rangle\langle 3| + |3\rangle\langle 2|) - 2\delta|2\rangle\langle 2| + 2\Delta|3\rangle\langle 3|\right). \quad (2.76)$$

If Δ is much larger than the line-width of that state, Γ, then this interaction Hamiltonian can be reduced to an effect two-level system by adiabatic elimination of the auxiliary level, $|3\rangle$. For a three-level system, the general state of the wavefunction at any point in time can be written as $|\psi(t)\rangle = c_1(t)|1\rangle + c_2(t)|2\rangle + c_3(t)|3\rangle$. The time-evolution of these coefficients can be found through using the time-dependent Schrödinger equation, such that:

$$\begin{aligned} i\dot{c}_1 &= \frac{\Omega_1}{2}c_3(t), \\ i\dot{c}_2 &= \frac{\Omega_2}{2}c_3(t) - \delta c_2(t), \\ i\dot{c}_3 &= \frac{\Omega_1}{2}c_1(t) + \frac{\Omega_2}{2}c_2(t) + \Delta c_3(t). \end{aligned}$$

In the regime where $\Delta \gg \Gamma$, there will only be a small likelihood of spontaneous emission from the excited state. The fast dynamics of the excited state therefore average to zero, and so $|3\rangle$ can be adiabatically eliminated (i.e. $\dot{c}_3 = 0$). The coefficients can consequently be rewritten such that:

$$\frac{\Omega_1}{2}c_1 + \frac{\Omega_2}{2}c_2 + \Delta c_3 = 0, \quad \Longrightarrow \quad c_3 = -\frac{1}{\Delta}\left(\frac{\Omega_1}{2}c_1 + \frac{\Omega_2}{2}c_2\right). \tag{2.77}$$

The coefficients can then be written as:

$$\begin{aligned} i\dot{c}_1 &= -\frac{\Omega_1}{2\Delta}\left(\frac{\Omega_1}{2}c_1(t) + \frac{\Omega_2}{2}c_2(t)\right) = -\frac{1}{4\Delta}\left(\Omega_1^2 c_1(t) + \Omega_1\Omega_2 c_2(t)\right), \\ i\dot{c}_2 &= -\frac{\Omega_2}{2\Delta}\left(\frac{\Omega_1}{2}c_1(t) + \frac{\Omega_2}{2}c_2(t)\right) - \delta c_2(t) = -\frac{1}{4\Delta}\left(\Omega_1\Omega_2 c_1(t) + (\Omega_2^2 + 4\Delta\delta)c_2(t)\right). \end{aligned}$$

The final Hamiltonian after this adiabatic elimination is therefore given by:

$$H = -\frac{\hbar}{2}\left(\frac{\Omega_1^2}{2\Delta}|1\rangle\langle 1| + \left(\frac{\Omega_2^2}{2\Delta} + 2\delta\right)|2\rangle\langle 2| + \frac{\Omega_1\Omega_2}{2\Delta}(|1\rangle\langle 2| + |2\rangle\langle 1|)\right). \tag{2.78}$$

This is an effective two-level system with an effective Rabi frequency between the states $|1\rangle$ and $|2\rangle$ given by the coefficients of the off-diagonal terms:

$$\Omega_R = \frac{\Omega_1\Omega_2}{2\Delta}. \tag{2.79}$$

As such, the three-level system can now be treated as a far simpler two-level system, with coupling between the states given by Equation 2.79.

The diagonal terms in Equation 2.78 represent an energy shift of the $|1\rangle$ and $|2\rangle$ states by amounts:

$$\frac{\hbar\Omega_1^2}{4\Delta} \quad \text{and} \quad \frac{\hbar\Omega_2^2}{4\Delta} + \hbar\delta, \tag{2.80}$$

respectively. These shifts are the AC-Stark shifts on states $|1\rangle$ and $|2\rangle$ due to the presence of Raman beams 1 and 2 respectively. However, in reality, Raman beam 1 will also induce an AC-Stark shift on state $|2\rangle$, as well as Raman beam 2 inducing an AC-Stark shift on state $|1\rangle$. Equation 2.81 can be straightforwardly extended to include these effects, such that:

$$\frac{\hbar}{4}\left(\frac{\Omega_1^2}{\Delta} + \frac{\Omega_2^2}{\Delta - \omega_0}\right) \quad \text{and} \quad \frac{\hbar}{4}\left(\frac{\Omega_2^2}{\Delta} + \frac{\Omega_1^2}{\Delta + \omega_0}\right) + \hbar\delta. \tag{2.81}$$

When used with two ground-state levels, Raman transitions have a very narrow line-width due to the negligible spontaneous decay rate from these states. Thus, if the same laser is used for both Raman beams, a narrow line-width can be maintained without the need for sophisticated external frequency stabilisation. This is in contrast to, for example, the 729 nm transition used for manipulation of the optical qubit [58]. Instead, the line-width of the Raman transition is determined by the length of the interaction time due to the Fourier limit:

$$\Delta\nu_{\mathrm{LW}} \approx \frac{\lambda}{\tau}, \tag{2.82}$$

where τ is the duration of the Raman pulse.

Spontaneous Scattering

Even when Δ is made to be very large, in reality there will always be a non-zero transfer of population to the auxiliary state $|3\rangle$. As $|3\rangle$ is an excited state, which will generally decay very quickly, this will lead to decoherence due to spontaneous scattering.

The rate of scattering is equal to the decay rate from the excited state, multiplied by the fraction of population in that state – i.e. $R = \Gamma\rho$, where Γ is the rate of decay from the excited state and ρ is the population of the excited state. For the ideal 3-level system presented here with $\delta = 0$, and with the approximations that $|\Delta| \gg \Gamma, \omega_0$, then this spontaneous decay rate is given by [59]:

$$R \simeq \frac{\Gamma}{4}\left(\frac{\Omega_1^2}{\Delta^2} + \frac{\Omega_2^2}{(\Delta-\delta)^2}\right). \tag{2.83}$$

2.4.1 Co-propagating Raman Fields

The geometry which the two Raman fields possess with respect to each other can have a significant impact on the nature of the transitions which can be driven. The first geometry which will be considered is that of co-propagating Raman beams, where the two beams propagate parallel to each other. In such a geometry, the difference in k-vector of these two beams is zero, and so the Lamb-Dicke factor is effectively zero, causing the electronic excitation to be insensitive to the ion's motion. This can be viewed in terms of momentum transfer, as the ion absorbs a photon from one field and emits a photon into the other field in the process of making the transition. If the absorbed and emitted photon propogate in the same direction, as is the case here, then there is no net transfer of momentum to the ion. In a similar way, if the vector difference $\vec{\Delta k}$ is not zero, however $\vec{\Delta k} \cdot \vec{z}_0$ is zero, then there is no component in the direction of oscillation and so no coupling to the motion in that direction. In this scenario, only carrier transitions can be driven by the Raman beams, where the vibrational state remains unchanged (i.e. $\Delta n = 0$). As the Lamb-Dicke

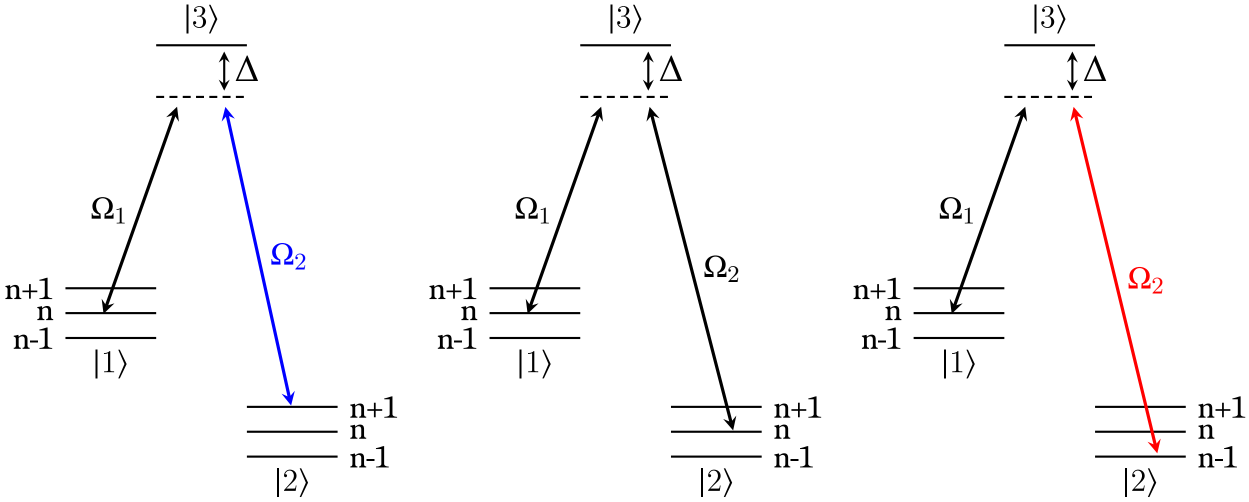

Figure 2.8: **Schematic of Sideband Raman Transitions**. a) A blue-sideband transition, where the final phonon number increases by 1. b) Raman transition displayed in Figure 2.7 b), where there is no change in the motional state of the ion. c) A red-sideband transition, where the motional state decreases by 1.

parameter gives a measure of the coupling strength between the electronic and motional states of the ion, so a low value of η is expected for this geometry, as only transitions which leave the motional state of the ion unchanged are allowed.

2.4.2 Counter-propagating Beams

As with one-photon transitions, transitions can also be driven on the red- and blue-sidebands using Raman transitions. In order to drive transitions which change the motional state of the ion, the geometrical configuration of the two beams must be such that there is coupling to the motional modes of the ion – i.e. some component of the k-vector must lie along the same direction as the motional modes. This can be seen when considering Equation 2.67. This Equation is equally applicable to Raman transitions, which can be most easily seen when considering the Raman transitions in the context of the two-level Hamiltonian given in Equation 2.78. In this situation, the $\eta = kx_0$ term in Equation 2.67 must be replaced by the difference in k-vector between the two beams $k \longrightarrow \Delta k = |\vec{k_1} - \vec{k_2}|$. Such a non-zero k-vector can be achieved by having the second beam propagate in a direction which has a component which is not parallel to the first beam. Figure 2.8 shows schematics of the subsequent transitions which can then be driven. Figure 2.8 a) shows a blue-sideband transition, where the frequency of the second Raman beam, Ω_2, is blue-detuned leading to a change in phonon number of +1. Figure b) shows a transition where Ω_2 is resonant with the carrier transition, and so the motional number remains unchanged, even though this transition still couples to the motional modes. Finally, Figure c) shows a red-sideband transition, with Ω_2 correspondingly red-detuned, leading to a change in phonon number of -1.

The final Section of this Chapter will now introduce how entangling operations can be implemented on multiple ions. These interactions can be implemented using both single-photon as well as two-photon transitions, such as the stimulated Raman transitions just discussed. .

2.5 Entangling Interactions

One of DiVincenzo's criteria for constructing a universal quantum computer is the availability of a universal set of quantum gates [60]. However, a universal set of quantum gates cannot be made solely from single-qubit quantum gates, requiring at least a two-qubit gate [61]. The following Section will now introduce one of the most well-known multi-qubit gates, the Mølmer-Sørensen (MS) gate [62], which enables multi-qubit entangling operations to be implemented using a bichromatic light field. The Section will first describe the logistics of how such a gate can be implemented, firstly on a single ion in order to give a thorough understanding of the situation. Following this, the implementation of the gate on two qubits will be discussed. Finally, extensions of the MS gate to other Hamiltonians such as the transverse Ising and XY models will be detailed.

2.5.1 Bichromatic Light Field and Single-Ion Motional Cat States

One of the most well-known schemes for generating entanglement between ions uses the collective motional modes to provide a coupling between the ions, whilst minimising the motional excitation [62, 63]. Such an interaction can be achieved by using a bichromatic light field, where a field containing two frequencies is used to couple to the motional modes.

A bichromatic light field is a field containing two frequencies. This can be very simply generated by summing two light fields with different frequencies, detuned by Δ from a common centre frequency ω_0. For the purposes of the entangling gates discussed here, the most relevant detuning is when these two frequencies are near to the frequencies of the red and blue sidebands.

The resulting Hamiltonian from this light field is then simply the sum of the Hamiltonians of the red and blue sidebands. Using Equation 2.68 with two light fields at the red and blue sideband frequencies, $\pm(\omega+\Delta)$, and with $\Omega_{n,n+1} = \Omega_{n,n-1} = \Omega$ this can be seen to take the form:

$$H_{\text{bic}} = \frac{i\eta\hbar\Omega}{2}\left(\sigma_+ a^\dagger e^{-i\Delta t} e^{i\phi_b} - \sigma_- a e^{i\Delta t} e^{-i\phi_b} + \sigma_+ a e^{i\Delta t} e^{i\phi_r} - \sigma_- a^\dagger e^{-i\Delta t} e^{-i\phi_r}\right), \tag{2.84}$$

where ϕ_b and ϕ_r are the phases of the blue and red detuned light fields respectively. By defining the two phases $\phi_+ = \frac{\phi_b+\phi_r+\pi}{2}$ and $\phi_- = \frac{\phi_b-\phi_r}{2}$, Equation 2.84 can be rearranged into the form:

$$H_{\text{bic}} = \frac{\eta\hbar\Omega}{2}\left\{\left(e^{i\phi_+}\sigma_+ + e^{-i\phi_+}\sigma_-\right)\left(a^\dagger e^{-i\Delta t}e^{i\phi_-} + ae^{i\Delta t}e^{-i\phi_-}\right)\right\}. \tag{2.85}$$

As ϕ_+ and ϕ_- are independent they are free to be chosen. The simplest value to choose is to set both of these phases equal to 0, and so Equation 2.85 can be simplified to:

$$H_{\text{bic}} = \hbar\eta\Omega\sigma_x\left(a^\dagger e^{-i\Delta t} + ae^{i\Delta t}\right). \tag{2.86}$$

This bichromatic Hamiltonian can be understood as an *off-resonantly* driven quantum harmonic oscillator (see Section 2.2.2). Instead of the linear displacement arising from a resonantly driven harmonic oscillator, the off-resonant bichromatic driving causes the wavefunctions to move on circular trajectories in phase space. The spin operators in Equations 2.85 and 2.86 cause this bichromatic driving force to depend on the internal (electronic) state of the ion, a quality which will be shown to give rise to particularly interesting dynamics in the following Sections.

Single-ion Motional Cat States

Superpositions of distinguishable, macroscopic quantum states were first introduced by Erwin Schrödinger back in the 1930s with his famous thought experiment involving a both dead and alive cat [64]. Since this point, superpositions of macroscopic, distinguishable quantum states have been referred to as “Schrödinger cat states". Such states resembling these cat states can be created using a single ion trapped in a harmonic potential by exploiting coupling between the electronic and motional states of the particle. The first experiment of cat-like states using what the authors termed a ‘mesoscopic’ or ‘intermediate size’ system entangled an ion’s motional state with its internal electronic states [65]. Cat states can be prepared through the use of a single, bichromatic laser pulse [49, 66]. To understand how a bichromatic light field can create such states, first consider an ion initialised in the electronic ground state and motional ground state:

$$|\psi_0\rangle = |\downarrow\rangle|0\rangle_m, \tag{2.87}$$

where $|\downarrow\rangle$ is the electronic ground state, and $|0\rangle_m$ is the motional ground state. As will become clear below, it is instructive to consider this state when the electronic state is written in terms of the eigenstates of the bichromatic Hamiltonian – from Equation 2.86 it can be seen that these are the X-basis states. In this case,
$|\downarrow\rangle = 1/\sqrt{2}(|\downarrow + \uparrow\rangle - |\downarrow - \uparrow\rangle) = 1/\sqrt{2}(|+\rangle - |-\rangle)$, and so:

$$|\psi_0\rangle = \frac{1}{\sqrt{2}}(|\downarrow + \uparrow\rangle - |\downarrow - \uparrow\rangle)|0\rangle_m = \frac{1}{\sqrt{2}}(|+\rangle - |-\rangle)|0\rangle_m. \tag{2.88}$$

Figure 2.9 a) shows this motional ground state (blue sphere), which has a Gaussian distribution in position-momentum space.

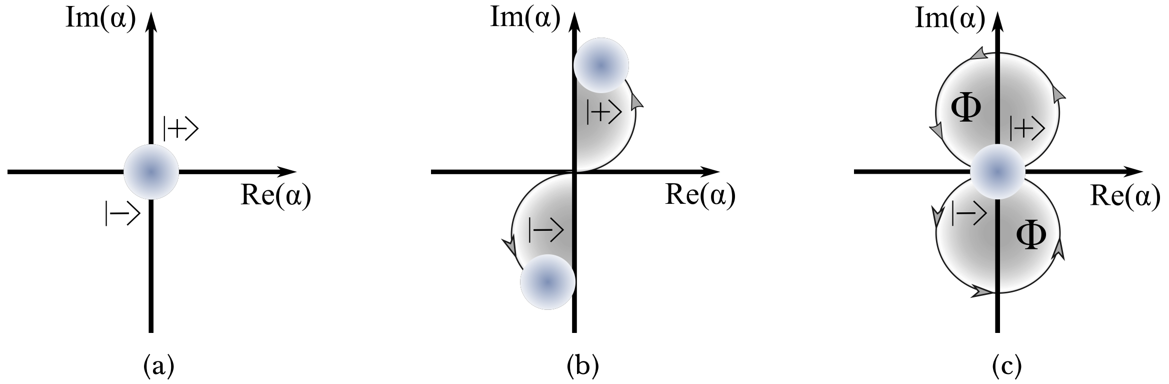

Figure 2.9: **Phase Space Representation of a Single-Ion Motional Cat State** a) The motional ground state has a Gaussian distribution in position-momentum space (blue sphere). b) When under the influence of a bichromatic light field, a state-dependent force acts on the motional ground state. The two orthogonal spin states, $|+\rangle$ and $|-\rangle$, are displaced in opposite directions, following circular trajectories in phase space. c) A complete circle is obtained every $\tau = 2\pi/\delta$, where δ is the detuning of the bichromatic beam.

Consider now the application of a detuned bichromatic light beam with frequencies $\omega_0 \pm (\omega_{\text{sb}}+\Delta)$, and Hamiltonian given by Equation 2.86, to this state. The propagator describing the evolution of the system under this Hamiltonian is subsequently [67]:

$$U(t) = D(\alpha(t))|+\rangle\langle+| + D(-\alpha(t))|-\rangle\langle-|, \tag{2.89}$$

where $D(\alpha(t)) = e^{\alpha a^\dagger - \alpha^* a}$ is a displacement operator (see Equation 2.41) with time-dependent amplitude $\alpha(t) = \frac{\eta\Omega}{2\delta}(1-e^{-i\Delta t})$. The bichromatic beam acts in a state-dependent way on the motional degree of freedom, $|0\rangle_m$, resulting in:

$$|\psi\rangle = D(\alpha(t))|\psi_0\rangle = \frac{1}{\sqrt{2}}(|+\rangle|\alpha(t)\rangle + |-\rangle| - \alpha(t)\rangle). \tag{2.90}$$

This is a motional cat state, where it can be seen that the $|+\rangle$ state has become entangled with a coherent state displaced to $|\alpha(t)\rangle$, and the $|-\rangle$ state has become entangled with a coherent state displaced to $|-\alpha(t)\rangle$. Figures 2.9 b) and c) show a pictorial representation of this. The two orthogonal spin states, $|+\rangle$ and $|-\rangle$ move in opposite directions in phase space. After application of the bichromatic beam for a time $\tau = 2\pi/\delta$, a complete circle in phase space is made and the two spin states recombine at the origin. The phase picked up, Φ, is proportional to the area enclosed by these trajectories. Both phases have the same sign as the states rotate in the same direction.

The probability for the ion to be found in the $|\uparrow\rangle$ state after application of the bichromat beam is then:

$$P_{|\uparrow\rangle} = |\langle + | \psi \rangle|^2 = \frac{1}{2} - \frac{1}{2}\exp\left(-2\left|\frac{\eta\Omega}{2\Delta}(1 - e^{-i\Delta t})\right|^2\right), \tag{2.91}$$

where Ω is the Rabi frequency of each beam on the carrier transition (assumed to be equal), and Δ is the (equal) detuning of each beam from its respective sideband.

2.5.2 The Mølmer-Sørensen Interaction

The application of the bichromatic beam to a single ion described above can now be extended to explore the dynamics from application of such a beam to multiple ions – so forming the basis for the Mølmer-Sørensen (MS) gate [62]. The MS gate will form the basis for many of the interactions considered in the remainder of this thesis, and so it is important that a thorough understanding is gained.

The MS gate couples spins through off-resonant excitation of vibrational modes [62], and is an extension to the motional cat state preparation described above. By again detuning the laser frequency by an amount close to the frequency of the common mode, so sitting at frequencies equal to $\omega_0 \pm (\omega_{\mathrm{sb}} + \Delta)$, entanglement can be deterministically created between the internal and motional states of the ion. The motional states of the ions then act as an effective 'bus' system for entanglement.

Figure 2.10 a) gives a pictorial illustration of the MS gate. In the Figure, the case for two ions is shown for simplicity (however the gate generalises to the multi-qubit case) with the bichromatic laser beam tuned away from the blue and red sidebands by an amount $\pm\Delta$ respectively. Consider the initial two-qubit state where both qubits are in the electronic ground state with phonon number n, i.e. $|\downarrow\downarrow, n\rangle$. If this state absorbs a photon from the negatively detuned laser beam, $-\omega_{\mathrm{sb}} - \Delta$, it will be off-resonantly excited to either of the states $|\uparrow\downarrow, n-1\rangle$ (following path P1) or $|\downarrow\uparrow, n-1\rangle$ (following path P1') with equal probability. If these states now absorb a photon from the positively detuned laser beam, $\omega_{\mathrm{sb}} + \Delta$, then they will transition to $|\uparrow\uparrow, n\rangle$. The same result occurs when the initial state first absorbs a photon from the positively detuned laser beam (following paths P2 or P2'), followed by a photon from the negatively detuned laser beam. It is crucial that the detuning of the two frequencies in the bichromat beam is the same, such that the sum of the two beat-note frequencies is $2\omega_0$. As such, providing the detuning Δ is sufficiently large to suppress population in the intermediate states, the ions undergo the transition $|\downarrow\downarrow, n\rangle \leftrightarrow |\uparrow\uparrow, n\rangle$.

The subsequent Hamiltonian of this bichromatic beam applied to two ions, with one of their shared motional centre-of-mass (COM) modes used for the interaction, is the sum of Equation 2.86 for each ion:

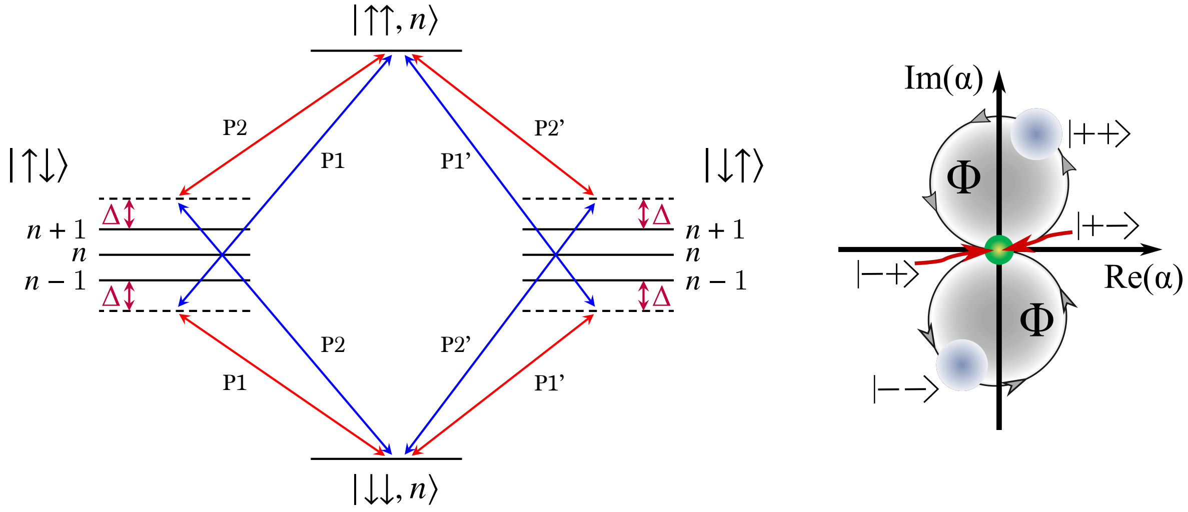

(a) (b)

Figure 2.10: **Illustration of the MS-Gate**. a) Two qubits illuminated by a bichromatic beam detuned from the red and blue sidebands by Δ. For two qubits which start in the electronic state $|\downarrow\downarrow\rangle$ and motional state n, there are four possible paths which can be followed: P1, P1', P2, and P2'. Along the first path, P1, the first qubit effectively undergoes a transition detuned by $-\Delta$ from the red sideband, with the second qubit effectively undergoing a transition detuned by $+\Delta$ from the blue sideband. In path P2, the first qubit effectively undergoes a transition detuned by $+\Delta$ from the blue sideband, with the second qubit effectively undergoing a transition detuned by $-\Delta$ from the red sideband. Paths P1' and P2' are identical to P1 and P2 respectively, except with the order of the qubits reversed. b) Phase-space representation of the MS-gate. The two electronic eigenstates $|++\rangle$ and $|--\rangle$ (blue spheres) experience a state dependent force, pushing them around circular trajectories in phase space. $|+-\rangle$ and $|-+\rangle$ (green) remain stationary during this interaction.

$$\begin{aligned} H_{\mathrm{MS}} &= \hbar\eta\Omega\left(\sigma_1^x(ae^{i\Delta t} + a^\dagger e^{-i\Delta t}) + \sigma_2^x(ae^{i\Delta t} + a^\dagger e^{-i\Delta t})\right) \\ &= \hbar\eta\Omega(\sigma_1^x + \sigma_2^x)(ae^{i\Delta t} + a^\dagger e^{-i\Delta t}). \end{aligned} \tag{2.92}$$

The evolution of the state under this Hamiltonian is obtained by again calculating the propagator, yielding [68]:

$$U(t) = e^{-iH_{\mathrm{MS}}t/\hbar} = e^{(\gamma(t)a^\dagger - \gamma(t)^* a)t} = D(\alpha S_x)e^{i\Phi(t)S_x^2}, \tag{2.93}$$

where $D(\alpha) = e^{\alpha a^\dagger - \alpha^* a}$ is a displacement operator with time-dependent amplitude $\alpha(t) = \int_0^t dt_1\gamma(t_1) = \frac{\eta\Omega}{\Delta}\left(e^{-i\Delta t} - 1\right)$, $S_x = \sigma_1^x + \sigma_2^x$ is the spin operator, $\Phi(t) = \mathcal{I}m \int_0^t dt_1\gamma(t_1)\int_0^{t_1} dt_2\gamma^*(t_2) = \left(\frac{\eta\Omega}{\Delta}\right)^2(\sin(\Delta t) - \Delta t)$ is a time-dependent geometrical phase, and $\gamma(t) = -i\eta\Omega e^{-i\Delta t}S_x$. Figure 2.10 b) shows a phase space representation of how this propagator acts. The two electronic eigenstates $|++\rangle$ and $|--\rangle$ (blue spheres) move in opposite directions in phase space, picking up a geometrical phase of Φ. $|+-\rangle$ and $|-+\rangle$ (green) remain stationary throughout these dynamics. At time $t = \tau = 2\pi/\Delta$, $D(\alpha)$ goes to zero, and the two wavefunctions return to the origin once more, having made a complete loop in phase space. At this point, the electronic and motional degrees of freedom of the ions become decoupled, with the motional degree of freedom returning to its initial state. The wavefunction, however, has picked up a phase Φ equal to:

$$\Phi(\tau) = 2\pi m \left(\frac{\eta\Omega}{\Delta}\right)^2, \tag{2.94}$$

where m is an integer. As the motional degree of freedom has returned to its initial state, this phase is part of the electronic state. By substituting this phase into Equation 2.93, H_{MS} reduces to an effective Hamiltonian given by:

$$H_{\text{MSeff}} = -\hbar J \sigma_1^x \otimes \sigma_2^x, \tag{2.95}$$

where $J = (\eta\Omega)^2/\Delta$ is the strength of the interaction between the two spins. It can be seen that this Hamiltonian describes pair-wise spin-flips, where spin 2 only flips if spin 1 flips, due to the $\sigma_1^x \otimes \sigma_2^x$ interaction.

If the sideband frequency is set such that $\Omega = \Delta/4\eta$, then at $\tau = 2\pi/\Delta$ a maximally entangled Bell state is formed for any initial motional state $|n\rangle$.

Practical Considerations for the MS Gate

Equation 2.95 will cause a maximally entangled Bell state to occur half-way through the dynamics as long as the intermediate states, $|\downarrow\uparrow\rangle$ and $|\uparrow\downarrow\rangle$, are negligibly occupied. This occurs when the actual motional excitation induced by the gate is minimised. Such a situation can be achieved by having a very large detuning, Δ, with respect to the Rabi frequency, Ω, when driving at the sideband frequency, ω_{sb}. However, in increasing Δ, the Rabi frequency of the MS gate, $\tilde{\Omega}_{\text{MS}}$, is reduced. As such, it is often advantageous to have a smaller Δ in order to retain a relatively fast gate-time (as will be seen in Chapter 8, a fast gate-time is on the order of $100\,\mu$s for this work) in which case there will no longer be a non-negligible population in $|\downarrow\uparrow\rangle$ and $|\downarrow\uparrow\rangle$. However, by choosing specific values for Δ, which are dependent on the Rabi frequency, Ω, when driving at the sideband frequency ω_{sb}, the population in these states can be made to go to zero at the point of maximal entanglement. The value of Δ for which this occurs is given by:

$$\Delta_{\text{ME}} = 2\sqrt{m}\eta\Omega, \tag{2.96}$$

where m is an integer. The maximum excitation which can be achieved during the interaction will then have mean quantum number $\tilde{n} = m/2$.

Extension beyond two qubits

The MS gate described above has only considered a two-qubit state, however it can be straightforwardly extended to an N-qubit state. To do this, the Pauli matrices should be extended to the spin operators, defined such that $S_N^x = \sum_i^N \sigma_i^x$. In doing so, the MS-interaction produces entangled states of the form [69]:

$$|\Phi\rangle = (|0\rangle^{\otimes N} + |1\rangle^{\otimes N}). \tag{2.97}$$

2.5.3 Effective Transverse-Field Ising Hamiltonian

The MS gate forms the basis for many interesting Hamiltonians, one of which is the transverse-field quantum Ising model. The Ising model can be obtained by adding an asymmetric detuning, δ, to the bichromat beam used to implement the MS interaction, so creating an additional effective transverse magnetic field. In adding this asymmetric detuning, the Hamiltonian for a qubit experiencing the bichromatic beam (Equation 2.86) becomes:

$$H = \frac{\hbar\eta\Omega}{2}(\sigma^+ e^{-i\delta t} + \sigma^- e^{i\delta t})(a^\dagger e^{-i\Delta t} + a e^{i\Delta t}). \tag{2.98}$$

An interesting point to now consider is how this Hamiltonian can be extended for more than one qubit – for example, for application of the bichromatic beam to a string of N qubits. In this case, the $\sigma_\pm$ operators can be replaced by the collective operators which act on the N qubits, $S_\pm = \sum_i^N \sigma_i^\pm$. In this case, Equation 2.99 becomes:

$$H = \frac{\hbar\eta\Omega}{2}(S_+ e^{-i\delta t} + S_- e^{i\delta t})(a^\dagger e^{-i\Delta t} + a e^{i\Delta t}). \tag{2.99}$$

The time evolution of this Equation can be determined by using the Magnus expansion, the detailed derivation of which is left to sources such as [47]. When in the *weak coupling regime*, characterised by $\eta\Omega \ll \Delta$ (i.e. the detuning from the sidebands is much greater than their respective resonant coupling strength), then Equation 2.99 reduces to:

$$H = \hbar J \sum_{i<j}^{N} \left(\sigma_i^+ \sigma_j^+ e^{-2i\delta t} + \sigma_i^+ \sigma_j^- + \sigma_i^- \sigma_j^+ + \sigma_i^- \sigma_j^- e^{2i\delta t} \right), \tag{2.100}$$

where $J = (\Omega\eta)^2/\Delta$ is the spin-spin coupling strength. This Hamiltonian is effectively a pure spin-spin Hamiltonian at all times during the dynamics, with the spin motion becoming virtually entangled. Three regimes of importance can be identified for Equation 2.100.

1. $\delta = 0$: In this case, Equation 2.100 straightforwardly reduces to the Hamiltonian of

the MS interaction:

$$\begin{aligned} H_{\mathrm{MS}} &= \hbar J \sum_{i<j}^{N} \left(\sigma_i^+ \sigma_j^+ + \sigma_i^+ \sigma_j^- + \sigma_i^- \sigma_j^+ + \sigma_i^- \sigma_j^- \right) \\ &= \hbar J \sum_{i<j}^{N} \sigma_i^x \sigma_j^x . \end{aligned} \tag{2.101}$$

2. $\delta \approx J$: When the detuning δ is non-zero, but on the order of the quantity J, then an interesting regime is reached. First, Equation 2.100 can be written in a time-independent form by using $H_{\mathrm{SS}} = H_{\mathrm{SS}} - H_0 + H_0$, where $H_0 = -\frac{\delta}{2} \sum_i \sigma_i^z$ [47]. Moving to an interaction picture with respect to H_0 then gives:

   $$H_{\mathrm{Ising}} = \hbar J \sum_{i<j} \sigma_i^x \sigma_j^x + \hbar B \sum_j \sigma_j^z, \tag{2.102}$$

   where $B = \delta/2$ is the *effective transverse magnetic field strength.* This Hamiltonian is the *quantum Ising model.*

3. $\delta \gg J$: The final regime is that where the detuning is far greater than J. In this case, the RWA can be applied to the exponential terms oscillating at $e^{\pm 2i\delta t}$, and so Equation 2.100 simplifies to:

   $$H_{\mathrm{XY}} = \hbar J \sum_{i<j} (\sigma_i^+ \sigma_j^- + \sigma_i^- \sigma_j^+). \tag{2.103}$$

   This is the XY model of hard-core, hopping bosons [23]. Note that the spin raising and lowering operators appear together, so as one spin excitation is removed, another one is added. As such, the number of spin excitations initially present in the system is conserved throughout the course of the dynamics.

2.5.4 Tunable-Range Interactions and the Spin-Spin Coupling Matrix

The above discussions have all considered the ideal case where the bichromatic beam couples to a single mode – the COM-mode – where the motion of all ions is identical (i.e. same phase and amplitude). For this situation, the Lamb-Dicke parameter for all ions in the string is identical. However, in reality it is often the case that the bichromatic beam will couple to additional modes of motion, such as the ‘stretch’ or ‘rocking’ mode [47]. Unlike the COM mode, these modes will not affect each ion in the same way and, as such, a non-uniform Lamb-Dicke parameter for each ion, η_i, will arise (see Section 3.1.3 of [47] for a detailed discussion). The structure of these additional modes will directly influence the spin-spin coupling strength, which becomes dependent on the particular ions, i.e. $J \longrightarrow J_{ij}$.

The physical interpretation of J_{ij} is that it describes the transmission of an effective spin-spin interaction through collective vibrational modes [22]. For a particular direction, here considered to be the transverse direction (although exactly the same holds for the axial direction), for a mode, n, J_{ij} takes the form [47]:

$$J_{ij} = \frac{\Omega_i \Omega_j}{2} \sum_{i,j}^{2N} \frac{\eta_{in}\eta_{jn}}{\Delta + (\omega_0 - \omega_n)},$$

where η_{in} is the Lamb-Dicke parameter for ion i and mode n, ω_0 is the centre frequency, and ω_n is the frequency of the mode n. Here, the sum goes to $2N$ as the transverse modes are considered (for which there are two contributions from a linear Paul trap), however for the axial modes this sum would instead go to N. As such, it can be seen that J_{ij} is determined by the characteristics of the transverse modes of motion and detuning Δ. The strength of this spin-spin interaction approximately follows a power-law dependence with distance between the ions [22, 47, 70–72]:

$$J_{ij} \sim \frac{J_{\max}}{|i-j|^{\alpha}}, \tag{2.104}$$

where $|i-j|$ is the distance between ions i and j, $J_{\max}$ is the maximum value of the coupling matrix such that $J_{\max} = \max|J_{ij}|$, and α is the *interaction range*. As the detuning of the bichromat, Δ, is changed, the coupling to each mode, and therefore the relative contribution of each mode to the dynamics, changes. As such, α can be modified by altering Δ. This leads to a *tunable range interaction*, where α can be tuned by altering both Δ and the frequency of the motional modes.

If only the COM mode is coupled to, then $\alpha \to 0$, and so $J_{ij} \to J$. In this case, an infinite-range interaction is achieved, where the spin-spin coupling between all ions is the same[2]. The counter-regime is when $\alpha = 3$, a situation where only nearest-neighbour interactions exist.

2.6 Conclusion

This Chapter has presented the theoretical basis upon which the remainder of this thesis is based. Perhaps of most relevance are the discussions regarding the interaction of a light field with a trapped atom, which give rise to a scheme to enable entangling gates to be implemented on trapped ions. The following Chapter will now introduce the experimental platform which is used to perform the experiments described in subsequent Chapters, detailing the most relevant experimental components as well as major upgrades performed during the course of this thesis.

---

[2] Such a regime cannot be achieved using the transverse motional modes of a linear Paul trap, due to the proximity of the radial modes to one-another. As such, it is not possible to couple solely to the COM-mode, as there will always be a significant amount of coupling to the other transverse modes. In principle, such a regime is possible by coupling instead to the axial modes of motion, where the separation between the motional modes is much greater than Δ.

Chapter 3

Experimental Setup & Characterisations

Having set up the theoretical basis for understanding quantum computations and simulations with trapped ions, this Chapter will now look at the experimental hardware on which the experiments described in this thesis were performed – termed the quantum simulation or 'QSim' experiment. The QSim experiment uses long, linear strings of calcium-40 ions confined in a linear Paul trap to implement quantum simulations. The Chapter will first give a brief overview of the existing setup, before detailing two major upgrades which were implemented during the course of this thesis. The first of these involves the setup of the MSquared laser system and optical setup in order to implement Raman gates. Characterisation measurements using this setup are presented in Chapter 8. The second is the replacement of the magnetic field coils with permanent magnets. Measurements demonstrating the associated improvement in coherence time will then be presented.

3.1 Overview of the Existing Setup

The major components of the experimental setup, including the ion trap, vacuum chamber, and main laser systems, have been previously well-detailed and characterised in [49, 58, 73–75]. This Section will therefore provide a brief overview of the major elements of the experimental system in order to establish a common terminology and understanding of the system, which is necessary to understand the remainder of this thesis.

3.1.1 Trap, Vacuum Vessel, and Major Laser Systems

The QSim experiment uses a macroscopic linear Paul trap with blade electrodes (often termed the 'Innsbruck trap') where the design has been based on [76]. This trap is distinct from the more well-known linear Paul traps as shown in Section 2.2 which have cylindrical-shaped RF electrodes, as the 'Innsbruck trap' has distinctive blade-shaped RF electrodes. Such a design allows increased machining and alignment precision of these electrodes. The trap has a blade-to-blade distance of 1.3 mm and tip electrode separation of 4.5 mm

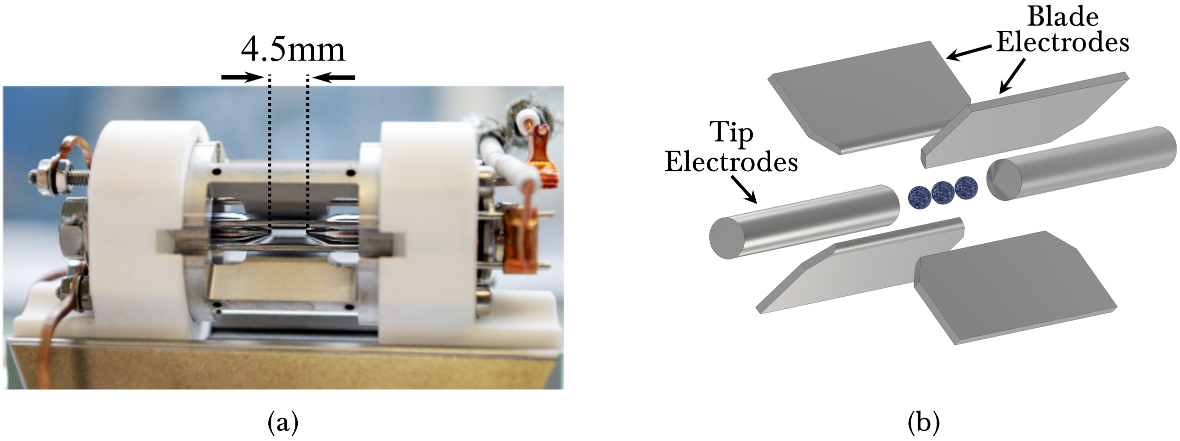

(a) (b)

Figure 3.1: **'Innsbruck Style' Macroscopic Linear Paul Trap** a) A picture of the trap itself, taken by M. Rambach. b) Illustrative rendering of the trap (not to scale). Two opposite blade electrodes receive an RF voltage at typical values on the order of 29 MHz, with the remaining two electrodes held at ground. This creates a 'time-varying saddle potential', which provides radial confinement of the ions (blue spheres) with a typical radial motional frequency around $2\pi\times2.7$ MHz. Two DC blade electrodes provide axial confinement. Typical voltages for the DC electrodes can vary from 9 V to 900 V, corresponding to axial motional frequencies in the range of $2\pi\times118$ kHz to $2\pi\times1.2$ MHz.

[49]. The tip electrodes have holes of diameter 0.5 mm drilled in them, allowing optical access along the ion string. Full simulations and subsequent characterisation measurements of the trap are detailed in [49]. Figure 3.1 a) shows a picture of the trap itself, with b) giving an illustrative rendering. The illustration shows a more expanded view of the trap; two opposite blade electrodes receive a radio-frequency (RF) voltage, with typical values for the RF on the order of 29 MHz. The two remaining electrodes are held at ground. This creates a 'time-dependent saddle potential', so confining the ions in the radial direction, with typical radial motional frequencies on the order of $2\pi\times2.7$ MHz. Two DC electrodes, supplied with voltages anywhere from 9 V to 900 V, provide axial confinement of the ions, resulting in axial frequencies in the range of $2\pi\times118$ kHz to $2\pi\times1.2$ MHz. As a result, the ions form long, linear chains along the middle of the trap. At present, the trap is able to hold in excess of 50 ions in a linear chain [77].

Throughout this thesis, the frequency of the radial modes is in the range $\omega_r = 2\pi\times2.65$-2.85 MHz, and of the axial mode is typically chosen to be $\omega_{ax} \approx 2\pi\times220$ kHz. In order to lift the degeneracy of the two radial modes, a DC-offset voltage is applied to the two blade electrodes held at ground. In this thesis, the frequency splitting of the radial modes induced by this voltage is in the range $\Delta_r = 2\pi\times30$-500 kHz.

The linear Paul trap is housed in a vacuum vessel with multiple optical access capabilities. Figure 3.2 a) shows a schematic of the vacuum chamber as viewed from above, with some of the main beam paths shown. The 854 nm and 866 nm 'repump' lasers remove

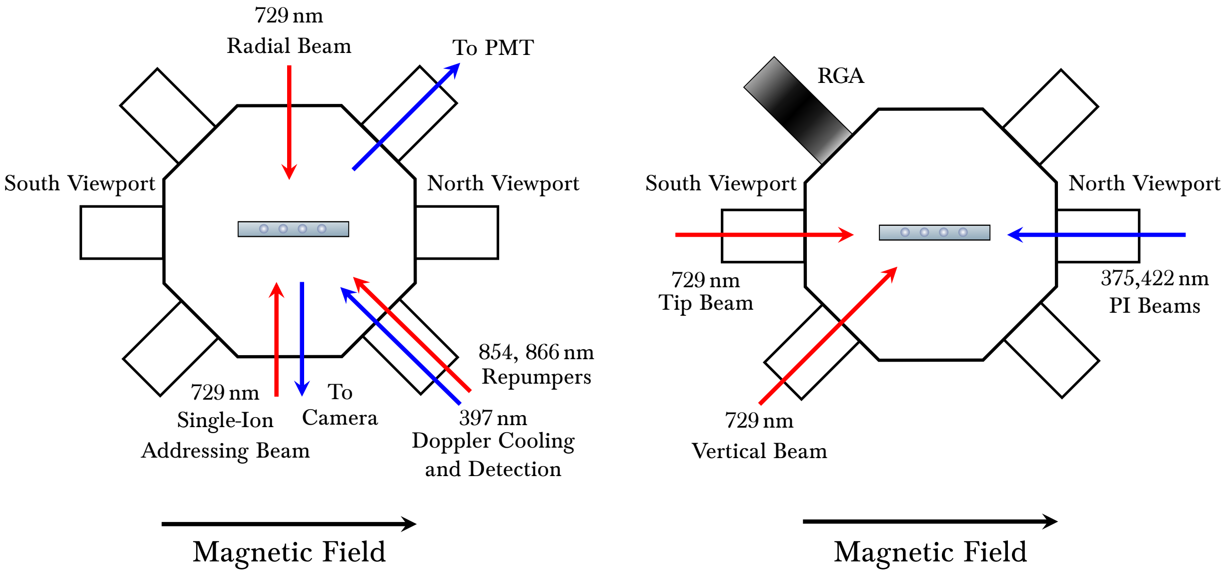

(a) Top view (b) Side view

Figure 3.2: **Schematic of the major beam paths into the vacuum chamber.** a) The beam paths as viewed from above the vacuum chamber. b) Beam paths as viewed from the side of the vacuum chamber. The residual gas analyser (RGA) is no longer in use.

population from the $D_{5/2}$ and $D_{3/2}$ levels respectively, and are used for initialisation of the qubit in the $S_{1/2}$ state. The 397 nm laser is used for both Doppler cooling of the ion string as well as read-out of the quantum state (i.e. detection). The fluorescence induced by this beam is collected via two paths: one leads to a photomultiplier tube (PMT)[1], and the second to an EMCCD Camera[2]. Also shown in this schematic are two beam paths from the 729 nm laser. The 729 nm laser is an ultra-stable, narrow linewidth laser which allows coherent manipulation of the qubit encoded in the $|S_{1/2}\rangle$ and $|D_{5/2}\rangle$ states. The laser, its locking schemes, and characterisation measurements are thoroughly described in [49, 58, 75]. Figure 3.2 a) shows the two most important 729 nm optical access paths for this thesis: the 'radial beam', which couples maximally to the radial modes of motion, and the 'single-ion addressing' beam. Both of these will be discussed in more detail below (see Section 3.1.2).

Figure 3.2 b) shows a schematic of the vacuum chamber from the side vantagepoint. This schematic shows the two photoionisation (PI) beams, which pass through a small hole drilled in one of the tip-electrodes and are used to ionise ^{40}Ca atoms for trapping. Passing through the hole of the opposite tip-electrode is another 729 nm path, the 'tip path' which couples maximally to the axial modes of motion. The final 729 nm beam path is the 'vertical' beam. This in fact enters the chamber at a 60° angle to the quantisation axis, so allowing coupling to both the radial and axial modes of motion when a mixture of circularly and linearly polarised light is used.

---

[1] Sens-Tech P25PC

[2] Andor iXon "Blue"

Originally, the South and North viewports had a pair of coils mounted on them, generating a constant magnetic field of approximately 4 G, used to split the ^{40}Ca^{+} levels into their Zeeman sub-levels. The axis of this magnetic field, which defines the quantisation axis, is along the axis of the ion trap, as shown in Figure 3.2. The upgrade of these coils to permanent magnets is discussed in Section 3.4.

Of these multiple 729 nm beam paths which are shown in the Figure, there are two main beam paths which are of particular relevance to this thesis, being the primary beams used in experiments such as those discussed in Chapters 6 and 7. These two paths will now be discussed in more detail to provide a sufficient understanding of the experimental setup.

3.1.2 Major 729 nm Beam Paths: Radial Beam and Single-Ion Addressing Beam

The 729 nm radial beam is a large beam which has been elliptically shaped through the use of beam-shaping optics. The elliptical shape of the beam profile allows the power in the beam to be used more efficiently, distributing the power such that all ions have approximately equal Rabi frequencies [47]. The radial beam can be used for implementing global rotations on the ion strings which affects all ions equally. In addition, this beam path can be used to implement entanglement operations on the ions through the use of a trichromatic beam (see Chapter 6). The radial beam is perpendicular to the trap axis, and so has maximum overlap with the radial modes of motion.

The QSim single-ion addressing system used in this thesis has been detailed and characterised thoroughly in [49]. It is a tightly-focussed beam (with a beam waist on the order of 2-3 μm) which allows spatially selective individual addressing of single ions. It is generated using an Acousto-Optic Deflector (AOD)[3]. When given an input frequency in the range of 50-100 MHz, the AOD deflects the incident beam by an amount proportional to the input frequency, so allowing the beam to be accurately spatially manipulated.

The single-ion addressing beam used for the experiments detailed in Chapters 6 and 7 was limited to addressing on the order of 20 ions. This was due to both aberrations arising from the beam no longer passing through the centre of the optics along the beam path, as well as clipping of the addressing optics along this path as the angle of deflection was changed by the AOD. However, the capabilities of the single-ion addressing setup was very recently upgraded, allowing addressing of over 50 ions to be achieved. The new system is detailed and characterised in [77].

Having described the major components of the pre-existing setup, the remainder of this Chapter will now describe two main improvements to the setup: The first of these is the setup and operation of a new laser, the ‘Raman Laser’, and the optical setup for imple-

---

[3] Gooch & Housego: 45060-5-6.5DEG-633

menting Raman transitions. This will subsequently be used in Chapter 8 to implement Raman transitions on the ground states of the $^{40}\mathrm{Ca}^{+}$ ion.

3.2 Raman Laser

This Section will describe the laser system used in the Raman setup, including its locking schemes, and is intended to be used as a manual for setting up and operating the laser system. Section 3.3 details the optical setup which this laser system is used with to implement the Raman gates, with characterisation measurements detailed in Chapter 8.

The Raman laser system consists of a pump laser operating at 532 nm[4], seeding a Titanium Sapphire crystal generating light at 788 nm[5]. This in turn is further frequency doubled to 394 nm[6] by an LBO crystal. Both the SolsTiS and ECD-X modules are controlled through the ICE-Bloc[7] control unit.

3.2.1 Generation of 788 nm Light from the SolsTiS Cavity

The 532 nm pump laser is converted to 788 nm light through the use of a titanium-doped sapphire crystal gain medium in the SolsTiS cavity. Figure 3.3 shows the optical setup of the pump beam and SolsTiS. The pump laser light (right of image) is coupled into the SolsTiS cavity using two in-coupling mirrors. The cavity is arranged in a bow-tie configuration so that the cavity oscillates on a single frequency, so avoiding spatial hole burning effects in the crystal. In addition, an optical diode (green) ensures that the cavity lases in only a uni-directional manner, so increasing output power and further ensuring only a travelling wave can exist in the cavity, again minimising spatial-hole burning [78].

Alignment of the pump beam into the SolsTiS

The 532 nm pump beam can be aligned relatively straightforwardly into the SolsTiS cavity. Using only low pump power (~100 mW), align the pump beam into the SolsTiS using the X-Y adjustments of the two in-coupling mirrors on the right of Figure 3.3. *The Z-alignment of these mirrors should never be touched.* Ensure the beam passes cleanly through the aperture placed before the SolsTiS cavity. Using a piece of paper, look for a faint green spot at the output of the cavity along the path to the wavemeter; if this is not present then readjust the in-coupling to the SolsTiS cavity until this can be seen. Move the second mirror of the in-coupling optics in both the X and Y directions while observing this spot in order to determine when clipping occurs, and so where the centre of the adjustment range is, before positioning the mirror so that the spot is in the centre of this adjustment range.

---

[4] Lighthouse Photonics Sprout

[5] MSquared SolsTiS-SRX

[6] MSquared ECD-X Doubling Cavity

[7] MSquared ICE-Bloc® photonic control platform

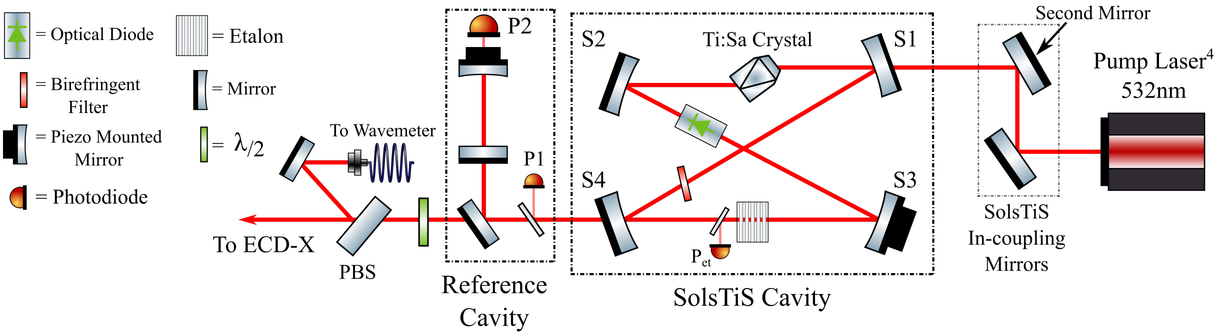

Figure 3.3: **788 nm light generation**. The pump beam at 532 nm is coupled into the SolsTiS cavity through the in-coupling mirrors. When in the SolsTiS, the pump beam is converted to 788 nm through use of a titanium-sapphire gain medium. Most of the light at 788 nm is then out-coupled to the ECD-X cavity. The wavelength of the light is stabilised through locking to the 'Reference Cavity', via a pick-off from the out-coupled light. A small portion of light is further picked-off and sent to the wavemeter for monitoring of the wavelength and mode structure.

While using an IR viewer to look at the piece of paper at the output of the SolsTiS, slowly increase the pump power to ~3.5 W. If a bright IR spot appears, the SolsTiS is lasing, and a power-meter can then be used in order to optimise the lasing using the in-coupling mirrors. If no lasing is seen, move the second mirror by approximately a quarter of a turn in the X-direction. Continue this if lasing is not seen, however ensure that the edge of the adjustment range is not neared. If lasing is still not seen, methodically move in the Y-direction by a small amount, followed by a scan of the X-range (effectively forming an X,Y raster). Again ensure that the edge of the adjustment range is not neared, as clipping on the internal optics of the SolsTiS with high pump power could potentially cause damage. When optimally aligned, an output of approximately 4 W at 788 nm should be achievable when the pump is set to 15 W. The SolsTiS cavity and reference cavity is a hermetically sealed unit which prevents humidity and contaminants from the air causing degradation of the SolsTiS output efficiency. *As such, the lid of the SolsTiS should never be removed.*

Once exiting the cavity, there are two options as to where the 788 nm light can be sent: one option is through the path leading to the wavemeter, with the other path directing the light to the ECD-X doubling cavity to be further frequency doubled. The amount of light directed into each of these paths can be adjusted using the half-waveplate, shown in Figure 3.3.

Setting the Wavelength

The SolsTiS cavity contains a motorised birefringent filter (red), controlled by the ICE-Bloc. This introduces a wavelength-dependent loss into the cavity, and so rotation of this element allows coarse tuning of the wavelength of the output light. A polarising beam splitter at the exit of the cavity is used to direct a portion of the 788 nm light to a wavemeter[8], which is used to monitor the frequency and mode of the 788 nm output. Through using the ICE-Bloc software to rotate the birefringent filter and monitoring the output on the wavemeter, a suitable setting for the wavelength can be chosen.

Further fine-tuning of the wavelength can then be achieved through adjustment of the spacing of the intracavity etalon (grey), also controlled by the ICE-Bloc. The etalon introduces a spectral loss to the cavity which can be tuned by adjusting the spacing of the etalon. This loss is a much sharper function of frequency than the birefringent filter, and so correspondingly provides a much finer-tuning of the wavelength.

This SolsTiS comes with an additional reference cavity module, shown in Figure 3.3. The 788 nm light generated from the SolsTiS can be frequency-locked to this reference cavity, as will now be described.

Locking the SolsTiS

There are two locking schemes in the SolsTiS module – locking of the etalon and locking to the reference cavity. A schematic overview of the components involved in the locking schemes is given in Figure 3.4.

To ensure the SolsTiS is operating single-mode and so maximise power output, the peak of the intracavity etalon transmission can be locked to the nearest longitudinal mode which is oscillating in the SolsTiS cavity. In order to achieve this, the spacing of the etalon can be dithered by a sine-wave with a frequency typically on the order of a few kilohertz. This causes amplitude fluctuations of the same frequency to be imprinted on the output light of the etalon, which is detected by the etalon photodiode P_{et}. This photodiode signal is then split into two paths: In one path, the signal is multiplied by the squared sine-wave signal. In the second path, it is multiplied by the squared inverted sine-wave signal. By subtracting and integrating these two signals, an error signal can be obtained which depends on the phase difference between the two signals [58]. When the etalon drifts away from the transmission maximum, the phase difference between the two signals will correspondingly change, with this change fed back to the etalon through servo electronics.

The linewidth of the laser can then be further reduced to less than 50 kHz [78] through locking the SolsTiS to the reference cavity. The reference cavity is an integrated, temperature controlled, sealed design with all optics mounted on Invar [78]. The SolsTiS cavity length can be locked to this reference cavity using a ‘side-of-fringe’ locking scheme, which feeds back to the piezo-mounted mirror in the SolsTiS cavity, S3. The major components of this scheme are shown in Figure 3.4. When the lock is first engaged, S3 is tuned until the SolsTiS is on resonance with the reference cavity. Once resonance is achieved, the side-of-fringe locking scheme is activated.

---

[8] HighFinesse WS7 MC8

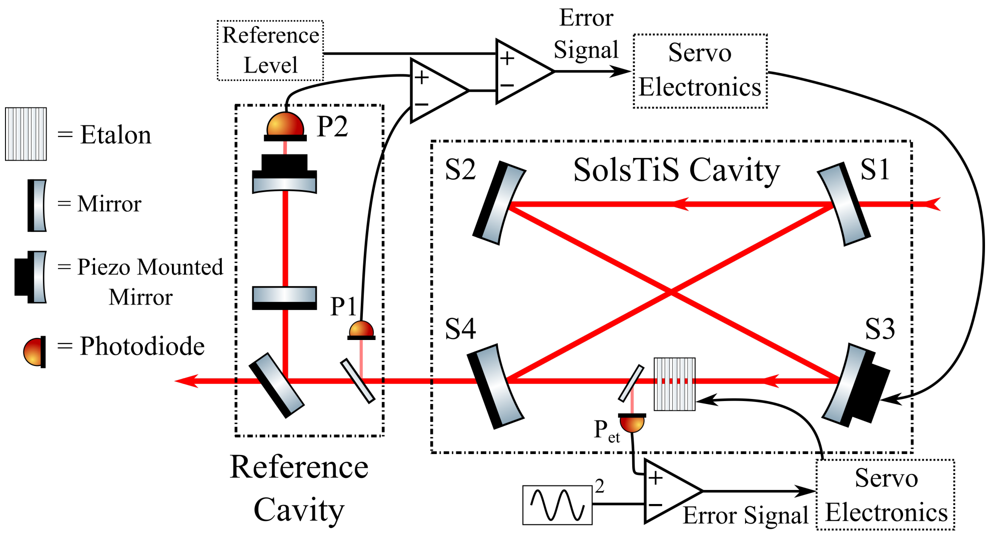

Figure 3.4: **Schematic of the SolsTiS locking schemes**. Only the elements relevant to the locking scheme are shown in the Figure. **Etalon locking**: The transmission from the etalon is combined with a sine-squared signal to form an error signal. This is fed back to the etalon through the servo electronics in order to keep the etalon locked to the nearest longitudinal mode of the SolsTiS cavity (see text). **Side-of-fringe locking**: The transmitted signal on P2 is first normalised by the signal on P1, before being subtracted from a reference level. As such, fluctuations in the intensity of the signal are directly proportional to fluctuations in the frequency, generating an error signal. This is fed back to S3 through servo electronics (see text).

The side-of-fringe locking technique is a simple, well-known method which stabilises the laser to the side of a cavity fringe [79, 80]. There are two photodiodes in the reference cavity, P1 and P2, which are used for the side-of-fringe locking, as can be seen in Figure 3.4. P1 monitors the output signal from the SolsTiS cavity, just before it enters the reference cavity. The transmission through the reference cavity is monitored on photodiode P2. The half-power point of the transmitted intensity on P2 is directly proportional to fluctuations in the laser frequency [79]. An error signal can then be generated by subtracting the transmitted signal from a reference level which is set to this half-power point, with the zero crossing of the error-signal corresponding to the half-power point. This error signal is fed back to S3 via servo-electronics, so keeping the SolsTiS cavity on resonance with the reference cavity.

The half-power point may also fluctuate due to changes in the intensity of the output light of the SolsTiS cavity. In order to differentiate frequency fluctuations from changes in the intensity, two photodiodes are necessary – P1 and P2. As P1 monitors the direct output from the SolsTiS cavity, it is used to normalise any intensity changes detected on P2 due to fluctuations in the intensity output of the SolsTiS cavity. This ensures that any changes in the transmitted half-power are as a direct result of fluctuations in frequency.

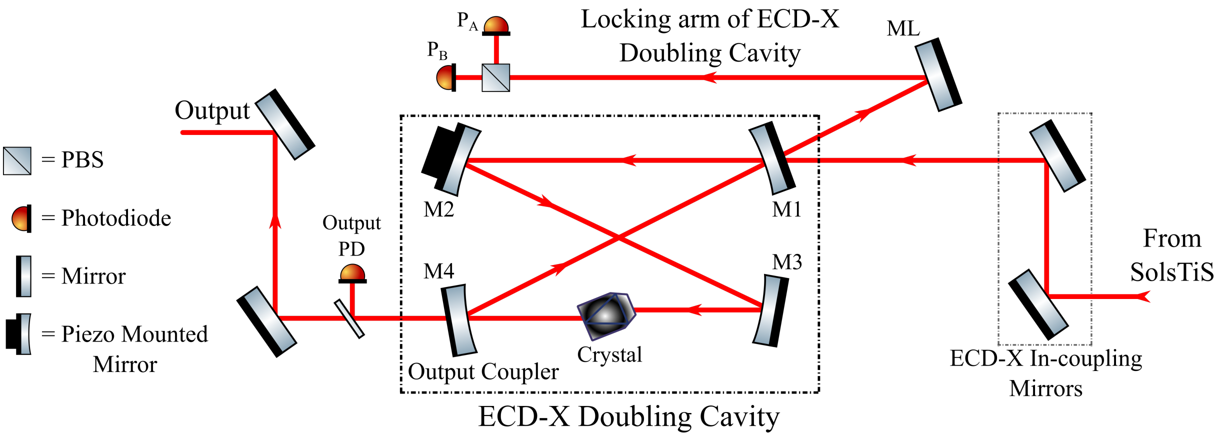

Figure 3.5: **Schematic of the 394 nm laser generation**. The 788 nm light (incident from the right) is further frequency doubled in the ECD-X Doubling Cavity to 394 nm light through an LBO crystal (black). The locking path (top) overlaps a reflected path from M1 with a transmitted path through M1 from M4.

When locked, the SolsTiS has a frequency drift due to drift of the reference cavity. This drift is quoted to be typically $< 100\,\mathrm{MHz/hr/°C}$ [78].

3.2.2 Generation of 394 nm Light

If the 788 nm is directed to the ECD-X doubling cavity, the frequency can be doubled to 394 nm using an LBO crystal. The wavelength of the output light cannot be independently tuned as with the SolsTiS, instead being entirely dependent on the input wavelength. As such, tuning of the frequency of the 394 nm light can only be done through alteration of the 788 nm frequency. The ECD-X cavity resonantly enhances the frequency doubling by using a bow-tie arrangement with highly reflective cavity mirrors, with the fundamental beam mode-matched to the cavity. When well-aligned, the piezo mounted mirror M2 can then be used to sustain the cavity lock. The ECD-X module uses the Hänsch-Couillaud technique [81] in order to lock the doubling cavity to the fundamental 788 nm beam, as will be discussed later in this Section.

Basic Alignment of the ECD-X Cavity

Unlike the SolsTiS, this cavity can be manually aligned. First, connect an oscilloscope to channels A and B on the ICE-Bloc. On the IceBloc software, choose the ECD Output PD for channel A and ECD lock error for channel B. This will give the readout from the Output PD (see Figure 3.5) and the error signal generated from P_A and P_B, respectively. Choose the scan parameters on the software to be approximately 6 GHz scan range with a time of 0.4 s – this moves the piezo on which M2 is mounted in order to scan the cavity.

Using the in-coupling mirrors and IR viewer, align the 788 nm input beam onto the centre of M2. Adjust the angle of the input beam such that the beam reflected from the back of M1 is also cleanly reflected into the locking arm of the cavity. Using the IR viewer, adjust M2 so that the beam is hitting the centre of M3. Likewise, adjust M3 so that the beam passes cleanly through the crystal and hits the centre of M4. Finally, follow the beam reflected from M4 and adjust M4 such that the spot overlaps with the input beam on M1. At this point, it can be helpful to use a piece of lens tissue to view the beams just after M1. Enough light will be let through the tissue so that both the transmitted incident beam as well as the beam which has done a round trip of the cavity are visible. Keep adjusting the mirrors until the beam which has done a single round trip of the cavity, and subsequently been reflected from M1, overlaps the original beam at all spots. Once this happens, the cavity should be nearly closed. Place a piece of paper at the output of the cavity and fluorescence from the crystal should be observed. If the crystal is not fluorescing, repeat the steps to overlap the beams above. If the cavity is close enough to being closed, a bright, flashing spot should be visible on the paper. This is the point of cavity-resonance which is being scanned over.

When the bright, flashing spot is visible on the paper, a peak should be visible on the ECD Output PD. If not, check that the spot from the pick-off mirror to the Output PD is centred on the photodiode and, if not, adjust this mirror accordingly. By tweaking mirrors M2, M3 and M4, along with the crystal, maximise the peak. At a maximum output of 2 W, this peak should reach approximately 2 V. Once this is achieved, the cavity is maximised.

Experience has shown that walking the mirrors either side of the crystal (that is, M2 & M3, and M3 & M4) is the most effective for maximising the output power. Leaving M1 untouched has the added benefit of leaving the locking arm relatively unchanged.

Due to the nature of the locking scheme (discussed in the next Section), the lock of the ECD-X cavity is very sensitive to the quality of the error signal produced. Ensure that the error signal is centred around the 0 V position, and is symmetric with respect to the crossing point. If not, ensure there is a signal on both P_A and P_B, and make small adjustments to ML in order to centre the signal around 0 V.

Locking the ECD-X Cavity – the Hänsch-Couillaud Technique

In order to frequency lock the doubling cavity to the fundamental laser beam, a locking method based on the Hänsch-Couillaud technique is used [81, 82]. The technique uses a polarisation analyser to detect changes in the polarisation of the reflected light in the cavity, which can then be directly related to changes in the frequency of the light. In the ECD-X cavity, such polarisation changes are detected using a polarising beam splitter with a photodiode on each output arm. When the cavity is resonant, the error signal from the polarisation analyser will become zero. It is this zero-crossing point which the cavity is then stabilised to by feeding back to the piezo mounted mirror in the cavity, M2.

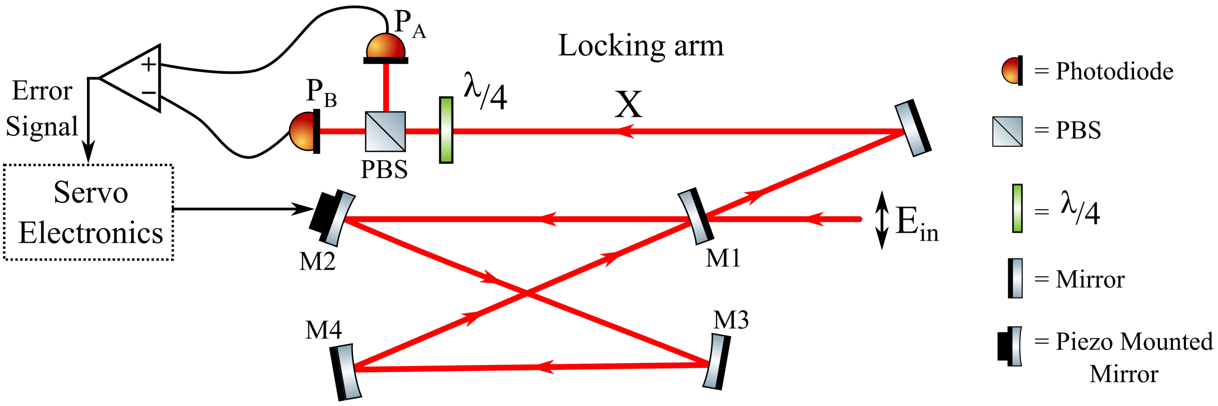

Figure 3.6: **Schematic of the ECD-X locking scheme**. Only the elements relevant to the locking scheme are shown in the Figure. The linearly polarised incident beam, E_{in}, is partly reflected and partly transmitted at mirror M1. For each subsequent round trip of the cavity, a small amount of the beam will leak out of the cavity at M1. When on resonance, the light at point X will remain linearly polarised. When out of resonance, the phase of the leaking light will develop an imaginary component and either lead or lag behind the incident beam, so leading to an elliptically polarised beam. This ellipticity will be detected through the $\lambda/4$ plate, PBS, and two photodetectors. The signal from the photodiodes is used to generate an error signal, which is fed back to M2 through the servo electronics.

Consider the input field to the cavity, E_{in}. At mirror M1, part of the input field is transmitted, which can be written as:

$$E_{\text{M1}} = \sqrt{T_{\text{M1}}}E_{\text{in}}, \tag{3.1}$$

where T_{M1} is the power transmission of the mirror. If losses from the mirror are neglected, i.e. $T_{\text{M1}} + R_{\text{M1}} = 1$ where R_{M1} is the reflectivity of the mirror, then the input field reflected by M1, and so contributing to the field at point X in Figure 3.6, is then:

$$E_{\text{X,r}} = \sqrt{R_{\text{M1}}}E_{\text{in}}e^{i\pi}. \tag{3.2}$$

Denoting the average reflectivity of mirrors M2 to M4 at the resonant wavelength as R, then the total build up of the field at M1 after many round trips of the cavity is given by [82]:

$$E_{\text{M1}} = \frac{\sqrt{T_{\text{M1}}}}{1 - \sqrt{R_{\text{M1}}(1-\gamma)}e^{i\phi}}E_{\text{in}}, \qquad \text{where } \gamma = 1 - R^3(1-g)(1-\Gamma_{\text{cav}}). \tag{3.3}$$

γ is the round-trip loss (excluding the transmission loss T_{M1}), g is the fractional loss per round-trip from passive processes which don't include losses from transmission, and Γ_{cav} is the nonlinear loss due to the crystal. The phase term, ϕ, is given by: $\phi = 2\pi L/\lambda + \phi_{Gouy}$, where L is the optical length of the cavity, λ is the wavelength of the input beam, and ϕ_{Gouy} is the Gouy phase shift which is accumulated over the round trip of the cavity [83].

At point X, the contribution to the field due to leakage out of the cavity through M1 is then given by:

$$E_{\mathrm{X,t}} = \sqrt{T_{\mathrm{M1}}(1-\gamma)}e^{i(\phi+2\pi\Delta L/\lambda)}E_{\mathrm{M1}}, \tag{3.4}$$

where ΔL is the cavity length detuning, which accounts for any difference in frequency which may be present between the input field and the field which builds up in the cavity. Therefore, the *total* field at point X (i.e. from both the reflected field and from the field leaking out of the cavity through M1) is given by the sum of Equations 3.2 and 3.4:

$$E_X = E_{\mathrm{X,r}} + E_{\mathrm{X,t}} = \sqrt{R_{\mathrm{M1}}}E_{\mathrm{in}}e^{i\pi} + \sqrt{T_{\mathrm{M1}}(1-\gamma)}e^{i(\phi+2\pi\Delta L/\lambda)}E_{\mathrm{M1}}. \tag{3.5}$$

Therefore, when a wave circulating in the ECD-X cavity is on-resonance it remains in phase with the incident field, i.e. $E_{\mathrm{X,r}}$ is in phase with $E_{\mathrm{X,t}}$ and has no imaginary part. As such, $E_{\mathrm{X}} = E_{\mathrm{X,r}} + E_{\mathrm{X,t}}$ remains linearly polarised. If, instead, the wave is out of resonance, there is a phase difference between the circulating field, $E_{\mathrm{X,t}}$, and the incident field, $E_{\mathrm{X,r}}$, with $E_{\mathrm{X,t}}$ being comprised of both a real and imaginary part. Therefore, the total field, E_{X}, becomes elliptically polarised. This ellipticity can subsequently be detected by the polarisation analyser. The detuning of the frequency from the resonant wavelength determines whether the circulating field leads the incident field or lags behind it, and so determines the sign of the phase shift. Therefore, depending on whether the light is right-handed or left-handed elliptically polarised, the sign of the detuning can be determined and subsequently corrected for.

Figure 3.6 shows a schematic of how this locking scheme is implemented in the ECD-X cavity, using the reflected signal from the back of M1 and the leakage from the cavity through M1. The polarisation is analysed using a quarter-waveplate, a polarising beam-splitter (PBS), and two photodiodes ($\mathrm{P_A}$ and $\mathrm{P_B}$). The difference between the voltage signals from the photodiodes is then used to form an error signal. This error signal is fed to servo-electronics, whose output goes to M2. When the ellipticity of the beam changes, the ratio of intensities incident on the two photodiodes will correspondingly change, and so the voltage output to M2 will change.

This entire laser system which has just been detailed is primarily used to drive Raman gates on the $^{40}\mathrm{Ca}^{+}$ ions. The following Section will detail the optical setup used to implement these Raman gates, with subsequent characterisation measurements presented in Chapter 8.

3.3 Raman Optical Setup

The following Section will present the optical setup built and used to enable Raman transitions to be driven between the ground states in $^{40}\mathrm{Ca}^{+}$. The Raman transitions can be driven by two laser beams detuned from the $|\mathrm{S}_{1/2}\rangle$ to $|\mathrm{P}_{3/2}\rangle$ dipole transition. Here, the detuning was chosen to be approximately $\Delta = 2\pi\times308\,\mathrm{GHz}$, such that the transition could be driven at a relatively fast rate, while spontaneous emission from the $|\mathrm{P}_{3/2}\rangle$ level was not a significantly limiting factor (see Chapter 8 for further discussions). The experimental design used here was inspired by the experiment described in [84].

Figure 3.7 shows a schematic layout of the setup on the optical table. The output from the laser (not shown), at approximately 1.2 W, is coupled into a clean-up fibre. The output from this fibre (lower left) is split into two main paths by a polarising beam splitter (PBS); the relative intensities in these two paths can be controlled by a half-wave plate positioned in front of the PBS. The reflected path passes through an acousto-optic modulator (AOM) denoted as AOM 1[9], and forms one arm of the counterpropagating fields, as will be explained in Section 3.3.2. The path transmitted by this PBS is further split into two paths, passing through AOMs 2 and 3[10], which form the copropagating fields as will now be discussed.

3.3.1 Copropagating Fields

A theoretical explanation of copropagating Raman fields was presented in Section 2.4.1. The copropagating fields are highlighted in Figure 3.7 by the grey, dotted box. The setup contained within the grey dotted box effectively forms a Mach-Zender interferometer, where a single, incident beam is split up before being re-interfered on a beam splitter. The two paths formed by the first PBS in the grey dotted box pass through AOMs 2 and 3 respectively. AOM 2 is driven at a constant frequency of 105 MHz[11]. The frequency of AOM 3 is provided by the second direct digital synthesiser (DDS) of the Pulse Box [85], and can be accurately controlled in an experimental sequence via the software [49]. The minus first order of these AOMs is overlapped at the second PBS in the grey dotted box, with both beams then coupled into the same fibre.

Figure 3.8 a) shows how these beams are subsequently outcoupled from the fibre and enter the vacuum chamber from the top viewport, at 60° to the trap axis, with the beams propagating parallel to each other. The beams pass through a half-waveplate before entering the vacuum chamber to allow the polarisation to be appropriately adjusted (see Section 8.1.1). The difference in $\boldsymbol{k}$-vector between these two beams is essentially zero, and so the Lamb-Dicke factor is also essentially zero. As the Lamb-Dicke parameter gives a measure of the coupling strength between the electronic and motional states of the ion, if $\eta \simeq 0$

---

[9] Gooch & Housego Crystalline Quartz 110MHz (I-M110-3C10BB-3-GH27)

[10] Gooch & Housego Crystalline Quartz 110MHz (I-M110-3C10BB-3-GH27)

[11] Rohde & Schwarz SMC100A Signal Generator

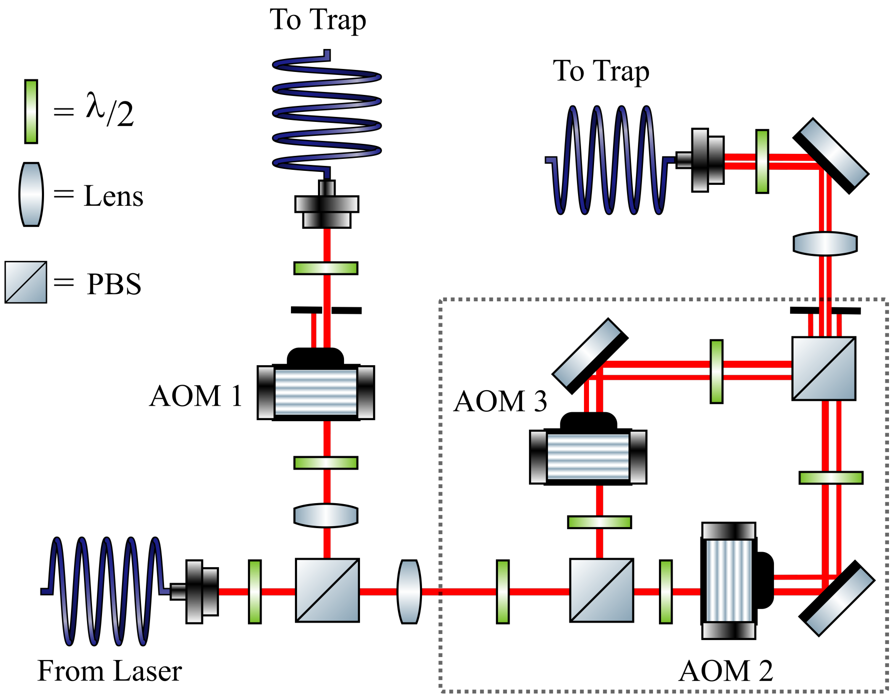

Figure 3.7: **Schematic of the Raman setup on the optical table**. The output from the laser (not shown) enters the optical setup from the clean-up fibre in the lower left corner. The beam is then split into two main paths by a PBS. The reflected path passes through AOM 1, forming one arm of the counterpropagating field setup. The transmitted path is further split into two more arms which pass through AOMs 2 and 3. Together, these two paths (outlined by the grey, dotted box) form the copropagating fields. Alternatively, one of these arms (normally the path through AOM 2) can be used in conjunction with the first path to form the counterpropagating fields. The minus first order of all AOMs is used.

then the electronic state of the ion is insensitive to the motional state, and so there is no coupling to the motional modes. Therefore, only carrier transitions can be driven by the copropagating fields, where the vibrational state remains unchanged. Appendix D.1 shows an explicit calculation of the Lamb-Dicke parameter for these exact experimental values and geometry.

3.3.2 Counterpropagating Fields

For a theoretical discussion of counterpropagating Raman fields, refer to Section 2.4.2. Experimentally, the counterpropagating fields are formed using the path reflected from the first PBS, which passes through AOM 1, in conjunction with the transmitted path which passes through AOM 2. In this configuration, AOM 2 is again driven at a constant frequency of 105 MHz. AOM 1 can be driven in two ways: firstly by three signal gener-

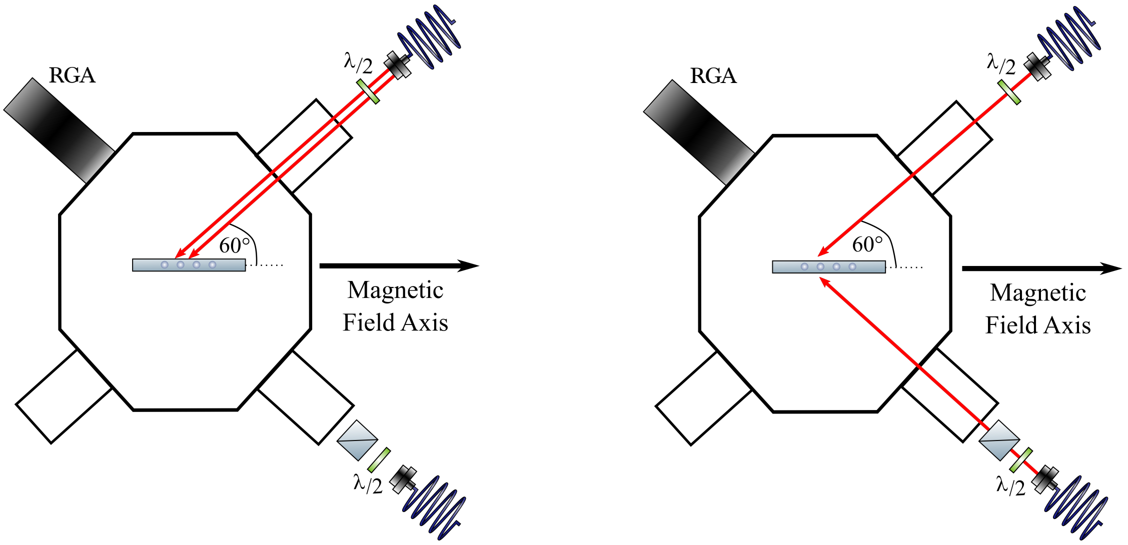

(a) Schematic of the copropagating field geometry.

(b) Schematic of the counterpropagating field geometry.

Figure 3.8: **Schematics of beam paths into the vacuum chamber**. a) The copropagating beams exit from the same fibre, entering the vacuum chamber from a top viewport at 60° to the magnetic field axis. b) One arm of the counterpropagating field enters the chamber from the top viewport at 60° to the magnetic field axis, with the second arm entering from a bottom viewport, also at 60° to the magnetic field axis. The beams subtend an angle of 120° to one-another and have a resultant $\boldsymbol{k}$-vector lying along the radial direction. The bottom beam passes through a PBS in order to ensure the polarisation is as pure as possible before entering the chamber. The top beam is not purified using a PBS so that two orthogonal polarisations can be used when driving the copropagating transitions. The residual gas analyser (RGA) is not in use.

ators[12], the frequencies of which can be controlled using the experimental software, and which can be used individually or in conjunction with one-another. In using two signal generators at the same time, two beams are produced from AOM 1, both of which are coupled into the same fibre, so producing the bichromatic light field used for generating entangling interactions. Similarly, if all three signal generators are used, three beams are consequently produced, so forming the trichromatic light field [47]. Alternatively, AOM 1 can be driven solely by the second DDS of the Pulse Box, producing a single beam. The minus first orders of the two paths through AOMs 1 and 2 are coupled into separate fibres leading to the trap.

Figure 3.8 b) shows how these beams enter the vacuum chamber from two different directions: the path from AOM 2 enters from the top, at 60° to the trap axis, while the path from AOM 1 enters from a bottom viewport also at 60° to the trap axis. The lower beam passes first through a half-waveplate to allow the polarisation to be adjusted, and

---

[12] Rohde & Schwarz SMCL 01 Signal Generator

then through a polarising beam splitter to ensure the polarisation of this beam is as pure as possible.

In contrast to the copropagating fields, for this geometry the difference in $\boldsymbol{k}$ vector between these two beams is non-zero and lies along the radial direction, with no component of $\boldsymbol{k}$ lying along the axial direction. The Lamb-Dicke factor in the radial direction is therefore also correspondingly non-zero, and is calculated to be $\eta = 0.18$ (see Appendix D.1 for an explicit calculation using the experimental parameters). As such, there is significant coupling to the radial motional modes, allowing transitions which change the vibrational state to be driven. It is this coupling to the radial modes of motion which allows entangling gates to be implemented on the ions, as will be shown in Section 8.4. As no component of $\boldsymbol{k}$ lies along the axial direction, there is consequently no coupling to the axial modes of motion.

The radial modes of motion in the QSim system are bunched together into a fairly narrow frequency window (~1 MHz for 20 ions), and so any applied bichromatic or trichromatic beam will couple to all modes with different strengths. As such, this geometry, coupling only to the radial modes rather than the axial modes, was chosen in order to implement more complex spin-spin interactions, such as those with a tunable interaction range α.

Chapter 8 presents results from characterisation measurements of this Raman setup, as well as the implementation of entangling gates using Raman transitions. The remainder of this Chapter will now look at the second major upgrade to the QSim system, and will describe the replacement of the magnetic field coils with permanent magnets in order to reduce decoherence experienced by the qubit due to magnetic field fluctuations.

3.4 Installation of Permanent Magnets

The final Section of this Chapter will introduce the second improvement made to the QSim experiment through installation of permanent magnets in order to reduce the magnetic field noise. In the QSim experiment, the degeneracy of the Zeeman levels in the $^{40}\mathrm{Ca}^{+}$ ion is lifted through application of an external magnetic field, so creating an energy splitting between the levels and consequently a quantisation axis. Previously, this magnetic field was generated using a pair of magnetic field coils with 350 windings each, mounted to the South and North viewports in a non-Helmholtz configuration [49]. A current of 1.4 A was used to produce a magnetic field of 4.10 G at the trap centre.

However, the ion is very sensitive to fluctuations in the magnetic field strength it experiences, as any external magnetic-field induces a change in the bare transition frequency, ν_0, of:

$$\Delta\nu = \frac{\mu_B}{h}\left(g_j^{(1)}m^{(\alpha)} - g_j^{(2)}m^{(\beta)}\right)B, \tag{3.6}$$

where μ_B is the Bohr magneton (μ_B/h =1.399 MHz/G), $g_j^{(i)}$ is the Landé g-factor of level i (≈ 2 for the $S_{1/2}$ level and ≈ 1.2 for the $D_{5/2}$ level), and $m^{(j)}$ the magnetic quantum number of the Zeeman level j. From Equation 3.6 it can be seen that if the strength of the applied magnetic field changes, then the splitting between the Zeeman levels will correspondingly fluctuate, and so will consequently the transition frequency of the ion. If this occurs during a measurement, the ion will move in and out of resonance with the laser and so the qubit will experience decoherence due to fluctuation of the ion's transition frequency.

Previous measurements found the strongest noise component produced by the coil arrangement was at the power-line frequency of 50 Hz, with a magnitude of 2×10^{-5}. This produced a change in magnitude of the magnetic field at the centre of the trap of 30 to 40 μG [49]. The 50 Hz noise component was primarily due to the presence of the electric cables supplying the coils. In order to reduce this noise component, the magnetic field coils were replaced with permanent magnets made of samarium cobalt (Sm_2Co_{17})[13]. This particular material was chosen due to its low temperature coefficient (0.015% change of field per K). A low temperature coefficient was necessary in order to ensure the magnetic field would be stable with respect to temperature fluctuations. The setup was influenced by the design in [86].

3.4.1 Design & Implementation

To hold the magnets in place, two copper holders were designed, with one each attached to the South and North viewports. Despite the low temperature coefficient of the magnets, the magnetic field produced will still be affected by temperature and so, to keep the magnetic field as constant as possible, it is crucial that temperature changes and gradients are kept to a minimum. As such, copper was chosen for the holders due to its high thermal conductivity, allowing any temperature gradients to quickly disperse throughout the material.

The copper holders are in turn supported in an outer casing of plastic, also attached to the South and North viewports of the vacuum vessel. The plastic casing acts as an insulator to prevent a significant temperature gradient forming between the copper holders and the environment. This will be of particular importance in the future when active temperature stabilisation of the magnets is implemented and the holders are no longer in thermal equilibrium with the environment.

Figure 3.9 shows the design of the copper holders and plastic casing. Figures 3.9 a) and b) show the copper holders, where the magnets are held in cylindrical holes of dimension

---

[13] BVI Magnet GMBH XGS24 LT: Diameter 6mm, length 10mm.

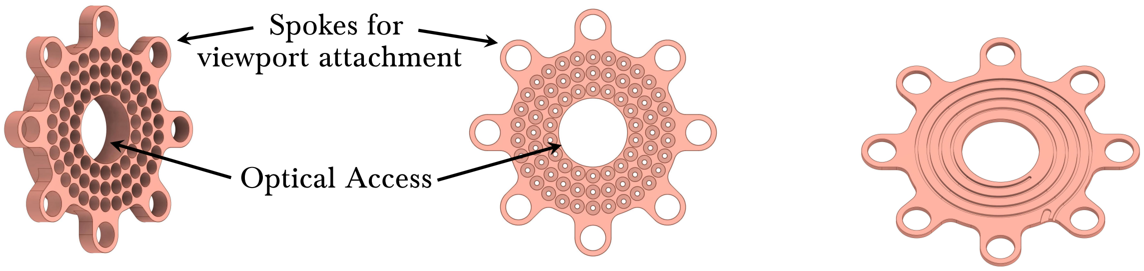

(a) Magnet Holder: Side View

(b) Magnet Holder: Front View

(c) Magnet Holder Lid

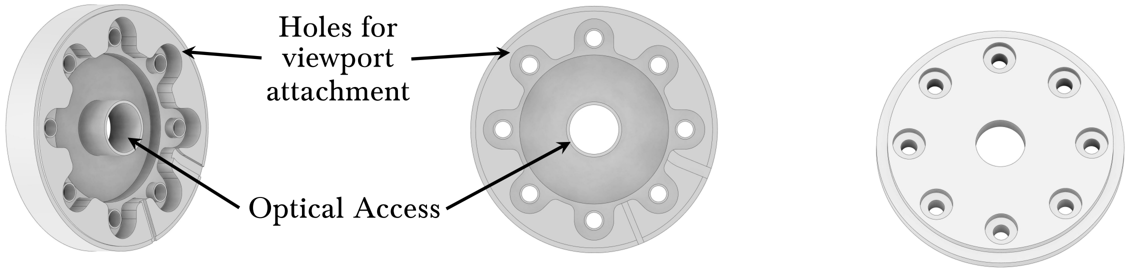

(d) Plastic Casing: Side View

(e) Plasting Casing: Front View

(f) Plastic Casing Lid

Figure 3.9: **Copper magnet holders and plastic housing**. a) & b) Copper Magnet Holders. Each copper holder contains 72 cylindrical holes of dimension 6 mm x 10 mm to hold the magnets. They are arranged in three concentric rings of radius 33 mm, 26 mm, and 19 mm. The samarium cobalt magnets fit in these cylindrical holes, designed so that the magnets sit flush against the walls and so are held in by friction. At the back of each of these cylindrical holes is a small opening, visible in Figure b), which allows the magnets to be pushed out when removal is necessary. c) Lid to the magnet holders. A spiral groove in the lid allows the inclusion of a heating wire if necessary. d) & e) Plastic Housing. The magnet holders are in turn housed in a plastic casing. f) Lid to the plastic holders. The holes allow the entire fixture to be attached to the screws of the South and North viewports of the vacuum chamber.

6 mm by 10 mm. The magnets sit flush against the copper in the cylindrical holes, and so are held in by friction. The holders have the potential to hold 72 magnets in total, arranged in three concentric rings of radius 33 mm, 26 mm, and 19 mm. In Figure 3.9 b) it can be seen that at the back of each cylindrical hole is a small opening, allowing the magnets to be pushed out when removal is necessary. There is a hole in the centre of the holders which allows optical access to the trap through the South and North viewports to be maintained. The 'spokes' extending from the holders allow attachment of the holder to the screws of the viewport. A magnetic field of 4.18 G is produced at the centre of the trap by using 30 magnets in the outer ring, 8 magnets in the middle ring, and 2 magnets in the innermost ring. This value was determined by measuring the resonance frequency of the $|\mathrm{S}_{1/2}, \mathrm{m_j} = +1/2\rangle \rightarrow |\mathrm{D}_{5/2}, \mathrm{m_j} = +5/2\rangle$ transition, and the $|\mathrm{S}_{1/2}, \mathrm{m_j} = +1/2\rangle \rightarrow |\mathrm{D}_{5/2}, \mathrm{m_j} = -3/2\rangle$ transition. By comparing the values of these two

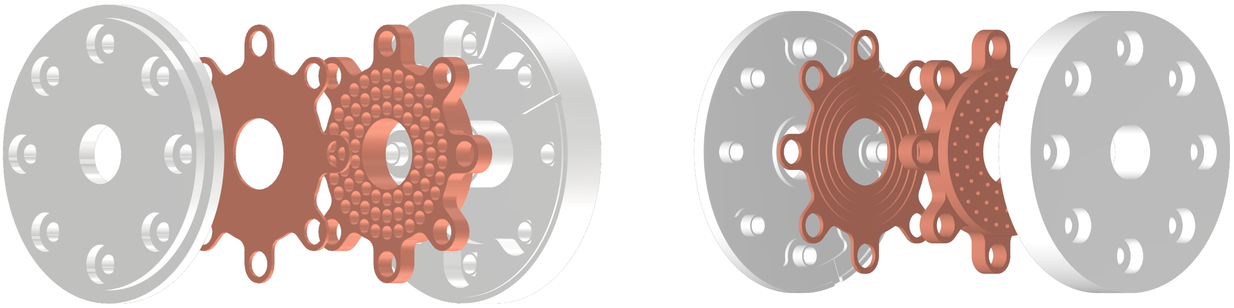

(a) Expanded view from the front

(b) Expanded view from the back

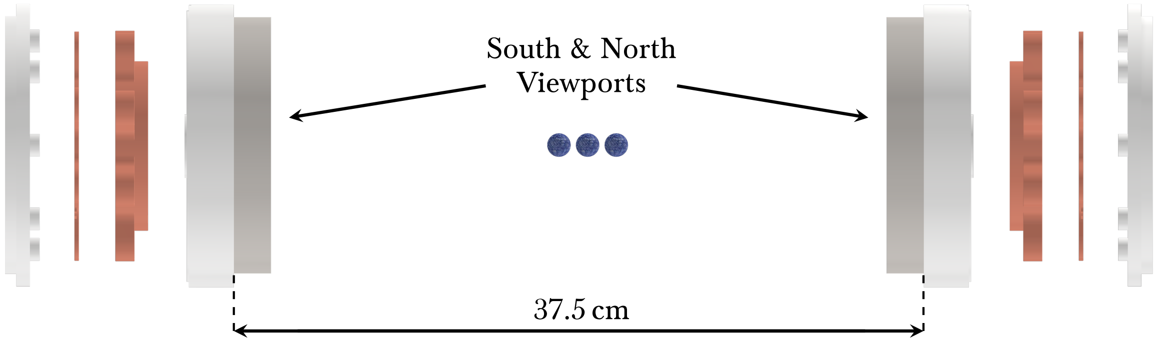

(c) Expanded view of how the assembly fits onto the South and North viewports

Figure 3.10: **Assembly of the magnet holders.** The copper holders fit snugly into the plastic housing. The plastic lid is held on by friction. The small holes at the back of the cylindrical holes where the magnets fit allow removal of the magnets when necessary. The whole assembly fits flush against the South and North viewports, mounted on the viewport screws and separated by 37.5 cm.

transitions, the magnetic field experienced by the ion can be straightforwardly calculated.

Figure 3.9 c) shows the lid for the copper holders. This lid (also made of copper) contains an additional spiral groove, designed to allow heating wires to be mounted in order to actively temperature stabilise the magnets in the future. The groove is designed so that a heating wire will follow the same inwards path as outwards path in order to minimise current loops which may cause stray magnetic fields.

Figures 3.9 d) and e) show the plastic casing in which the copper holders are housed. These have a corresponding opening in the centre to allow optical access and holes, allowing attachment to the screws of the viewports. Figure f) shows the lid for the plastic casing.

Figure 3.10 shows how the copper holders and plastic casing are assembled. The copper holder fits snuggly into the plastic housing, with the plastic lid being held on by friction. The screws from the viewport pass through the spokes of the copper holder and holes in the plastic housing, as well as their respective lids, to ensure firm fixture of all components. The small opening in the back of each cylindrical hole, allowing for removal of the magnets when necessary, can be seen in Figure 3.10 b). Figure 3.10 c) shows how the whole assembly fits flush against the South and North viewports, being mounted on the viewport screws. The two assemblies are separated by 37.5 cm.

3.4.2 Coherence Time Measurements

In order to characterise the stability of the new magnetic field produced by the permanent magnets, two different Ramsey measurements (see Section 2.3.1) were performed. The first of these probed the $|S_{1/2}, m_j = +1/2\rangle$ to $|D_{5/2}, m_j = +5/2\rangle$ transition (this will be referred to as the $|S_{1/2}\rangle$ to $|D_{5/2}\rangle$ transition in the following for brevity). The second measurement probed the coherence in the $D_{5/2}$-state manifold, between the $|D_{5/2}, m_j = -3/2\rangle$ and $|D_{5/2}, m_j = +5/2\rangle$ Zeeman levels (this will be referred to as the D-state manifold in the following). For the measurements in the D-state manifold, the laser frequency approximately drops out, and so this transition is primarily sensitive only to magnetic field fluctuations, and is relatively insensitive to fluctuations in the laser. As such, a comparison of the two coherence measurements can give an indication of not only the stability of the magnetic field, but also of the laser itself.

To perform the coherence measurements on the $|S_{1/2}\rangle$ to $|D_{5/2}\rangle$ transition, the qubit was first optically pumped into the $|S_{1/2}\rangle$ state, before being prepared in a superposition of $|S_{1/2}\rangle$ and $|D_{5/2}\rangle$ by using a $\pi/2$ pulse. After a wait-time of τ, a final $\pi/2$ pulse was applied, the phase of which was scanned. By using a least-squares sine fit to the phase scan, the contrast at that particular wait-time τ – given by the amplitude of the fit – can be extracted. An exponential fit to the decay of the contrast for different wait-times provides an estimate of the coherence time of the system.

To perform the measurements in the D-state manifold, the qubit was again optically pumped into the $|S_{1/2}\rangle$ state, before being prepared in a superposition of $|D_{5/2}, m_j = -3/2\rangle$ and $|D_{5/2}, m_j = +5/2\rangle$ using a $\pi/2$ pulse on the $|S_{1/2}, m_j = +1/2\rangle$ to $|D_{5/2}, m_j = +5/2\rangle$ transition, followed by a π-pulse on the $|S_{1/2}, m_j = +1/2\rangle$ to $|D_{5/2}, m_j = -3/2\rangle$ transition. This transfers all population from the $|S_{1/2}\rangle$ state into the D-state manifold. The same process as with the $|S_{1/2}\rangle$ to $|D_{5/2}\rangle$ transition was then followed in order to extract the contrast as a function of wait-time, and consequently the coherence time.

Figures 3.11 a) and b) show the extracted contrasts as a function of the wait-time τ in-between $\pi/2$ pulses for a magnetic field generated by the original coils. The coherence times were estimated to be 23.9±0.9 ms on the $|S_{1/2}\rangle$ to $|D_{5/2}\rangle$ transition, and 7.9±0.3 ms in the D-state manifold. The implication of the coherence time in the D-state manifold

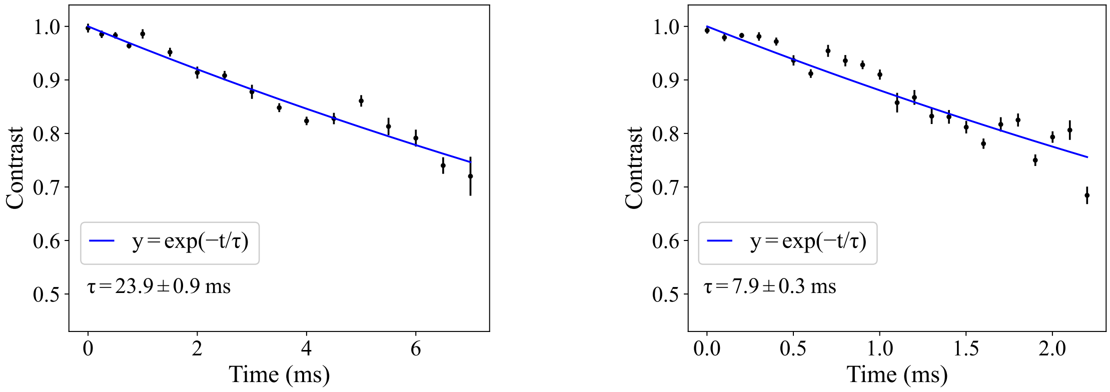

(a) Coils: $|S_{1/2}\rangle$ to $|D_{5/2}\rangle$ transition.

(b) Coils: D-state manifold.

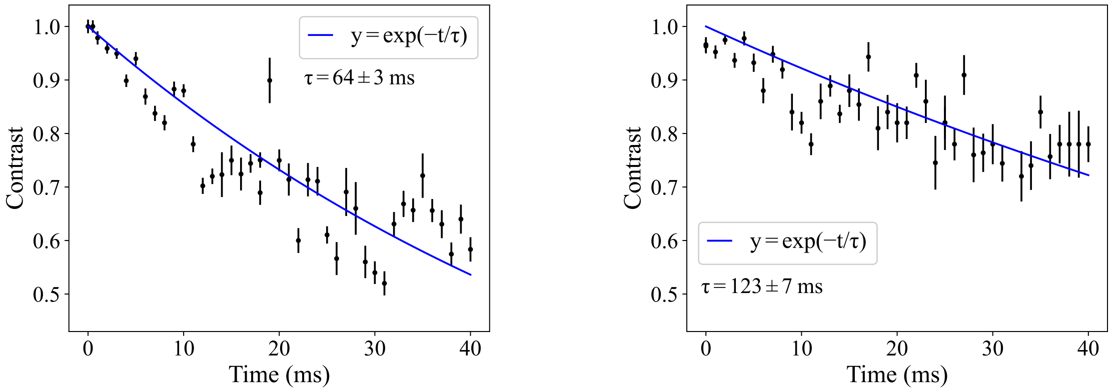

(c) Permanent magnets: $|S_{1/2}\rangle$ to $|D_{5/2}\rangle$ transition.

(d) Permanent magnets: D-state manifold.

Figure 3.11: **Ramsey measurements on the $|S_{1/2}\rangle$ to $|D_{5/2}\rangle$ transition and in the D-state manifold**. For all plots, the measured contrast (black points) is fitted with a least-squares exponential decay (blue line) in order to extract the coherence time. a) Coherence probed with the original coils on the $|S_{1/2}\rangle$ to $|D_{5/2}\rangle$ transition, with an extracted coherence time of 23.9±0.9 ms. b) Coherence probed with the original coils in the D-state manifold, with an extracted coherence time of 7.9±0.3 ms. c) and d) As with a) and b) but after exchanging the coils with the permanent magnets. c) Extracted coherence time of 64±3 ms. d) Extracted coherence time of 123±7 ms. All fits have been constrained to pass through 1 at 0 ms. Errors bars are extracted from the covariance matrix of the sine fit used to extract the contrast.

being significantly shorter than that of the $|S_{1/2}\rangle$ to $|D_{5/2}\rangle$ transition is that the main limitation to the qubit coherence in this case is from magnetic field noise, and not laser noise. However, it should be noted that, as there is no measured data for wait-times close to these estimated coherence times, there could be additional noise processes causing the contrast to drop more significantly at later wait times. Therefore, the true coherence time of the system may actually be shorter than these estimates.

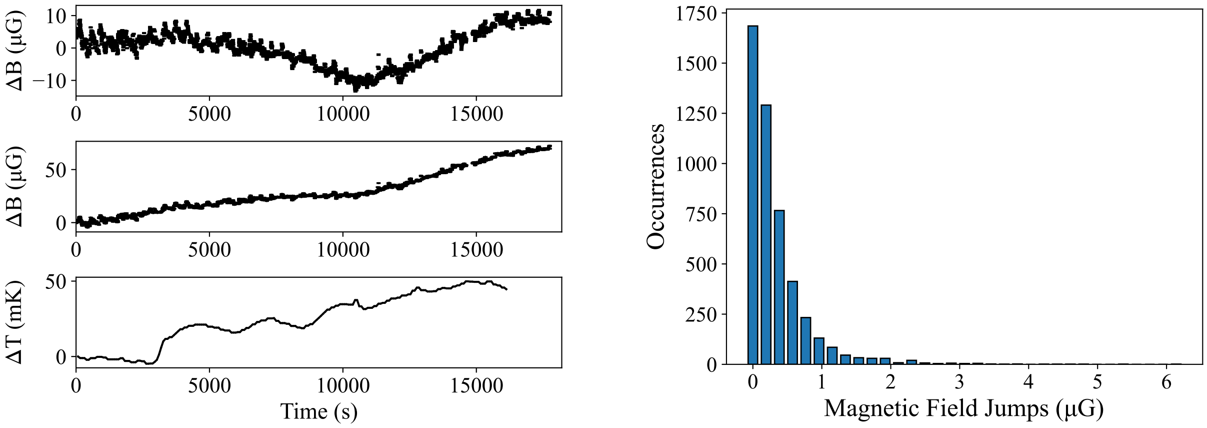

(a) Evolution of the magnetic field both with (top) and without (middle) the linear drift subtracted. Bottom: Evolution of temperature

(b) Distribution of magnetic field jumps

Figure 3.12: **Long-term magnetic field behaviour**. a) Evolution of the magnetic field over 4 hours. **Top**: Without the linear drift subtracted. **Middle**: With the linear drift subtracted. **Bottom**: Evolution of the temperature inside the μ-metal shielding, measured at the same time as the magnetic field measurement. b) Histogram showing the distribution of measured magnetic field jumps. Optimal bin widths were determined using the Knuth binning method [87].

Figures 3.11 c) and d) show the extracted contrasts as a function of wait-time for a magnetic field generated by the permanent magnets. The associated coherence times were found to be 64±3 ms on the $|S_{1/2}\rangle$ to $|D_{5/2}\rangle$ transition, and 123±7 ms in the D-state manifold. There is a marked improvement in the coherence times of both the $|S_{1/2}\rangle$ to $|D_{5/2}\rangle$ transition and in the D-state manifold, with the most marked improvement seen in the D-state manifold. Such an improvement in the D-state manifold shows that decoherence due to magnetic field fluctuations has been significantly reduced. Not only this, but the lower coherence time on the $|S_{1/2}\rangle$ to $|D_{5/2}\rangle$ transition compared to the D-state manifold shows that the coherence of the qubit is now limited by laser noise, rather than the magnetic field.

3.4.3 Long-term Magnetic Field Stability

Having established a marked improvement in the coherence time of the qubit, the long-term stability of the magnetic field (on the order of hours) was subsequently measured. Such measurements aimed to characterise the stability of the magnitude of the magnetic field experienced by the qubit over long time-scales, as well as determine whether there were drifts in the magnetic field which could not be explained by changes in temperature. This stability was investigated by measuring the observed phase shift on 20 ions using a Ramsey experiment with a τ = 10 ms wait-time in the D-state manifold. The D-state manifold was chosen for these measurements due to its relative insensitivity to the laser, and so any observed dynamics can be primarily attributed to changes in the magnetic field.

Figure 3.12 a) shows the evolution of the magnetic field at the position of the ions as a function of time, where a linear drift of approximately $70\,\mu$G can be seen in the middle Figure. At the same time, the temperature inside the closed μ-metal shielding was recorded using an NTC thermistor, with a corresponding increase in temperature of 50 mK observed over this timescale, also shown in Figure 3.12 a) (bottom). Figure 3.12 a) (top) shows the evolution of the magnetic field with the linear drift additionally subtracted. Without the linear drift, a much smaller change with a magnitude on the order of $10\,\mu$G is observed.

The evolution of the magnetic field also allowed jumps in the magnetic field between adjacent measurements (separated by approximately 3 s) to be observed. Figure 3.12 b) shows the distribution of measured magnetic field jumps. From this histogram, it can be seen that the largest jumps recorded are on the order of $4\,\mu$G. These jumps were found to be caused by the movement of the nearby lift. Smaller, more frequent jumps were correlated to the movement of chairs within the laboratory area.

3.4.4 Additional Coils for Linear Gradient Compensation

The arrangement of the permanent magnets leads to a linear magnetic field gradient at the position of the ions. This gradient was measured using a Ramsey-type experiment in the D-state manifold, and found to be on the order of 0.28 G/m. To compensate for this gradient, a pair of coils[14] with 130 windings, mounted to the South and North viewports, is used to provide a constant linear magnetic field gradient which exactly cancels the gradient experienced by the ions. These coils are driven with a constant current of 15 mA, which is actively stabilised by a home-built PI-regulator with a stable reference resistor[15] [49]. In addition, to ensure the zero-crossing in this linear gradient coincides with the centre (i.e. null) of the trap, 4 additional windings are present on the South viewport. This ensures that no extra DC offset from these coils affects the ions, and so any fluctuations in the compensation field should have a minimal effect on the ions. It can also be seen that any frequency fluctuations which may be introduced by these coils are not the limiting factor with regards to the coherence time of the qubit, as from Section 3.4.2 it was concluded that the coherence time of the qubit is now limited by laser noise, rather than by magnetic field noise.

---

[14] 130 Windings per coil, resistance $1.3\,\Omega$ per coil.

[15] Vishay, VCS 302

Chapter 4

Gate Set Tomography & Beam Path Characterisations

In moving to quantum computers and simulaters which may possess an advantage over their classical counterparts, it is necessary to implement high-fidelity quantum gate operations, often in long sequences [88]. However, in practically performing quantum operations, there will always be errors in their implementation which arise due to noise processes such as those discussed in Section 2.1.2. Such errors can be either coherent (such as over/under rotations) or incoherent (e.g. dephasing). By identifying the noise types present in a system and their various magnitudes, it is possible to implement ways to correct for or improve upon them, and so improve the performance of the quantum device.

There are many ways in which noise can enter into a quantum system, however this Chapter will focus on characterising two main sources of errors which can arise from implementing gate operations using the 729 nm laser in the QSim experiment: Imperfections arising from the single-qubit operations themselves, and drifts in the system from fluctuations in the beam paths and/or movement of the ion string. The first part of this Chapter will give an overview of some of the most well-known protocols which can be used to characterise quantum operations, most notably that of gate set tomography (GST). The GST protocol will be subsequently used in the main part of this Chapter to provide a characterisation of the 729 nm single-qubit operations, with its experimental implementation and consequent measurement results being presented. Following this, a characterisation of the drifts present in the system will be given using two methods. The first of these will use a GST-like implementation to determine significant drift frequencies which were detected. The second uses two beam paths to extract information about slow drifts which may be present in said paths, leading to phase noise in the system.

4.1 Single-Qubit Characterisation Protocols

There are many existing protocols which aim to assess the quality of logic operations performed on qubits, all of which follow the same basic framework [88]:

1. A set of quantum circuits are experimentally implemented on the qubit(s)
2. The data from these experiments is analysed according to a specific algorithm
3. The outcome from the analysis provides an estimate of some aspects of the quantum operation on the qubit

Each protocol has its own strengths and weakness. For example, some protocols such as holistic benchmarking assess the performance of the entire set of qubit(s) and circuits [89, 90]. Alternatively, protocols such as component benchmarking [91–93] only partially characterise the system. Finally, there are of course tomographic methods [38, 94–97], which yield highly detailed, predictive models of each quantum operation. Which protocol should be chosen is highly situation-dependent; for example if only partial characterisation of the system is required, then it is more suitable to use a protocol such as component benchmarking rather than holistic benchmarking.

The following Sections will now discuss several well-known protocols which are often used in characterising single-qubit operations. A large amount of mathematical notation will be introduced, which will be needed to understand the subsequent description of GST.

4.1.1 Quantum State Tomography

Quantum state tomography (QST) [94, 95] attempts to characterise an unknown state of interest, ρ, by experimentally measuring all of its components and using them to reconstruct ρ. QST assumes that many identical copies of ρ are available, and so the reconstruction can then be achieved by performing a series of measurements on that state which are termed informationally complete – that is their outcomes, E_j, collectively span Hilbert-Schmidt space. Such measurements could be, for example, in the X-, Y-, and Z-bases. The probability to observe a certain measurement outcome, E_j, is then given by:

$$p_j(\rho) = \mathrm{Tr}(\rho E_j). \tag{4.1}$$

However, practically only a finite number of measurements can be performed, and so the probabilities can only be *estimated* from the data. The probability of getting a certain measurement outcome, E_j, given that the measurements are repeated N times, is then given by:

$$p_j(\rho) = \mathrm{Pr}(j|\rho) \approx \frac{f_j}{N}, \tag{4.2}$$

where f_j is the frequency with which the outcome E_j is observed.

Linear Inversion

For simplicity, linear algebra can be used to write these expressions in a more useful format. A state of interest, $\rho = |\psi\rangle\langle\psi|$, which is to be reconstructed, can be expressed in this formalism as a Hilbert-Schmidt space vector $|\rho\rangle\rangle = \sum_i |i\rangle\rangle\langle\langle i|\rho\rangle\rangle$. $|\rho\rangle\rangle$ is simply a column vector in the Hilbert-Schmidt space, which is a vector space of 2×2 Hermitian matrices, with $\langle\langle\rho|$ the corresponding row vector [98]. Similarly, the jth possible outcome from a measurement on this state can be denoted by $\langle\langle E_j|$, where $j = 1 \ldots N_1$ and N_1 is the total number of (distinct) measurement outcomes. Therefore, the probability of obtaining the jth outcome can be expressed as:

$$p_j = \langle\langle E_j|\rho\rangle\rangle = \sum_i \langle\langle E_j|i\rangle\rangle\langle\langle i|\rho\rangle\rangle = \mathrm{Tr}(E_j\rho). \tag{4.3}$$

Equation 4.3 can be simplified by defining a matrix, A, which is comprised of all possible outcomes $\langle\langle E_j|$, such that:

$$A = \begin{pmatrix} \langle\langle E_1| \\ \langle\langle E_2| \\ \vdots \\ \langle\langle E_{N_1}| \end{pmatrix}. \tag{4.4}$$

As such, Equation 4.3 can be written as $\vec{p} = A|\rho\rangle\rangle$, where the jth element of $\vec{p}$ is p_j which is the probability of getting the outcome E_j. One crucial assumption of QST is that all measurement effects, E_j, are known/chosen in advance of the state tomography being performed, and so consequently the matrix A is also known. Then, if A is a square matrix with all eigenvalues non-zero, it is possible to construct its inverse, and so the state $|\rho\rangle\rangle$ can be reconstructed from simple linear algebra to be:

$$|\rho\rangle\rangle = A^{-1}\vec{p}. \tag{4.5}$$

Therefore, by measuring the probabilities to get the outcomes $|E_j\rangle\rangle$, the matrix A can be determined, and consequently $|\rho\rangle\rangle$ can be reconstructed. Figure 4.1 (top) shows a simple schematic of QST; the state of interest, ρ, can be characterised by using a set of informationally complete known measurements, M, which have outcomes E_j. Informationally complete refers to the property that each quantum state can be uniquely determined by its measurement statistics [99].

4.1.2 Quantum Process Tomography

Quantum process tomography (QPT) is conceptually similar to QST, however aims to characterise a quantum process or gate, G, rather than a state, ρ [94, 100]. QPT can be achieved by using a set of informationally complete measurement states with the set of

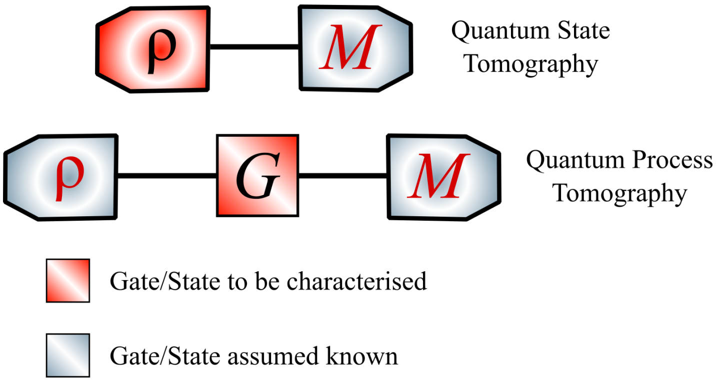

Figure 4.1: **Schematic of the structure of circuits for QST and QPT**. **Top**: QST. A state of interest, ρ, is characterised by using a set of informationally complete and known measurements, M, with outcomes E_j. **Bottom**: QPT. A gate, G, is characterised using a set of informationally complete M known measurements, and a set of informationally complete known initial states ρ. Here, 'informationally complete' refers to the property that each quantum state can be uniquely determined by its measurement statistics [99]. M and ρ are coloured red to reflect that, in reality, these measurement and state preparations are often not exactly known and/or cannot be perfectly implemented.

outcomes $\{\langle\langle E_i|\}$, as well as a set of informationally complete initial states $|\rho_i\rangle\rangle$. Figure 4.1 (bottom) shows a schematic of the process of QPT: an (assumed to be known) initial state $|\rho_i\rangle\rangle$ is prepared, evolved under the gate to be characterised, G, and finally measured using (assumed to be known) measurement operators M, with possible outcomes $\{|E_j\rangle\rangle\}$. The probability of observing an outcome E_j is then given by:

$$P_{ji} = \mathrm{Tr}(E_j G \rho_i) = \langle\langle E_j|G|\rho_i\rangle\rangle. \tag{4.6}$$

As with QST where the matrix A was defined, a second matrix B can here be defined which contains the set of initial states ρ_i, such that:

$$B = \begin{pmatrix} \langle\langle \rho_1| \\ \langle\langle \rho_2| \\ \vdots \\ \langle\langle \rho_{N_2}| \end{pmatrix}, \tag{4.7}$$

where N_2 is the number of initial quantum states to be used. A matrix P, whose elements are P_{ji}, can then be constructed such that $P = AGB$.

In a similar manner to QST, it is assumed that all measurement effects $|E_j\rangle\rangle$ are known, as well as all initial states $|\rho_i\rangle\rangle$, and so therefore all elements of A and B must therefore also be known. The gate G can then be constructed (again assuming A and B are square and all eigenvalues are non-zero) from:

$$G = A^{-1} P B^{-1}. \tag{4.8}$$

In QPT, small errors in the calibration of gates used to implement different measurements can propagate to the final results, and so these results can consequently be invalidated.

4.1.3 Randomised Benchmarking

Both QST and QPT rely on a crucial assumption, that the unknown state or gate is reconstructed relative to some reference operations, be these prepared states or measurement operations, which are assumed to be perfectly known and implemented without errors. However, in practice this is not achievable, and there will always be errors in the state preparation and measurement operations. It is therefore necessary to consider other techniques which are able to characterise not only states and/or gates, but also the preparation and measurement operations which are used to implement them.

A widely used method for characterising a set of gates, which also includes state preparation and measurement (SPAM) errors, is the technique of randomised benchmarking [92, 101–105]. This is a method whereby many random circuits from the Clifford group [101] are performed on one or more ions in order to measure the error rate of a set of quantum gates [92, 103, 106]. For a single qubit, the Clifford group can be constructed from the Pauli operations. The mathematical description of randomised benchmarking is highly involved and not relevant for the remainder of this Chapter, and so is left to external sources [92, 93, 103].

Randomised benchmarking has been used to characterise both single-qubit gates [102, 105], and multi-qubit gates [104]. There has also been a recent proposal for randomised benchmarking in the analogue setting, whereby a family of Hamiltonians native to the system can be characterised [107], although most randomised benchmarking protocols are digital in nature. Both randomised benchmarking and GST attempt to characterise gate sets of interest, however they do this in different ways. Randomised benchmarking specifically randomises sequences of gates from the Clifford group in order to gain information about a noise channel, Λ. It does this by averaging Λ over specific unitary operations, U, which are chosen according to a certain probability distribution, a process known as ‘twirling’ [108]. However, this causes randomised benchmarking to be intrinsically less sensitive to coherent errors which can arise through implementation of the gates, such as low-frequency drift. In addition, the only way to assign error bars to values calculated from randomised benchmarking is through bootstrapping [109]. In contrast, GST uses structured, periodic circuits in order to amplify errors in the gate set, making it sensitive to coherent errors, with the ability to provide rigorous confidence-interval error bars [97, 109]. As such, randomised benchmarking and GST can be viewed as two complimentary protocols which aim to address different needs; randomized benchmarking requires a fairly simple analysis of the data, however is relatively insensitive to coherent errors, whereas GST, although being more sensitive to these errors, requires a complex analysis procedure for the data [88, 109]. For characterising only single-qubit gates in the QSim system (the analysis of which is correspondingly computationally unintensive), it is advantageous to be sensitive to both coherent and incoherent errors and consequently it was decided to implement GST rather than randomised benchmarking in order to achieve this.

4.1.4 Gate Set Tomography Protocol

It was discussed in the previous Sections how both QST and QPT assume the initial states and final measurement gates are known and can be perfectly implemented. This leads to a problem if the state preparation and/or measurement gates are faulty, as the resultant outcomes from the QST and QPT estimates will also then be faulty. GST circumvents this problem by including SPAM gates in the gate-set which is being estimated, while still requiring the same number of measurements as QST (and less than QPT) [88], with the aim to characterise an unknown set of both states and gates. It works by running a specific set of structured circuits which vary in length in order to generate a data-set, and then testing various detailed, gate-level error models to see how well they fit the data-set. The method keeps modifying and testing the models until one is found that agrees as well with the data as any model (within the specified parameters) can. It has been experimentally demonstrated multiple times [96, 110], including on trapped ions [97, 98, 111].

The following Section will discuss the relevant theoretical background to the implementation of GST in the QSim experiment, assuming that every gate operation is Markovian. The discussion will broadly follow those given in [38, 88, 97, 98], however will be constrained to the sections relevant to implementation in the QSim system, with more detailed explanations left to the above-mentioned references.

GST models the quantum system of interest as a 'black-box' device. It assumes that the only operations available are:

- Initialisation of the system
- A two-outcome measurement of the system, where the results can then be determined
- A set of logic gates $G_1 \dots G_k$

The method assumes that all of the effects of these operations are unknown, and can only be determined by analysing the data. A gate-set is then defined as being a complete description of the black box, expressed mathematically as: $\mathcal{G} = \{|\rho\rangle\rangle, \langle\langle E|, \{G_k\}\}$, where $\mathcal{G}$ represents the gate set, and E is the observable being measured. GST aims to reconstruct $\mathcal{G}$ purely from the outcomes of measurements on the black box system. Every GST sequence starts with a 'preparation' sequence, and ends with a 'measurement' sequence. In-between these sequences is an 'operation of interest'. This operation is chosen to be a short sequence repeated an integer number of times. As GST includes SPAM gates in the gate-set of interest itself, only a single initial state needs to be prepared, and only a single measurement basis needs to be used. This is a more realistic approximation to standard experimental procedures, where the initial state will often be a ground state of the qubit, and the measurement is often a σ_z measurement.

GST can be most optimally performed by using a hybrid scheme to analyse the data-set, using a combination of linear inversion GST (LGST) and maximum likelihood estimation (MLE), both of which will be explained in the following Sections. LGST has the bonus that it cannot become trapped in any local maxima which might exist in a likelihood function, unlike maximum-likelihood algorithms [88, 98]. However, it has a decreased accuracy in comparison to MLE, and as such can be used to provide a good starting point for MLE to optimise on [98].

Linear Inversion GST

LGST is a simple algorithm which can provide a low-precision estimate of the gate set of interest, $\mathcal{G}$, using measurement outcomes from a specific set of short circuits. These measurement outcomes can be analysed using linear algebra in a similar manner to the discussions of QST and QPT given previously [88].

LGST attempts to reconstruct a set of gates denoted as $\{G_k\}$, where the probability outcomes for each gate, P_k, form the matrix:

$$[P_k]_{ij} = \langle\langle E_i'|G_k|\rho_j'\rangle\rangle, \tag{4.9}$$

where ρ' and E' denote that these preparation and measurement outcomes are not known. Each element of $[P_k]$ can be measured, and ρ_j' and E_i' can be prepared/measured. As with QST and QPT, the matrices A and B can again be defined, and so Equation 4.9 can be expressed as:

$$P_k = AG_kB. \tag{4.10}$$

However, the difference in the case of LGST is that the elements of A and B are not assumed to be known, in contrast to QST and QPT where this was a crucial underlying assumption. As neither A nor B are known, so Equation 4.10 cannot be solved directly for G_k.

In order to compensate for this, additional probabilities can instead by measured. It transpires that the measurements of most use are those which would correspond to performing QPT on the identity operation, the outcome probabilities of which, $\mathbb{J}_{ij}$, are given by a Gram matrix such that:

$$\begin{aligned} \mathbb{J}_{ij} &= \langle\langle E_i'|\rho_j'\rangle\rangle \\ \implies \mathbb{J} &= AB. \end{aligned} \tag{4.11}$$

Assuming A and B are square with all eigenvalues non-zero, Equation 4.11 can then be inverted so that $\mathbb{J}^{-1} = B^{-1}A^{-1}$. Multiplying Equation 4.10 by this inversion yields

$$\begin{aligned} \mathbb{J}^{-1}P_k &= B^{-1}G_kB, \\ \implies G_k &= B\mathbb{J}^{-1}P_kB^{-1}, \end{aligned} \tag{4.12}$$

where G_k has been solved for in the second line. Equation 4.12 is therefore an expression for the set of gates $\{G_k\}$ up to a *gauge transformation* given by B. This gauge transformation cannot be known, and is also not physically important, as B can be set to any matrix which is invertible in order to reconstruct the set of gates, up to gauge freedom [88]. Choosing a suitable gauge will be discussed later in Section 4.1.4. As well as the set of gates G_k, the preparation and measurement gates can also be extracted using LGST by constructing vectors of observable probabilities $[\vec{\tilde{\rho}}]_j$ and $[\vec{\tilde{E}}]_k$ such that:

$$[\vec{\tilde{\rho}}]_j = \langle\langle E'_j|\rho\rangle\rangle \implies \vec{\tilde{\rho}} = A|\rho\rangle\rangle, \tag{4.13}$$

$$[\vec{\tilde{E}}]_k = \langle\langle E|\rho'_k\rangle\rangle \implies \vec{\tilde{E}}^{\mathrm{T}} = \langle\langle E|B, \tag{4.14}$$

where the unprimed quantities denote the ideal, target preparation and measurement outcomes, as opposed to the primed, unideal preparation and measurement outcomes which are actually implemented. These probabilities can be straightforwardly measured by performing QST on each preparation state, ρ', and measurement outcome, E'. By using Equation 4.11, these Equations can be written as:

$$|\rho\rangle\rangle = B\mathbb{J}^{-1}\vec{\tilde{\rho}}, \tag{4.15}$$

$$\langle\langle E| = \vec{\tilde{E}}^{\mathrm{T}}B^{-1}. \tag{4.16}$$

Therefore, Equations 4.12, 4.15, and 4.16 show that LGST has reconstructed the gate sets as well as preparation and measurement gates, up to a gauge transformation B, as the outcome probabilities from circuits can have multiple equivalent estimates. Any two sets of gates which are equivalent up to a gauge transformation will describe this set of outcome probabilities equally well, and will have the same fidelity with regards to the true gate set [38]. However, such gauge freedom can have a significant effect on the matrices which represent the gates, and correspondingly on the estimated quantities of interest such as the fidelity. Often, it can be most useful to fix a gauge after performing an initial GST analysis, and then reanalysing the data. This will be discussed further in Section 4.1.4.

Although the LGST algorithm can obtain self-consistent gate estimates, it is not constrained to produce physical estimates – with often an unphysical gate set being a more optimal fit to the data than a physical one [38]. As such, LGST is a low-accuracy method for obtaining an estimate of a feasible gate set. However, it can provide a useful starting point for further methods, such as maximum likelihood estimation, to subsequently optimise on, as will now be discussed.

Maximum Likelihood Estimation

The practical implementation of GST uses LGST as a starting point for MLE, which then improves on the estimates provided by LGST. MLE has a number of advantages over LGST, most notable is that it can be straightforwardly adapted to non-linear data sets, which are commonly found in GST data sets. Such nonlinearities arise in GST as gates often appear repeatedly in circuits, and so the probability of getting a certain outcome from a circuit is a nonlinear function of the parameters of the gate set [88, 98]. Further to this, LGST is not constrained to produce physical estimates, a problem which can be straightforwardly solved by using MLE [38]. It is natural to question why LGST is therefore even necessary in this context, however in dealing with non-linear data sets, MLE has a particular drawback; the problem may become NP-hard [98]. By first performing LGST, although the outcome is not necessarily optimal, it is close to the optimal point, and therefore provides a reasonable starting point for MLE [98]. In implementing MLE, the data is assumed to be Markovian; that is, the data sets are assumed to be independent of one another.

MLE works by taking a theoretical model and maximising the likelihood, $\mathscr{L}$, of observing the measured data by modifying the parameter values of its model. The algorithm systematically searches through parameter values, θ, for the best estimator, θ_{opt}, of the chosen distribution which maximises the probability of observing the data that has been measured, i.e. it maximises $\mathscr{L}$ for the parameter θ.

A likelihood function can be constructed for the gate sets of interest in GST as follows: if the predicted probability of observing an outcome from implementing a gate sequence, s, is given by p_s, and the corresponding actual observed frequency of the outcome is given by f_s, then $\mathscr{L}$ is given by [98]:

$$\mathscr{L}(\mathscr{G}) = \prod_s p_s^{Nf_s}(1-p_s)^{N(1-f_s)}, \tag{4.17}$$

where N is the number of measurements. In practice, it can often be simpler to deal with the log-likelihood function, which is correspondingly given by [97]:

$$\ln(\mathscr{L}) = N\sum_s (f_s \ln(p_s) + (1-f_s)\ln(1-p_s)). \tag{4.18}$$

Equation 4.18 therefore compares the theorised set of probability outcomes from the model, p_s, to the actual set of measured frequencies, f_s, of the data set, for a single experimental implementation of a gate sequence, s. The GST algorithm consequently maximises the log-likelihood of the entire data set, $\ln(\mathscr{L})$, in order to produce an estimate for the gates.

Gauge Fixing

The final part in the theoretical discussion of GST is concerned with the reconstruction of gate sets up to a gauge transformation. Gauge transformations are a concept which occur in a wide variety of areas, with one of the most well-known examples arising in electrodynamics: For example, the magnetic field, $\boldsymbol{B}$, can be written in terms of the magnetic vector potential, $\boldsymbol{A}$, such that $\boldsymbol{B} = \nabla \times \boldsymbol{A}$. However, $\boldsymbol{B}$ can just as well be written in terms of $\boldsymbol{A}$ and an additional potential, $\nabla\phi$, yielding $\boldsymbol{B} = \nabla \times (\boldsymbol{A} + \nabla\phi) = \nabla \times \boldsymbol{A}$ (as $\vec{\nabla} \times \vec{\nabla}\phi = 0$). Therefore, shifting the magnetic vector potential by the gradient of a scalar function yields the same unique $\boldsymbol{B}$. This shifting by $\nabla\phi$ is termed a gauge transformation.

A similar situation is found when performing GST experiments. This can be seen more clearly from Equations 4.12, 4.15, and 4.16, where the true gate-set, initial state, and measurement outcomes were not fully recovered, but rather solved up to a gauge transformation given by the matrix B [112]. As such, a GST experiment cannot be distinguished from the same GST experiment performed in another gauge [88]. Therefore, as the choice of gauge has no bearing on the outcome, the experimenter is free to choose a suitable gauge. However, care must be taken as, although the choice of gauge transformation has no bearing on the outcome probabilities of the experiment, it can have a large amount of influence on those quantities which quantify the distance between two gates, such as fidelity [88, 97].

The most optimal way to deal with this problem is to perform gauge optimisation, where the estimated gate-set returned by GST analysis is reported in a gauge in which a gauge-dependent metric, which reflects how ‘close’ the estimated gate set is to the ideal gate set, is optimised. Another way of viewing this is that the gauge is chosen to make the estimated gates match the true gates as closely as possible [88, 112]. The way in which a suitable gauge can be practically chosen is discussed in the next Section.

4.1.5 Experimental Implementation for 729 nm Qubit Rotations

Thanks to the development of the python pyGSTi[1] module by Sandia National Laboratories [113], GST has a relatively straightforward experimental implementation, with the experiments here all performed using a single ion[2]. This package is (among many other applications) specifically designed to generate a complete set of gate sequences, $\mathscr{G}$, for GST, as well as providing an analysis software for the subsequent measurement results. For the GST used in acquiring the following data, all gate sets use only $\pi/2$ single-qubit rotations, with the protocol comprised of three sections: (i) initialisation (ii) a series of gates

---

[1] pyGSTi open-source software `https://www.pygsti.info/`

[2] There are multiple extensions to this basic variant of GST, including for two qubits.

termed a ‘gate sequence’ (iii) measurement. The exact gate sequences which are implemented are calculated in order to amplify all physical parameters in the gate set, making GST intrinsically sensitive to coherent errors, unlike with randomised benchmarking [97].

Two different gate sets were generated in order to analyse all single qubit rotations achievable by using the radial beam (σ_x, σ_y rotations) and addressing beam (σ_z rotations) in the QSim system (see Section 3.1.2). One gate set analysed $\pi/2$ gates around the X- and Y-axes – denoted as G_x and G_y – and the second analysed $\pi/2$ gates around the X- and Z-axes, denoted as G_x and G_z. The gate set for analysis of G_x and G_y was comprised of 793 gate sequences, with lengths up to and including 32 individual gates, and for analysis of G_x and G_z 527 gate sequences were used, again with lengths up to and including 32 individual gates. The discrepancy in the number of gate sequences between these two implementations is due to the qubit being prepared and measured in the Z-basis. Because of this, the X and Y rotations are symmetric, however this degeneracy is lifted for the Z rotations, allowing the number of necessary sequences for G_x and G_z to be reduced.

The experimental protocol used to implement GST is the following: The system is first initialised in $|0\rangle$ ($\rho = |0\rangle\langle 0|$), before a single gate sequence is applied, with a final state measurement in σ_z ($E = |1\rangle\langle 1|$) being performed. Each experiment involving a single gate sequence was repeated 100 times in order to gain significant statistics. This procedure was repeated for each of the 793(527) gate sequences necessary for $\mathrm{G}_x\mathrm{G}_y$ ($\mathrm{G}_x\mathrm{G}_z$) gate tomography. This experimental sequence, when averaged over the repeats, generates 793(527) data points, each corresponding to the average excitation of the ion from a single gate sequence. This set of 793(527) data points, as well as the set of gate sequences implemented, can then be analysed using the pyGSTi module.

The pyGSTi module has several ways to choose a suitable gauge (that is, a suitable value for the matrix B in Equations 4.12, 4.15, and 4.16), either using standard ‘built-in’ techniques, or through user-defined gauge optimisation parameters. For the standard method, the pyGSTi module first finds an estimate for the gate by performing standard LGST followed by MLE without considering a gauge, as discussed in the previous Sections. It then varies over all possible gauges for this gate set in order to minimise a squared Frobenius distance [97] between the estimated gate set and the ideal gate set, choosing this minimised gauge as the final result. The squared Frobenius distance is chosen as a metric to minimise on due to it being well-behaved as well as reasonably fast to compute, in comparison to other metrics such as the trace or diamond distance [88].

4.1.6 Results

In analysing the data-set generated from GST, the gates in the optimisation sequence were modelled to be completely positive trace preserving (CPTP) in order to constrain the results to be physically realistic [38, 88, 98], and all errors are reported to the 95% confidence level. There are many metrics calculated through the analysis performed by

Table 4.1: Infidelity results from G_xG_y (Left) and G_xG_z (Right) GST analysis.

Gate	Infidelity, $r(E)$
G_x	0.0006(7)
G_y	0.0005(7)

Gate	Infidelity, $r(E)$
G_x	0.0010(15)
G_z	0.0076(45)

the pyGSTi module, not all of which are reported or discussed here.

Average Gate Infidelity

In reporting a meaningful error in an implemented gate, a metric must be chosen to quantify this value. There are multiple metrics which can be used, however in the following the average gate infidelity (referred to in the following simply as the infidelity) has been chosen, not least due to its relative simplicity as a metric. This infidelity quantifies how close the experimentally measured outcome is to the theoretical description [114]. Although the infidelity is relatively insensitive to noise which is not strictly stochastic (and so this metric can be seen as not capturing relevant coherent contributions to the errors) [115], in the following the noise processes are assumed to be Markovian, and so under such an assumption this metric well-represents the noise processes. In addition, there are arguments for it being a more relevant error metric from a computational standpoint than other error metrics [92].

The infidelity metric is an average over all pure states, ψ, and the overlap these states have with an error, $E(\psi)$. It is defined as [115, 116]:

$$r(E) = 1 - \int \mathrm{d}\psi \ \mathrm{Tr}(\psi E(\psi)). \tag{4.19}$$

This metric corresponds to an error rate for a measurement in an expected eigenbasis of the system, and so gives a measure of the discrepancy between the expected state and the measured state [115].

Table 4.1 displays the infidelity results from the implementation of the two GST characterisation measurements. From the G_xG_y GST, the average gate infidelity for G_x is 0.0006(7) and for G_y is 0.0005(7). For G_xG_z tomography, G_x is 0.0010(15) and G_z is 0.0076(45). The gate infidelities from the G_xG_y GST are very similar, which is to be expected due to these rotations being performed with the same beam (the radial beam). The gate infidelities from the G_xG_z analysis differ more substantially, with the increased error associated with G_z expected due to the inherent instability of the addressing beam which implements this gate, on accounts of its very small beam waist (on the order of $2\,\mu\mathrm{m}$ [77]).

Table 4.2: SPAM results from G_xG_y analysis.

G_xG_y	Fidelity	Infidelity
Preparation	0.9999(14)	0.0001(14)
Measurement $\|0\rangle$	0.9999(21)	0.0001(21)
Measurement $\|1\rangle$	0.9986(66)	0.0014(66)

Table 4.3: SPAM results from G_xG_z analysis.

G_xG_z	Fidelity	Infidelity
Preparation	0.9999(14)	0.0000(14)
Measurement $\|0\rangle$	0.9999(2)	0.0000(2)
Measurement $\|1\rangle$	0.9999(2)	0.0000(2)

State Preparation and Measurement (SPAM) Errors

The GST analysis not only provides information on the errors of G_k gates, but also allows an estimation of the SPAM errors. Tables 4.2 and 4.3 show the results from this analysis for both of the GST measurements, with the errors in state preparation, as well as measurement errors of the two states $|0\rangle = |{\downarrow}\rangle = |\mathrm{S}_{1/2}, \mathrm{m_j} = +1/2\rangle$ and $|1\rangle = |{\uparrow}\rangle = |\mathrm{D}_{5/2}, \mathrm{m_j} = +5/2\rangle$ given.

For the G_xG_y analysis, the probability of successful state preparation (equivalent to the optical pumping success probability) was found to be 0.9999(14), and for the G_xG_z measurement, was found to be 0.9999(14), which agree with each other within error. These values are in agreement with measurements made previously which estimated the probability of successful state preparation to be on the order of 99.9% [23]. For the G_xG_y analysis, the measurement error for $|0\rangle$ is 0.0001(21), and for $|1\rangle$ is 0.0014(66). For the G_xG_z measurement, the measurement error for $|0\rangle$ is 0.0000(2) and for $|1\rangle$ is 0.0000(2).

Calculation of Error Bars using Confidence Regions

So far, the discussion has been confined to finding an estimate of a gate set which is as close as possible to the true gate set being characterised. However, there will of course be an associated error associated with how good the estimate of the gate set was, a calculation which can be achieved using GST. Blume-Kohout describes a procedure for assigning likelihood ratio confidence regions in QST in [117], which forms the basis for calculating error bars in GST.

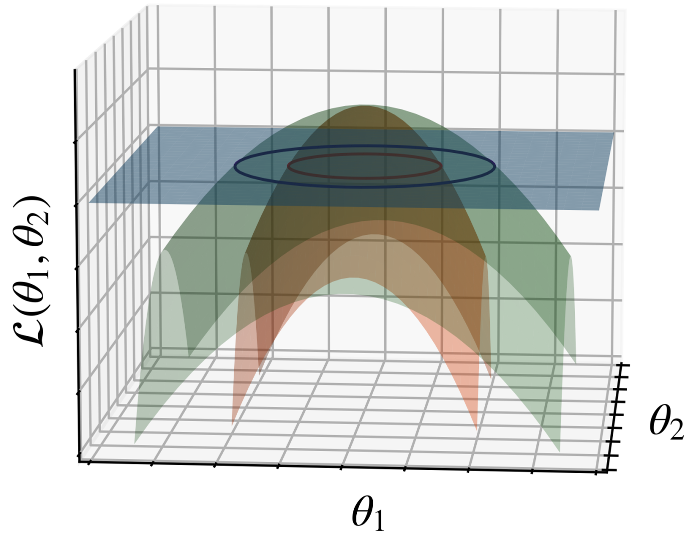

Figure 4.2: **Confidence regions from curvature of the likelihood function.** Two simulated quadratic likelihood functions (red and green) are plotted to demonstrate how the certainty with which the maximum of the likelihood function can be estimated is dependent on the curvature of the likelihood function itself. The maximum of functions with greater curvature (e.g. red) can be predicted with much greater accuracy than functions with more gentle curvature (e.g. green). A confidence level (blue plane) naturally encompasses a wider range of values for functions with more gentle curvature, so corresponding to a larger error bar on values derived from such functions.

Likelihood functions fundamentally assume that the real parameters of the real gate set, $\vec{\theta}_{\mathrm{T}}$, are close to the optimal parameters obtained through MLE, $\vec{\theta}_{\mathrm{opt}}$, and so the set of $\vec{\theta}$ which have a likelihood above a particular threshold will provide a suitable confidence region. To determine this region, the log-likelihood function can be approximated as a quadratic function, whose shape can then be given by the Hessian of the log-likelihood at the point around the maximum likelihood estimate [97, 109]. The variance of a maximum likelihood function can then be estimated using this.

The Hessian is the matrix of all second derivatives of the likelihood function, $\mathscr{L}$, with respect to the parameters, $\vec{\theta}$, i.e.

$$H(\vec{\theta}) = \frac{\partial^2 \ln\mathscr{L}(\vec{\theta})}{\partial\theta\partial\theta'} = \begin{pmatrix} \frac{\partial^2 \ln\mathscr{L}(\vec{\theta})}{(\partial\theta_1)^2} & \frac{\partial^2 \ln\mathscr{L}(\vec{\theta})}{\partial\theta_1\partial\theta_2} & \cdots & \frac{\partial^2 \ln\mathscr{L}(\vec{\theta})}{\partial\theta_1\partial\theta_n} \\ \frac{\partial^2 \ln\mathscr{L}(\vec{\theta})}{\partial\theta_2\partial\theta_1} & \frac{\partial^2 \ln\mathscr{L}(\vec{\theta})}{(\partial\theta_2)^2} & \cdots & \frac{\partial^2 \ln\mathscr{L}(\vec{\theta})}{\partial\theta_2\partial\theta_n} \\ \vdots & \vdots & \ddots & \vdots \\ \frac{\partial^2 \ln\mathscr{L}(\vec{\theta})}{\partial\theta_n\partial\theta_1} & \frac{\partial^2 \ln\mathscr{L}(\vec{\theta})}{\partial\theta_n\partial\theta_2} & \cdots & \frac{\partial^2 \ln\mathscr{L}(\vec{\theta})}{(\partial\theta_n)^2} \end{pmatrix}, \tag{4.20}$$

where $\vec{\theta} = (\theta_1, \theta_2, \ldots, \theta_n)$ is an n-dimensional vector of parameters. The curvature of the likelihood function is given by these second derivatives, giving an indication of the certainty with which parameters can be estimated. Figure 4.2 shows how the curvature of the likelihood function can dictate the certainty with which the maximum (i.e. optimal point) can be estimated: if the likelihood function has a greater curvature, as shown by the red function, then the maximum of this function is estimated with more certainty. Conversely, likelihood functions with less curvature, as shown by the green function, have a greater uncertainty. If a confidence level (blue plane) is then imposed on these functions, it will encompass a wider range of values for functions with more gentle curvature, so corresponding to a larger error bar on values derived from such functions. As such, the Hessian – in representing the curvature of the likelihood function – can be used to give an indication of the uncertainty with which the parameters have been estimated.

The Hessian can be directly related to the variance of the maximum likelihood function through the expression:

$$\mathrm{var}(\vec{\theta}) = (-\langle H\rangle)^{-1} = \left(-\left\langle\left[\frac{\partial^2 \ln\mathscr{L}(\vec{\theta})}{\partial\theta\partial\theta'}\right]\right\rangle\right)^{-1}, \tag{4.21}$$

where $\langle\rangle$ is the expected value (e.g. the mean). The pyGSTi module calculates error bars for the quantities derived from the GST analysis using this method. It first calculates $H(\vec{\theta})$ for $\ln(\mathscr{L})$ of the best-estimate gate set. The calculated Hessian is then inverted, and scaled such that it defines an ellipsoid which coincides with $\mathscr{L}$ [88]. This method provides the errors for all values given in this Section.

Model Violations of the Data Sets

One of the main assumptions underlying GST is that the noise processes experienced by the qubit is Markovian – that is, the noise in the applied gates is memoryless and uncorrelated in time, as well as being independent of any gates which might have recently been applied. As such, the state of the qubit at time $t + 1$ should be determined solely by the state of the qubit at time t and the operation applied to the qubit at time t. However, for real quantum systems, the repeated quantum operations are never truly identical, due to experimental imperfections. This non-repeatability is non-Markovianity, and can be estimated from GST. There are also many other examples of non-Markovian behaviour which can affect the qubit. For example, slow drifts can introduce non-Markovian noise

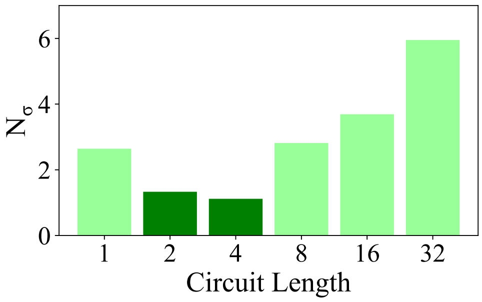

(a) Model violation for $G_x G_y$ GST

L	$2\Delta\ln(\mathscr{L})$	k	N_σ
1	59.57	37	2.62
2	93.29	77	1.31
4	190.26	170	1.10
8	441.68	366	2.80
16	694.00	570	3.67
32	1007.43	774	5.93

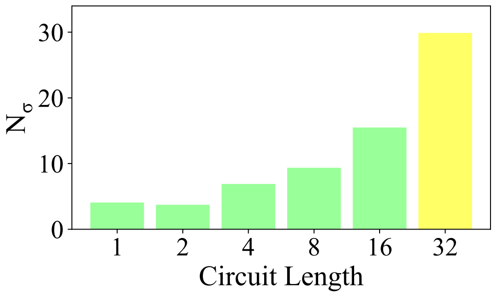

(b) Model violation for $G_x G_z$ GST

L	$2\Delta\ln(\mathscr{L})$	k	N_σ
1	65.31	33	3.98
2	102.48	62	3.64
4	246.97	135	6.81
8	457.29	250	9.27
16	802.72	379	15.4
32	1458.10	508	29.8

Figure 4.3: **Model Violations** The amount of model violation, N_σ, as a function of the length of the implemented circuit, L. a) For the $G_x G_y$ gate sequence, there is a relatively low level of circuit violation, even for circuit lengths up to length 32. b) For the $G_x G_z$ gate sequence, there is a significant amount of model violation, especially for longer circuit lengths. Shown in the tables for both gate sequences are the relevant numerical values extracted for the calculation of the model violation.

into the system, as well as correlations between errors in consecutive gates. For these processes, the outcome of GST analysis will be a significant 'badness of fit' in the results (although it is assumed that the data is sufficiently Markovian that the GST estimate will still be fairly reliable). This can be seen as a violation of the model, and therefore as non-Markovianity. The pyGSTi module allows an analysis of the non-Markovianity of the data to be performed.

A measure of how well the estimated model fits the data can be determined from the log-likelihood function $\ln(\mathscr{L})$, calculated during the MLE step in GST, by using Wilks' theorem [118]. The most optimal fit to the data is the one where, for each gate sequence s implemented, the probability of observing an outcome, p_s, is equivalent to the actual observed frequency of that outcome, f_s, i.e. $p_s = f_s$. This can be obtained by using N_s free parameters in the model, where N_s is the number of gate sequences implemented (i.e. assuming one free parameter per gate sequence). The log-likelihood outcomes from fitting the estimated model to the data, $\ln(\mathscr{L})$, can then be compared with the outcome from fitting this optimal fit to the data, $\ln(\mathscr{L}_{\text{opt}})$. $\ln(\mathscr{L}_{\text{opt}})$ will be the maximum value possible with the most free parameters [119].

In the context of GST, Wilks' theorem states that if the gate set model estimated by GST is a valid, close fit to the data with N_p free parameters (where $N_p < N_s$), then the comparison between these two likelihood functions, defined as $2(\ln(\mathscr{L}_{\text{opt}}) - \ln(\mathscr{L})) = 2\Delta\ln(\mathscr{L})$, can be approximated as a random variable drawn from a χ^2 distribution, with mean k and standard deviation $\sqrt{2k}$, where $k = N_s - N_p$ [97].

If $2\Delta\ln(\mathscr{L})$ could reasonably have been sampled from a χ^2 distribution, that is if it lies within the interval $[k - \sqrt{2k}, k + \sqrt{2k}]$, then the estimated GST model fits the data as well as can be hoped, and so there is no substantial evidence for non-Markovianity. However, if $2\Delta\ln(\mathscr{L})$ is so high that it is lies outside this range and so is unlikely to have been sampled from a χ^2 distribution, then there is evidence for non-Markovian processes being involved in the generation of the data. Therefore, a lower $\Delta\ln(\mathscr{L})$ corresponds to a better agreement between the model and the data.

The amount of model violation can then be quantified by N_σ, which is the number of standard deviations by which $2\Delta\ln(\mathscr{L})$ exceeds the expected value when a χ^2 distribution is assumed:

$$N_\sigma = \frac{2\Delta\ln(\mathscr{L}) - k}{\sqrt{2k}}. \tag{4.22}$$

Figure 4.3 gives an indication of the level of model violation experienced by the two GST protocols implemented in the previous Section. Figure 4.3 a) shows that, for the $\mathrm{G}_x\mathrm{G}_y$ gate sequence, there is a low level of model violation, as the separation in standard deviations, N_σ, between the ideal and measured models is low. This indicates that the assumption of purely Markovian noise is reasonable. With Figure 4.3 b), it can be seen that the model violation for the $\mathrm{G}_x\mathrm{G}_z$ gate sequence is significantly larger, especially for longer circuit lengths. For a circuit length of 32, the model violation is on the order of 5 times larger than for the $\mathrm{G}_x\mathrm{G}_y$ gate sequence. These results imply that there may be non-Markovian noise processes having a significant impact on the results which are not captured by the assumed model. These results are not necessarily surprising: the addressing beam (implementing G_z gates) has a very small beam waist as noted previously, and so will be highly susceptible to drifts from beam pointing and movement of the ion in the trap, so manifesting as non-Markovianity in the data-set. This feature would not be expected to be present in the $\mathrm{G}_x\mathrm{G}_y$ data set as this beam is extremely broad in comparison to a single ion, and so drifts from beam pointing and movement of the ion should not significantly affect the data-set.

4.2 Characterisation of Beam Drifts using GST

The GST analysis discussed so far has assumed a stable, repeatable implementation of the protocol over the course of the measurement time – which is on the order of hours.

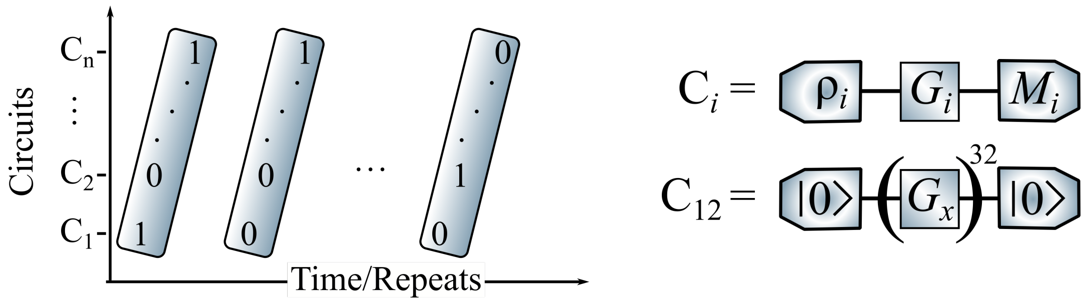

Figure 4.4: **Rastering of data to provide time-series data**. **Left** The data is rastered in order to provide information as to the drifts which may be present in the data. A circuit, C_1 is implemented once, with the outcome and time at which the measurement was performed recorded. The second circuit C_2 is then implemented, and so on to circuit C_n. The entire set of circuits $C_1 \dots C_n$ is then repeated many times over the course of several hours. **Right** Examples of the circuits which are implemented. These circuits are the same as used for the GST discussed previously.

However, in reality it is likely there will be drifts occurring due to beam pointing and movement of the ion in the trap, causing this assumption to break down. In fact, it was even seen in the previous Section that there is significant non-Markovianity present in the G_xG_z data-set. By implementing a slightly modified protocol to the one discussed so far in order to gather data, the pyGSTi package is able to analyse drifts over time. By looking at the long term drifts in the data set, the motional stability of the experiment with respect to the beam paths and ion confinement can be inferred. The following protocol which will now be outlined is based on [111], where a highly detailed explanation of the protocol and analysis is given.

4.2.1 Protocol

With the GST implemented so far, a circuit is implemented on the ion, repeated 100 times to acquire significant statistics, before the next circuit is implemented. To look for evidence of drifts using GST, a subtle change to this experimental protocol is required. Figure 4.4 shows how this should be done through the use of *rastering*. A circuit, C_1, should be implemented once, with the outcome recorded, before the next circuit C_2 is implemented, the outcome recorded, and so on to the final circuit C_n. This entire set of circuits $C_1 \dots C_n$ is then repeated many times, over the course of multiple hours, in order to determine whether drifts are present in the dataset. The outcome of this implementation is a sequence of 0s and 1s which may vary with time, denoted as a vector $\vec{x}$. As such, this protocol requires the use of time-stamped data – that is, when the outcome from implementation of a circuit is recorded, the time at which the circuit was measured must also be recorded. The circuits used for looking for drifts are the same as those used for standard GST.

Having collected the time-stamped, rastered dataset, $\vec{x}$, the data is then transformed into the frequency domain, first by standardising it through subtracting the mean and dividing by the variance. The amplitudes in the frequency-domain are then given by [111]:

$$\vec{\tilde{x}} = \begin{cases} \frac{\hat{T}(\vec{x} - \bar{x}\mathbb{I})}{\sqrt{\bar{x}(1-\bar{x})}}, & \text{for } 0 < \bar{x} < 1 \\ (0, 1, 1, \ldots)^{\intercal}, & \text{otherwise,} \end{cases} \tag{4.23}$$

where $\bar{x}$ is the mean of $\vec{x}$, and the elements of the matrix $\hat{T}$ are given by:

$$T_{\omega,m} = \sqrt{\frac{2^{1-\delta_{\omega,0}}}{n}} \cos\left(\frac{\omega\pi}{n}\left(m + \frac{1}{2}\right)\right), \tag{4.24}$$

with $\omega, m = 0, \ldots, n-1$. $\hat{T}$ is a discrete cosine transform with orthogonal normalisation. The power at a given frequency, ω, is then given by $|\tilde{x}_\omega|^2$. It can therefore be seen that, in the frequency domain, each $\tilde{x}_\omega$ is a weighted sum of n bits. The weightings in Equation 4.24 ensure that the shot noise inherent to such experiments is averaged out [111]. A null hypothesis test can then be performed on this data to determine whether temporal instabilities are present, as will now be explained.

Each implemented circuit, C_i, has an arbitrary probability distribution of possible outcomes. However, although arbitrary, the crucial point is that this probability distribution should be *static* if there are no temporal instabilities present. From Equation 4.23, if there are no temporal instabilities, then the power spectra of the Fourier-transformed time-series data would follow a χ_1^2 distribution, and only contain terms which have an expected value of 1 due to the presence of shot noise. By looking for values of $|\tilde{x}_\omega|^2$ that are larger than the $(1-\alpha)$ percentile of the χ_1^2 distribution, where α is a pre-defined confidence level often chosen to be 5%, powers in the spectra which are too high to be consistent with a dataset with no drifts can be determined.

To construct a null hypothesis to test for such inconsistencies, it is useful to consider that the expected value of $\vec{\tilde{x}}$, i.e. $\langle\vec{\tilde{x}}\rangle$, is a probability distribution for a particular circuit: that is, $\langle\vec{\tilde{x}}\rangle = \vec{\tilde{r}}$. As such, the null hypothesis which can be used is that the change in the probability distribution of a particular circuit, $\tilde{r}_\omega$, is zero for all non-zero frequencies and for every circuit which is implemented – i.e. $\tilde{r}_\omega = 0$ (there is no drift present). For each value of ω, and for every circuit C_i, a test is then performed to determine the value of $\tilde{r}_\omega$.

In order to determine whether a resulting outcome of $\tilde{r}_\omega > 0$ is statistically significant, a ***p-value*** is calculated [120]. The p-value is a measure of how likely it is to observe that result (or a result which is even more extreme) if the null hypothesis is true [120, 121]. If the outcome of the p-value is less than the predefined significance level, α, then there is a statistical incompatibility between the null hypothesis and the data set. Often, however somewhat arbitrarily, α is defined to be 5%, such that if $p < 0.05$ then the null hypothesis is rejected [120, 121]. As such, for the data here, if the spectral power is greater than the 95%

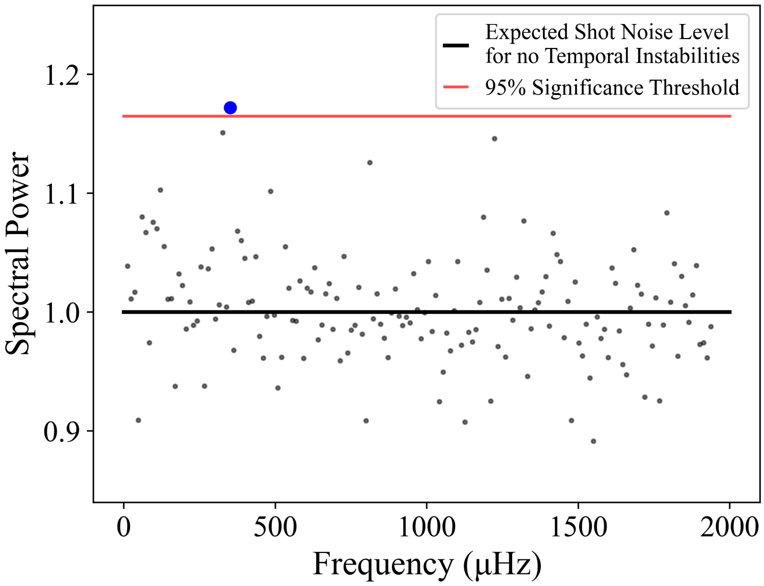

Figure 4.5: **Spectral power of the drift frequency components from drift analysis**. Plotted are the spectral powers of detected frequencies from implementation of the drift analysis. Points in grey are those which are below the 95% significance threshold level. Only one frequency, shown in blue at $351\,\mu$Hz with a p-value of 8.68×10^{-5}, was found to be above the 95% significance threshold. The black line is the spectral power expected due to shot noise with no temporal instabilities present. The red line (at a value of 1.16) signifies the 95% significance threshold level.

significance level, then it can then be concluded that $\tilde{r}_\omega > 0$, and so the null hypothesis is violated.

4.2.2 Results

Figure 4.5 shows the results from the implementation of the drift analysis on a single ion, using G_xG_z GST circuits over a period of 18 hours and 36 minutes, where 161 repeats were taken. As the radial beam implementing G_x gates is over two orders of magnitude larger than the addressing beam implementing the G_z rotations, any detected instabilities can be assumed to be due to either drifts of the addressing beam, or drifts in the position of the ion in the trap. The expected spectral power due to shot noise is shown as a solid black line at a spectral power value of 1.0. The significance level of $(1-\alpha) = 95\%$ is shown as the solid red line. Frequencies with a spectral power above this level can be considered inconsistent with the null hypothesis. Only one frequency (shown in the Figure as an enlarged blue point) exceeded the 95% significance threshold, at $351\,\mu$Hz with a p-value of 8.68×10^{-5} and spectral power of 1.17. This corresponds to drifts on timescales of 5 hours.

4.3 Characterisation of the 729 nm Beam Path Stability

The final Section of this Chapter will look at contributions to the phase noise experienced by the ions due to instabilities in the 729 nm beam paths. Phase noise detected on the ions can occur from two main sources: phase noise from the laser itself, or instabilities in the beam path from laser to ion. These two sources of phase noise can be distinguished by using a Ramsey-type experiment which exploits two different beam paths as will now be described.

Consider a single ion addressed by light from two separate beam paths, termed 1 and 2 (restricted to the one dimensional case for clarity, although this of course generalises to three dimensions). The light incident on the ions from each path has the form $e^{i(\omega_1 t_1+\phi_1)}$ and $e^{i(\omega_2 t_2+\phi_2)}$ respectively. From Section 2.3.1, the probability of being found in the excited state when a Ramsey experiment is performed, with a waiting time of τ, is: $P = 1/2(1 - \cos(\Delta\omega\tau + \phi))$, where $\Delta\omega$ is the detuning of the laser with respect to the transition frequency of the ion.

If an experiment is now performed where the first and second pulses of the Ramsey experiment are from two different beam paths, rather than the same beam path as has previously been assumed (however assuming that the light in both beam paths originates from the same laser source), then the expression for the probability of being found in the excited state during a Ramsey experiment becomes $P = 1/2(1 - \cos(\Delta\omega\tau + (\phi_1 - \phi_2)))$, assuming that there is no difference in laser frequency between the two paths. Correlations in time between measurements of consecutive Ramsey experiments can then be expressed in the form:

$$\mathscr{C}_{i,j} = \langle (2P_i - 1)(2P_j - 1)\rangle = \langle \cos(\Delta\omega t_i + (\phi_1 - \phi_2)_i)\cos(\Delta\omega t_j + (\phi_1 - \phi_2)_j)\rangle. \tag{4.25}$$

Assuming that the laser is exactly resonant with the ion transition frequency (and so $\Delta\omega = 0$), these correlations simplify to:

$$\mathscr{C}_{i,j} = \langle (\cos(\Delta\phi_i))(\cos(\Delta\phi_j))\rangle, \tag{4.26}$$

where $\Delta\phi_i = (\phi_1 - \phi_2)_i$. Assuming that the beam path fluctuations in the two paths are independent, the phases from the two separate beam paths will then be uncorrelated, and so Equation 4.26 can be expressed as:

$$\mathscr{C}_{i,j} = \langle \cos(\Delta\phi_i - \Delta\phi_j)\rangle. \tag{4.27}$$

Therefore, the correlations between two such Ramsey experiments can be used to measure the differences in phases between the first and second laser pulse. As this experiment is insensitive to laser phase noise for short (on the order of a few microseconds) Ramsey

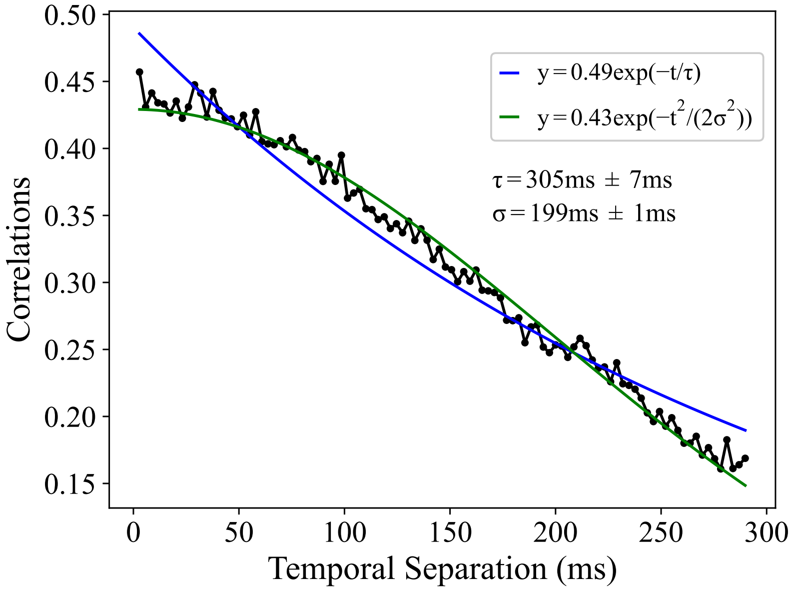

Figure 4.6: **Auto-correlations from a single-ion experiment**. Plotted are both exponential (blue line) and Gaussian (green line) fits to the data (black points). The Gaussian decay better fits the data, indicating that the decay in correlations is predominantly affected by slow phase noise.

probe times, instabilities in the path lengths are the only contributions to the phase noise, and so the dynamics of these correlations will reveal information about fluctuations in the path lengths from one experiment to the next.

Practically, this experiment was implemented using the radial beam path and the addressing beam path, separated by a short wait time on the order of $2\,\mu$s, with the phase of the second pulse then scanned over. Correlations between a phase scan at time t_i and time t_j were then calculated for the entire duration of the experiment. As each phase-scan is of a sinusoidal form, correlations between two phase scans are equivalent to the average over a sine-squared function, which can only have a maximum value of 0.5. Two experiments were performed: firstly on a single ion where auto-correlations were looked at, and secondly on a four-ion chain which allowed investigations of cross-correlations.

Auto-Correlations from 1 Ion

Figure 4.6 shows the results from performing such an experiment on a one-ion system. The Figure shows the correlations of the ion with itself as a function of the length of time separating the two measurements. Shown are two fits to the data: an exponential decay (blue line) and a Gaussian decay (green line). This provides useful information about the source of errors producing this decay in the system; for fast frequency noise, an exponential decay of the correlations can be expected. For low-frequency noise, the decay-curve is likely to be non-exponential, with a Gaussian shape expected [122]. It can be seen

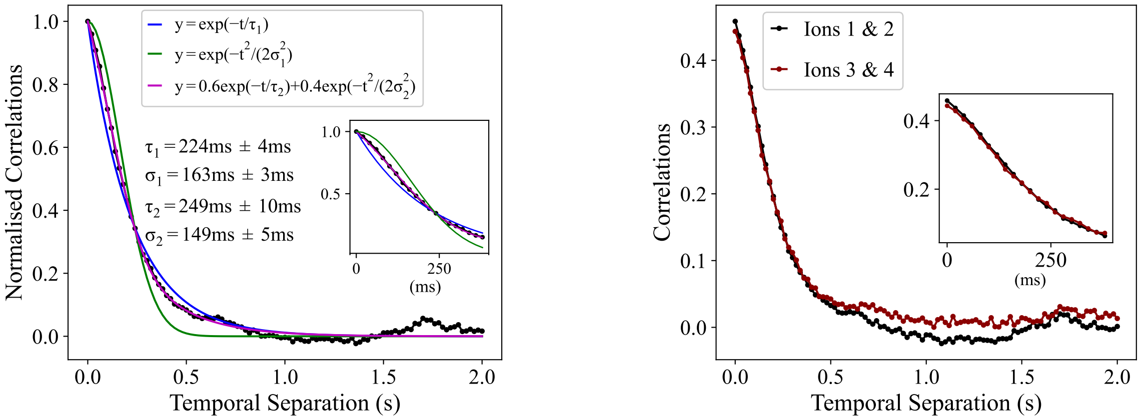

(a) Normalised summed correlations

(b) Correlations

Figure 4.7: **Correlations from a 4-ion experiment**. a) The normalised summed correlations over ions 1 & 2, and 3 & 4 as a function of temporal separation (black points). Plotted are both exponential (blue line) and Gaussian (green line) fits to the data. Inset: Correlations and associated fits at short times. An additional fit (magenta) of a sum of exponential and Gaussian decays represents the data better at short times. b) Correlations between ions 1 & 2 (black points) and ions 3 & 4 (red points) which have been summed in a). Inset: Correlations at short times. The lack of an appreciable drop in correlations at short times indicates there is no significant contribution to the decay from very high-frequency noise.

that a Gaussian decay better fits the decay of these correlations over the short time-scales probed in the experiment, indicating that the correlations here are predominantly affected by slow phase noise. This is consistent with phase noise produced by fluctuations in the beam path, which would be expected to be slow drifts.

The correlations decay over a time-scale of approximately 300 ms, which is much larger than the current coherence time of the system (on the order of 64 ms for the $|S\rangle$ to $|D\rangle$ transition as discussed in Section 3.4), and so it can be concluded that phase instabilities introduced by path length fluctuations are not, currently, a dominant source of noise in the system.

Cross-Correlations from 4 Ions

Although providing a large amount of information as to the path length instabilities present in the system, the experiments performed with one ion are not able to provide information for the time $t = 0$ (as the ion should always be perfectly correlated with itself at this point). In order to address this issue, experiments can be performed with multiple ions, and the correlations between the ions at time $t = 0$ can then be examined, providing information as to whether very-high frequency noise is present in the system. Figure 4.7 a) shows the results from a measurement similar to that performed in the previous Section, however performed with four ions. The Figure shows the summed correlations between ions 1 & 2 and 3 & 4 (black points), normalised to 1. In the Figure, several different fits to the data are shown. For long-time separations, the data can be well described by an exponential decay (blue line). At shorter times, an exponential fit no longer truly captures the behaviour of the data, however a Gaussian decay (green line) is also not ideal. The most optimal fit to the data is found to be from a sum of both exponential and Gaussian terms of the form:

$$y = 0.6e^{-t/\tau} + 0.4e^{-t^2/(2\sigma^2)}, \tag{4.28}$$

with $\tau = 249\,\mathrm{ms}$ and $\sigma = 149\,\mathrm{ms}$, shown by the magenta line. Such a fit describes the data well out to at least 300 ms. This shows that the decay of correlations between ions experiences contributions from both higher-frequency, Markovian noise as well as lower-frequency Gaussian noise. Figure 4.7 b) shows the individiual correlations between ions 1 & 2 (black points) and 3 & 4 (red points). This contains information about the correlations between the ions at time $t = 0$. As there is no appreciable drop in correlations at this point, it can be concluded that there are no significant contributions to the decay from very high-frequency noise, such as high-frequency acoustic noise, which would lead to a significant decrease in correlations at very short times.

Chapter 5

Theoretical Consideration of Randomised Measurements

When performing quantum computations and simulations, it is important to have ways of characterising the system of interest; to ensure it is performing as intended and to measure quantum properties of interest. Small systems, comprised of only a few qubits, are relatively easy to characterise, for example through quantum state tomography (QST) [95, 123]. For such small systems, QST is readily implementable using an experimentally feasible number of measurements.

However, the number of measurements necessary to characterise a system of interest using QST grows exponentially with the number of qubits. This quite clearly leads to a problem in developing intermediate-scale quantum simulators of up to ~100 qubits [18]. Indeed, even above about eight qubits [95], the number of measurements required to perform quantum state tomograpy simply becomes infeasible to experimentally implement. With the current progress in developing complex, many-body quantum systems which have ever-increasing numbers of qubits [124], it is necessary to develop new and evermore sophisticated methods to characterise systems of interest. The following Chapter will look at several novel, theoretical proposals which can be experimentally implemented in order to characterise quantum systems of several tens of ions, and so extract important information about these systems.

This Chapter lays the theoretical foundations for the subsequent experiments presented in Chapters 6 and 7, where the protocols detailed here will be experimentally implemented on 10-ion partitions of ion-strings of up to 20 ions. The first protocol presented is the theoretical underpinning for the publication *'Probing Rényi entanglement entropy via randomized measurements'* [24], the second is the theoretical basis for the publication *'Quantum Information Scrambling in a Trapped-Ion Quantum Simulator with Tunable Range Interactions'* [25], and the third is published in *'Cross-Platform Verification of Intermediate Scale Quantum Devices'* [26].

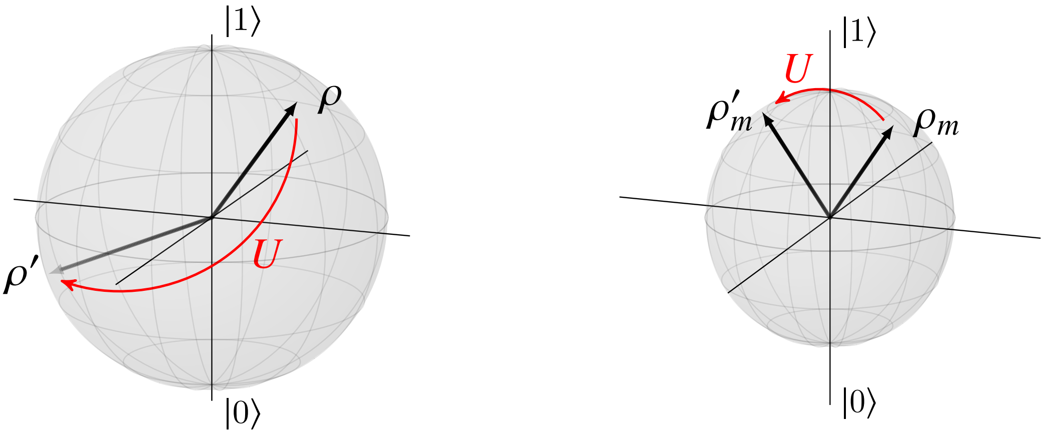

(a) Pure State, $|r| = 1$. (b) Mixed State, $|r| < 1$.

Figure 5.1: **Illustration of random rotations on the Bloch sphere**. a) An initial pure state, $\rho = |\psi\rangle\langle\psi|$, under application of a unitary operation drawn from the CUE, U, is rotated to any other point on the Bloch sphere with equal probability. The Bloch vector length, $|r| = 1$, is preserved under this rotation. b) An initial partially mixed state, ρ_m, is rotated to any other point on the shrunken Bloch sphere with equal probability. For this state, $|r| < 1$, however the purity is still preserved under this rotation.

5.1 Statistical Correlations between Randomised Measurements

In attempting to develop more sophisticated methods of characterising larger systems, a significant amount of effort has recently been invested into looking at how statistical correlations between randomised measurements can be used to extract useful information from many-body quantum systems [26, 125–130]. Randomised measurements are defined here as unitary operations which are randomly drawn from the circular unitary ensemble (CUE) [131]. The CUE consists of symmetric $n \times n$ unitary matrices together with their Haar measure (i.e. invariance under left and right translation) [132, 133]. Each element of the CUE is therefore a Haar-invariant unitary matrix such that, when applied to a single qubit (and for $n = 2$), any initial state on the surface of the Bloch sphere is rotated to any other point on the surface of the Bloch sphere with equal probability. Figure 5.1 gives a pictoral demonstration of this. In a), an initial pure state, $\rho = |\psi\rangle\langle\psi|$, which correspondingly has a Bloch vector length $|r| = 1$ (recall from Section 2.1.2 that the purity of a state, $\mathrm{Tr}(\rho^2)$, is proportional to the length of the Bloch vector), is rotated by a random unitary U to the state $\rho' = |\psi'\rangle\langle\psi'|$, with the purity of the state conserved – that is, ρ' also has length $|r| = 1$. Figure 5.1 b) shows this process for a partially mixed state, ρ_m. ρ_m can be visualised on a Bloch sphere with radius less than 1, i.e. $|r| < 1$. In the same way as for the pure state, this state will be rotated with equal probability to any other point on its shrunken Bloch sphere, preserving both the purity of the state and consequently the length of the Bloch vector.

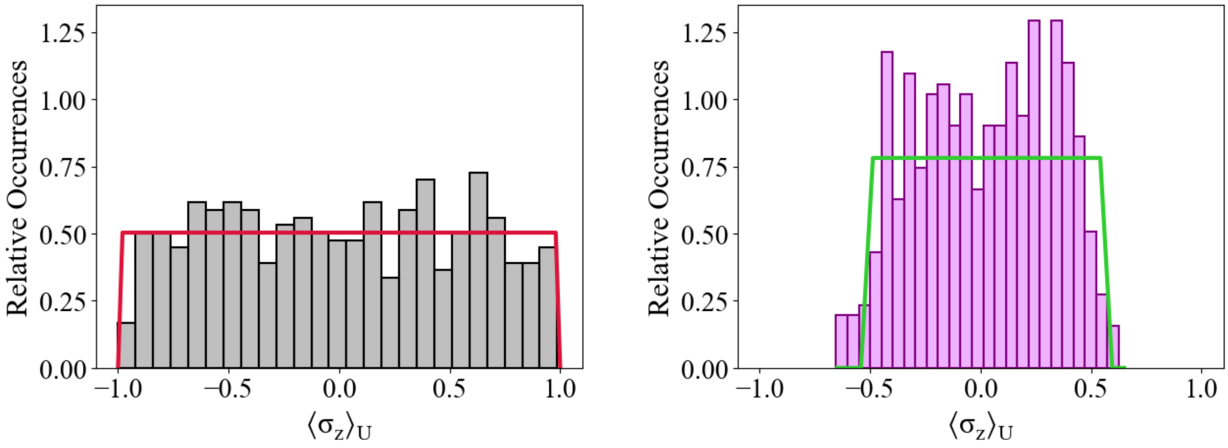

(a) Pure state

(b) Mixed State

Figure 5.2: **Histograms showing the width of the distribution of measurement outcomes, $\langle\sigma_z\rangle$, after application of random rotations U.** Shown is experimental data where the relative occurrences of $\langle\sigma_z\rangle$ measurement outcomes for different random unitaries, U, is plotted. a) Measurement outcomes from a pure state. The measurement outcomes uniformly cover the full range $-1 \leq r \leq 1$, reflecting that the purity of the state is equal to 1. b) Measurement outcomes from a partially mixed state. The measurement outcomes cover a smaller range than in a), showing that the Bloch vector length, $|r|$, is reduced (i.e. the state lies inside the pure-state Bloch sphere), and so the purity is correspondingly less than 1. Solid lines are a guide to the eye to demonstrate the uniform distribution.

A physical understanding of how randomised measurements can provide insights into the properties of an arbitrary state can be obtained from these illustrations. By applying a random unitary, U, to a single qubit and performing state readout (with sufficient repetitions of this process), and then repeating this process for many different random unitaries, the shape of the Bloch sphere can effectively be mapped out. This information about the shape of the Bloch sphere can then be extracted from the distribution of measurement outcomes from performing qubit readout by measuring in $\langle\sigma_z\rangle$. Figure 5.2 shows experimental data to illustrate the distribution of these probabilities for two different states. Figure 5.2 a) shows the distribution of $\langle\sigma_z\rangle$ outcomes for a pure state. As $|r|$, and so $\mathrm{Tr}(\rho^2)$, is always one, random rotations of this vector lead to a uniform distribution of measurement outcomes covering the full range $-1 \leq r \leq 1$. Conversely, Figure 5.2 b) shows this distribution for a partially mixed state, where $|r|$, and so also the purity, is always less than one. As such, the quantum state lies inside the pure-state Bloch sphere, with random rotations consequently leading to a distribution of measurement outcomes in a reduced interval. When considering multiple qubits, information about the purity of the state can also be extracted, except now by using sums of statistical correlations between the measurement outcomes of the randomised measurements.

When single qubit readout is performed, each qubit is measured in a fixed (logical) basis, in this work assumed to be the Z-basis. An outcome from a measurement on the state, denoted by $s = (s_1, \ldots, s_N)$ (as an example, for a two-qubit state these measurement outcomes would correspond to 00, 01, 10, 11), is then given by $P(s) = \mathrm{Tr}\left(U\rho U^{\dagger}|s\rangle\langle s|\right) = \langle s|U\rho U^{\dagger}|s\rangle$. The important quantity is the statistical cross-correlations between these measurement outcomes from randomised measurements, with the sum over these correlations taking the mathematical form,

$$\overline{\mathscr{C}} = \sum_{s,s'} P(s)P(s'). \tag{5.1}$$

It is these statistical correlations, extracted from randomised measurements, which can provide information into the dynamics of many-body quantum systems, so providing the basis for the three, theoretical protocols which will now be detailed in the following Sections.

5.2 The Second-Order Rényi Entropy

One of the most important quantites to measure in many-body quantum systems is that of entanglement. Entanglement can be considered an almost crucial property for quantum simulators and computers, and large amounts must be generated if they are to achieve advantages over their classical analogues [29]. A widespread question in quantum information is how to characterise this entanglement, as well as any correlations which may exist, in complicated quantum systems comprised of 10s of qubits. The first protocol which will be introduced aims to gain information about entanglement in a system through extracting the second-order Rényi entropy using randomised measurements.

At present, there are several methods available in order to probe entanglement in many-body systems. A well-known example is through the use of matrix product state tomography, where short-range correlations between qubits can be used to provide a simplified description of the wave function of the system [134, 135]. Although requiring far fewer measurements than full QST, such methods generally require a priori knowledge of the system, and only work effectively on weakly-entangled states.

An alternative method to probe the entanglement structure of a quantum system is through measuring the second-order Rényi entropy of its different partitions. The following Section details a novel, theoretical protocol for measuring the second-order Rényi entropy through statistical correlations between randomised measurements [125, 127]. This Section is the theoretical underpinning for Chapter 6, where this protocol is experimentally implemented for partitions of up to 10 ions in 10- and 20-ion chains.

5.2.1 Obtaining the Second-Order Rényi Entropy from Randomised Measurements

The Rényi entropy is a well-known entanglement entropy and is the more general form of the von Neumann entropy introduced in Section 2.1.2, which can be regarded as the 'quantum analogue' of the classical Shannon entropy. The general form of the Rényi entropy for a given quantum system described by density matrix ρ, is given by [136]:

$$S^{(\alpha)}(\rho) = \frac{1}{1-\alpha}\log_2\left(\sum_i^n p_i^\alpha\right), \tag{5.2}$$

where α is the order of the Rényi entropy, and i the possible measurement outcomes of ρ with probability p_i. The first-order Rényi entropy from this expression, i.e. in the limit where $\alpha \rightarrow 1$, is the well-known von Neumann entropy.

Of interest in this Section is the second-order Rényi entropy. For a reduced density matrix, ρ_A, which describes a subsystem A of the total system ρ, the second-order Rényi entropy is then given by

$$S^{(2)}(\rho_A) = -\log_2 \mathrm{Tr}(\rho_A^2). \tag{5.3}$$

This entropy is particularly useful due to its non-linear dependence on the density matrix, $\mathrm{Tr}(\rho_A^2)$, as will be discussed later in this Section. It can already be seen that Eq. 5.3 provides a direct relation between the entropy of the system and its purity (and therefore also to the length of the Bloch vector). For pure quantum states, where $\mathrm{Tr}(\rho^2) = 1$, it can be seen that $S^{(2)}(\rho) = 0$.

Several different protocols already exist enabling a measurement of $S^{(2)}(\rho)$. For example, collective measurements can be made on two identical copies ρ of a quantum system, as demonstrated in [137–140]. In [139], such a protocol was implemented in a six-site Bose-Hubbard system, realised with atoms in an optical lattice where it was used to study entanglement growth and thermalisation.

However, such protocols cannot be practically implemented on all quantum platforms – for example in trapped ion platforms, it is not usually feasible to prepare two identical copies of a quantum system at the same time. This motivated the search for an alternative protocol which would allow a measurement of $S^{(2)}(\rho_A)$ to be performed using only a single copy of the quantum system at any one time [24, 127]. Such a protocol was consequently developed through extending the proposals of [125–127, 141], using the fact that information about the second-order Rényi entropies of a system is contained in statistical correlations between the outcomes of measurements performed in random bases. This is the protocol which will now be detailed in the remainder of this Section, and correspondingly experimentally implemented in Chapter 6.

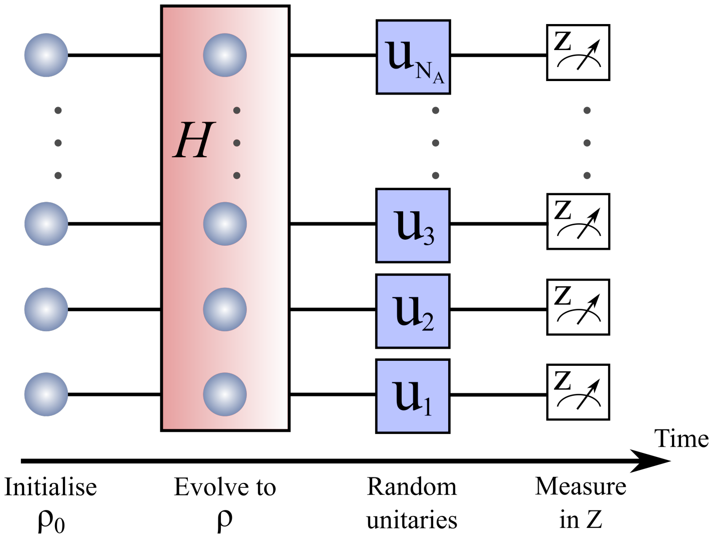

Figure 5.3: **Schematic of the measurement procotol**. The system is first initialised in the state ρ_0. A Hamiltonian (pink) is applied, thus evolving the system in time to the state of interest ρ. Local, random unitaries, u_i (shown in blue), are applied to each qubit in the system, before a measurement in the Z-basis is performed. This sequence is repeated multiple times for the same random unitaries in order to gather sufficient statistics. The entire process is then repeated for many different, randomly drawn local unitaries.

To understand how the protocol works, an example implementation will now be described which will provide an insight into how the second-order Rényi entropy can be determined from randomised measurements. Figure 5.3 shows a schematic of the protocol for a system of N qubits, where the state is prepared in an initial state ρ_0. The system is then evolved under a Hamiltonian (shown in pink in the Figure) to the state which is of interest, ρ. The randomised measurement approach [125] is to then apply local random unitaries, u_i (shown in blue in the Figure), to the individual qubits such that $U = u_1 \otimes .. \otimes u_N$, where each u_i is drawn independently from the CUE [131]. Single qubit readout is then performed, where each qubit is measured in a fixed (logical) basis, here assumed to be the Z-basis. An outcome from a measurement on this state, denoted by $s = (s_1, \dots, s_N)$, is then given by $P(s) = \mathrm{Tr}\left(U\rho U^\dagger |s\rangle\langle s|\right) = \langle s|U\rho U^\dagger|s\rangle$. For each set of random unitaries, U, repeated measurements are made to obtain sufficient statistics, and the entire process repeated for many different randomly drawn instances of U. This protocol can then provide access to the second-order Rényi entropy as will now be discussed.

If a subsystem A comprised of N_A qubits is considered, the purity of its reduced density matrix, ρ_A, is given by $\mathrm{Tr}(\rho_A^2)$. The second-order Rényi entropy of ρ_A can then be found from the cross-correlations of excitation probabilities using the relation [24, 125]

$$S^{(2)}(\rho_A) = -\log_2 \overline{X}, \quad \text{with } X = 2^{N_A} \sum_{s_A, s'_A} (-2)^{-\mathscr{D}(s_A, s'_A)} P(s_A) P(s'_A), \tag{5.4}$$

where $P(s_A) = \langle s_A | U_A \rho_A U_A^\dagger | s_A \rangle$ are the excitation probabilities for the measurement outcomes s_A of partition A, $U_A = U|_A$ is the restriction of the random unitaries U to A, and $\overline{\ldots}$ is the 'ensemble average' over the cross-correlations of the excitation probabilities $P(s_A)$ (where the average is taken over U). $\mathcal{D}(s_A, s'_A)$ works in essence as a weighting factor, quantifying the number of spin flips needed to convert s_A into s'_A. For example, $\mathcal{D}(s_A, s'_A)$ for the states $s_A = 0000$ and $s'_A = 1000$ is 1, as one spin flip is necessary to convert s_A to s'_A. $\mathcal{D}(s_A, s'_A)$ is known as the *Hamming distance.*

From comparing Equations 5.3 and 5.4, it can be seen that $\overline{X}$ is equal to the purity $\mathrm{Tr}(\rho_A^2)$ of the density matrix ρ_A. As such, the purities can be inferred from the statistical distribution of the weighted sum of cross correlations $\sum_{s_A, s'_A} (-2)^{-\mathcal{D}(s_A, s'_A)} P(s_A) P(s'_A)$, where an average over the distribution is then taken. Equation 5.4 therefore provides access to the purity, and consequently to the second-order Rényi entropy, of a multiqubit state, as well as to the purities/entropies of all of its subsystems, all at the same time.

5.2.2 Entanglement Information from the Second-Order Rényi Entropy

So far, the discussion has been constrained to discussing $S^{(2)}(\rho)$ and how measurements of the excitation probabilities can lead to information about the purity and entropy of the quantum system of interest and its associated subsystems. However, information about the presence of entanglement can subsequently be extracted from $S^{(2)}(\rho)$.

The relation between $S^{(2)}(\rho)$ and entanglement can be understood as follows: Imagine a two-particle system described by the density matrix ρ_{AB}, as illustrated in Figure 5.4. Figure 5.4 a) depicts a measurement of the density matrix of the system ρ_{AB} (denoted by the grey, shaded area), for example through full QST which will allow the entire information of the system to be accessed. Figure 5.4 b) instead represents measurements of the reduced density matrices, ρ_A (the blue area) and ρ_B (the green area), where then only the states of particles A and B respectively can be reconstructed. For a separable (product state), $\rho_{AB} = \rho_A \otimes \rho_B$, however if entanglement is present between A and B (i.e. the state is non-separable), then $\rho_{AB} \neq \rho_A \otimes \rho_B$. For a non-separable state, this separate measurement of the subsystems can be viewed as, in effect, a loss of information with regards to the full system ρ_{AB}, where the 'lost information' is represented in Figure 5.4 b) as the sections of ρ_{AB} which aren't encompassed by either ρ_A or ρ_B. A loss of information from a system corresponds to an increase in its entropy and, as such, measurements of the subsystems of an entangled state lead to a loss of information of the whole system, and a corresponding increase in entropy. Therefore, if the entropy of part A and/or part B is greater than the entropy of the total system, i.e. if $S^{(2)}(\rho_A) = S^{(2)}(\rho_B) > S^{(2)}(\rho)$, then it can be concluded that entanglement (specifically bipartite entanglement) exists between A and B [36]. This is the crucial insight which allows entanglement information to be deduced from entropy measurements of a complete system as well as of its subsystems.

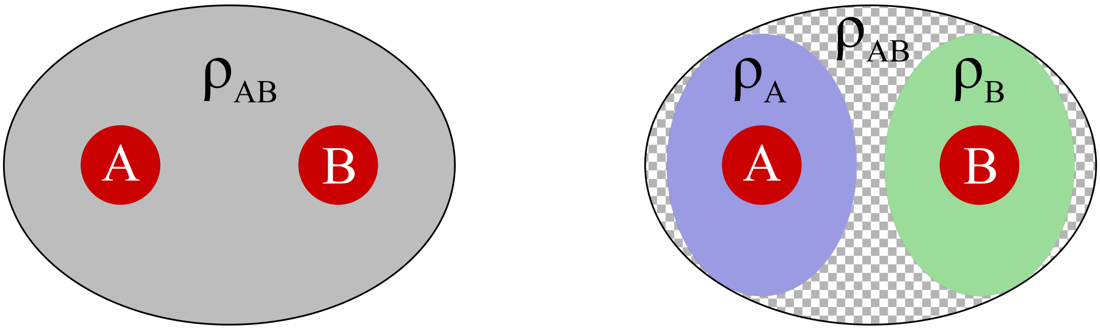

(a) Measurement of the full density matrix ρ_{AB}.

(b) Measurement of the reduced density matrices, ρ_A and ρ_B.

Figure 5.4: **Illustration of extraction of entanglement information from system entropies**. For simplicity, a two-qubit system comprised of qubits A and B is considered. a) A measurement of the combined density matrix, ρ_{AB} (grey, shaded area) is made, allowing access to the full information of the system. b) Measurements of the reduced density matrices, ρ_A (blue area) and ρ_B (green area) are made. For a pure, non-separable (i.e. entangled) state, $\rho_{AB} \neq \rho_A \otimes \rho_B$. This is represented in the Figure by the combination of density matrices ρ_A and ρ_B not fully encompassing ρ_{AB}. In this situation, $S^{(2)}(\rho_A) = S^{(2)}(\rho_B) > S^{(2)}(\rho)$.

5.2.3 Scaling of the Number of Measurements

The number of measurements necessary to access the purity of a multiqubit state is an important figure of merit to know. The scaling of the number of necessary measurements for this protocol was determined from numerical simulations [24]. In order to measure the purity of a pure, product state (or subsystem of a state) of N_A qubits with a statistical error of 0.12, the number of measurements required was found to be,

$$N_{\text{meas}} = 2^{(0.8\pm0.1)N_A + 7.7\pm0.3}. \tag{5.5}$$

Although still an exponential scaling, this protocol scales far better than QST which requires at least 2^{2n} measurements for an n-qubit system [142]. For entangled pure states the number of required measurements can even be significantly lower [24]. It is therefore fully feasible to obtain the purity of systems comprised of tens of qubits using this method.

The improved scaling of this protocol compared to QST can be understood as the full density matrix, ρ, is not being measured, but rather terms which are non-linear in ρ, such as ρ^2, are being measured. As such, not all the information about the system is being extracted, but rather a reduced amount of (important) information.

This Section has looked at the theoretical background to a novel protocol for determining whether bipartite entanglement exists in a quantum system. The protocol has several advantages over previous protocols to determine $S^{(2)}(\rho)$: It makes no prior assumptions

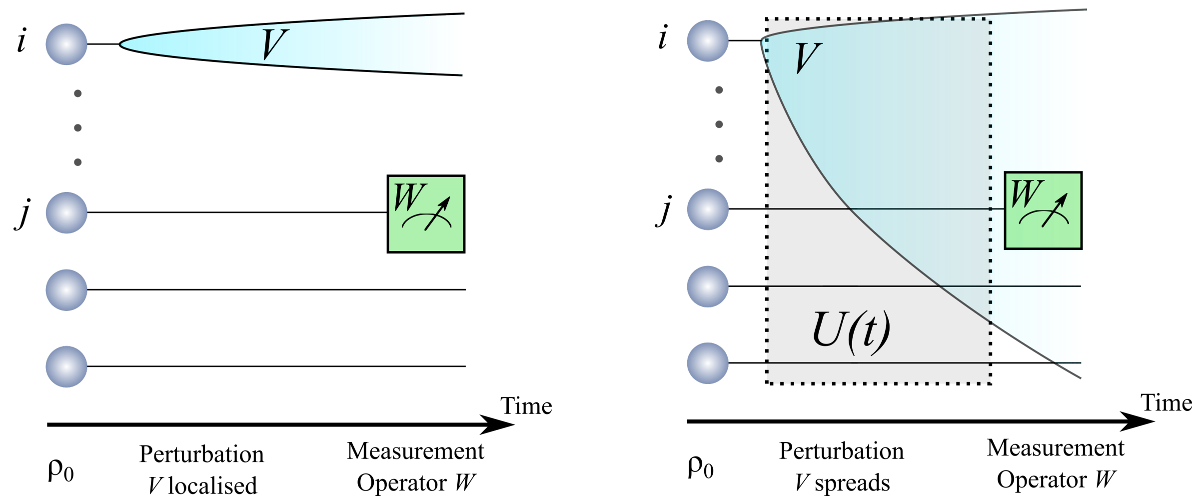

(a) Local operator V remains localised, so commuting with $W(t)$.

(b) Local operator spreads under $U(t)$, and so V and $W(t)$ no longer commute.

Figure 5.5: **Schematic of operator localisation/spreading and corresponding commuting/noncommuting of operators** a) A local perturbation, V, is applied to a single qubit in the system. In the absence of unitary time-evolution, the perturbation remains localised, and there is correspondingly no overlap between V and a local measurement operator $W(t) = U^\dagger(t)WU(t)$ at a later time t. Therefore, V and $W(t)$ commute. b) In the presence of a unitary time-evolution operator $U(t)$ (shown by the dotted grey box), the initial local perturbation spreads out over the system, and there is a corresponding overlap between V and the local measurement operator $W(t)$. As such, $W(t)$ is effectively delocalised, and so no longer commutes with V.

on the state of the system being measured, working for both weakly and strongly entangled states. This is in contrast to protocols such as matrix product state tomography, which only work reliably for weakly entangled states [134]. The protocol can also be implemented in any quantum platform with single particle readout and control.

5.3 Mapping Statistical Correlations to Out of Time Ordered Correlators

The second protocol which will now be presented in this Section provides a way to measure the effect of information spreading in a quantum system. When evolving under a Hamiltonian, quantum information spreads out or ‘scrambles’ across a system’s degrees of freedom. Such scrambling can be characterised by measuring quantities known as out-of-time-ordered correlators (OTOCs) [143]. OTOCs are a growing area of interest, especially in the context of characterising many-body dynamics, and can be used to identify quantum chaos – furthering the understanding of how quantum information propagates and scrambles in such systems [144].

To understand what OTOCs are and how they can be used to characterise quantum chaos, consider Figure 5.5, which shows a system of N qubits. Figure 5.5 a) shows an initial local perturbation V to the system at qubit i. In the absence of evolution under an operator $U(t)$, this perturbation remains localised, and so commutes at a later time with a measurement operator W on qubit j – that is, there is no overlap between operators V and W. Figure 5.5 b) shows this situation when the system instead undergoes unitary time evolution under $U(t)$ after application of V and before application of $W(t) = U^{\dagger}(t)WU(t)$. During evolution under $U(t)$, V spreads out over the system such that, at a later time t there is a non-zero overlap between V and $W(t)$, and so V no longer commutes with $W(t)$ [145].

The amount of this noncommutativity between V and $W(t)$ – which can also equivalently describe the amount of scrambling experienced by $W(t)$ – can then be quantified by the OTOC, which takes the form

$$O(t) = \frac{\mathrm{Tr}(\rho_0 W(t) V^{\dagger} W(t) V)}{\mathrm{Tr}(\rho_0 W(t)^2 V^{\dagger} V)}, \tag{5.6}$$

where ρ_0 is the initial quantum state. It can be seen that when no scrambling occurs (so when V and $W(t)$ commute), then $O(t) = 1$. The time-dependence of the OTOC in Equation 5.6 is powerful, as it allows different regimes of scrambling to be identified, such as ‘fast-scrambling’, which has application to black hole physics [146–148], to ‘slow scrambling’, which is one of the characteristics of many-body localisation [149–151].

Despite the potential importance of OTOCs in characterising many-body systems, it is still experimentally challenging to measure these dynamical correlation functions in real space and time, as their time-dependence means they cannot be measured through directly using time-ordered correlation functions [143, 152]. Several methods already exist to experimentally measure $O(t)$, for example by using time-reversal operations [143, 146, 153, 154] or through the use of auxiliary qubits [155]. However, protocols based on time-reversal are still challenging to experimentally implement for many experimental platforms – such as Hubbard systems or those with local interactions.

5.3.1 Measuring statistical correlations: The “Modified OTOC”

The protocol presented in the following Section provides the ability to measure OTOCs without the need for time-reversal or ancilla qubits/systems. They are instead extracted through statistical correlations, with these statistical averages meaning the OTOC extracted through this method is naturally robust against certain types of decoherence and noise, such as depolarisation and read-out errors. The mathematical basis for this technique is very involved and so will not be discussed in detail here, however is covered explicitly in [129].

The protocol provides a method to measure what are termed “modified OTOCs”. These modified OTOCs can be expressed in the form [129]:

$$O_n(t) = \frac{\sum_{A,B_n \subseteq A} \mathrm{Tr}\,(W(t)_A (VW(t)V)_A)}{\sum_{A,B_n \subseteq A} \mathrm{Tr}\,(W(t)_A (W(t))_A)}\ . \tag{5.7}$$

These summations are performed over all partitions, A, in the system that include the set $B_n = \{1, \cdots, n\}$ of the first n spins. The traces are the reduced traces over the operators such that $W(t)_A = \mathrm{Tr}_A(W(t))$, and $(VW(t)V)_A = \mathrm{Tr}_A(VW(t)V)$. Equation 5.7 can then be interpreted as a sum of out-of-time-ordered functions of the reduced operators $W(t)_A$ and $(VW(t)V)_A$.

Equation 5.7 quickly converges to the unmodified OTOC of Equation 5.6 as $n \longrightarrow N$, where N is the number of qubits in the system [129]. Therefore, in order to measure the unmodified OTOC $O(t)$, the series of modified OTOCs $O_0(t), O_1(t), \ldots$ can be measured until the series converges to $O(t)$.

Full convergence to $O(t)$ often requires significant experimental effort [129], however approximate convergence to $O(t)$ can instead be obtained by measuring lower orders of $O_n(t)$ which requires fewer experimental measurements. Therefore, by experimentally measuring sufficient numbers of the modified OTOCs (it will be seen in Chapter 7 that measuring up to $n = 2$ can, in fact, be sufficient), then the unmodified OTOC $O(t)$ can be approximated, allowing access to information about scrambling within a quantum system.

The protocol described here is a method to measure the modified OTOCs of Equation 5.7 using statistical correlations between measurements. The protocol uses local unitary operations to prepare a random initial state, which is then evolved under a many-body Hamiltonian, before a measurement of W is performed. Figure 5.6 provides an example schematic of how the protocol can be implemented in a spin-system to first measure $O_0(t)$, to which there are two main steps. In both cases, an initial product state $\rho_0 = |k_0\rangle\langle k_0|$ is prepared, where (for example) $|k_0\rangle = |\downarrow, \downarrow, \ldots, \downarrow\rangle$. Local, random unitaries $u = u_1 \otimes \cdots \otimes u_N$ are then applied to $|k_0\rangle$, so preparing the state $|\psi\rangle_{u,k_0}$, where the local unitaries are drawn randomly from the CUE [131]. The next section then has two variants:

- In Step 1, shown left in Figure 5.6, the system is dynamically evolved under a Hamiltonian H, before the operator W is measured. This sequence is repeated many times with the same random unitaries, so giving access to the operator $\langle W(t)\rangle_{u,k_0} = {}_{u,k_0}\langle\psi|W(t)|\psi\rangle_{u,k_0}$. This operator is the expectation value of W for each set of different unitaries u which have been applied.
- Step 2, shown right in Figure 5.6, is almost identical, however a local operator V is applied before the time evolution under H. Repeating the second step, again many times and with the same random unitaries and local operator, provides access to the operator ${}_{u,k_0}\langle\psi|V^{\dagger}W(t)V|\psi\rangle_{u,k_0}$.

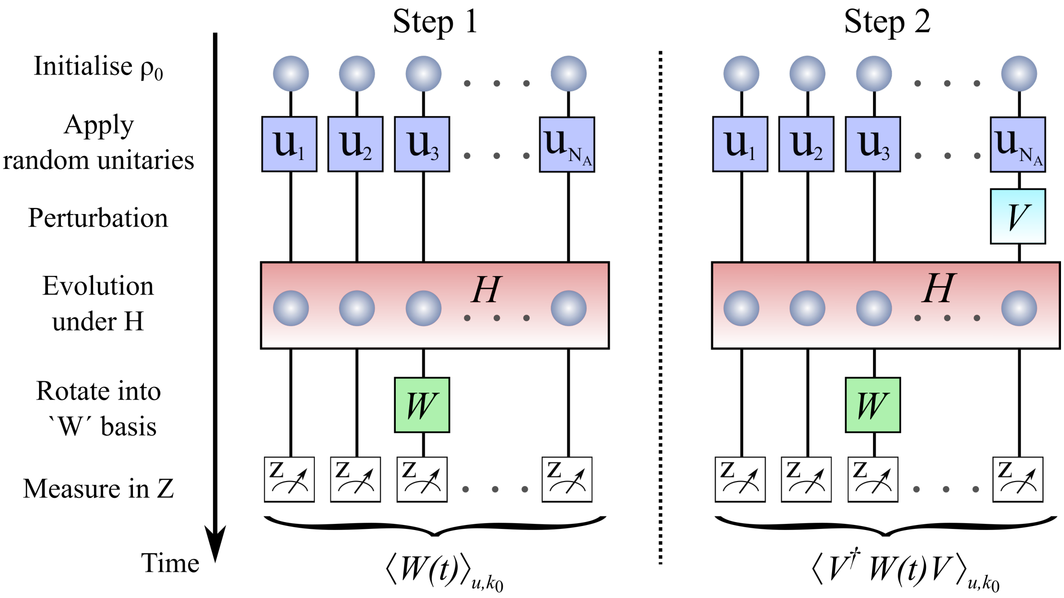

Figure 5.6: Example schematic of how the protocol can be implemented in order to measure the operators $\langle W(t)\rangle_{u,k_0}$ and $\langle V^\dagger W(t) V\rangle_{u,k_0}$ in a spin system. The system is first initialised in state $\rho_0 = |k_0\rangle\langle k_0|$. Local, random unitaries (shown in blue) are then applied in order to prepare a randomised initial state. Depending on whether Step 1 or Step 2 is being implemented, the perturbation V is applied to a single qubit. The system is then time-evolved under a Hamiltonian H (shown in pink), where $U(t) = e^{iHt/\hbar}$, with a measurement in W finally performed.

Finally, these steps are repeated for many different random unitaries, u. From these measurements, statistical correlations can be constructed of the form:

$$O_0(t) = \frac{1}{d_0^{(L)}} c_{k_0} \overline{\langle W(t)\rangle_{u,k_0} \langle V^\dagger W(t) V\rangle_{u,k_0}} \ , \tag{5.8}$$

where $d_0^{(L)} = c_{k_0} \overline{\langle W(t)\rangle_{u,k_0} \langle W(t)\rangle_{u,k_0}}$ is a normalising factor, with weight c_{k_0}, and $\overline{\ldots}$ averages over the applied random unitaries u.

Equation 5.8 can be generalised to ‘higher orders’, taking the form [129]:

$$O_n(t) = \frac{1}{d_n^{(L)}} \sum_{k_s \in E_n} c_{k_s} \overline{\langle W(t)\rangle_{u,k_s} \langle V^\dagger W(t) V\rangle_{u,k_0}} \ , \tag{5.9}$$

where $d_n^{(L)} = \sum_{k_s \in E_n} c_{k_s} \overline{\langle W(t)\rangle_{u,k_s} \langle W(t)\rangle_{u,k_0}}$ is a normalising factor, with weights c_{k_s}. $O_n(t)$ is a sum of functions like $O_0(t)$, but for different initial states $|k_s\rangle$. These different initial states are all product states of the form $|k_s\rangle = |\uparrow, \downarrow, \ldots\rangle$, such that $|k_0\rangle = |\downarrow, \downarrow, \ldots, \downarrow\rangle$, $|k_1\rangle = |\uparrow, \downarrow, \ldots, \downarrow\rangle$, $|k_2\rangle = |\downarrow, \uparrow, \ldots, \downarrow\rangle$, $|k_3\rangle = |\uparrow, \uparrow, \ldots, \downarrow\rangle$ and so on [129]. To approximate $O_n(t)$, the initial states must belong to the set $E_n = \{k_0, ..., k_{2^n-1}\}$, and the *same random*

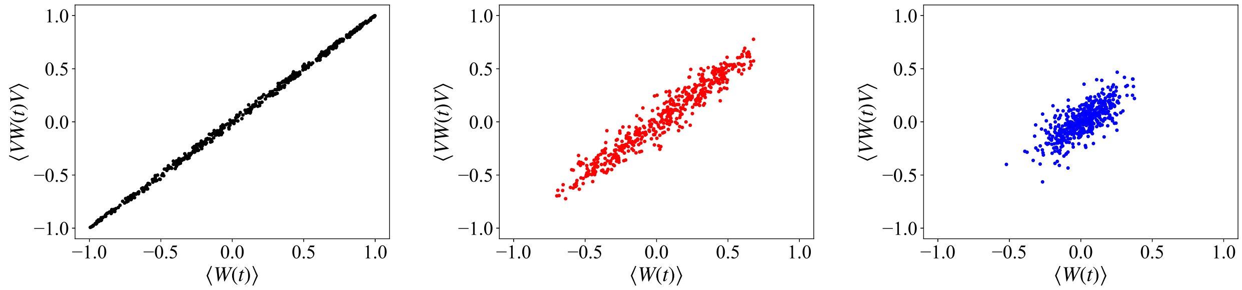

(a) $t = 0\,\mathrm{ms}$ (b) $t = 2\,\mathrm{ms}$ (c) $t = 6\,\mathrm{ms}$

Figure 5.7: **Simulated correlations between $\langle W(t)\rangle$ and $\langle VW(t)V\rangle$ for the initial state $|k_0\rangle = |\downarrow\cdots\downarrow\rangle$.** The figures show simulated data for a 6-spin system undergoing a H_{Ising}-type interaction of the type described in Section 2.5.3, using a coupling strength of $J_{\mathrm{max}} = \max|J_{ij}| = 410\,\mathrm{s}^{-1}$, with randomly drawn unitaries, quantum projection noise, and assuming 400 repeats for each data point. $V = \sigma_z$ is applied to ion 1, and $W = \sigma_x$ applied to ion 4. a) At $t = 0$, i.e. no evolution under $U(t)$, there are full correlations between $\langle W(t)\rangle$ and $\langle VW(t)V\rangle$. b) and c) At later times of evolution under $U(t)$, the correlations between $\langle W(t)\rangle$ and $\langle VW(t)V\rangle$ decrease, due to the increased overlap between the operators V and $W(t)$. This can be seen as a shrinking and broadening of the correlations, which clusters around 0.

unitaries should be used for all different initial states.

The measurement protocol for these higher orders is very similar to $O_0(t)$, and as an example a brief overview of the measurement protocol $O_1(t)$ and $O_2(t)$ will now be described. To measure these terms, additional measurements for different initial states are also needed. For measuring $O_1(t)$, Step 1 in the previous Section is repeated for an additional initial state $|k_1\rangle$. When combined with the results from measurements of $O_0(t)$, Equation 5.7 can then provide access to $O_1(t)$. Likewise, for measuring $O_2(t)$, Step 1 must be repeated for the initial states $|k_1\rangle$, $|k_2\rangle$, and $|k_3\rangle$. Again, when combined with the results from measurements of $O_0(t)$, Equation 5.7 provides access to $O_2(t)$.

Crucially, for $c_{k_s} = (-2)^{-\mathcal{D}(k_0,k_s)}$, where $\mathcal{D}(k_0, k_s)$ is the Hamming distance, Equation 5.8 can be shown to be equivalent to the modified OTOCs of Equation 5.7 (see Appendix A of [129]). As such, the protocol provides a way to measure modified OTOCs using statistical correlations.

In order to give context to the above discussions, the following section will demonstrate the results from simulations which compare modified OTOCs to the exact OTOC. Firstly, Figure 5.7 shows the expected correlations between $\langle W(t)\rangle$ and $\langle VW(t)V\rangle$ at different times during evolution under $U(t)$ for a 6-spin simulated experiment, using 500 different random unitaries. The perturbation $V = \sigma_z$ was applied to spin 1, and measurement operator $W = \sigma_x$ applied to spin 4. Unitary evolution from application of a H_{Ising} model of interacting spins was performed, as detailed in Section 2.5.3, with $J_{\mathrm{max}} = \max|J_{ij}| =$

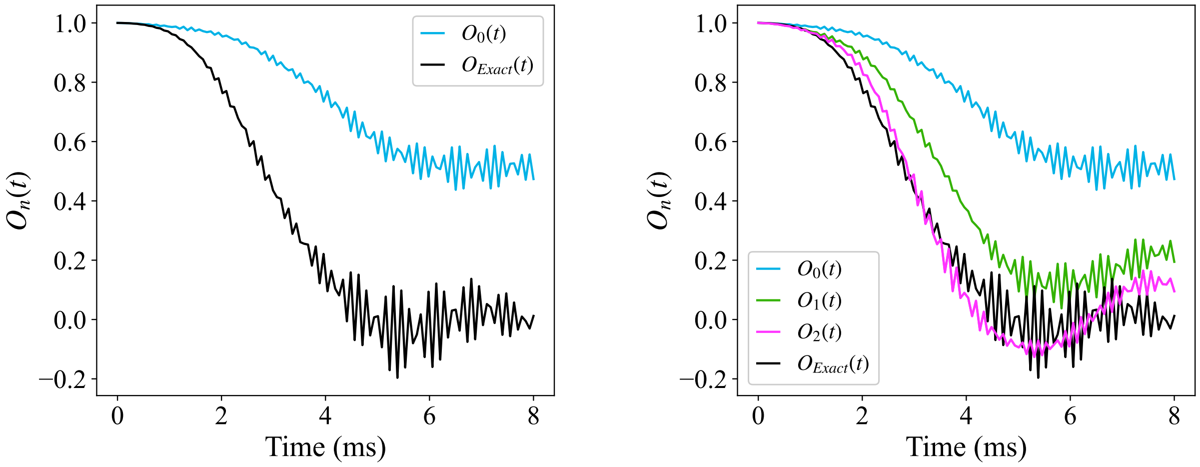

(a) Comparison of $O_0(t)$ with $O_{Exact}(t)$

(b) $O_n(t)$ for $n = 0, 1, 2$ compared with $O_{Exact}(t)$

Figure 5.8: **Simulated comparison of the exact OTOC, $O_{Exact}(t)$, to modified OTOCs for a 6-spin system.** a) Evolution of the exact OTOC, calculated from Equation 5.6, is shown (black line) alongside evolution of $O_0(t)$ (blue line). b) Higher order modified OTOCs, $O_1(t)$ (green line) and $O_2(t)$ (pink line), are shown for comparison against the exact OTOC. For all plots, a Hamiltonian of the form H_{Ising} was assumed with $J_{\text{max}} = 410\,\text{s}^{-1}$, $V = \sigma_z$ applied to ion 1, and $W = \sigma_x$ applied to ion 4, with the data simulated for 500 random unitaries.

$410\,\text{s}^{-1}$. Figure 5.7 a) shows that, at $t = 0$ (i.e. no evolution under $U(t)$), there are perfect correlations between $\langle W(t)\rangle$ and $\langle VW(t)V\rangle$. This is to be expected as there should be no overlap between the operators V and $W(t)$ at this point (see again Figure 5.5 a)). Figures 5.7 b) and c) show how, as the interaction time is then increased, the correlations between $\langle W(t)\rangle$ and $\langle VW(t)V\rangle$ decrease. This shows that there is a corresponding increase in the overlap between the V and $W(t)$ operators, due to the delocalisation of $W(t)$.

Figure 5.8 a) shows how the exact OTOC from Equation 5.6, $O(t) = O_{Exact}(t)$, and the 0th-order modified OTOC of Equation 5.8, $O_0(t)$, both measured at spin-4, evolve as a function of time, so giving an indication of how well $O_0(t)$ approximates the true OTOC $O(t)$. The Figure shows the exact solution to Equation 5.6, shown by the black line, alongside $O_0(t)$ (blue line) for the simulated data of the 6-spin system described above. As can be seen, $O_0(t)$ has many of the same features of $O(t)$, with $O_0(t)$ beginning at 1 before reducing with time. However, $O_0(t)$ does not approximate $O(t)$ particularly well, as the dynamics are much slower than $O(t)$.

Figure 5.8 b) shows the higher order modified OTOCs, $O_1(t)$ and $O_2(t)$, of Equation 5.9, alongside $O_0(t)$ and the exactly solved OTOC (black) for comparison. It can clearly be seen that the higher orders progressively match the true OTOC increasingly well, with $O_2(t)$ having the best match out of those plotted. It will be shown in Chapter 7 that it is,

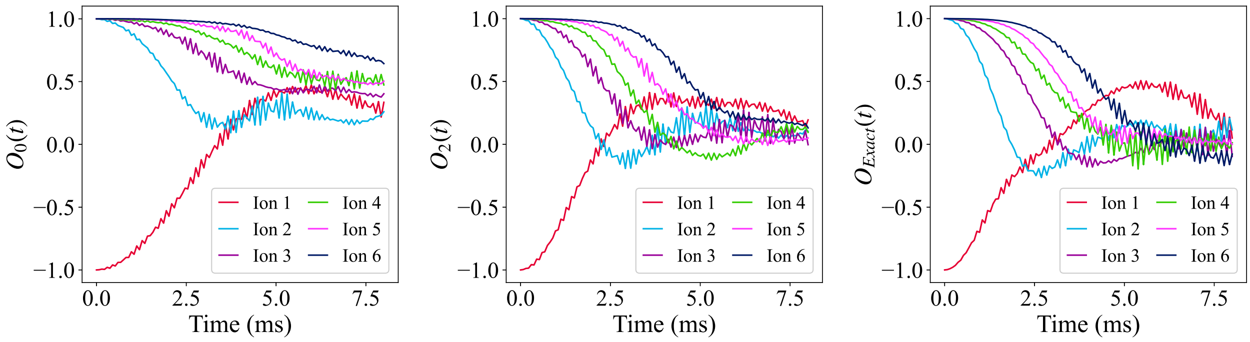

(a) $O_0(t)$ (b) $O_2(t)$ (c) $O_{Exact}(t)$

Figure 5.9: **Evolution of OTOCs for each ion in a simulated 6-spin system**. a) and b) The evolution of the modified OTOCs $O_0(t)$ and $O_2(t)$ respectively are shown for each ion $W = \sigma_x^i$ with $i = 1 \dots 6$. c) The evolution of the exact OTOC for each ion is shown for comparison. For all plots, a Hamiltonian of the form H_{Ising} was assumed with $J_{\text{max}} = 410\,\text{s}^{-1}$, $V = \sigma_z$ applied to ion 1, and the data simulated for 500 random unitaries.

in fact, sufficient to measure up to $O_2(t)$ to approximate $O(t)$, and so this is the highest-order modified OTOC plotted here.

For full completeness, Figure 5.9 shows the modified OTOCs for all ions (i.e. for $W = \sigma_x^i$ for $i = 1 \dots 6$). a) and b) show O_0 and O_2 respectively, with c) showing the exactly solved OTOC as a comparison. It is clear that the evolution of O_0 for each ion, as shown in panel a), is too slow when compared to the exactly solved OTOC of panel c). The evolution of O_2 for each ion (panel b)), resembles the exact OTOC far better than O_0, with the speed of the dynamics approximately comparable.

This Section has detailed a theoretical protocol to measure approximations to OTOCs through statistical correlations. The protocol requires no time-reversal operations or use of auxiliary qubits, and so is of an advantage in experimental platforms in which protocols requiring these implementations are challenging to implement. The protocol will be experimentally implemented in the QSim system on ion strings of up to 10 qubits in Chapter 7.

5.4 Cross-Platform Verification through Local Randomised Measurements

The final protocol discussed in this Chapter will move away from characterising a single quantum device, and instead develop a method which will allow the comparison of two separate quantum platforms through randomised measurements. The motivation will be to develop a protocol which can be implemented separately in time and space on two (potentially very different) quantum devices, which can allow two separately prepared states to be compared.

Recently, various procedures have been developed which allow the performance of a quantum device to be verified, such as direct fidelity estimation [134, 156], and randomised and cyclic benchmarking [91, 92, 106, 157, 158]. Verification procedures such as these compare an experimentally implemented (noisy) quantum state/process with a known theoretical target state/process. However, this requires the target state to be known, and so a key challenge is the direct comparison of two a priori unknown quantum states prepared on two separate devices, at different locations in time and space. Such protocols will become of ever-increasing importance as larger many-body systems are developed, and so comparison to classical simulations requires increasing classical computational power (i.e. becoming evermore computationally difficult). In such regimes, it will be necessary to be able to compare two quantum machines in order to verify their correct operation [26].

5.4.1 Two-Platform Fidelity Estimation

The protocol presented here measures how closely two separate platforms have prepared the same state, ρ, through looking at the overlap between the two prepared quantum states by defining a fidelity F_{max}. A fidelity measure of two pure, quantum states, denoted by $|\psi_1\rangle$ and $|\psi_2\rangle$, is commonly defined as the overlap between the two states: $F_{\text{pure}} = |\langle\psi_1|\psi_2\rangle|^2$. However, with the development of quantum technologies leading to ever larger quantum systems with corresponding exponentially increasing complexity, it is likely that a fidelity measure for mixed states will become increasingly useful [159]. A set of criteria which constrain fidelity measures to those which are truly suitable for mixed states was proposed by Jozsa in 1994 [160]. F_{max} is one such mixed state fidelity measure which satisfies all of Jozsa's axioms, and is defined as [159]:

$$F_{\text{max}}(\rho_1, \rho_2) = \frac{\text{Tr}(\rho_1\rho_2)}{\max\{\text{Tr}(\rho_1^2), \text{Tr}(\rho_2^2)\}} \,. \tag{5.10}$$

This equation gives a measure of the overlap between the density matrices ρ_1 and ρ_2, normalised by the maximum of their respective purities. In this equation, the density matrices do not necessarily have to be of the entire system, but can also be of subsystems. F_{max} can then be used to quantify the degree to which two quantum platforms have prepared the same, potentially mixed, quantum state.

5.4.2 Fidelity Estimation from Statistical Correlations

The protocol gives a method to obtain F_{max} from statistical correlations between randomised measurements. Whereas in Section 5.2 entanglement entropies were obtained from the reduced density matrices of single systems, that is, the interest was in $\text{Tr}(\rho^2)$, in this protocol the interest is in the overlap between density operators of two systems – i.e.

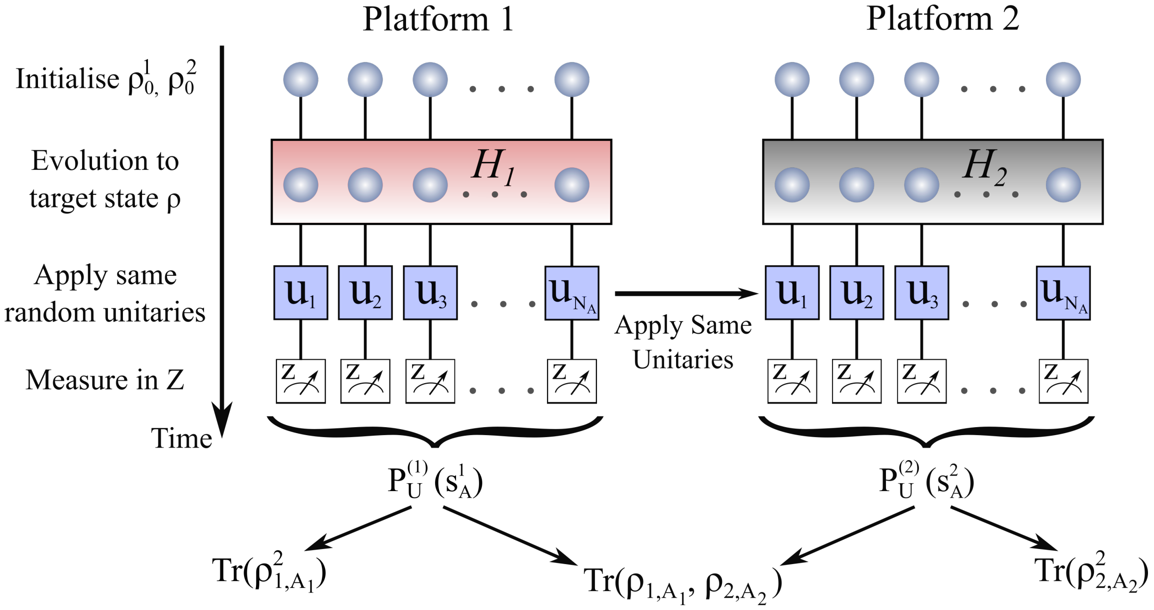

Figure 5.10: **Schematic of the fidelity estimation protocol using randomised measurements**. Two platforms, separated in time and space, prepare an identical state of interest ρ. By applying local, random unitaries to this state and measuring $\langle \sigma_z \rangle$, the excitation probabilites for these two platforms, $\mathrm{P}_U^1(s_A^1)$ and $\mathrm{P}_U^2(s_A^2)$, can be accessed. If *identical* random unitaries are applied to both platforms, then the overlap between the two density matrices, $\mathrm{Tr}(\rho_1\rho_2)$, can be extracted from these excitation probabilites using Eq. 5.11.

the interest lies in the quantity $\mathrm{Tr}(\rho_1\rho_2)$. Although the fidelity F_{max} can be obtained from full quantum state tomography (QST) of both platforms 1 and 2 [95], in reality the exponential scaling of QST with the system or subsystem size practically limits the system to 8 qubits [95]. Although, as previously discussed, alternative efficient tomographic methods have been implemented [134, 135], such methods require previous knowledge of the state of interest. The protocol presented here, although also scaling exponentially, still scales much more favourably with the system/subsystem size – as will be shown below – as well as requiring no a priori knowledge of the state of interest. This allows the possibility of practical cross-platform verification for systems of tens of qubits which can be currently realised on state-of-the-art quantum devices.

Figure 5.10 gives a schematic overview of how the protocol could be implemented on two quantum platforms consisting of N_1 and N_2 qubits at different locations and at different points in time. The general protocol is as follows: The quantum platform should first be initialised in ρ_0^i, where $i = 1, 2$ represents either Platform 1 or Platform 2. This state should then undergo a dynamical evolution to the state of interest, ρ. This dynamical evolution is not constrained to be solely a unitary evolution under a Hamiltonian native to the system, but could be a variational process to prepare the state, or some other feasible form of state preparation such as trotterisation [49, 161]. Following preparation of the evolved state ρ, local random unitaries are drawn from the CUE [131] and sent, through classical communication, to both quantum platforms. These random unitaries are applied to spins $k = 1, \ldots, N_A$ and can be considered as the application of a single global random unitary $U_A = \otimes_{k=1}^{N_A} U_k$, which is a product of these local random unitaries. Finally, single-qubit readout in the Z basis is performed, projecting the system into the state $|s_A\rangle = |s_1 \ldots s_{N_A}\rangle$. A crucial point to note is that the *same* random unitaries must be applied to both platforms in order to extract the fidelity overlap between the two states.

Repeating this protocol many times for the same U_A provides an estimate of the outcome probabilities $P_U^i = \mathrm{Tr}(U_A \rho_{i,A_i} U_A^\dagger |s_A\rangle\langle s_A|)$, where again $i = 1, 2$ represents either Platform 1 or Platform 2. This entire procedure, including the repeats, is then itself repeated for many different random unitaries U_A. From this, the overlap between the two, potentially reduced, density matrices, $\mathrm{Tr}(\rho_{1,A_1}, \rho_{2,A_2})$ can be estimated from the second-order cross-correlations between the two platforms:

$$\mathrm{Tr}(\rho_{1,A_1}, \rho_{2,A_2}) = 2^{N_A} \sum_{s_A^1, s_A^2} (-2)^{-\mathscr{D}(s_A^1, s_A^2)} \overline{P_U^{(1)}(s_A^1) P_U^{(2)}(s_A^2)}, \tag{5.11}$$

where N_A is the number of qubits, $\mathscr{D}(s_A^1, s_A^2)$ is the Hamming distance between s_A^1 and s_A^2 (see Section 5.2), and $\overline{\ldots}$ is the ensemble average over the random unitaries.

From comparing Equation 5.11 to Equation 5.4, it can be seen there are many similarities. Equation 5.4 flows naturally from Equation 5.11 when only one platform is used – that is, when $i = j$. In this case, the purity is determined from the auto-correlations between $P_U^i(s_A)$ and $P_U^i(s'_A)$.

This protocol requires the random unitaries and the measurement outcomes to be classically communicated between the two platforms. It requires no a priori knowledge of the quantum state of interest, and the states can be both pure or mixed, full states or subsystems. This is of particular significance as it allows the comparison of subsystem fidelities for various sizes.

5.4.3 Scaling of the Number of Measurements

One of the most important properties of any protocol which aims to determine fidelities of systems, or between systems, is that of the number of measurements needed in order to perform the protocol to a statistically significant level. Statistical errors are intrinsic to this protocol due to the finite number of projective measurements, N_m, which are taken per random unitary, as well as the corresponding finite number of random unitaries, N_u, then applied. The scaling of this protocol with N_m and N_u can be determined by simulating experiments of the type shown in Figure 5.10 where N_m and N_u are varied, and the resulting statistical error on the fidelity F_max then calculated [127]. To infer F_max to a statistical error of ≤ 0.05, with a fixed number of random unitaries of $N_\mathrm{u} = 100$, two different scalings were found. For pure product states, the number of measurements necessary scaled as $N_\mathrm{m} \sim 2^{(0.8\pm0.1)N_A}$, where N_A is the size of the system. For pure entangled states, the scaling is even better, with the number of necessary measurements given by $N_\mathrm{m} \sim 2^{(0.6\pm0.1)N_A}$ [26]. In comparison, full quantum state tomography scales at least as 2^{2N_A} [142] in order to achieve similar statistical errors, and so the novel protocol presented here scales significantly better than QST.

The improved scaling of pure entangled states compared to pure product states implies that the fidelity estimation of pure entangled states is less susceptible to statistical errors. This can be understood as fluctuations and errors in the random unitaries which are applied are less significant for pure entangled states, as the subsystems of these states are already mixed. In comparison, for pure product states, the subsystems are also correspondingly pure, and so errors from the random unitaries will have a more significant effect on these states.

5.5 Conclusion & Further Work

This Chapter has looked at how statistical correlations from the implementation of local, random unitaries can provide access to many properties of quantum many-body systems. It should be clear from this Chapter that randomised measurements have the potential to provide a vast number of ways to characterise quantum systems, only some of which have been discussed in this Chapter. Of direct interest for the future is a novel method of using randomised measurements in detecting mixed state entanglement [162]. As discussed in Section 5.4, in moving to larger quantum systems, it is likely that characterisation of mixed states will become of increasing interest [159], and so such protocols to detect entanglement in mixed states will become of increasing importance.

The following two Chapters will now present experimental implementations of the three protocols described in this Chapter in the QSim system.

Chapter 6

Probing Entanglement Entropies via Randomised Measurements

The ultimate aim of quantum simulators is to be able to study systems which cannot be investigated classically, for example by being too computationally demanding for classical machines to feasibly process. There are many platforms which can be used for quantum simulation and computation, such as photons [163–165], superconducting qubits [19, 166, 167], optical lattices [168, 169], and trapped ions [14, 17, 170, 171].

A large amount of recent media excitement has focussed on superconducting qubits, especially given the announcement from Google of 'quantum supremacy', where the authors claimed to have performed a task on their superconducting quantum processor beyond the capabilities of even the best classical supercomputers [19][1]. Trapped-ion based platforms have many attractive qualities, and are significant rivals to these well-known superconducting platforms [174], especially with the development of industry-based trapped-ion quantum computers [171]. Trapped ions also have attractive qualities over superconducting platforms, being almost unrivalled in particular when it comes to single-particle control, allowing the preparation and manipulation of individual qubits.

This Chapter will now look at the trapped-ion based quantum simulation (QSim) system from the perspective of its quantum simulation capabilities and will introduce the many-body dynamics which underpin quantum simulation of spin models in the system. The experimental implementation of spin models in the QSim system has already been well-explored in literature such as [47, 49, 175] and so will not be discussed in any detail here. However the most important techniques, including the experimental implementation of both the transverse Ising and XY-Models in the QSim system, will be explained and discussed.

Once a good understanding of how quantum simulations can be performed in the QSim

---

[1] Although this claim is disputed in articles such as [172, 173].

system has been gained, the Chapter will go on to introduce the experimental implementation of the first of the three theoretical protocols described in Chapter 5: Namely, measuring the second-order Rényi entropy through using randomised measurements (see Section 5.2). Results from application of the protocol to 10-ion partitions of chains of up to 20-ions will be presented and discussed. In addition, the application of the protocol to a 10-ion chain in the presence of disorder will be presented. This will allow a first look into the potential of the protocol to investigate many-body localised dynamics. The experimental results discussed in this Chapter were published in *'Probing Rényi entanglement entropy via randomized measurements'* [24].

6.1 Quantum Simulation with Ion Strings

Trapped ions are promising platforms for use in quantum simulation for a variety of reasons. They can be easily confined for days on end (in fact, in the QSim system, a single ion can remain trapped for weeks), with read-out of the quantum-state being a non-destructive process (in contrast to optical lattices which often use destructive time-of-flight measurements [169]). Trapped ions allow almost unrivalled control of single-particles, allowing accurate manipulation of the system – a requirement which is particularly crucial when implementing the theoretical protocols discussed in Chapter 5. The following Section will now outline how quantum simulations are implemented on chains of trapped ions in the QSim system, with the aim of the Section to give an indication of how the system is operated on an 'everyday' basis.

6.1.1 Implementing Transverse Ising and XY-Models

The theoretical background to both the transverse Ising and XY-models (see Section 2.5.3) will not be covered again here. Instead, the implementation of these models in the QSim system will now be explored. Currently in the QSim system, entangling dynamics are most often implemented on the radial modes of motion. To implement the pure MS gate, coupling to the axial modes of motion is preferable due to their large frequency separation, where it is possible to couple to purely the COM mode. In contrast, the radial modes of motion are bunched together into a fairly narrow frequency window (~1 MHz for 20 ions), and so any applied bichromatic beam will couple to all modes with different strengths. As such, the radial modes offer the possibility to implement more complex spin-spin interactions, such as those with a tunable interaction range, α. Therefore, all motional modes and entangling gates discussed from this point onwards will refer to the radial modes of motion, driven with the 729 nm radial beam (see Section 3.1.2).

Both the transverse Ising and XY-Models can be implemented using a bichromatic light field, in a similar way to that of the MS gate. This bichromatic light field contains the frequencies $\omega_{\pm} = \omega_0 \pm (\omega_{\mathrm{SB}} + \Delta)$, where ω_0 is the resonance frequency of the transition, ω_{SB}

the frequency of a (radial) motional sideband, and Δ the detuning of the bichromatic beam from that sideband. In the QSim system, these values are typically on the order of $\omega_{\mathrm{SB}} = 2\pi\times 2.7\,\mathrm{MHz}$ and $\Delta = 2\pi\times 40\,\mathrm{kHz}$. As the radial modes of motion are not well separated in frequency space for these trapping parameters, the bichromatic beam off-resonantly couples all ions on the qubit transition to all of the transverse collective motional modes of the ion string. By adding an additional detuning such that the bichromatic frequencies are then given by $\omega_{\pm} = \omega_0 \pm (\omega_{\mathrm{SB}} + \Delta) + \delta$, the transverse Ising Hamiltonian can be realised, given by:

$$H_{\mathrm{Ising}} = \hbar \sum_{i<j} J_{ij} \sigma_i^x \sigma_j^x + \hbar B \sum_j \sigma_j^z, \tag{6.1}$$

where $\sigma_i^{\beta}(\beta = x, y, z)$ are the spin-1/2 Pauli operators for the ith spin, J_{ij} is the spin-spin coupling matrix, and B is the effective transverse magnetic field strength. It can be seen that this Hamiltonian describes pair-wise spin-flips (due to the $\sigma_i^x \sigma_j^x$ interaction), with the transverse magnetic field component, $\hbar B \sum_j \sigma_j^z$, arising from the additional detuning δ where $B = \delta/2$. The strength of the spin-spin interactions follows an approximately power-law dependence with distance between the ions $|i - j|$, given by $J_{ij} \sim J_{\mathrm{max}}/|i - j|^{\alpha}$ where J_{max} is the maximum value of the coupling matrix, $J_{\mathrm{max}} = \max|J_{ij}|$ [47].

In taking the transverse field component to a regime where $B \gg J_{\mathrm{max}}$, typically around $\delta = 2\pi\times\ 3\,\mathrm{kHz}$ for the QSim system, the transverse field Hamiltonian reduces to the XY-model of interacting spins, given by:

$$H_{\mathrm{XY}} = \hbar \sum_{i<j} J_{ij} (\sigma_i^+ \sigma_j^- + \sigma_i^- \sigma_j^+), \tag{6.2}$$

where $\sigma_i^+(\sigma_i^-)$ are the spin-raising(lowering) operators acting on spin i, and all other parameters are as defined above. Note that the spin raising and lowering operators appear together, so as one spin excitation is removed, another one is added. As such, the number of spin excitations initially present in the system is conserved throughout the course of the dynamics.

So far, the discussion has been limited to implementing the transverse field and XY-model Hamiltonians using only a bichromatic light field. However, in reality (and in the QSim system), if a bichromatic light field is used then unbalanced AC-stark shifts will often arise from off-resonant coupling of the 729 nm light field to other transitions in $^{40}\mathrm{Ca}^+$ (predominantly between the $\mathrm{S}_{1/2}$ and $\mathrm{P}_{1/2}$, $\mathrm{P}_{3/2}$ levels, and between the $\mathrm{D}_{5/2}$ and $\mathrm{P}_{3/2}$ level). Such uncompensated AC-Stark shifts act as additional, local effective magnetic fields $B_j^{stark} \sigma_j^z$, which can cause the dynamics to become distorted. In order to balance these AC-stark shifts, an additional third light field is applied at the same time as the bichromatic light field to form a trichromatic field. A typical frequency for this third light field in the QSim system is $\omega_{\mathrm{tri}} = \omega_0 + 2\pi\times 1.2\,\mathrm{MHz}$, with the power of it scanned daily in order to optimally balance these AC-Stark shifts.

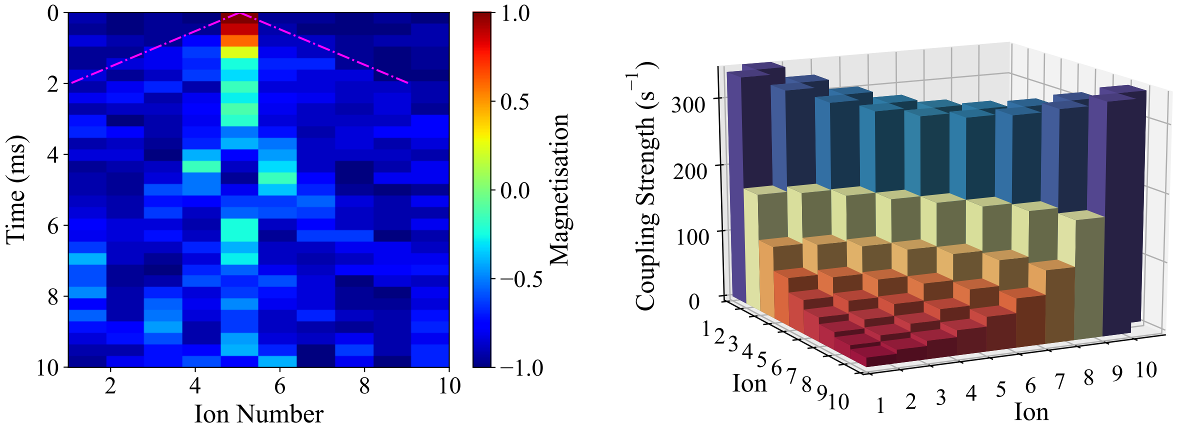

(a) Single ion walk

(b) J_{ij} coupling matrix

Figure 6.1: **Evolution of a 10-ion string under H_{XY}.** a) An initial state was prepared with ion 5 in $|\uparrow\rangle$ and all other ions in $|\downarrow\rangle$. This state was then evolved under H_{XY}, causing the excitation to 'flip-flop' out over the ion string. The dashed pink lines highlight the rate at which the excitation spreads out. b) The J_{ij} coupling matrix associated with the evolution shown in a), with $J_{\mathrm{max}} = 420\,\mathrm{s}^{-1}$. The coupling between ions falls off with an approximately power-law decay as the distance between the ions increases.

Figure 6.1 a) shows an example of the XY-model Hamiltonian of Equation 6.2 implemented on a 10-ion chain in the QSim system using the trichromatic light field. The 10-ion string, confined with radial frequency $\omega_{\mathrm{r}} = 2\pi\times 2.71\,\mathrm{MHz}$ and axial frequency $\omega_{\mathrm{ax}} \approx 2\pi\times 220\,\mathrm{kHz}$, was first initialised in the ground state using optical pumping and sideband cooling, before being prepared in an initial product state with ion 5 in the excited $|\uparrow\rangle$ state, and all other ions remaining in $|\downarrow\rangle$. Upon application of H_{XY} with $\Delta = 2\pi\times 40\,\mathrm{kHz}$ and $\delta = 2\pi\times 3\,\mathrm{kHz}$ (termed a 'quench'), the initial excitation in the system 'flip-flops' out through the system. When the excitation reaches the edges of the ion string it is reflected, causing coherent re-interference of the excitation e.g. on ion 5 at approximately 6 ms interaction time, where a clear increase in excitation can be seen. The excitation in the string needs a finite amount of time to initially spread out over the ion string, with this spread indicated by the dashed pink lines in the Figure.

Figure 6.1 b) shows the corresponding J_{ij} coupling matrix between all ions for the 10-ion evolution shown in Figure 6.1 a). This matrix shows that the coupling between nearest neighbours is the strongest (highest bars). The coupling strength then falls off as the distance between the ions increases, with the weakest coupling between the ions at opposite ends of the ion string (i.e. ions 1 and 10). For this evolution, $J_{\mathrm{max}} = 420\,\mathrm{s}^{-1}$.

6.1.2 Estimating the Coupling Matrix, Dispersion Relation, and α

In order to characterise the many-body dynamics occurring in the system, it is often necessary to know the values of several properties of interest. The importance of this can be seen, for instance, when several measurements – which are intended to be either similar or even identical – are being performed over several days. In this case, it is necessary to know characteristic quantities which can confirm the system is behaving in the same way on these different days.

One of these properties which can be extracted is the spin-spin coupling matrix, J_{ij}, as shown in Figure 6.1 b). It is possible to directly measure each element of the J_{ij} coupling matrix [47], however this becomes fairly time-intensive for larger spin chains. It is more common in the QSim system to instead estimate the J_{ij} coupling matrix by comparing the dynamics to a classical simulation. The evolution of an ion string under both H_{Ising} and H_{XY} can be well-simulated on a classical computer by using the experimental parameters of the system such as the trapping parameters and bichromatic detunings. The evolution of this classical simulation can then also be visually checked to be consistent with the measured evolution in the QSim system. The coupling matrix, J_{ij}, which is obtained from the classical simulation can then be assumed to be a good approximation to that of the real experimental coupling matrix. All J_{ij} values quoted in this thesis are extracted using this method.

The next property of interest to be discussed is the *dispersion relation*, often denoted by ϵ_k. The behaviour of a single-ion excitation evolving under H_{XY} is a collective excitation of the many-body system, and can be treated as a pseudo- or quasiparticle injected into the system at ion 5 which has particle-like properties. This excitation then propagates out over the string with an associated group velocity given by $v_g = \partial\epsilon_k/\partial k$, where ϵ_k is the effective dispersion relation and k the wavevector of the quasiparticle [176]. For the general case of k excitations, the kth-spin wave excitation is formed by acting on the ground state with the creation operator $\sigma_k^+ = \sum_j A_j^k \sigma_j^+$, where A_j^k are the amplitudes of the spin waves such that $|k\rangle = \sigma_k^+|0\rangle$. Therefore, the Hamiltonian which describes the state with a single quasiparticle (i.e. the single-excitation subspace) can be expressed as $H = \sum_k \epsilon_k \sigma_k^+ \sigma_k^-$. The dispersion relation can therefore be extracted by diagonalising the J_{ij} coupling matrix [47]. In and of itself, the dispersion relation is not often used as a characterisation of the system (or at least not for the purposes of this thesis), however it provides straightforward access to the power-law decay of the spin-spin interactions, as will now be seen.

The spin-spin coupling interaction should fall off with an approximately power-law decay, the exponent of which is given by α. To estimate α, there are several possible methods which are well-discussed in [47]. However, in the QSim system, the most straightforward way to estimate this value is through comparison of the experimentally obtained dispersion relation to a dispersion relation obtained from a theoretical J_{ij} matrix with an exact power-law dependence. Having extracted the experimental dispersion relation, $\epsilon_k^{(\mathrm{exp})}$, through diagonalising the J_{ij} matrix, a theoretical J_{ij} matrix with an exact power-law dependence, $J_{ij}^{(\mathrm{th})} = J_{\max}/|i-j|^{\alpha}$, can be generated for a value of α. By diagonalising this theoretical matrix, a theoretical dispersion relation, $\epsilon_k^{(\mathrm{th})}$, can consequently be extracted. Through minimising the quantity $|\epsilon_k^{(\mathrm{exp})} - \epsilon_k^{(\mathrm{th})}|$ for different values of α, the value of α which describes the experimental system as best as possible can therefore be obtained.

Having now given an overview of how spin models are practically implemented in the QSim system, the remainder of this Chapter will now present the experimental results from measuring the second-order Rényi entropy through using randomised measurements.

6.2 Probing Rényi Entanglement Entropy via Randomised Measurements: Measurement Protocol

This Section will present results from an experimental implementation of the Rényi protocol on partitions of up to 10-ions of 20-ion chains. For all experiments, the ion chains were evolved under the long-range XY model [22] with a transverse field as discussed in the previous Section. First, results from implementation of the protocol on a 10-ion string will be presented, followed by results from 10-ion partitions of a 20-ion string. Finally, results from application of the protocol to a 10-ion system where an additional disorder was applied during evolution of the ion string under H_{XY} will be presented.

6.2.1 10- and 20-ion Experimental Results

Figure 6.2 shows an example of a 20-ion string where the local, random unitaries are performed on the middle 10 ions. The experimental implementation of these unitaries is described in more detail later in this Section and in Section 6.4.2. These unitaries can be visualised as random rotations of the spin orientations. For a single-spin pure state, shown left in the Figure by the grey Bloch sphere and histogram, the distribution of $\langle \sigma_z \rangle$ measurement outcomes spans the full range $-1 \le \langle \sigma_z \rangle \le 1$, corresponding to a Bloch vector length of $|r| = 1$. For a single-qubit mixed state, shown by the purple Bloch sphere and histogram, $|r| < 1$ and so $\langle \sigma_z \rangle$ takes on values in a reduced range. For multiple qubits this understanding can be generalised by now considering the quantity X, where $X = 2^{N_A} \sum_{s_A, s'_A} (-2)^{-\mathscr{D}(s_A, s'_A)} P(s_A) P(s'_A)$ (see Equation 5.4 of Chapter 5). X is the weighted sum of cross-correlations, whose mean value corresponds to the purity of the (sub)system in question – i.e. $\mathrm{Tr}(\rho^2) = \overline{X}$. Cross-correlations for different partition sizes of the 20-ion string are shown in Figure 6.2 (centre/right) by the histograms. Grey indicates the distribution for the initial pure state, and purple is the distribution for the state time-evolved under H_{XY} to 10 ms. It can be seen that the mean value of X (dashed line) for the initial pure state is much larger than for the state time-evolved to 10 ms, indicating that the subsystems are mixed after this evolution.

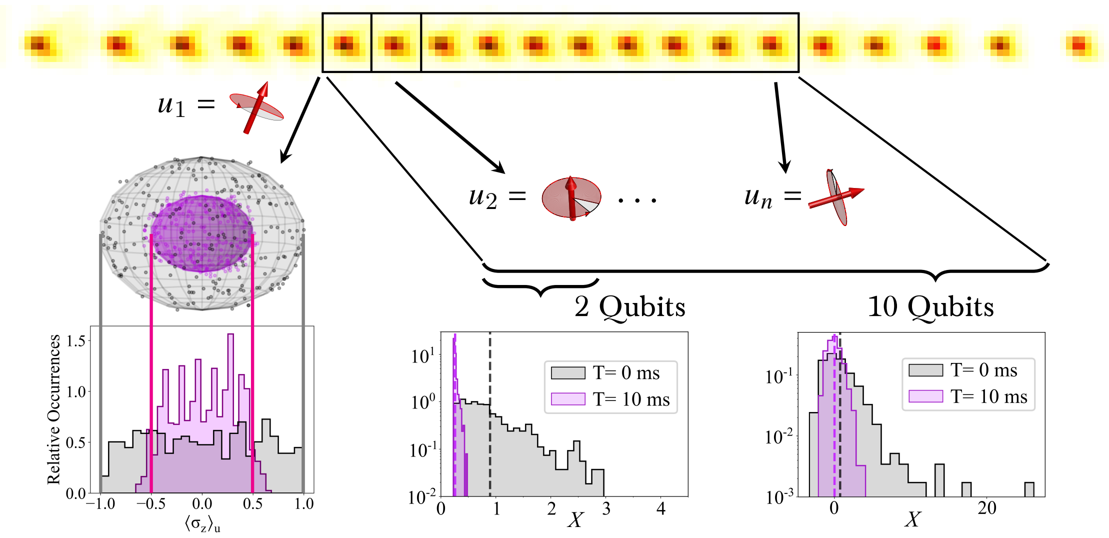

Figure 6.2: **Measurement Protocol**. **Left**: The single-qubit Bloch sphere. The purity is directly related to the width of the distribution of measurement outcomes after application of random rotations. Initial pure state (grey) and mixed state (purple) cases are shown. **Centre/Right**: Extension of the protocol to multiple qubits. Here, the purity is directly related to the mean value of the cross-correlations X after application of random rotations. For an initial pure, product state (grey histograms), the mean value of X, as well as the spread of the distribution, for the subsystems is much larger than after 10 ms evolution under H_{XY} (purple histograms), where the subsystems are expected to be mixed.

For all measurements, the system was first prepared in the Néel ordered product state, $\rho_0 = |\psi\rangle\langle\psi|$ with $|\psi\rangle = |\uparrow\downarrow\uparrow\ldots\downarrow\rangle$, which has previously been shown to generate interesting entangled states [124]. The state was prepared by addressing every second ion with a single-ion addressed pulse (implementing a σ_z rotation) sandwiched between two global $\pi/2\ \sigma_x$ rotations with opposite phase. This state was subsequently time-evolved under H_{XY} into the state $\rho(t)$. The coherent interactions arising from this time evolution generated entanglement in the system. Following this, randomised measurements on $\rho(t)$ were performed through individual rotations of each qubit by a random unitary, u_i, sampled from the CUE [131].

In order to practically implement these individual rotations on the ions, each random local unitary, u_i, was first decomposed into rotations around the three axes of the Bloch sphere. Any arbitrary, local unitary can be decomposed into a combination of rotations (combined with global phase shifts) and so can, effectively, be translated into rotation angles around the X-, Y- and Z-axes, such that:

$$u = R_z(\theta_3)R_y(\theta_2)R_z(\theta_1). \tag{6.3}$$

Here, the global phase has been dropped, and $R_i(\theta) = e^{i\sigma_i\theta/2}$ are rotations by θ around the $i = x, y, z$ axes, with σ_i the Pauli matrices. The calculation of these angles is cov-

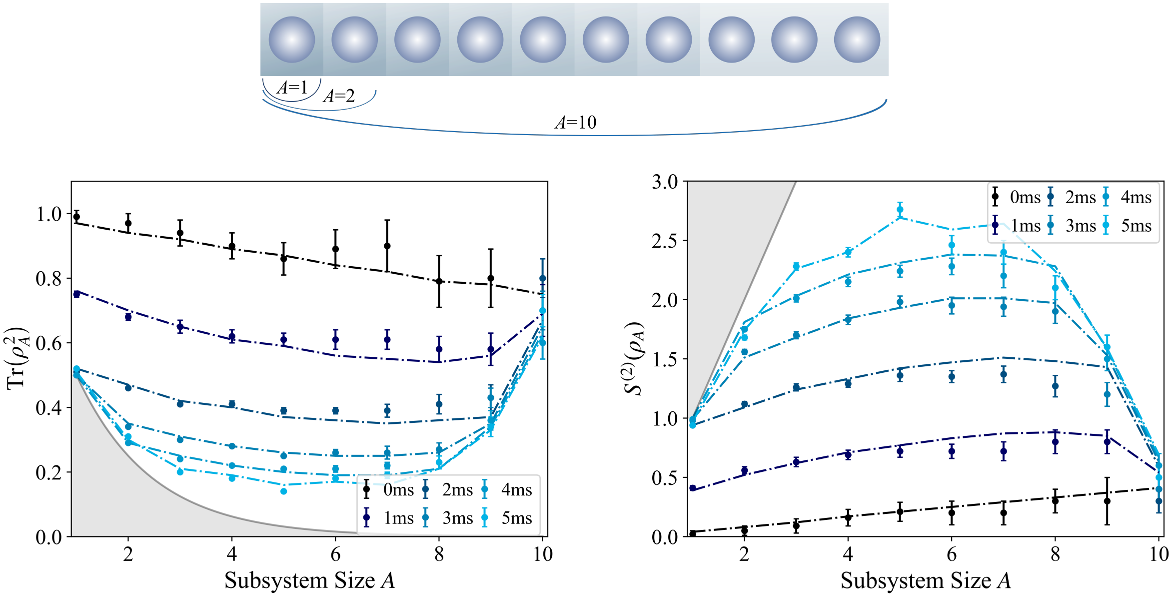

(a) Purity

(b) Rényi Entropy

Figure 6.3: **Purity and second-order Rényi entropies of a 10-qubit system**. The measured purity, (a), and second-order Rényi entropy, (b), of a Néel state, time-evolved under H_{XY}, are shown as a function of subsystem sizes, A, for 6 different evolution times. Each subsystem is comprised of those connected partitions which include qubit 1. For all data points, $N_M = 150$ and $N_U = 498$. Error bars are the standard errors of the mean $\overline{X}$.

ered in detail in Appendix C.1. These local rotations around the three axes were physically implemented through using a combination of global and single-ion rotations. In the QSim system, the addressing beam can be used to directly implement local $\sigma_x(\sigma_y)$ rotations through resonantly addressing a single ion. However, it is more commonly used to implement local $\sigma_x(\sigma_y)$ rotations through off-resonant addressing, which induces an AC-Stark shift on the ion in question (implementing a σ_z rotation), so significantly reducing cross-talk between ions in contrast to resonant addressing [49, 77]. More explicitly, a local $\sigma_x(\sigma_y)$ rotation is implemented through this off-resonant addressing by first using a global $\pi/2$ $\sigma_x(\sigma_y)$ rotation applied to all the ions using the radial beam, followed by a local σ_z on the ion of interest using the addressing beam, followed by a final global $\pi/2$ $\sigma_x(\sigma_y)$ rotation again on all ions, however with opposite phase to the first one. That is, $R_x^{(\mathrm{loc})}(\theta) = R_x^{(\mathrm{glo})}(-\pi/2)R_z^{(\mathrm{loc})}(\theta)R_x^{(\mathrm{glo})}(\pi/2)$. For $\theta = \pi$, this sequence prepares the addressed ion in the excited state, while returning all other ions to the ground state.

In order to ensure that the implementation of each of the local unitaries, u_i, was stable against small drifts of physical parameters (such as beam pointing instabilities or drifts of the ion string), two random unitaries were concatenated to form $u_i' = u_i^{(1)}u_i^{(2)}$. This concatenated unitary was then implemented as one single, random unitary (see Section 6.4.2 for further details on this aspect). Having applied these concatenated unitaries, a state measurement in the Z-basis was performed. To measure the entropy of a quantum

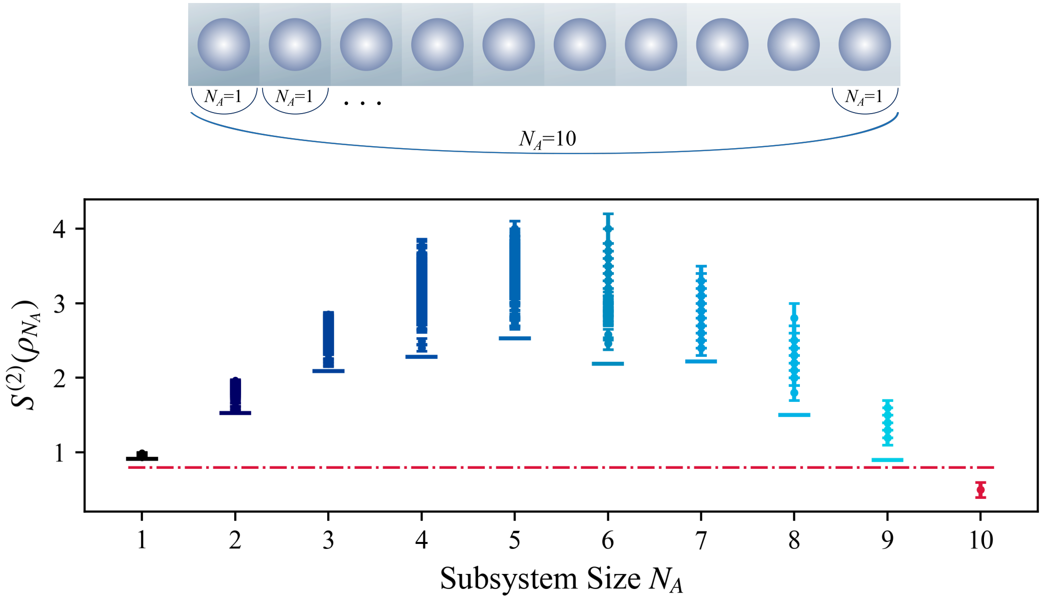

Figure 6.4: **Second-order Rényi entropy, $S^{(2)}(\rho_A)$, of all $2^{10} - 1 = 1023$ partitions at $t = 5\,\mathrm{ms}$.** N_A denotes the number of ions in each subsystem. $N_M = 150$ and $N_U = 498$. The solid blue lines are at three standard deviations below the smallest measured entropy for subsystems 1-9. The red line is at three standard deviations above the full system entropy.

state of N ions, N_U sets of single-qubit random unitaries, where $U = u_1 \otimes .. \otimes u_N$, were applied. For each set of applied unitaries, U, the measurement was repeated N_M times in order to gain sufficient statistics.

The results from application of the protocol to 10-ion partitions of both 10- and 20-ion chains will now be presented.

10-ion Results

The 10-qubit state, ρ_0, was prepared and subsequently time-evolved under H_{XY}, for $\tau = 0, ..., 5\,\mathrm{ms}$ in steps of $1\,\mathrm{ms}$. Figure 6.3 shows the measured purities a) and entropies b) of all those connected partitions which include qubit 1 during this quench – for example, the two qubit subsystem, $A = 2$, is simply ion 1 and ion 2. It can be seen that the overall purity (and therefore entropy) of the entire 10 qubit system remained at a constant value of $\mathrm{Tr}(\rho^2) = 0.74 \pm 0.07$, within error, throughout the entire time evolution. This implies that the time evolution was approximately unitary. Figure 6.3 shows that, even at short evolution times, the single-spin subsystem becomes quickly entangled with the rest of the system. This can be seen through the rapid decrease (increase) of the single-spin purity (entropy) up until the single-qubit state becomes completely mixed. For a single-qubit system, the fully mixed state has a purity (entropy) of $\mathrm{Tr}(\rho^2) = 1/2$ ($S^{(2)}(\rho) = 1$). At longer times, the purity (entropy) of larger subsystems continues to decrease (increase), as they

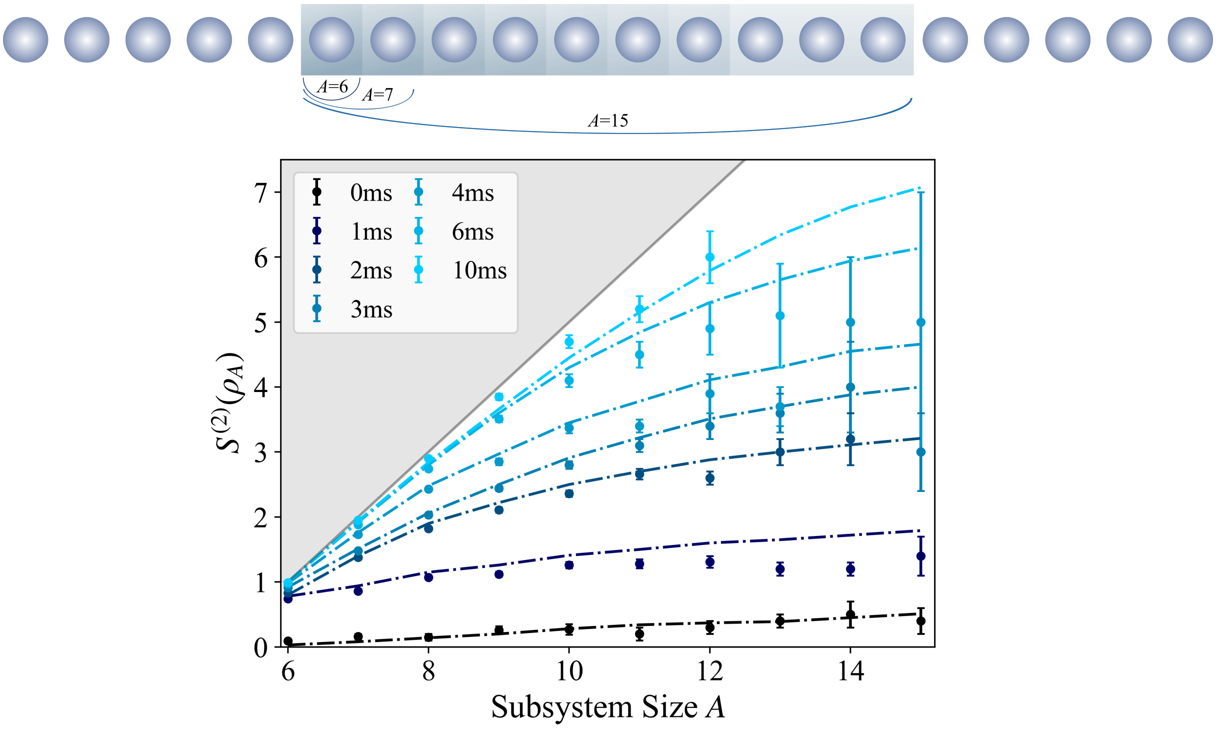

Figure 6.5: **Second-order Rényi entropy of 1- to 10-qubit partitions of a 20-qubit system**. The initial low-entropy Néel state evolves under H_{XY} within 10 ms into a state with high-entropy partitions, corresponding to nearly fully mixed subsystems. The data points for partitions A = 14-15 at 6 ms and partitions A = 13-15 at 10 ms time evolution are not shown due to their large statistical error bars. For all data points, $N_M = 150$ and $N_U = 498$.

become entangled with the rest of the system.

In addition to accessing the entropy of those connected partitions including qubit 1, the protocol also allowed access to the entropy of all $2^{10} - 1 = 1023$ partitions. Figure 6.4 shows the entropy for all partitions (not just the connected partitions) of the system at $t = 5$ ms evolution time. Shown in the Figure is the entropy for each subsystem, with the solid lines representing the point three standard deviations below the smallest measured entropy for subsystems 1-9. For the 10-ion entropy the red line represents the point three standard deviations above the full system entropy. Since the second-order Rényi entropy of every subsystem is, within this three standard deviation figure, larger than for the total 10-qubit system, this demonstrates that entanglement exists between all $2^9 - 1 = 511$ bipartitions of the 10-qubit system to the three standard deviation level.

20-ion Results

Following the 10-qubit experiment, a 20-qubit experiment was performed in a similar manner. The entropy growth of the central part of the chain was measured after time-evolution under the XY Hamiltonian for partitions of up to 10 qubits. Figure 6.5 (top) shows a schematic of this, where the measured partitions are those connected partitions which include ion 6. Figure 6.5 shows the resulting entropy growth of these partitions after different evolution times under H_{XY} for up to 10 ms, with the results consistent with the formation of highly entangled states. The entropy is seen to increase rapidly over the 10 ms time evolution, with the reduced density matrices of up to 7 qubits becoming nearly fully mixed. The results for partitions 14-15 at 6 ms and partitions 13-15 at 10 ms time evolution are not shown due to their large statistical error bars. Such errors, arising from $\Delta(\mathrm{Tr}(\rho^2))/\mathrm{Tr}(\rho^2)$, are due to the very small values of $\mathrm{Tr}(\rho^2)$ which occur for these highly mixed, large subsystems. The small values of $\mathrm{Tr}(\rho^2)$ naturally lead to large statistical errors.

This 20-ion measurement clearly highlights the ability of the protocol to access the entropy of highly mixed states, despite the larger statistical errors compared to pure states.

6.3 Disorder

Recently, quantum thermalisation and many-body localisation have drawn increasing attention, with substantial efforts being invested in understanding these two, related concepts [177]. Following a quench, quantum systems will often approach a state of thermal equilibrium, where quantum correlations which form at short times become scrambled over the system. However, a many-body localised (MBL) system is one that does not thermalise, instead retaining these initial quantum correlations even to long times [177]. The MBL phase is predicted to exist in the presence of strong disorder and sufficiently short-ranged interactions [178] for one-dimensional systems [179].

Before detailing the effects of disorder on the protocol, it is important to first discuss two regimes which can arise from the presence of disorder: Anderson localisation and many-body localisation. The following Section will now discuss the distinctions between these two localised phases.

6.3.1 Anderson (Non-Interacting) and Many-Body Localisation

In order for a closed quantum system to achieve thermalisation purely through its own dynamical evolution, the system must be acting as its own reservoir [180]. However, closed systems exist where this is not the case. Such ‘localised’ systems were first identified by Anderson in 1958, who suggested that materials may undergo a phase transition from conducting to insulating when changes in the disorder in the material are made [181]. Such systems then do not act as reservoirs for themselves, and so do not thermalise. They can retain a ‘memory’ of the initial state of the system, whereas the local properties of a system’s initial state are ‘hidden’ for a system which has thermalised under unitary time evolution [180]. Anderson’s localised systems, and a large amount of the consequent research into

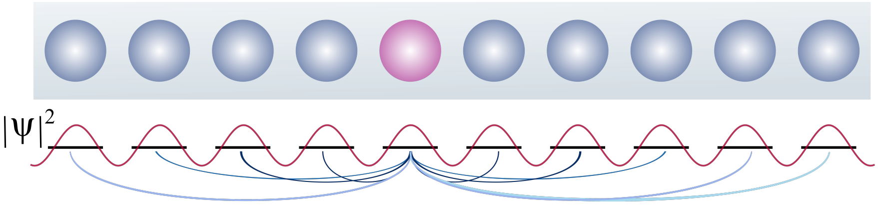

(a) No disorder: Extended wavefunction

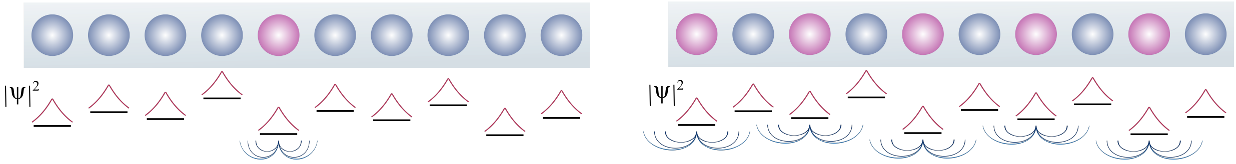

(b) Disorder: Anderson Localisation

(c) Disorder: Many-body Localisation

Figure 6.6: **Illustration of Anderson localisation and many-body localisation.** a) A chain of ten ions with no disorder. After a quench, an initial excitation on ion 5 (shown in pink) is able to spread over the entire ion chain, due to the extended wavefunction (shown by the red, sinusoidal line). Blue lines indicate the propagation of correlations across the string. b) When disorder is present, the energy levels of each ion are shifted out of resonance with one-another, and the single-particle states become localised (red lines). The initial excitation consequently becomes localised, with no propagation of information across the chain. c) For highly-excited systems, the disordered system remains interacting, with correlations and entanglement still propagating through the system, albeit at a slower rate than for the case without disorder. This is a hallmark of the many-body localised phase.

localised systems, only considered non-interacting systems or those in the low-temperature limit. However, localisation can occur in highly-excited states of strongly-interacting many-body systems, a phenomenon which has been termed ‘many-body localisation’. Many-body localised systems also do not thermalise, however interactions still exist within these systems, unlike in Anderson localised systems.

Figure 6.6 illustrates these three different regimes (non-localised, Anderson localised, and many-body localised). a) illustrates an example of a chain of 10 ions with an initial excitation at ion 5, where no disorder is present. Here the eigenstates are extended (represented by the red, sinusoidal function) and, under application of a Hamiltonian such as H_{XY}, an initial excitation can spread out over the ion-chain, with thermalisation being achieved at long evolution times. If an amount of disorder is now added which randomly changes the energy levels of the single ions in the chain, as shown in Figure 6.6 b), then the single-particle eigenstates become exponentially localised. The propagation of an initial excitation over the ion chain is subsequently hindered, and no inter-particle interactions occur, leading to Anderson localisation. Anderson localisation occurs at low energies, and so a single excitation in a 10-ion chain is well within this regime. In an Anderson localised phase, the many-particle eigenstates can be expressed as products of single-particle eigenstates. Crucially, there is no propagation of correlations or entanglement over the chain.

Many-body localisation can be thought of as almost a ‘high-energy’ version of Anderson localisation, where interactions remain present in the system. Figure 6.6 c) illustrates the case where the system becomes many-body localised. As MBL occurs at high-energy, here an initial Néel ordered state is considered instead of a single excitation. With many-body localisation, the single-particle states can still be assumed to be localised as with Anderson localisation. However, the system remains interacting, allowing the propagation of correlations and entanglement through the system. A many-body localised system will not thermalise, even at very long times, retaining a memory of its initial state [182].

In order to study the dynamical properties of these many-body states, the entropy growth of arbitrary, highly entangled states during their time-evolution can be used as a universal tool [183]. The rate at which entropy grows can be used to distinguish between thermalised states and localised states in interacting many-body quantum systems. In a thermalising system, such as in interacting many-body systems without disorder, a linear entropy growth is generally predicted following a quantum quench [177, 183]. This linear entropy growth is assumed to persist until a saturation point is reached, which signals thermalisation of the system. In contrast, the MBL phase is characterised by the absence of thermalisation, the system’s remembrance on the initial state [182] at late times and, in particular, a logarithmic entropy growth [184, 185] which constitutes the distinguishing feature between a MBL state and a non-interacting Anderson insulator.

Experiments to probe this entropy growth have already been realised with superconducting qubits using tomography [186], and in ultracold atoms based on full-counting statistics of particle numbers [187]. However, for long-range interacting models, the situation is less clear, with an ongoing theoretical debate into the persistence and stability of localisation in such systems [139, 179, 188], alongside first experimental investigations [189]. Currently, the measurement of a long-time entropy growth rate is beyond the present capabilities of the QSim system, due to its limited coherence time. However, as a first investigation into the applicability of the measurement protocol in probing MBL in long-range interacting systems, an observation of the strong diminishing effect of local, random disorder on the entropy growth rate at early times, and the emergence of localisation, will now be presented.

6.3.2 10-ion Entanglement Spreading with Disorder

To look at the effects of disorder on entropy growth in a 10-ion system, an additional disorder term was added to the H_{XY} Hamiltonian, such that $H = H_{\mathrm{XY}} + H_{\mathrm{D}}$. The disorder potentials were generated using the single-ion addressing beam to implement independent AC-Stark shifts on all the ions simultaneously. By applying multiple frequencies to the AOD (see Section 3.1.2), multiple beams are consequently produced, allowing application of independent beams to multiple ions at the same time. These AC-Stark shifts introduce

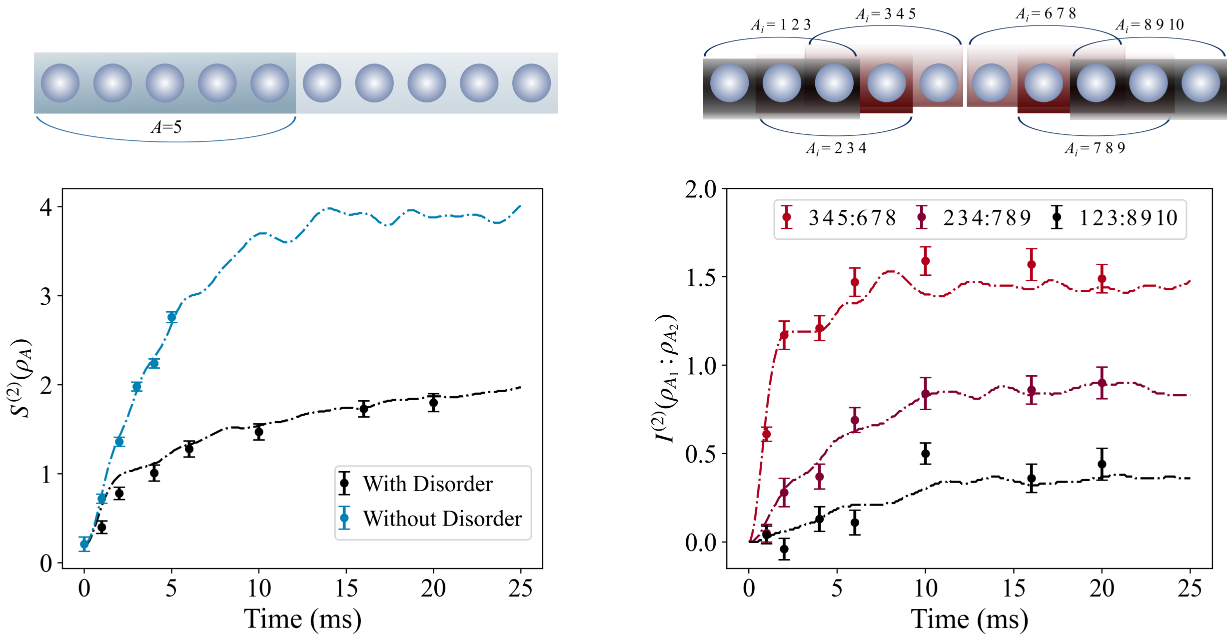

(a) Half-chain entropy growth

(b) Mutual Information

Figure 6.7: **Spread of quantum correlations under H_{XY} both in the presence and absence of disorder.** (a) Entropy growth of the subsystem comprised of ions 1-5 as a function of time without disorder (blue points) and with disorder (black points). (b) Second-order Rényi mutual information of selected subsystems versus time (see Equation 6.5). The decrease of the mutual information $I^{(2)}(\rho_{A_1}, \rho_{A_2})$ with distance between subsystems is a manifestation of the inhibition of correlation spreading by local disorder. Lines are a simulation of the system dynamics including the effects of decoherence.

a time-independent alteration to the transverse field term in the Hamiltonian, with the disordered Hamiltonian then taking the explicit form:

$$H = \hbar \sum_{i<j} J_{ij}(\sigma_i^+ \sigma_j^- + \sigma_i^- \sigma_j^+) + \hbar \sum_j \Delta_j \sigma_j^z, \tag{6.4}$$

with Δ_j the magnitude of disorder applied to ion j and σ_j^z the spin-1/2 Pauli operator. This additional disorder term effectively implements local σ_z^i rotations on all ions during evolution of the system under H_{XY}.

The initial Néel state was quenched with the new Hamiltonian $H = H_{\mathrm{XY}} + H_{\mathrm{D}}$, where a static, random disorder strength Δ_j was drawn uniformly from the range $[-3J_{\max}, 3J_{\max}]$, for $J_{\max} = 420\,\mathrm{s}^{-1}$. Ten sets of single-qubit random unitaries, $U = u_1 \otimes .. \otimes u_N$, were subsequently applied for a single instance of the static random disorder, where $N_M = 150$ repeats of each set of random unitaries were again taken in order to gather sufficient statistics. This procedure was repeated for 35 instances of static random disorder, each measured for 10 different single-qubit random unitaries. The combined ensemble average was taken over both the random unitaries and static random disorders in order to access the disorder-averaged purity, and consequently the disorder-averaged second-order Rényi entropy. Figure 6.7 a) shows the measured evolution of the second-order Rényi entropy of the subsystem $A = 1, \ldots, 5$ with the remainder of the system as a function of time. Shown in the plot is the behaviour in both the absence (blue) and presence (black) of local random disorder. In the absence of disorder, it can be seen that the entropy exhibitis a rapid, linear growth. This is consistent with the expected behaviour of a thermalising, many-body system. In the presence of disorder, after an initial rapid evolution, a considerable slowing of the dynamics is observed, with a small, but non-vanishing, growth rate at later times; a behaviour consistent with the formation of a MBL system.

6.3.3 Magnetisation Dynamics

The difference in dynamics between the systems with and without disorder can be further highlighted by looking at the magnetisation dynamics under the evolution of H_{XY} and $H_{\mathrm{XY}} + H_{\mathrm{D}}$. Figure 6.8 a) and c) show the dynamical evolution of the magnetisation $\langle \sigma_z^i \rangle$, which is proportional to the probability of finding a qubit excitation at site i, under application of H_{XY} and $H_{\mathrm{XY}} + H_{\mathrm{D}}$ respectively. The plots display how the 5 excitations of the initial 10-ion Néel ordered state disperse under application of the respective Hamiltonians. For the disordered Hamiltonian, a single instance of disorder was first applied, and the state subsequently time evolved to generate the magnetisation dynamics. This was repeated for all 35 randomly drawn disorder patters, and the dynamics averaged over the disorder. The averaged dynamics retain many of the same characteristics of the initial Néel ordered state, indicating that there is a remembrance of the initial state during the dynamics. This is a scenario consistent with an MBL phase. In addition to this, Figures 6.8 b) and d) show the corresponding evolution of the single-spin magnetisation, both without disorder and in the presence of disorder. With no disorder present, the initially localised excitations rapidly disperse throughout the system, resulting in an approximately equal magnetisation for all ions at longer times. In the presence of disorder, a stationary magnetisation is observed, showing evidence of a localised phase.

6.3.4 Spread of Correlations

The existence of a localised phase within a system can also be indicated by the spread, and corresponding decay, of correlations. The total amount of both classical and quantum correlations between two subsystems, A_1 and A_2, can be characterised using the second-order Rényi mutual information, $I^{(2)}(\rho_{A_1} : \rho_{A_2})$, defined as [138]:

$$I^{(2)}(\rho_{A_1} : \rho_{A_2}) = S^{(2)}(\rho_{A_1}) + S^{(2)}(\rho_{A_2}) - S^{(2)}(\rho_{A_1 A_2}). \tag{6.5}$$

Figure 6.7 b) shows the evolution of $I^{(2)}$ for various pairs of subsystems in the presence of disorder – the darker the line colour, the further away the subsystems are from each

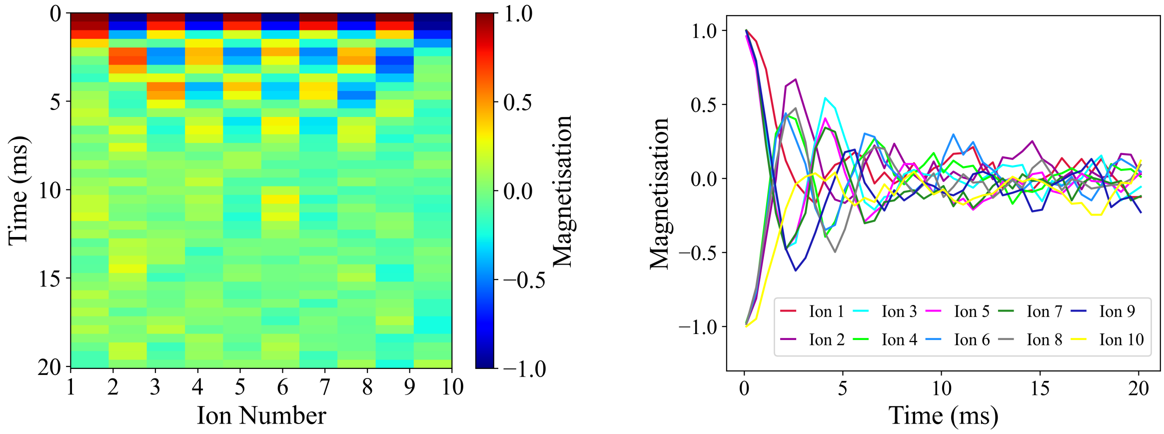

(a) Magnetisation dynamics

(b) Spatially-resolved magnetisation dynamics

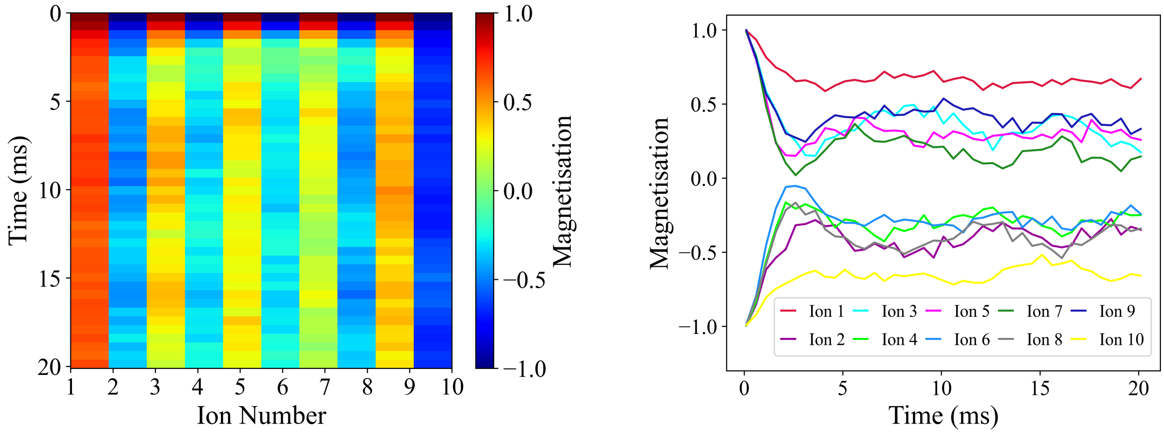

(c) Disordered magnetisation dynamics

(d) Spatially resolved magnetisation dynamics in the presence of disorder

Figure 6.8: **Magnetisation dynamics both in the presence and absence of disorder.** Shown are the time-evolutions of a 10-ion initial Néel ordered state under the Hamiltonians H_{XY} and $H_{\mathrm{XY}} + H_{\mathrm{D}}$. a) and b) With no disorder present, the initially localised excitations disperse rapidly throughout the system. c) and d) Magnetisation dynamics in the presence of disorder, averaged over all 35 random realisations of disorder. A stationary magnetisation arises, showing evidence of a localised phase.

other. The Figure shows that, for all pairs of subsystems, $I^{(2)}$ saturates quickly to an approximately constant value, with this constant value decreasing the further away the two subsystems are. This decay of correlations indicates localisation has occurred as a result of the presence of disorder in the system.

6.4 Characterisation of System Dynamics

The following Section will present several measurements of the system and its dynamics which aid in characterising the measurement protocol. These measurements look at the increase/decrease of spin excitation number during evolution under H_{XY}, decoherence which arises from application of the random unitaries, and cross-talk between ions arising from the single-ion addressing beam.

6.4.1 Conservation of Excitation Number and Decoherence

The number of excitations in the system should be conserved under a time evolution governed by an ideal XY Hamiltonian. However, this conservation of excitation can be violated due to two main reasons. First is the finite lifetime of the excited $\mathrm{D}_{5/2}$ state, resulting in decay to the $\mathrm{S}_{1/2}$ state. Second are imperfections in the laser-ion interaction, for example high-frequency laser phase noise or a disruption of the spin-spin coupling due to motional heating, which can give rise to spin flips. To probe whether these effects caused the conservation of excitations to be violated, a 20-ion Néel ordered initial state was evolved under H_{XY} from 0 to 60 ms, with the number of excitations at varying time-steps during this evolution plotted. Figure 6.9 shows the corresponding dynamics of the number of excitations in the system as a function of the evolution time under H_{XY}. From the Figure, it can be seen that the excitation number, given by the data (points), is not strictly conserved throughout the course of the dynamics, with the probability for 10 excitations in the system falling throughout the dynamics, and the probability for other numbers of excitations (most significantly 9 excitations) increasing.

The excitation number dynamics can be modelled by assuming a spontaneous decay rate from the $\mathrm{D}_{5/2}$ state of Γ, and an additional incoherent spin flip rate, γ_{flip}, which is assumed to be independent of the electronic state (i.e. the same for both $\mathrm{D}_{5/2}$ and $\mathrm{S}_{1/2}$). Therefore, the probability, p, for a single ion to be in the excited state evolves according to:

$$\frac{dp}{dt} = -(\Gamma + \gamma_{flip})p + \gamma_{flip}(1-p). \tag{6.6}$$

The solution to this equation is of the form:

$$p(t) = p_{eq} + (p_0 - p_{eq})e^{-\lambda t}, \tag{6.7}$$

where $p_{eq} = \gamma_{flip}/\lambda$ is the steady-state probability, p_0 is the probability of being initially

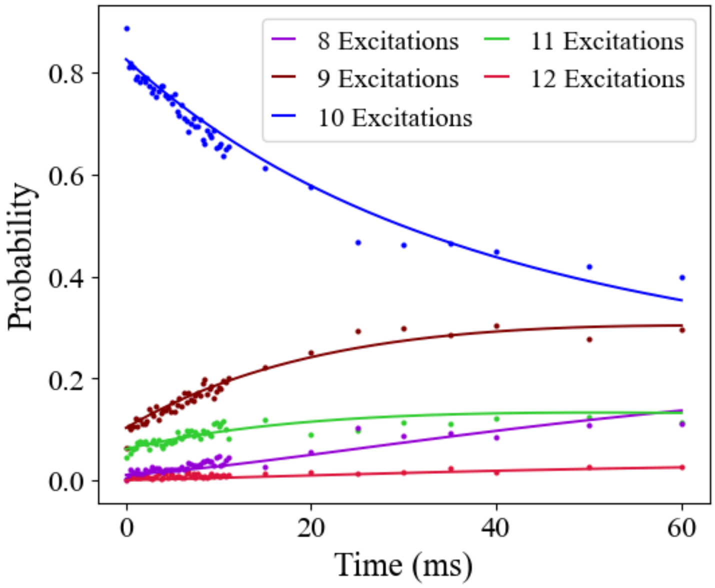

Figure 6.9: **Excitation number dynamics under the XY Hamiltonian, starting from a 20-ion Néel ordered state.** During the course of the dynamics, the probability for 10 excitations to be present in the system (blue points) falls, with the probability for other excitations to be present correspondingly increasing. A fit of the model given in Equation 6.8 (lines) to the data (points) is shown for 8 to 12 excitations.

in the excited state, and $\lambda = 2\gamma_{flip} + \Gamma$.

This model can be extended to explain the dynamics with N ions. Assume that N_1 ions are initially in the excited state, each with probability $p_1(t) = p_{eq} + (1 - p_{eq})e^{-\lambda t}$ to be found in the excited state at a later time t. Consequently there will be $N_2 = N - N_1$ ions initially in the ground state, each with probability $p_2(t) = p_{eq}(1-e^{-\lambda t})$ to be in the excited state at a later time t.

At a given time t, the probability for k ions to be in the excited state, $p_k(t)$, can be expressed as a function of k_1, which represents the ions which were initially excited, and k_2, which is the number of ions which were initially in the ground state, with $k = k_1 + k_2$. $p_k(t)$ can then be expressed as:

$$p_k(t) = \sum_{k_1=k_{min}}^{k_{max}} p_1^{k_1}(1-p_1)^{N_1-k_1} p_2^{k_2}(1-p_2)^{N_2-k_2} \binom{N_1}{k_1}\binom{N_2}{k_2}, \tag{6.8}$$

where $k_{min} = \max(0, k - N_2)$ and $k_{max} = \min(k, N_1)$. Figure 6.9 fits Equation 6.8 to the data (lines) assuming a spontaneous decay rate of $\Gamma = \tau^{-1}$ with $\tau = 1.17\,\mathrm{s}$ [49]. This fit is optimised for a single-ion spin flip rate of $\gamma_{flip} = 0.69\,\mathrm{s}^{-1}$. Therefore, for a 20-ion Coulomb crystal prepared in the Néel-ordered state and illuminated by a bichromatic beam with $\Delta = 2\pi \times 40\,\mathrm{kHz}$ detuning, it would take on average 70 ms for an unwanted spin flip caused by laser-ion interactions to occur. This is in contrast to the average time for a spin flip caused by spontaneous decay to occur, which is about every 100 ms.

6.4.2 Characterisation of Local Random Unitaries

The local unitaries applied to each ion were drawn randomly from the CUE [131]. In the ideal case, this will rotate the Bloch vector describing a single qubit (prepared in a pure state) to any other point on the Bloch sphere with equal likelihood. As such, the distribution of measured spin projections should be uniform along any direction of projection. However, systematic errors, such as minor miscalibrations of the global $\pi/2$-pulses, will affect the distribution of random unitaries. This can then give rise to erroneous (or even unphysical) purity values when using the random measurement protocol to determine the purity of a given qubit state. A second source of errors that can also bias the purity estimates towards lower values is decoherence occurring during application of the local random unitaries. Both of these effects can be detected by a straightforward measurement which looks at the distribution of measured spin projections after application of the random unitaries to a qubit in an initial pure state, as will be shown in this Section.

To make the drawing of random unitaries from the CUE more robust against miscalibrations or drifts of experimental control parameters, two random unitaries (assumed to be drawn from a possibly imperfect distribution) were concatenated to obtain a random unitary with a distribution that is closer to the ideal one – i.e. the applied random unitary is given by $u_i' = u_i^{(1)} u_i^{(2)}$ where $u_i^{(1)}$ and $u_i^{(2)}$ are both random unitaries drawn from the CUE.

The explicit sequence of pulses which the QSim system would in principle use to implement two such concatenated unitaries is given in Equation C.4 of Appendix C.1. However, this pulse-sequence can be simplified by merging the two consecutive rotations around the Z-axis into a single rotation. In addition, as the final readout measurement is performed in the Z-basis, the final Z-rotation in Equation C.4 will have no effect on the measurement result, and so this final rotation can be dropped. Therefore, the local concatenated unitary which is physically implemented in the QSim system takes the form:

$$u = R_y(-\pi/2) R_z(\theta_4) R_y(\pi/2)\, R_z(\theta_3)\, R_y(-\pi/2) R_z(\theta_2) R_y(\pi/2)\, R_z(\theta_1). \tag{6.9}$$

Here, the local rotations around the Y-axis have been replaced by a combination of a local σ_z rotation sandwiched between two global $\pi/2$ rotations around the Y-axis with opposite phase, (see Section 6.2). The single-ion addressing beam can only implement σ_z rotations of a positive rotation angle. As such, when a negative rotation angle, θ, was necessary, these were replaced by a rotation angle of $2\pi - \theta$.

In order to minimise decoherence which can arise from implementation of the local unitaries, it was advantageous to minimise the duration of the total pulse length of the single-ion addressing beam. The total pulse length was naturally given by the sum of the single-

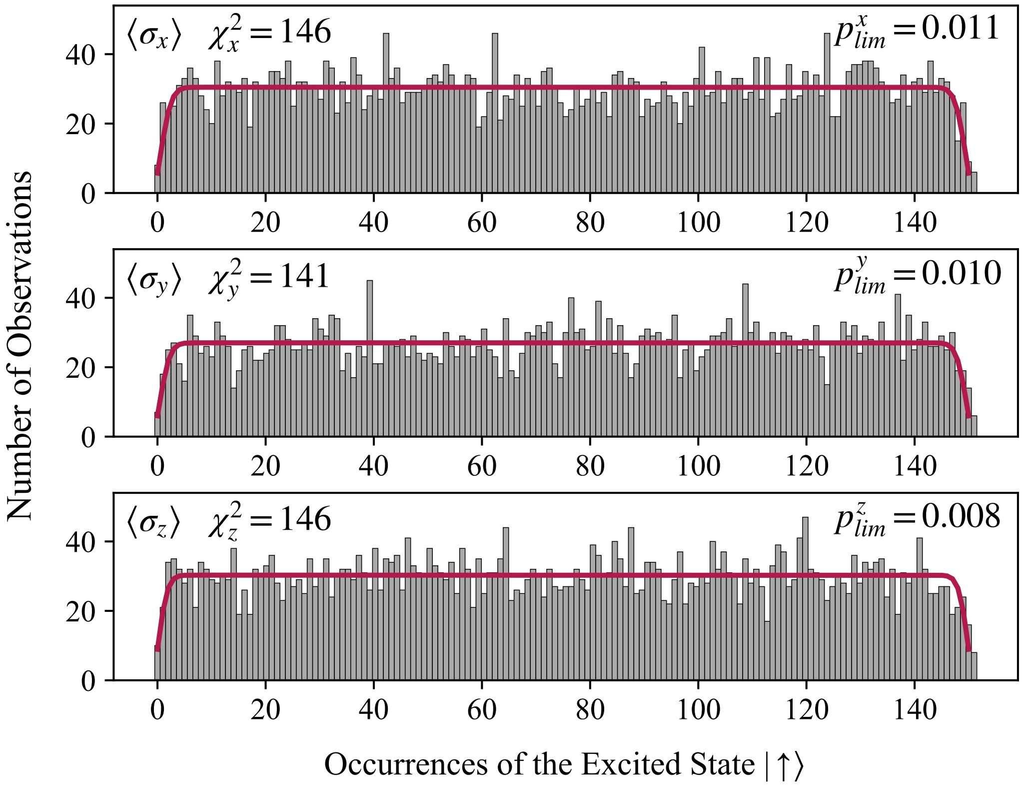

Figure 6.10: **Single-qubit spin projections into the X-, Y-, and Z-bases after application of randomised unitaries.** Randomised measurements were performed on a 10-ion string where all spins were initially prepared in $|\downarrow\rangle$. Shown are the resultant measured single-qubit outcomes when projective measurements in σ_x, σ_y, and σ_z were made. A fit to the data (red line) takes into account decoherence from application of the random unitaries, as well as quantum projection noise. χ^2 tests to evaluate the goodness-of-fit for each distribution are consistent with the expected value of $\chi^2_{ideal} = 149$.

ion addressed pulses on each ion. To minimise the duration of the total rotation, θ, all rotation angles were shifted by a fixed amount, such that $\theta \longrightarrow \tilde{\theta} = \mathrm{mod}(\theta_i - \alpha, 2\pi)$, where α minimizes the function $\sum_i \tilde{\theta}$ and i indexes the ions. In addition, the rotation axis of subsequent resonant global pulses in the equatorial plane was shifted accordingly by the angle α.

Decoherence from Application of Randomised Unitaries

In the ideal case, the distribution of measured spin projections arising from application of the random unitaries should be uniform along any direction of projection. However, the concatenation of random unitaries which was performed in order to improve the robustness of the implemented distribution also increases decoherence as it naturally requires more rotations. To investigate these effects, a 10-ion string was optically pumped into a nearly perfectly pure state (with probability ~99.9% [47]) before applying the laser pulses implementing the (double) random unitaries, and carrying out a subsequent quantum measurement detecting the spin projections in either σ_x, σ_y, or σ_z. A total of $N_U = 498$ different unitaries were used for the measurement. For each unitary, the quantum state was prepared and measured $N_M = 150$ times. Figure 6.10 shows the three resulting spin projection distributions from this measurement. The histograms show, for finding an ion m times ($0 \leq m \leq N_M$) in the $D_{5/2}$ state, the number of times this was observed. It can be seen that all three histograms are reasonably flat, however the distribution falls off towards the extreme values in all cases, indicating that the state produced after application of the random unitaries is not perfectly pure. Therefore, there is some decoherence present arising from implementation of the concatenated random unitaries.

This decoherence can be modelled as a depolarising channel, $\rho \longrightarrow \lambda\rho + \frac{1-\lambda}{2}\mathbb{I}$. The probability distribution for finding the ion in the excited state, $f(p)$, can then be fitted with a box-like distribution which is convolved with quantum projection noise. The box-like distribution is defined as:

$$f(p) = \begin{cases} 0, & p < p_{lim} \quad \text{or} \quad p > 1 - p_{lim} \\ 1/(1 - 2p_{lim}), & p_{lim} < p < 1 - p_{lim}. \end{cases} \tag{6.10}$$

Figure 6.10 shows the fit of such a box-like distribution which is subsequently convolved with quantum projection noise to the three measured distributions. From the fits, it was found that $p^x_{lim} = 0.011$, $p^y_{lim} = 0.010$, and $p^z_{lim} = 0.008$ when detecting in the X-, Y-, or Z-bases respectively. The corresponding average loss of purity per qubit is then found to be $\gamma = 0.019$. This results in a reconstructed purity for a 10-qubit product state of $(1-\gamma)^{10} \approx 0.82$. For testing the goodness-of-fit of this model to the measured distributions, a χ^2-test was performed. For each of the distributions, the resulting χ^2 was found to be $\chi^2_X = 146$, $\chi^2_Y = 141$, and $\chi^2_Z = 146$. These values are all consistent with the expected value of $\chi^2_{ideal} = 149$.

Cross-talk Between Neighbouring Ions

The final test performed to characterise the system was to investigate whether cross-talk between neighbouring ions, induced by imperfect focusing of the strongly-focused single-ion laser beam, could give rise to correlations between the recorded probabilities on different ions.

In order to quantify potential correlations which may exist, the Pearson correlation coefficient was calculated, which gives a measure of the strength of association between two (assumed to be normally distributed) quantities. Here, these two quantities are the probabilities p_i^α, p_j^α of ions i and j being found in the excited state, for a measurement in α (where $\alpha \in \{\sigma_x, \sigma_y, \sigma_z\}$). The strength of these correlations are defined as:

$$\rho_{ij}^\alpha = \mathrm{cov}(p_i^\alpha, p_j^\alpha)/(\sigma_{p_i^\alpha}\sigma_{p_j^\alpha}), \tag{6.11}$$

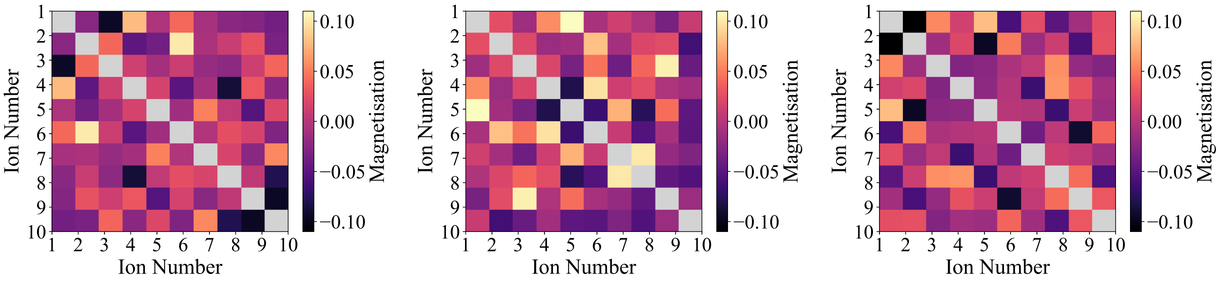

(a) Measurement in σ_x (b) Measurement in σ_y (c) Measurement in σ_z

Figure 6.11: **Correlations between ions when measuring in all three bases.** Randomised measurements were performed on 10 ions all prepared in $|\downarrow\rangle$. Shown are the correlations between the outcome probabilities p_i, p_j for ion i and j being found in the excited state for measurements in all three bases.

where $\mathrm{cov}(p_i^\alpha, p_j^\alpha) = \langle p_i^\alpha p_i^\alpha \rangle - \langle p_i^\alpha \rangle \langle p_j^\alpha \rangle$ is the covariance between p_i^α and p_j^α, and $\sigma_{p_i^\alpha}$ ($\sigma_{p_j^\alpha}$) is the standard deviation of p_i^α (p_j^α). The Pearson coefficient can therefore be seen as a normalised covariance. The results from this calculation are shown in Figure 6.11 for measurements in σ_x, σ_y, and σ_z (the same dataset is used as in the previous Figure). It can be seen visually that the correlation coefficients between p_i^α and p_j^α do not appear to be significant.

However, in order to more rigorously quantify whether these correlations are significant or not, Fisher's combined probability test can be used. First, a null hypothesis is stated, which in this case is that *there are no correlations present (i.e. no cross-talk between ions).* The p-value of each correlation value is then calculated, where the p-value is the probability that the correlation value in question would have been obtained if there were no correlations present. Fisher's test combines the p-values for all ρ_{ij}s from the measurements in one basis into one test statistic, allowing easier evaluation of the results, and is calculated using:

$$\chi^2 = -2 \sum_{i<j} \ln p_{ij}, \tag{6.12}$$

where p_{ij} is the p-value for the correlation between ions i and j.

First, the 'threshold' value of χ^2 should be calculated – i.e. the maximum value of χ^2 which it is possible to have assuming the data is uncorrelated. This value was calculated by simulating 10,000 uncorrelated datasets of 498 values and found to be $\chi^2_{sim} = 89.9 \pm 0.13$ where the error is the standard error. The values of χ^2 for the datasets shown in Figure 6.11 were then calculated to be: $\chi^2_x = 75.2$, $\chi^2_y = 87.4$, and $\chi^2_z = 78.5$. As all three of these values are below the threshold of χ^2_{sim}, it can be concluded that this test did not detect significant correlations between the operations carried out on different ions.

Chapter 7

Probing Scrambling and Cross-Platform Verification using Randomised Measurements

This Chapter will detail the experimental implementation of the second and third theoretical protocols described in Chapter 5. The first of these protocols to be discussed will look at how scrambling in a many-body quantum system can be probed through statistical correlations between randomised measurements. The experimental implementation of this protocol will investigate operator spreading in chains of up to 10 ions by measuring modified OTOCs up to the second order. The measurements are performed for two different interaction ranges, allowing investigations into operator spreading in both ballistic and non-ballistic regimes. The experimental results discussed in the Chapter were published in *'Quantum Information Scrambling in a Trapped-Ion Quantum Simulator with Tunable Range Interactions'* [25], with the theoretical basis for the protocol published in [129].

In the second part of this Chapter the experimental implementation of the third protocol, which allows a direct comparison of two quantum states prepared on two (potentially very different) quantum devices, will be presented. Through a fidelity measurement using randomised measurements, the overlap of the two quantum states can be obtained, with the application of the protocol shown in 'proof-of-principle' experiments on chains of 10 ions. The protocol will first be demonstrated for two classically simulated quantum devices, before comparison of an experimentally prepared quantum state with a classically simulated quantum state will be presented. Following this, a comparison between two quantum states prepared sequentially on the same experimental platform will be shown. The theoretical basis to this protocol, as well as the experimental results, were published in *'Cross-Platform Verification of Intermediate Scale Quantum Devices'* [26], with the data from [24] (also shown in Chapter 6) used as the experimental device.

7.1 Probing Scrambling through Out-of-Time-Ordered Correlators

This Section will present results from the application of the protocol described in Section 5.3 to chains of ten ions. The measurements presented in this Section look at scrambling in a 10-ion string under evolution of the Ising Hamiltonian for two different power-law exponents, $\alpha = 0.85$ and $\alpha = 1.21$. This explores the effect of scrambling for a long-range interaction ($\alpha = 1.21$) and for an even longer-range interaction ($\alpha = 0.85$). The Section will present results from measurements of modified OTOCs up to order 2 (i.e. $O_0(t)$, $O_1(t)$, and $O_2(t)$), and compare them to the exact OTOC, $O(t)$.

7.1.1 Measurement Protocol

As a reminder from Section 5.3, the modified OTOCs are defined as:

$$O_n(t) = \frac{\sum_{k_s \in E_n} c_{k_s} \overline{\langle W(t) \rangle_{u,k_s} \langle V^\dagger W(t) V \rangle_{u,k_0}}}{\sum_{k_s \in E_n} c_{k_s} \overline{\langle W(t) \rangle_{u,k_s} \langle W(t) \rangle_{u,k_0}}} , \tag{7.1}$$

with weights c_{k_s} chosen such that $c_{k_s} = (-2)^{-\mathcal{D}(k_0,k_s)}$. Equation 7.1 quickly converges to the true OTOC $O(t)$ as $n \to N$, where N is the number of qubits in the system [129]. As full convergence to $O(t)$ would require significant experimental effort [129], an approximate convergence to $O(t)$ was instead investigated, with measurements of $O_0(t)$, $O_1(t)$, and $O_2(t)$ performed, all of which required less experimental effort. This allowed an approximation to $O(t)$ to be obtained using Equation 7.1. The three experimental protocols for measuring $O_0(t)$, $O_1(t)$, and $O_2(t)$ are very similar, however $O_1(t)$ and $O_2(t)$ require multiple initial states to be used, in combination with the measurement results from $O_0(t)$. The measurement protocol to measure $O_0(t)$ will therefore first be explicitly described, with the necessary modifications for measurements of $O_1(t)$ and $O_2(t)$ explained after.

Measuring $O_0(t)$

To measure $O_0(t)$, the system was first initialised in the ground state, $\rho_0 = |k_0\rangle\langle k_0|$, with $|k_0\rangle = |\downarrow\downarrow \ldots \downarrow\rangle$. Local, random unitaries $u = u_1 \otimes .. \otimes u_N$ were applied to $|k_0\rangle$, so preparing the state $|\psi\rangle_{u,k_0}$, where the local unitaries were drawn randomly from the CUE [131]. The next step then had two variants:

1. The system was dynamically evolved under H_{Ising}. The operator $W = \sigma_i^x$, for ions $i = 1 \ldots N$, was then measured by applying a σ^x rotation to all ions, before standard state-readout in the Z-basis was performed.
2. A local operator $V = \sigma_1^z$ was applied to ion 1 before the system was dynamically evolved under H_{Ising}. The operator $W = \sigma_i^x$, for ions $i = 1 \ldots N$, was then measured

by applying a σ^x rotation to all ions, before standard state-readout in the Z-basis was performed.

The same random unitaries were used in both Steps 1 and 2. Each step was repeated $N_m = 150$ times, and then the whole process was itself repeated for $N_u = 500$ random unitaries. The local unitaries were applied by using a combination of global rotations and off-resonant, single-ion addressed pulses (see Section 6.2).

When averaged over the repetitions, N_m, Step 1 is a measurement of $\langle W(t)\rangle_{u,k_0}$ and Step 2 a measurement of $\langle V^\dagger W(t)V\rangle_{u,k_0}$. Therefore, by combining both of these steps and averaging over the random unitaries, the 0th order modified OTOC, $O_0(t)$, can be calculated using Equation 7.1.

Measurement Protocol for $O_1(t)$ and $O_2(t)$

The measurement protocol for $O_1(t)$ and $O_2(t)$ is very similar to the protocol described in the previous Section, however additional measurements for different initial states are also needed. For measuring $O_1(t)$, Step 1 in the previous Section is repeated for an additional initial state $|k_1\rangle = |\uparrow\downarrow \ldots \downarrow\rangle$. When combined with the results from measurements of $O_0(t)$, Equation 7.1 can then provide access to $O_1(t)$. Likewise, for measuring $O_2(t)$, Step 1 must be repeated for the initial states $|k_1\rangle = |\uparrow\downarrow \ldots \downarrow\rangle$, $|k_2\rangle = |\downarrow\uparrow \ldots \downarrow\rangle$, and $|k_3\rangle = |\uparrow\uparrow \ldots \downarrow\rangle$. Again, when combined with the results from measurements of $O_0(t)$, Equation 7.1 provides access to $O_2(t)$. For all initial states, the same random unitaries were used.

7.1.2 Results

The first measurement using OTOCs as a probe of scrambling used the measurement protocol for $O_0(t)$ (described above) to investigate how a measurement of $W = \sigma^x$ at ion 5 is affected by the application of operator $V = \sigma^z$ at ion 1, for a single initial state $|k_0\rangle$. This can be seen in the decay of correlations between $\langle W(t)\rangle_{u,\mathrm{k}_0}$ and $\langle V^\dagger W(t)V\rangle_{u,\mathrm{k}_0}$ as the system is evolved under H_{Ising}. Figure 7.1 shows the measured expectation values $\langle W(t)\rangle_{u,\mathrm{k}_0}$ against the values $\langle V^\dagger W(t)V\rangle_{u,\mathrm{k}_0}$ for different evolution times under H_{Ising}. At time $t = 0$, the system has not evolved under H_{Ising}, and so the perturbation V applied to ion 1 therefore has not spread out over the system. Consequently, the measurement of W at ion 5 is unaffected by whether the perturbation V has been applied or not, and so strong correlations can be seen (limited by quantum projection noise) between $\langle W(t)\rangle_{u,\mathrm{k}_0}$ and $\langle V^\dagger W(t)V\rangle_{u,\mathrm{k}_0}$, as seen in Figure 7.1 a). Figures b) and c) show these same correlations after evolution of the system under H_{Ising} for times $t = 2\,\mathrm{ms}$ and $t = 5\,\mathrm{ms}$. At later times, the perturbation V at ion 1 has spread over the system, and so has affected the measurement of W at ion 5. Therefore, the correlations between $\langle W(t)\rangle_{u,\mathrm{k}_0}$ and $\langle V^\dagger W(t)V\rangle_{u,\mathrm{k}_0}$ correspondingly decrease, with almost no correlations present by time $t = 5\,\mathrm{ms}$.

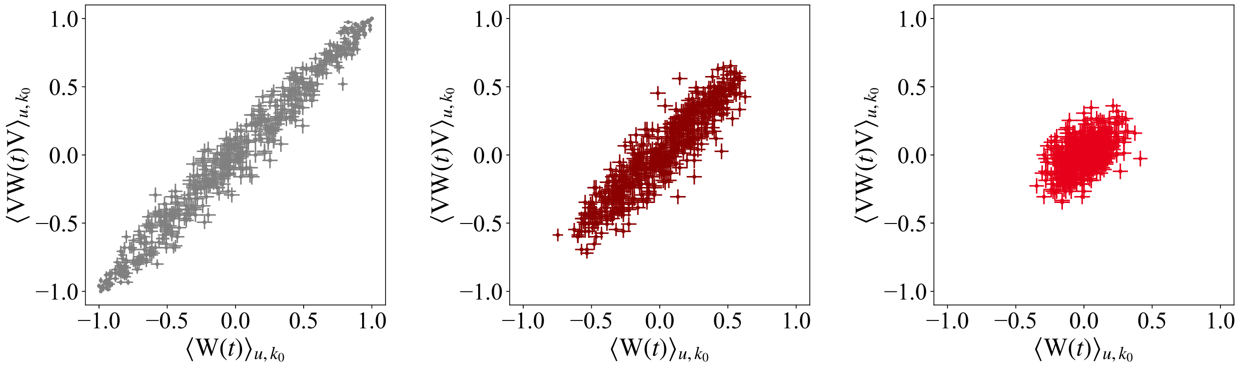

(a) $\tau = 0\,\mathrm{ms}$ (b) $\tau = 2\,\mathrm{ms}$ (c) $\tau = 5\,\mathrm{ms}$

Figure 7.1: **Operator spreading under H_{Ising}.** Correlations between $\langle W(t)\rangle_{u,k_0}$ and $\langle V^{\dagger}W(t)V\rangle_{u,\mathrm{k}_0}$ for different evolution times under H_{Ising} ($J_{ij} = 380\,\mathrm{s}^{-1}$, $\alpha = 1.21$, and $\delta = 2\pi{\times}3\,\mathrm{kHz}$). a) Initially at $t = 0\,\mathrm{ms}$, there are almost perfect correlations between the two observables. b) and c) With increasing evolution time, these correlations decrease, until at $t = 5\,\mathrm{ms}$ almost no correlations are left between the two observables. All measurements were repeated 150 times, with 500 random unitaries used. Error bars (denoted by the crosses) are calculated from quantum projection noise.

These measurements can also be compared to Figure 5.7 in Section 5.3, where correlations between $\langle W(t)\rangle$ and $\langle VW(t)V\rangle$ were presented for simulated data on a 6-qubit system. Similar dynamics are present between the simulated and measured systems, with the correlations decreasing in time before virtually no correlations are present after several milliseconds evolution under H_{Ising}.

The rigorous mathematical relation between exact OTOCs and modified OTOCs is not discussed in this thesis, being shown explicitly in [129]. Instead, the remainder of this Section will now show measurements of the modified OTOC in a 10-ion system in order to provide insights into operator spreading under different interaction ranges in the QSim system. Figure 7.2 shows the results of the modified OTOC measurements for two different power law exponents, following the measurement protocol described previously. Shown in the Figures are the 0th, 1st, and 2nd order OTOCs, as well as the exactly solved OTOC (bottom) for each ion as a function of evolution time under H_{Ising}. The left column shows the OTOCs for $\alpha = 0.85$, and the right column for $\alpha = 1.21$. Also shown in the Figures as dashed lines are the simulated dynamics of the system. It can be seen that, for all ions, the modified OTOCs $O_0(t)$, $O_1(t)$, and $O_2(t)$ display qualitatively similar behaviour to the exact OTOC, $O(t)$, shown in the bottom panel. At $t = 0\,\mathrm{ms}$, near-perfect anti-correlations are present for ion 1 and near-perfect correlations for all other ions, for both values of α and all orders of modified OTOC. However, there are clear differences between the dynamics for the different α values. Most obviously, the spreading of the operator wavefront is significantly faster for $\alpha = 0.85$ than for $\alpha = 1.21$.

The most natural aspect to consider next is how well the measured modified OTOCs

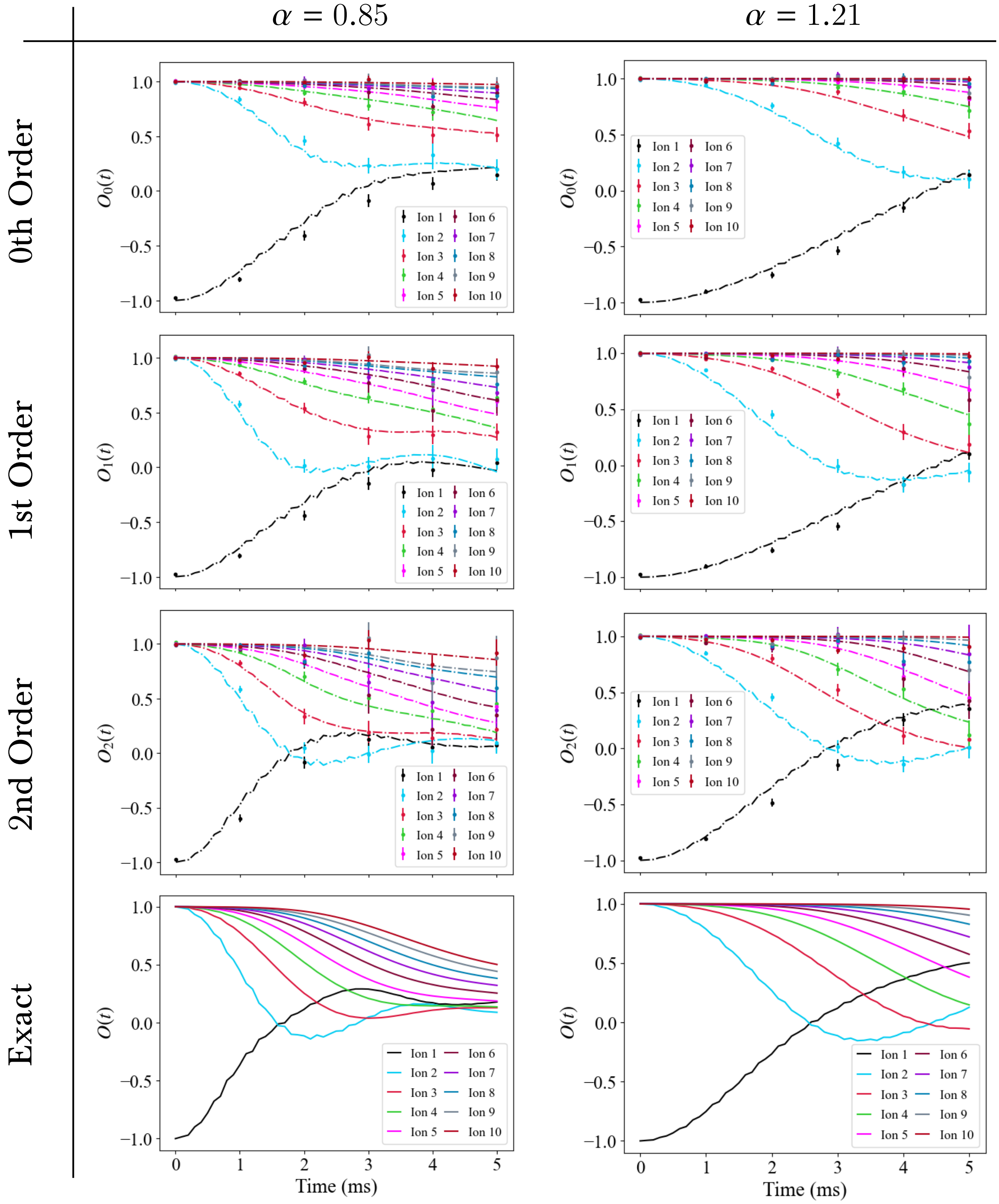

Figure 7.2: **Measured evolution of modified OTOCs, $O_0(t)$, $O_1(t)$, and $O_2(t)$ for $\alpha = 0.85$ and $\alpha = 1.21$.** For all measurements, the local operators were $V = \sigma_1^z$ and $W = \sigma_i^x$ for ion $i = 1, 2, \ldots, 10$. For $\alpha = 0.85$, $J_{ij} = 510\,\mathrm{s}^{-1}$, and for $\alpha = 1.21$, $J_{ij} = 380\,\mathrm{s}^{-1}$. The top row shows the 0th order modified OTOC, $O_0(t)$, for both values of α. 2nd and 3rd rows show the corresponding measurements for $O_1(t)$ and $O_2(t)$ respectively. The bottom row shows the exact OTOC $O(t)$. Dashed lines are numerical simulations assuming unitary dynamics. Errorbars are calculated from Jackknife sampling [190].

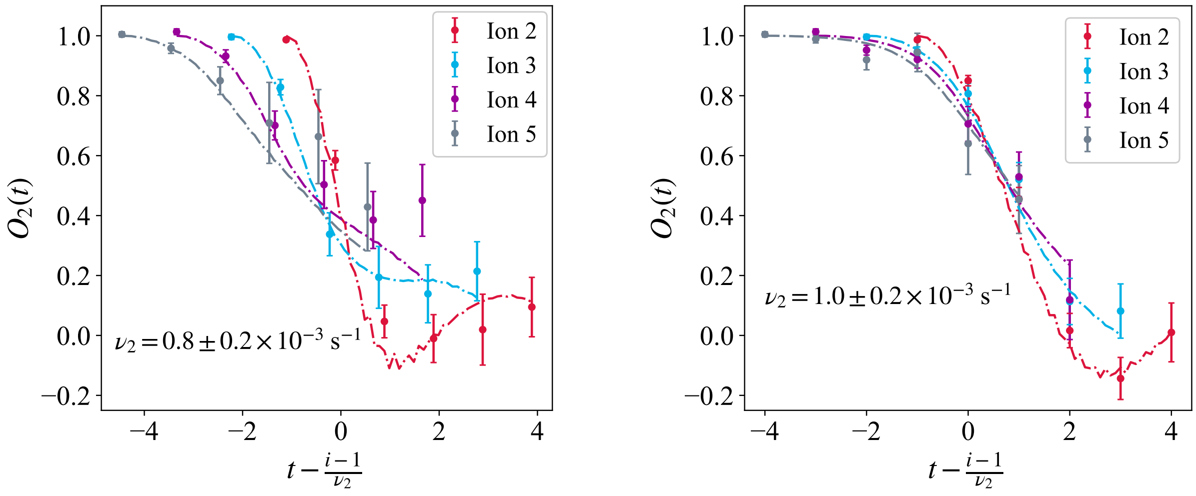

(a) $\alpha = 0.85$

(b) α=1.21

Figure 7.3: **Dynamics of operator spreading**. Plotted are the evolution of OTOCs plotted against rescaled time for $\alpha = 0.85$ and $\alpha = 1.21$. For all measurements, the local operators were $V = \sigma_1^z$ and $W(t) = \sigma_i^x$ for ion $i = 2, \ldots, 5$. ν_2 was fitted such that the best collapse of the data was obtained at the $O_2(t) = 0.5$ level (see text). Dashed lines are numerical simulations. Error bars are calculated from Jackknife sampling [190].

approximate the exact OTOC $O(t)$. From Figure 7.2 it can be seen that, for both values of α, the dynamics of $O_0(t)$ progress at a much slower rate than those of $O(t)$. However, by comparing $O_2(t)$ to the exact OTOC $O(t)$, it can be seen that an approximate convergence to $O(t)$ is obtained for $n = 2$. This agrees with what would be expected from theory, where $O_0(t)$ would be expected to be a poorer approximation to $O(t)$ than higher-order terms such as $O_2(t)$ [129]. At later evolution times such as $t = 4, 5$ ms, the measurements of $O_2(t)$ do begin to differ more substantially from the exact OTOC $O(t)$. This can be attributed to slight mismatches in the Hamiltonian parameters (such as J_{ij} and α) used to calculate $O(t)$ in comparison to the true parameters implemented in the experiment. Mismatches between these parameters are to be expected, as the standard techniques used to measure the experimental parameters of the QSim system are only estimates of the true values (see Section 6.1).

7.1.3 Dynamics of Operator Spreading

The spreading of the operator wavefront in a system with the long-range interactions implemented in the QSim system is not expected to be purely ballistic [191]. The exact shape and dynamics of the spatial-temporal profile of both time ordered [176, 192] and out-of-time-ordered [193–198] correlations is currently the subject of intense theoretical investigation. This protocol has the ability to provide further insight into such open questions, as information as to the nature of the operator wavefront expansion can be extracted by looking at the collapsed dynamics. The time axis of the $O_2(t)$ data shown in Figure 7.2 can be rescaled such that $t \to t - (i-1)/\nu_2$, where i is the individual ion and ν_2 is

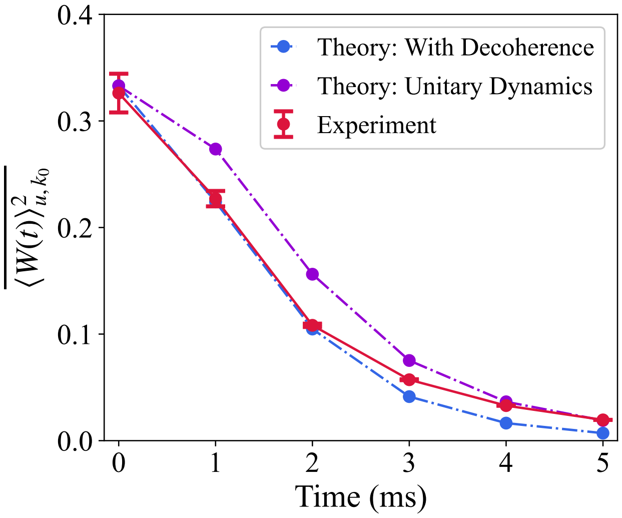

Figure 7.4: **Decay of Statistical Auto-Correlations**. Shown are the statistical auto-correlations, $\overline{\langle W(t) \rangle^2}_{u,k_0} = \overline{\langle \sigma_i^x(t) \rangle^2}_{u,k_0}$, averaged over all ions $i = 1, \ldots, 10$, as a function of evolution time under H_{Ising}. Experimental data is shown in red, alongside the simulated dynamics both with (blue) and without (purple) decoherence. Lines are a guide to the eye.

the velocity at which $O_2(t)$ spreads out over the ion string. Figure 7.3 shows this rescaled data for ions $i = 2, \ldots, 5$ and both values of α. The values of v_2 for each α were extracted through generating data by interpolating the OTOC for all time-steps, and then extracting the time for which $O_2(t_v) = 0.5$. By fitting this data with the linear function $t_v = (i-1)/v_2$, a value for v_2 can be extracted [25].

In Figure 7.3 a) ($\alpha = 0.85$) it can be seen that the data does not collapse to a single curve. This implies that the shape of the operator wavefront is not conserved in both time and space, and so the dynamics cannot be ballistic. Instead, the decay of $O_2(t)$ appears to broaden over the course of the dynamics, an observation consistent with theoretical predictions of the dynamics for $\alpha < 1$ [198]. In contrast, it can be seen in Figure 7.2 b) ($\alpha = 1.21$) that the dynamics do collapse to approximately a single curve. This is consistent with a ballistic spreading of the operator wavefront with an extracted velocity of $v_2 = 1000 \pm 200\,\text{s}^{-1}$.

7.1.4 Detecting Scrambling via Statistical Auto-Correlations

As a final probe of quantum information scrambling in a many-body system, the decay of statistical moments of the form $\overline{\langle W(t) \rangle^2}_{u,k_0}$ can be looked at. $\overline{\langle W(t) \rangle^2}_{u,k_0}$ can be accessed through considering statistical auto-correlations between the randomised measurements in Step 1 of the measurement protocol for the initial state $|k_0\rangle$.

Figure 7.4 shows the measurement of $\overline{\langle W(t)\rangle^2}_{u,k_0} = \overline{\langle \sigma_i^x(t)\rangle^2}_{u,k_0}$ at different evolution times under H_{Ising}, where $\overline{\langle W(t)\rangle^2}_{u,k_0}$ has been averaged over all ions $i = 1, \dots, 10$. $\overline{\langle W(t)\rangle^2}_{u,k_0}$ can be seen to decay with increasing evolution time under H_{Ising}. For unitary dynamics, this would be a direct signature of operator spreading and, hence, scrambling [199]. However, it should be noted that $\overline{\langle W(t)\rangle^2}_{u,k_0}$ decays not only through scrambling but also through decoherence, which causes the system to move towards a state with reduced magnetisation. Therefore, the decay of $\overline{\langle W(t)\rangle^2}_{u,k_0}$ seen in Figure 7.4 is driven both by scrambling and by decoherence. This can be seen by comparing the measured decay of $\overline{\langle W(t)\rangle^2}_{u,k_0}$ to simulated decays of the operator under purely unitary dynamics, and also dynamics with decoherence included. Figure 7.4 also shows such dynamics (purple and blue points respectively), where it can be seen the experiment matches well the simulated dynamics under decoherence.

7.1.5 Robustness to Decoherence

The presence of decoherence in the system dynamics will drive the system towards a steady state that has a reduced magnetisation, compared to evolution under purely unitary dynamics. In this way, both decoherence and scrambling lead to a decay of the operator $\overline{\langle W(t)\rangle^2_{u,k_0}}$. However, the modified OTOC given in Equation. 7.1 is normalised with respect to $\overline{\langle W(t)\rangle^2_{u,k_0}}$, and as such is robust to forms of decoherence which reduce this operator, such as depolarising noise and read-out errors.

For a more quantitative example of the robustness of the protocol to decoherence, it should be noted that the numerical simulations shown in Figure 7.2 are for unitary dynamics, and so explicitly do not include the effects of decoherence in the system. Given the good agreement between the simulation and measured data, this implies that the measurement protocol is not affected by global dephasing of the experimental system.

7.1.6 Conclusion

This Section has detailed the experimental implementation of the theoretical protocol described in Section 5.3 on chains of 10 ions. It has shown how the dynamics of operator spreading over an ion chain under evolution of H_{Ising} can be accessed by using the protocol. Further, it provides insights into the ballistic/non-ballistic nature of operator spreading in the QSim system, which is determined by the interaction range α. The speed with which the operator wavefront spreads through the system can also be extracted through examining the spatial-temporal profile of the OTOC. The protocol has been shown to be robust to certain types of decoherence, including through comparison of the data to unitary dynamics, showing that global dephasing of the experimental system has no effect on the protocol.

7.2 Cross-Platform Verification

The second part of this Chapter will now be devoted to the final protocol, described in Section 5.4. The protocol provides a way to verify a quantum state prepared on two different quantum devices, where the state can be prepared at potentially very different points in time and space. This will become of ever-increasing importance as technological developments continue to move towards regimes where comparison with classical simulations will become too computationally demanding to be feasibly realised. In order to provide a 'proof-of-principle' demonstration of the cross-platform verification protocol detailed in Section 5.4, the following Sections will present three examples of the process. The first of these will present purely classically simulated data, with the fidelity between two classically simulated states presented. Following this, an experiment-theory verification will be performed, where experimental data will be compared to a classical simulation of the experiment (both with and without decoherence effects included). The final Section will present the results from experiment-experiment verifications, where one set of data taken from the experiment will be split into two equal partitions, with these two partitions subsequently compared against one another. The experimental data used for these proof-of-principle demonstrations is the same data as that used in Chapter 6 and [24], where a 10-ion chain is evolved under H_{XY}.

7.2.1 Theory-Theory Verification

For the theory-theory verification, two classically-prepared states, which are simulated as though prepared using the dynamics of the QSim experiment, are compared using the protocol. The classical simulation solved the master equation, where decoherence including decay from the excited state ($\Gamma = \tau^{-1}$ with $\tau = 1.17\,\mathrm{s}$) as well as effects from unwanted spin flips (assumed rate of $\gamma_{flip} = 0.69\,\mathrm{s}^{-1}$) were included (see Section 6.4.1). These two theory states should be identical, however effects from finite sampling mean the calculated fidelity will never be exactly equal to one. Therefore, a comparison of the two theory states gives an indication of how errors from finite sampling processes will impact the final fidelity estimation results.

As a reminder from Section 5.4, the mixed state fidelity which will be used to quantify the overlap between two (possibly mixed) states, ρ_1 and ρ_2, is:

$$F_{\max}(\rho_1, \rho_2) = \frac{\mathrm{Tr}(\rho_1 \rho_2)}{\max\{\mathrm{Tr}(\rho_1^2), \mathrm{Tr}(\rho_2^2)\}} \,. \tag{7.2}$$

To estimate $\mathrm{Tr}(\rho_1, \rho_2)$ the same local, random unitaries $u = u_1 \otimes .. \otimes u_{N_A}$, where N_A is the number of qubits in the (sub)system, are applied to the two different devices. The overlap between the two (potentially reduced) density matrices can then be estimated from the cross-correlations between the two devices using:

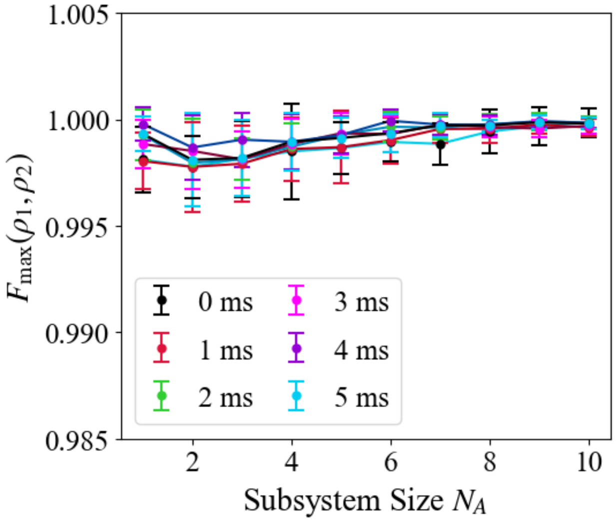

Figure 7.5: **Theory-Theory Verification**. Plotted is the calculated fidelity, $F_{\max}$, as a function of subsystem size, N_A, for different evolution times under H_{XY} for two classically simulated states. For all data points, $N_U = 500$ and $N_M = 150$. Error bars are calculated from the standard deviation.

$$\mathrm{Tr}(\rho_{1,A_1}, \rho_{2,A_2}) = 2^{N_A} \sum_{s_A^1, s_A^2} (-2)^{-\mathfrak{D}(s_A^1, s_A^2)} \overline{P_U^{(1)}(s_A^1) P_U^{(2)}(s_A^2)} \,, \tag{7.3}$$

where N_A is the number of qubits, $s_A = (s_1, \ldots, s_{N_A})$ is an outcome from a measurement on the state, $\mathfrak{D}(s_A^1, s_A^2)$ is the Hamming distance, and $\overline{\ldots}$ is the ensemble average over the random unitaries. Therefore, Equation 7.2 gives a measure of the overlap between the two density matrices ρ_1 and ρ_2, normalised by their purities. Consequently, it gives an estimation of the degree to which two quantum platforms have prepared the same, possibly mixed, state.

Figure 7.5 shows the results from calculating this fidelity for two classically simulated states. The states were initialised in the Néel-ordered configuration and subsequently evolved under H_{XY} for up to 5 ms. The simulation was performed assuming 500 random unitaries, each with 150 repeat measurements, as is the case with the real experimental data shown in the following Sections. As such, it can be seen that the drop in fidelity occurring from implementation of the protocol and finite sampling is <0.5%. Therefore, it can be assumed that repeat measurements on the order of 150 will be sufficient to provide a reasonable estimate of $F_{\max}$.

7.2.2 Experiment-Theory Results

In a first proof-of-principle demonstration of how the protocol can be used with real experimental data, the data used in Chapter 6 and [24] for chains of 10 ions was compared with

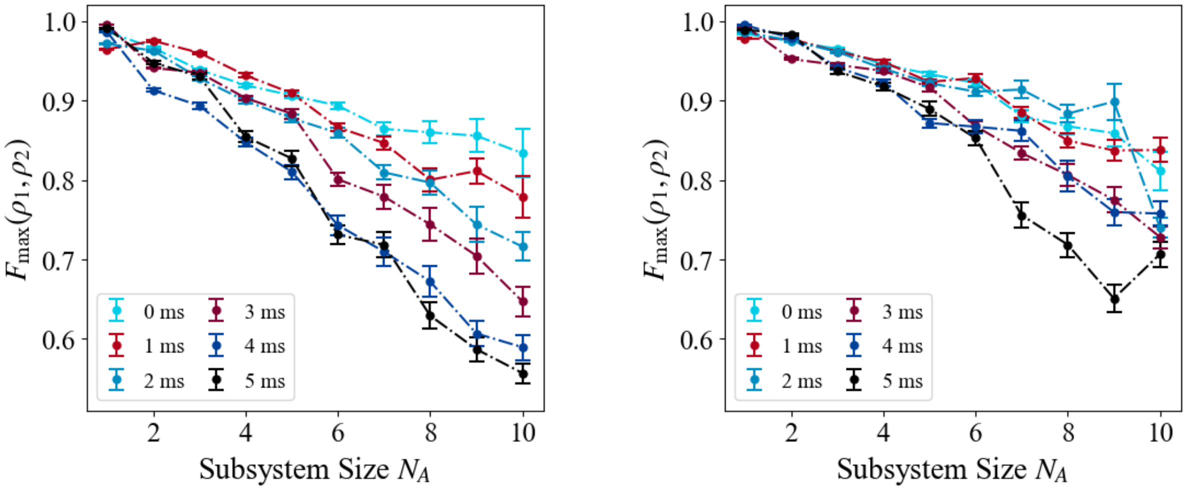

(a) Simulated unitary dynamics

(b) Simulated dynamics including decoherence

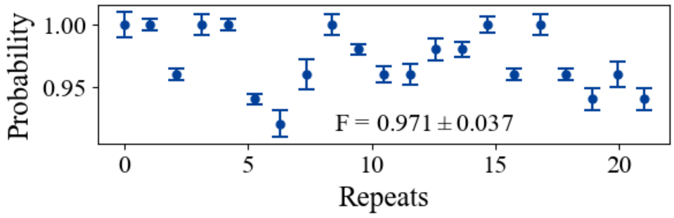

(c) Néel State Preparation

Figure 7.6: **Experiment-Theory Verification**. Shown are the estimated fidelities $F_{\max}$ as a function of subsystem size N_A for different evolution times under H_{XY}. In a) the theoretical simulation is performed for unitary dynamics. In b), it is performed with decoherence included. For both sets of data, $N_U = 485$, $N_M = 150$, $J_{\max} = 420\,\mathrm{s}^{-1}$, and $\alpha = 1.24$. Errorbars are calculated from Bootstrap sampling [190]. c) Initial Néel State fidelity. Each point is the probability of a successful Néel state preparation calculated for 50 repeat measurements. This was repeated sequentially 20 times. Error bars are calculated from quantum projection noise.

a classical simulation of the experiment to demonstrate the protocol. The experimental data was used as ρ_1, with the classical simulation being ρ_2. As a reminder of the experimental data, a 10-ion initial Néel-ordered state was evolved under H_{XY} for up to 5 ms to the state ρ. Randomised rotations were subsequently performed on the evolved state ρ and a measurement in the Z-basis performed (see Section 6.2). The classical simulation was the same as that described in the previous Section.

Figure 7.6 shows the estimated fidelity results from applying the protocol to the experimental data and classical simulation. Figure 7.6 a) shows the results from a comparison of the experimental data and a classical simulation with purely unitary dynamics. Figure 7.6 b) shows the results where the classical simulation contained additional decoherence.

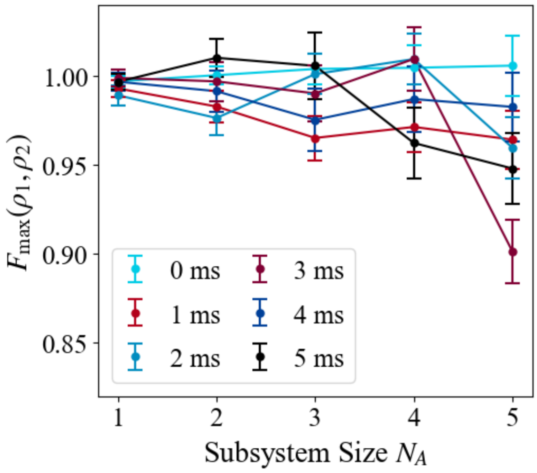

Figure 7.7: **Experiment-Experiment Verification**. Plotted are the estimated fidelities $F_{\max}$, of two states prepared sequentially in the same experiment as a function of reduced subsystem size $N_A = 1, \ldots, 5$ for different evolution times under H_{XY}. For all data points, $N_U = 485$, $N_M = 75$, $J_{\max} = 420\,\text{s}^{-1}$, and $\alpha = 1.24$. Error bars are estimated from Bootstrap sampling with 500 repetitions [190].

In both cases, the classical simulation was performed by solving the master equation.

Figure 7.6 c) shows the results from an independent fidelity measurement of an experimentally prepared initial Néel-ordered state in the QSim system. The calculated fidelity from this measurement was found to be 0.971 ± 0.037. This fidelity was obtained by calculating the overlap between the measured state and the ideal state, which is straightforward as the Néel state is a simple product state. The fidelity of the initial Néel state preparation was re-checked each time five random unitaries had been applied. If the fidelity was found to be less than 97% then the system was recalibrated. This ensured that the initial state was always prepared to a high standard.

However, it can be seen in Figure 7.6 a) and b) that, even at 0 ms when the system has not undergone any evolution under H_{XY}, there is a decrease in the estimated fidelity $F_{\max}$ with the size of the subsystem. Given the experimentally verified high preparation fidelity of the initial Néel-ordered state, the decrease in fidelity with system size must therefore be primarily due to experimental imperfections in the application of the random unitaries. Such experimental imperfections can take two forms: First are errors from over/under rotations. This is, in effect, a difference between the experimentally applied unitary, and the ideal unitary used in the simulation. From Section 4.1.6, it can be seen that the most significant errors in the implemented gates are from σ^z rotations, and so such over/under rotations are most likely to occur from use of the single-ion addressing beam. The second source of error is depolarising noise from application of the unitaries. For further discussions and characterisations of such errors, see Chapters 4 and 6. Further discussions on how such errors can influence the protocol itself are left to [26].

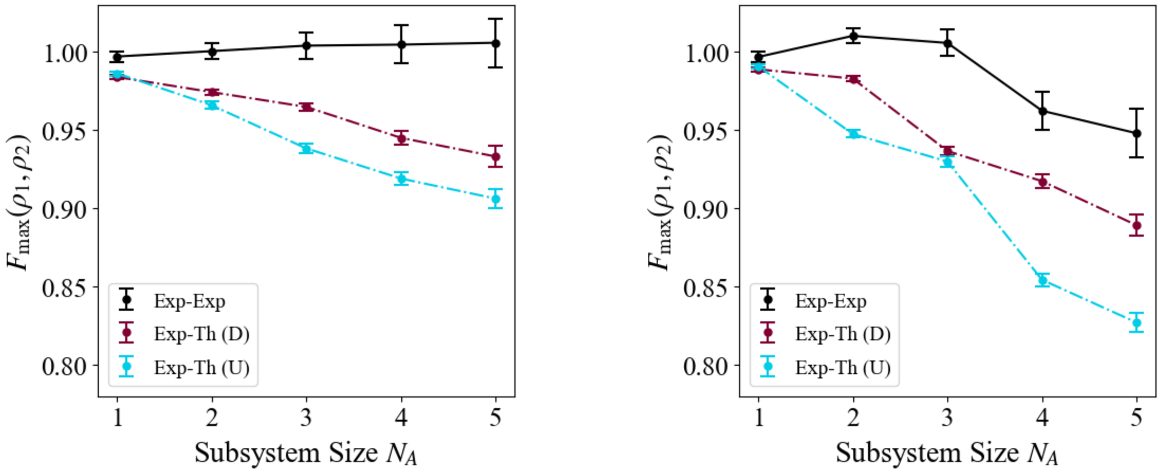

(a) 0 ms evolution time

(b) 5 ms evolution time

Figure 7.8: **Experiment-Experiment Verification and Experiment-Theory Verification**. Experiment-experiment fidelities plotted alongside experiment-theory fidelities from Figure 7.6 for reduced subsystems $N_A = 1, \ldots, 5$. a) Plotted are the estimated fidelities $F_{\max}$ at 0 ms. b) Estimated fidelities at 5 ms evolution under H_{XY}. For all data points, $N_U = 485$. For experiment-experiment data points $N_M = 75$, and for experiment-theory data points $N_M = 150$. Error bars are estimated from Bootstrap sampling [190].

Even out to 5 ms evolution time, where the initial Néel ordered state has evolved into a highly entangled state, there is still a relatively high fidelity between the experiment and classically simulated system – with fidelities on the order of 70% for the case where the simulated system includes decoherence. This is quite remarkable given the complex many-body dynamics the system has undergone during this process, suggesting that the many-body dynamics in the QSim system are relatively well understood.

7.2.3 Experiment-Experiment Results

As a second demonstration of the usefulness of the protocol in the cross-platform verification of two independent quantum devices, the fidelities of two sets of experimental data, obtained sequentially on the same experimental platform, were compared. The data from Chapter 6 and [24] for chains of 10 ions was again used for this demonstration. In this case, a single data set with 150 repeat measurements was split into two equal partitions, corresponding to the states ρ_1 and ρ_2, each with 75 repeat measurements.

Figure 7.7 shows the results from estimations of the fidelities for these experimental datasets as a function of reduced subsystem size $N_A = 1, \ldots, 5$. It can be seen from the Figure that, at all evolution times under H_{XY}, the fidelity remains high, at around 90% or above. Figure 7.8 a) shows the experiment-experiment fidelities plotted alongside the experiment-theory fidelities from Figure 7.6 for 0 ms, with b) showing the same for 5 ms. It can be clearly seen that the experiment-experiment fidelities are significantly higher than the theory-experiment fidelities, even for the situation where decoherence is included in the classical simulation. This implies that, even though there is a difference between the unitaries prepared in the QSim system and the ones which are classically simulated (as deduced from Figure 7.6), the random unitaries implemented in the QSim system are highly repeatable, being well-reproduced each time.

7.2.4 Conclusion

The final Section of this Chapter has presented a first experimental implementation of the cross-platform verification protocol (introduced in Chapter 5), which allows a direct fidelity measurement between two quantum devices. The protocol was demonstrated through several proof-of-principle implementations using experimental data from the QSim system. Initially, the protocol was demonstrated on two classically simulated states which aimed to implement the dynamics of the QSim system in a theoretical system. Following this, experimental data from chains of 10 ions was compared to a classically simulated state, both with and without the effects of decoherence. For the simulation with decoherence, fidelities for the overlap of the two states were on the order of 70%, even after several milliseconds of evolution under H_{XY}. This is quite remarkable, as by this point the experimental system had undergone complex, many-body dynamics, so evolving into a highly entangled state. In a second implementation, the fidelities of two sets of experimental data, prepared sequentially in the QSim system, were compared. The fidelity results from application of the protocol to these data sets was significantly higher than when comparing the classically simulated and experimental states. From this, it can be concluded that the unitaries implemented in the QSim system differ from those implemented in the classical simulation. However, the unitaries which were implemented in the QSim system were highly-repeatable and well-reproduced each time.

The protocol itself is advantageous as it requires significantly fewer measurements than other protocols such as quantum state tomography, and requires no previous knowledge of the states being compared. As such, it is expected that the protocol can provide a useful verification technique for quantum simulators and computers consisting of several tens of qubits.

Chapter 8

Implementation and Characterisation of a Stimulated Raman Transition Setup

In attempting to demonstrate the advantages quantum simulators may have over their classical counterparts, a huge amount of effort is currently being invested in the realisation of scalable quantum simulation [19, 200, 201]. With regards to trapped-ion platforms, demonstrations of the usefulness of quantum simulators in comparison to their classical counterparts will most likely require the use of larger numbers of ions [202], for example with longer strings of ions or trap geometries creating 2D ion crystals [203, 204]. Although moving to larger numbers of ions has the potential to increase the 'computing power' of a quantum simulator, working with increasing numbers of ions comes with its own technical challenges which must be overcome.

One such challenge which is particularly relevant to the QSim experiment is that of the speed with which entangling gates can be implemented on long strings of ions. It is important that the interaction time required to implement such entangling gates is shorter than the coherence time of the system, in order to allow correlations to propagate over the entire ion string. The coherence time of the optical qubit discussed so far is limited by a number of effects, such as noise from frequency and intensity fluctuations of the 729 nm laser system, as well as environmental noise due to magnetic field fluctuations. In addition to this, the excited state of the optical qubit, the $|D_{5/2}\rangle$ state, has an intrinsic finite lifetime of ~1 s, which is limited by spontaneous decay from this state. Therefore, the entangling gates must occur on timescales which are at least shorter than this lifetime.

However, the optical qubit has a relatively small Lamb-Dicke parameter, on the order of $\eta = 0.041$ for a single ion at the standard trap parameters used in the QSim experiment (where the radial trapping frequency is on the order of $\omega_\mathrm{r} = 2\pi\times\ 2.7\,\mathrm{MHz}$). This results in a relatively low coupling strength between the electronic and motional modes, so limiting the speed of multi-qubit gates. As such, it is prudent to consider whether an alternative qubit can be used for performing quantum operations.

The level scheme of $^{40}\mathrm{Ca}^{+}$ allows a qubit to be encoded in several ways. An alternative approach to the optical qubit is to encode the qubit in the Zeeman levels of the ion's electronic ground state, $|\mathrm{S}_{1/2}, \mathrm{m}_\mathrm{j} = \pm 1/2\rangle$, with the splitting between these levels induced by an externally applied magnetic field. By encoding the qubit in these two ground state Zeeman levels, there is (in the ideal case) no decay due to spontaneous emission from the excited state. As such, encoding the qubit in the ground states of the ion has the potential for a drastically increased coherence time compared to the optical qubit.

For the QSim system, the splitting between the ground states in $^{40}\mathrm{Ca}^{+}$ is relatively small, on the order of 11 MHz[1]. Transitions between these ground states can be driven by RF radiation resonant with the transition. However, in practice there are several disadvantages to this: One of the most relevant to this discussion is that, due to the long wavelength of RF radiation, the Lamb-Dicke parameter is very small, and so entangling gates would occur on significantly longer timescales than those which can be currently implemented using the optical qubit for similar incident radiation powers. Therefore, extremely large incident RF radiation powers would be necessary to drive entangling operations on timescales which are significantly shorter than those currently achievable with the optical qubit. In addition, the wavelength of RF radiation is so large that spatially selective excitation is essentially impossible. Therefore, if a single-ion addressing scheme for the ground-state qubit were to be required in the future, this would not be possible using a highly-focussed beam of RF radiation, as is used for the optical qubit (there are, however, schemes for addressing single ions in frequency space rather than position space using RF radiation and a spatially varying magnetic field [205–207]).

Given all these considerations, it was decided to implement a setup where the qubit was encoded in the ground states of $^{40}\mathrm{Ca}^{+}$, with coherent manipulations of these levels performed using a *stimulated Raman transition* scheme. These Raman transitions use UV-radiation, which has a significantly (on the order of 5 times as much for the parameters used here) increased Lamb-Dicke parameter in comparison to the 729 nm transition used in the optical qubit. This has the potential to allow entangling operations to occur on timescales which are several times shorter than currently achievable with the optical qubit. Raman transitions have already been successfully demonstrated by many groups using wavelengths between 393 nm and 400 nm [84, 208–211].

The following Chapter will present results from the implementation of a new stimulated Raman transition setup in the QSim experiment. The new experimental setup is detailed in Chapter 3. The Chapter will first discuss how the qubit can be encoded in the electronic levels of a $^{40}\mathrm{Ca}^{+}$ ion and manipulated with Raman transitions, as well as the considerations which must be taken into account when using a qubit encoded in an ion, as opposed to the ideal 3-level system discussed in Section 2.4. Following this, experimental data for characterisation measurements of the setup will be presented and discussed. Finally, entangling gates will be experimentally demonstrated on the ground state qubit for up to

---

[1] For the currently applied magnetic field of 4.18 G

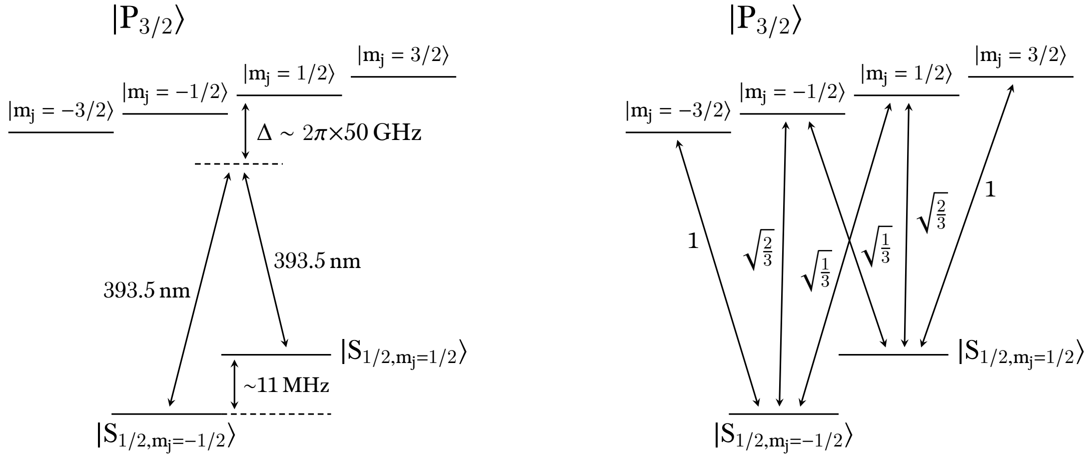

(a) Raman transitions in ^{40}Ca$^+$, including Zeeman splitting of the $|S_{1/2}\rangle$ and $|P_{3/2}\rangle$ levels.

(b) Clebsch-Gordan coupling coefficients between the $|S_{1/2}\rangle$ and $|P_{3/2}\rangle$ states.

Figure 8.1: **Schematic of Raman transitions in ^{40}Ca$^+$.** a) The $|S_{1/2}\rangle$ level is split into two non-degenerate Zeeman levels, and the $|P_{3/2}\rangle$ level is split into four non-degenerate Zeeman levels. The two ground state levels are coupled through two light fields at ~393.5 nm. b) The Clebsch-Gordan coefficients between the $|S_{1/2}\rangle$ and $|P_{3/2}\rangle$ levels, which influence the coupling strengths between these levels. All values are positive.

three ions. Both MS gates and Ising-type interactions will be demonstrated.

8.1 Stimulated Raman Transitions for a Real Atom

In reality, stimulated Raman transitions are more complicated than the ideal 3-level system described in Section 2.4. Figure 8.1 a) illustrates how Raman transitions can be driven in ^{40}Ca$^+$. Here, the two ground state electronic levels of ^{40}Ca$^+$, $|S_{1/2}, m_j = -1/2\rangle$ and $|S_{1/2}, m_j = +1/2\rangle$, are used to encode the qubit states $|0\rangle \equiv |\downarrow\rangle$ and $|1\rangle \equiv |\uparrow\rangle$ respectively. The $|P_{3/2}\rangle$ electronic level is used as the auxiliary state. The ground states couple to the $|P_{3/2}\rangle$ state through electric dipole transitions at wavelengths of ~393.5 nm. It can be seen from Figure 8.1 a) that the $|P_{3/2}\rangle$ state is not a single level, as was assumed in Section 2.4, but is split into four Zeeman levels, and so a 6-level system must actually be considered. Each of these Zeeman levels has a different coupling strength to the ground state levels, which depends on both the Clebsch-Gordan coefficients as well as the polarisation of the driving field. Figure 8.1 b) shows the relevant Clebsch-Gordan couplings between the $|S_{1/2}\rangle$ and $|P_{3/2}\rangle$ levels.

Another way in which the Raman transition in ^{40}Ca$^+$ differs from the ideal scenario explored in Section 2.4 is through decay from the auxiliary level. For the ideal qubit, it was assumed that the decay from this auxiliary state was negligible, however when encoding the qubit in an ion this is no longer true. The $|P_{3/2}\rangle$ level has a lifetime of $\tau = 6.9$ ns [49].

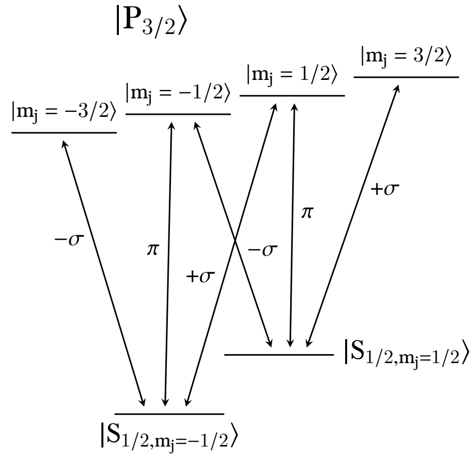

Figure 8.2: **Schematic of the polarisations which drive transitions between the Zeeman levels.** Due to selection rules, transitions between the Zeeman levels must be driven with specific polarisations, shown in the Figure.

The rate at which photons are scattered from this state during a Raman transition is given by $R = \frac{\Gamma}{4\Delta^2}(\Omega_1^2 + \Omega_2^2)$, where $\Gamma = 1/\tau$ is the decay rate, Ω_i is the Rabi frequency of beam i when resonant with the $|S_{1/2}\rangle$ to $|P_{3/2}\rangle$ transition, and Δ is the detuning of the beams from the $|P_{3/2}\rangle$ state (see Section 2.4). Here, any Ω is defined as being 2π multiplied by the inverse of the time taken to go from $|\downarrow\rangle$ to $|\uparrow\rangle$ and return back to $|\downarrow\rangle$ again – that is, $\Omega = 2\pi/T$ with T the time period of the transition. The decay from application of the Raman beams is a significant quantity as it will lead to decoherence of the qubit, and so it is crucial to reduce this rate as much as possible in comparison to the rate at which Raman transitions can be driven. The decay rate from $|P_{3/2}\rangle$ during a Raman transition can be reduced by increasing the Raman detuning Δ, however this in itself can be problematic as moving further away from $|P_{3/2}\rangle$ reduces the Raman Rabi frequency, defined as $\Omega_R = \frac{\Omega_1\Omega_2}{2\Delta}$. As such, a balance must be struck where the dynamics can proceed at a rate which is fast enough in order to not suffer from qubit decoherence due to factors such as magnetic field fluctuations, without suffering from significanct decoherence due to decay from the $|P_{3/2}\rangle$ state.

8.1.1 Polarisation

The polarisation vector of the incident light field, $\boldsymbol{\epsilon}$, plays a crucial role in determining the Rabi frequency of a particular transition between the $|S_{1/2}\rangle$ and $|P_{3/2}\rangle$ Zeeman manifolds [49, 212]. Therefore, for a Raman transition to occur, the polarisation vector of the beams must be chosen such that one or more transitions which couple to both ground states are allowed by selection rules. The following Section will show how the optimal polarisation of the beams can be determined by considering both the polarisation vector of the incident light field as well as its direction of propagation with respect to the magnetic field.

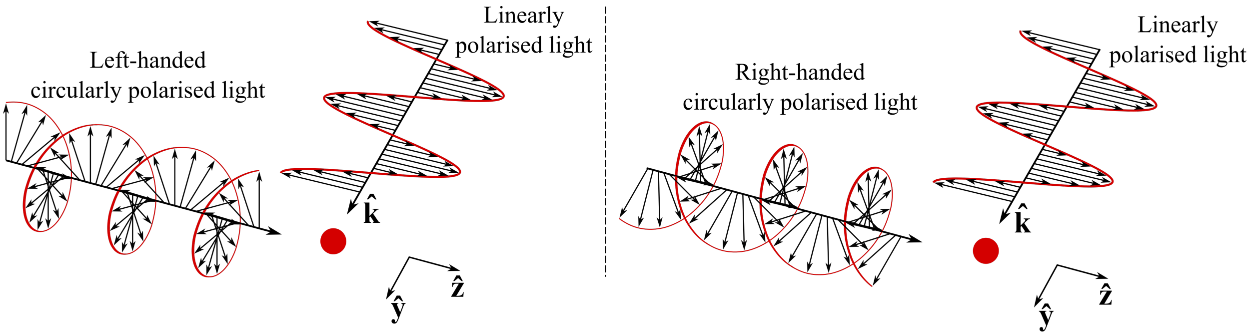

Figure 8.3: **Definition of the propagation and polarisation vectors.** The z-axis is aligned along the quantisation axis. **Left** Linearly polarised light alongside left-handed circularly polarised light with respect to an ion. **Right** Linearly polarised light alongside right-handed circularly polarised light. The vector $\hat{\boldsymbol{k}}$ defines the direction of propagation.

Figure 8.2 shows which polarisations drive the relevant transitions in $^{40}\text{Ca}^{+}$, with π-polarised light driving $\Delta \text{m}_\text{j} = 0$ transitions and circularly polarised light driving $\Delta \text{m}_\text{j} = \pm 1$ transitions. It can be seen that for a Raman transition to occur between the ground states, one beam must have components of π-polarised light, and one beam components of either $\pm\sigma$-polarised light. However, not only the polarisation vector but also the angle the incident light makes to the magnetic field – termed the 'propagation vector' $\hat{\boldsymbol{k}}$ – must be considered when determining whether a specific transition will be driven by the incident light field. An incident light field propagating at an arbitrary angle to the magnetic field axis will now be considered for different polarisations, and the corresponding contributions such a light field makes to driving the $\Delta \text{m}_\text{j} = 0, \pm 1$ transitions will be derived. For reasons of simplicity, the incident light field will be constrained to propagate in the y-z plane.

The polarisation vector of any laser field can be expressed in terms of three polarisation basis vectors. A natural set of basis states to use is that where the three polarisations correspond to the three possible changes in projection of the angular momentum eigenvalue which can occur in a dipole transition – i.e. $\Delta \text{m}_\text{j} = 0, \pm 1$ [211]. Defining the z-axis by the quantisation axis (which is along the magnetic field direction and trap axis), then a suitable set of three basis states can be written as:

$$\boldsymbol{\epsilon}_0 = \begin{pmatrix} 0 \\ 0 \\ 1 \end{pmatrix} = \hat{\boldsymbol{z}}, \quad \boldsymbol{\epsilon}_+ = \frac{1}{\sqrt{2}} \begin{pmatrix} 1 \\ i \\ 0 \end{pmatrix} = \frac{1}{\sqrt{2}}(\hat{\boldsymbol{x}} + i\hat{\boldsymbol{y}}), \quad \boldsymbol{\epsilon}_- = \frac{1}{\sqrt{2}} \begin{pmatrix} 1 \\ -i \\ 0 \end{pmatrix} = \frac{1}{\sqrt{2}}(\hat{\boldsymbol{x}} - i\hat{\boldsymbol{y}}), \tag{8.1}$$

where $\boldsymbol{\epsilon}_0$ drives the $\Delta \text{m}_\text{j} = 0$ transition, $\boldsymbol{\epsilon}_+$ drives the $\Delta \text{m}_\text{j} = +1$ transition, $\boldsymbol{\epsilon}_-$ drives the $\Delta \text{m}_\text{j} = -1$ transition, and $\hat{\boldsymbol{x}}, \hat{\boldsymbol{y}}, \hat{\boldsymbol{z}}$ are the Cartesian unit vectors. An example of this can be seen pictorally in Fig. 8.3. The linearly polarised light in this Figure propagates along $\hat{\boldsymbol{y}}$, while oscillating in $\hat{\boldsymbol{z}}$, with the polarisation vector then given by $\boldsymbol{\epsilon} = \boldsymbol{\epsilon}_0$. The right- and left- handed circularly polarised fields oscillate in the x-y plane while propagating along $\hat{\boldsymbol{z}}$, and as such have polarisation vectors of $\boldsymbol{\epsilon} = \boldsymbol{\epsilon}_\pm$ respectively.

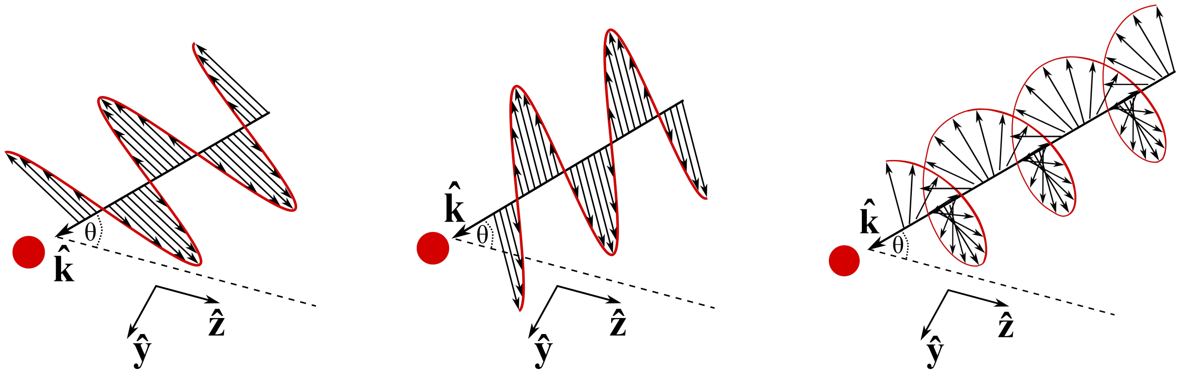

(a) Linearly polarised vector with polarisation in the y-z plane

(b) Linearly polarised vector with polarisation perpendicular to the magnetic field axis

(c) Left-handed elliptically polarised vector.

Figure 8.4: **Polarisation vectors propagating at an arbitrary angle θ to the quantisation axis.** a) A linearly polarised vector with a component of the polarisation vector parallel to the quantisation axis. b) A linearly polarised vector where the polarisation vector is always perpendicular to the quantisation axis. c) An elliptically polarised field. In all Figures, the z-axis is aligned along the quantisation axis.

Any polarisation vector propagating at an arbitrary angle θ to the quantisation axis can then be expressed in terms of these three basis states, where θ is defined as being the angle between the direction of propagation, $\hat{k}$, and the magnetic field axis $\hat{z}$ (shown in Figure 8.4). Three useful examples of this will now be given. The first two of these consider only linearly polarised light, and will be of significance later on in Sections 8.1.3 and 8.3.2. The final example gives the general case for an elliptically polarised beam.

First, consider Fig. 8.4 a), which depicts a polarisation vector linearly polarised in the plane formed by the direction of propagation of the beam and $\hat{z}$ (i.e. the y-z plane). The propagation direction $\hat{\boldsymbol{k}}$ can be resolved along $\hat{y}$ and $\hat{z}$. When $\hat{\boldsymbol{k}}$ is resolved along $\hat{y}$, $\boldsymbol{\epsilon}$ oscillates solely along $\hat{z}$, and so $\boldsymbol{\epsilon} = \sin\theta\hat{z} = \sin\theta\boldsymbol{\epsilon}_0$. When resolved along $\hat{z}$, $\boldsymbol{\epsilon}$ oscillates solely along $\hat{y}$, and so $\boldsymbol{\epsilon} = \cos\theta\hat{y}$. Therefore, using the relation $\hat{y} = \frac{1}{\sqrt{2}i}(\boldsymbol{\epsilon}_+ - \boldsymbol{\epsilon}_-)$, this polarisation vector takes the form:

$$\boldsymbol{\epsilon}_{\mathrm{lin}\|} = \frac{1}{\sqrt{2}i}\cos\theta(\boldsymbol{\epsilon}_+ - \boldsymbol{\epsilon}_-) + \sin\theta\boldsymbol{\epsilon}_0. \tag{8.2}$$

Next consider Figure 8.4 b), where a linearly polarised vector propagates at an angle θ to the quantisation axis, with polarisation *perpendicular* to the plane formed by the quantisation axis and the direction of propagation of the beam. In this scenario, upon resolving the propagation direction into $\hat{y}$ or $\hat{z}$, there is no component of the polarisation vector which is aligned along $\hat{z}$, and so there can be no component of $\boldsymbol{\epsilon}_0$; regardless of the incident angle the propagation vector makes to the quantisation axis, the polarisation vector still oscillates only along $\hat{\boldsymbol{x}}$. Using the relation $\hat{\boldsymbol{x}} = \frac{1}{\sqrt{2}}(\boldsymbol{\epsilon}_+ + \boldsymbol{\epsilon}_-)$, the perpendicular vector can then be expressed as:

$$\boldsymbol{\epsilon}_{\mathrm{lin}\perp} = \frac{1}{\sqrt{2}}(\boldsymbol{\epsilon}_+ + \boldsymbol{\epsilon}_-). \tag{8.3}$$

That is, there is no component of the field that can drive the $\Delta\mathrm{m} = 0$ transition, with this field driving the $\Delta\mathrm{m} = \pm 1$ transitions with equal intensity. It should be noted that this expression has no dependence on θ as there is no polarisation component in the y-z plane.

Finally consider the most general case shown in Figure 8.4 c), where an elliptically polarised vector propagates at an angle of θ to the quantisation axis. There are three main components to this vector: First is the component along $\hat{\boldsymbol{x}}$ which, as was discussed for $\boldsymbol{\epsilon}_{lin\perp}$, has no dependence on θ. The other two components are those components resolved through θ to lie along $\hat{\boldsymbol{y}}$ and $\hat{\boldsymbol{z}}$. Combining these three components yields:

$$\boldsymbol{\epsilon}_{\mathrm{el}} = E_1\hat{\boldsymbol{x}} + E_2\cos\theta e^{i\phi}\hat{\boldsymbol{y}} + E_2\sin\theta e^{i\phi}\hat{\boldsymbol{z}}, \tag{8.4}$$

where E_1 and E_2 are the magnitudes of the polarisation components which are orthogonal to $\hat{\boldsymbol{k}}$, and $e^{i\phi}$ the relative phase between these two components. By using the relations $\hat{\boldsymbol{x}} = \frac{1}{\sqrt{2}}(\boldsymbol{\epsilon}_+ + \boldsymbol{\epsilon}_-)$, $\hat{\boldsymbol{y}} = \frac{1}{\sqrt{2}i}(\boldsymbol{\epsilon}_+ - \boldsymbol{\epsilon}_-)$, and $\hat{\boldsymbol{z}} = \boldsymbol{\epsilon}_0$, Equation 8.4 can be expressed as:

$$\boldsymbol{\epsilon}_{\mathrm{el}} = \frac{E_1}{\sqrt{2}}(\boldsymbol{\epsilon}_+ + \boldsymbol{\epsilon}_-) + \frac{E_2}{\sqrt{2}i}\cos\theta e^{i\phi}(\boldsymbol{\epsilon}_+ - \boldsymbol{\epsilon}_-) + E_2\sin\theta e^{i\phi}\boldsymbol{\epsilon}_0,$$

$$\Longrightarrow \boldsymbol{\epsilon}_{\mathrm{el}} = \frac{1}{\sqrt{2}}(E_1 - iE_2\cos\theta e^{i\phi})\boldsymbol{\epsilon}_+ + \frac{1}{\sqrt{2}}(E_1 + iE_2\cos\theta e^{i\phi})\boldsymbol{\epsilon}_- + E_2\sin\theta e^{i\phi}\boldsymbol{\epsilon}_0. \tag{8.5}$$

It can be seen that Equation 8.5 reduces to Equations 8.2 & 8.3 for the cases where $E_1 = 0$ and $E_2 = 0$ respectively.

As mentioned previously, for Raman transitions to occur one beam must have a component of the polarisation parallel to the magnetic field to drive the $\Delta\mathrm{m_j} = 0$ transition, and the second beam must have a polarisation component perpendicular to the magnetic field, to drive either of the $\Delta\mathrm{m_j} = \pm 1$ transitions. An example of polarisations and incident angles that would then maximise the coupling strength (i.e. such that all the light from both beams is used in driving the transition) would then be: One beam with polarisation $\boldsymbol{\epsilon}_{\mathrm{lin}||}$ with an incident angle of $\pi/2$ (so driving only the $\Delta\mathrm{m_j} = 0$ transition), and the second beam with right-handed circularly polarised light at an incident angle of $\theta = 0$ – i.e. $\boldsymbol{\epsilon}_{\mathrm{el}}$ with $E_1 = E_2 = \frac{1}{\sqrt{2}}$ and $\phi = \pi/2$ (so driving only the $\Delta\mathrm{m_j} = +1$ transition).

The next Section will introduce another factor that must be taken into consideration before deciding which polarisations should be used for the driving fields.

8.1.2 AC-Stark Shifts

In reality, driving the Raman transitions with polarisations yielding maximum coupling between the ground states is not necessarily the best solution. In particular, differential AC-Stark shifts arising from application of the Raman beams – that is, AC-Stark shifts which shift the $|\mathrm{S}_{1/2}, \mathrm{m_j} = -1/2\rangle$ and $|\mathrm{S}_{1/2}, \mathrm{m_j} = +1/2\rangle$ states by different amounts – can be highly problematic [39, 208, 211]. Differential AC-Stark shifts can be minimised by using specific polarisations for the driving beams.

The light shift on the upper and lower states, $|\downarrow\rangle$ and $|\uparrow\rangle$, is given respectively by:

$$\delta^{\mathrm{AC}}_{|\uparrow\rangle} = \frac{\Omega^2_{\sigma^+,|\uparrow\rangle} + \Omega^2_{\sigma^-,|\uparrow\rangle} + \Omega^2_{\pi}}{4\Delta}, \qquad \delta^{\mathrm{AC}}_{|\downarrow\rangle} = \frac{\Omega^2_{\sigma^+,|\downarrow\rangle} + \Omega^2_{\sigma^-,|\downarrow\rangle} + \Omega^2_{\pi}}{4\Delta}, \tag{8.6}$$

where $\Omega_{\sigma^\pm,k}$, for $k = |\uparrow\rangle, |\downarrow\rangle$, is the resonant Rabi frequency on the transition between the k and $|\mathrm{P}_{3/2}\rangle$ Zeeman levels driven by $\sigma^\pm$ polarised light, and Ω_π is the resonant Rabi frequency on the transitions driven by π-polarised light. Ω_π is the same for both $|\downarrow\rangle$ and $|\uparrow\rangle$, as these states couple with identical Clebsch-Gordan coefficients to the $|\mathrm{P}_{3/2}, \mathrm{m_j} = -1/2\rangle$ and $|\mathrm{P}_{3/2}, \mathrm{m_j} = +1/2\rangle$ states respectively (as can be seen from Figure 8.2).

If these light shifts are not the same for both levels, the qubit can acquire an additional, overall phase given by:

$$\phi_{\mathrm{AC}} = (\delta^{\mathrm{AC}}_{|\uparrow\rangle} - \delta^{\mathrm{AC}}_{|\downarrow\rangle})\tau = \frac{(\Omega^2_{\sigma^+,|\uparrow\rangle} + \Omega^2_{\sigma^-,|\uparrow\rangle} - \Omega^2_{\sigma^+,|\downarrow\rangle} - \Omega^2_{\sigma^-,|\downarrow\rangle})\tau}{4\Delta}, \tag{8.7}$$

where τ is the length of time the beam is applied for. Under such circumstances, the quantum phase of qubit superpositions or of multi-ion entangled states evolves not only according to the intended gate operations, but also undergoes an additional rapid phase evolution which can be seen to be dependent on the intensity of the two beams [208]. As such, the polarisation of the beams should be chosen such that the differential shift is reduced to zero.

A straightforward way to drive the Raman transitions with no differential AC-Stark shift is to use linear polarisation for both beams [211]. From Equations 8.2 and 8.3, it can be seen that both parallel and perpendicular linearly polarised light drive the $\Delta \mathrm{m_j} = \pm 1$ transitions with equal strengths. In this situation, $\Omega^2_{\sigma^+,|\uparrow\rangle} = \Omega^2_{\sigma^-,|\downarrow\rangle}$ and $\Omega^2_{\sigma^-,|\uparrow\rangle} = \Omega^2_{\sigma^+,|\downarrow\rangle}$ due to the symmetric Clebsch-Gordan coefficients of these transitions. As such, the AC-Stark shifts on the two ground states from coupling to the Zeeman levels of the $|\mathrm{P}_{3/2}\rangle$ level will cancel, and ϕ_{AC} will become 0.

Even though this choice of polarisation is not optimal for coupling between the ground states, and so the Raman Rabi frequency will be reduced, this is the arrangement chosen for the experiments which will be presented in Section 8.3 in order to reduce any unwanted effects from differential AC-Stark shifts.

8.1.3 Raman Rabi Frequency

The Raman Rabi frequency, Ω_R, derived in Section 2.4, is given by $\Omega_\mathrm{R} = \Omega_1\Omega_2/2\Delta$, where Ω_i is the (resonant) Rabi frequency of beam i, and Δ the (assumed equal) detuning of the beams from resonance. This equation can also be expressed in terms of the parameters of the two Raman beams, such as the beam waists, propagation angles, and powers. The Rabi frequency for any general transition driven by an oscillating electric field, $\boldsymbol{E} = |\boldsymbol{E}_0|\boldsymbol{\epsilon}\cos(\omega t)$, with $\boldsymbol{\epsilon}$ the polarisation vector, is given by [212]:

$$\Omega = \frac{e|\boldsymbol{E}_0|}{\hbar}\langle 1|\boldsymbol{r}\cdot\boldsymbol{\epsilon}|2\rangle, \tag{8.8}$$

with $\boldsymbol{r}$ the position of the electron. For simplicity, the Rabi frequencies for a linearly polarised vector with polarisation in the y-z plane (now referred to as Ω_1), and for a linearly polarised vector with polarisation perpendicular to the magnetic field axis (referred to as Ω_2), propagating at angles θ_1 and θ_2 respectively to $\hat{z}$ (see Figure 8.4) will now be considered[2]. As such, the two Rabi frequencies are:

$$\Omega_1 = \frac{e}{\hbar}\left(\frac{1}{\sqrt{2}i}\cos\theta_1\langle 1|\boldsymbol{r}\cdot(\boldsymbol{\epsilon}_+ - \boldsymbol{\epsilon}_-)|2\rangle + \sin\theta_1\langle 1|\boldsymbol{r}\cdot\boldsymbol{\epsilon}_0|2\rangle\right)\sqrt{I_1}, \tag{8.9}$$

$$\Omega_2 = \frac{e}{\sqrt{2}\hbar}\langle 1|\boldsymbol{r}\cdot(\boldsymbol{\epsilon}_+ + \boldsymbol{\epsilon}_-)|2\rangle\sqrt{I_2} \tag{8.10}$$

where I_i is the intensity of beam i. Considering that, for a Raman transition to occur in $^{40}\mathrm{Ca}^+$, one beam must drive a $\Delta \mathrm{m_j} = 0$ transition and the other a $\Delta \mathrm{m_j} = \pm 1$ transition, the Raman Rabi frequency therefore becomes:

$$\Omega_\mathrm{R} = \frac{1}{2\Delta}\left(\frac{e}{\hbar}\right)^2\frac{\sin\theta_1}{\sqrt{2}}\mathcal{D}^2\sqrt{I_1 I_2}, \tag{8.11}$$

where $\mathcal{D}$ is the reduced dipole matrix element of the $|1\rangle$ to $|2\rangle$ transition. For the $|\mathrm{S}_{1/2}\rangle$ to $|\mathrm{P}_{3/2}\rangle$ transition in $^{40}\mathrm{Ca}^+$, the magnitude of this value can be calculated to be $\mathcal{D} = 4.091a_0$, where a_0 is the Bohr radius [213]. Finally, the intensity of the beams can be expressed in

---

[2] This treatment can be straightforwardly extended to two general, elliptically polarised beams by using Equation 8.5

terms of their power and respective beam waists. Assuming the ion sits in the centre of the beam waists, each of which is elliptical in shape, the Raman Rabi frequency becomes:

$$\Omega_{\mathrm{R}} = \frac{1}{2\Delta}\left(\frac{4.091 a_0 e}{\hbar}\right)^2 \frac{\sin\theta_1}{\sqrt{2}\pi}\sqrt{\frac{P_1 P_2}{w_1^x w_1^y w_2^x w_2^y}}, \tag{8.12}$$

where P_i is the power in beam i, which has x-waist w_i^x and y-waist w_i^y.

8.2 Experimental Protocol

Having now discussed the main considerations which should be taken into account when working with Raman transitions in an ion, as opposed to the ideal 3-level system presented in Section 2.4, the following section will give a brief overview of the experimental protocol used to enable Raman transitions to be driven between the ground states in $^{40}\mathrm{Ca}^+$ in the QSim system.

The Raman transitions can be driven by two laser beams detuned from the $|\mathrm{S}_{1/2}\rangle$ to $|\mathrm{P}_{3/2}\rangle$ dipole transition by approximately $\Delta = 2\pi \times 308\,\mathrm{GHz}$. For detailed descriptions of the setup, operation, and locking schemes of the lasers and cavity used to produce these two beams, refer to Section 3.2. For a detailed description of the optical setup, see Section 3.3. There are several differences in the experimental protocol used to control Raman transitions in the QSim system, compared to that which controls the 729 nm transitions. The following Section will now explain the typical steps which are used in performing coherent manipulations on the ground state qubit with Raman transitions.

Qubit Initialisation/State Preparation The qubit is first initialised in the $|\downarrow\rangle = |\mathrm{S}_{1/2}, \mathrm{m_j} = -1/2\rangle$ state (this is in contrast to the optical qubit, where typically the qubit is initialised in the $|\mathrm{S}_{1/2}, \mathrm{m_j} = +1/2\rangle$ state). This state was chosen for qubit initialisation as, when detection is performed the 'ground' state ($|\downarrow\rangle = |\mathrm{S}_{1/2}, \mathrm{m_j} = -1/2\rangle$) fluoresces while the 'excited' ($|\downarrow\rangle = |\mathrm{S}_{1/2}, \mathrm{m_j} = +1/2\rangle$) state remains dark (due to the qubit readout scheme described below). This matches the ground/excited state fluorescence of the optical qubit, and so allowed easier integration of the ground state qubit into the experimental control software. Qubit initialisation is performed using optical pumping on the 729 nm transition. The efficiency of this state preparation was measured by taking 2400 repeat measurements on 5 ions and averaging over the results. The measured fidelity was then calculated to be 99.8±0.3%, with the error calculated from the standard deviation of the measurements.

Qubit Readout The qubit readout process when using Raman transitions to perform coherent operations is more complicated than with the optical qubit. With the optical qubit, readout is performed using 397 nm light, with only the 'ground' $|\downarrow\rangle = |\mathrm{S}_{1/2}\rangle$ state scattering photons, so being recorded as 'bright', while the 'excited' $|\uparrow\rangle = |\mathrm{D}_{5/2}\rangle$ state remains dark. When using Raman transitions with the ground state qubit, both of the qubit levels can scatter photons near 397 nm. Therefore, in order to discriminate between $|\downarrow\rangle = |\mathrm{S}_{1/2}, \mathrm{m_j} = -1/2\rangle$ and $|\uparrow\rangle = |\mathrm{S}_{1/2}, \mathrm{m_j} = +1/2\rangle$, the population in $|\uparrow\rangle$ must first be optically transferred to the $|\mathrm{D}_{5/2}\rangle$ state (a process referred to as 'shelving'), before laser flourescence detection with the 397 nm beam can be performed. The $|\downarrow\rangle$ state therefore fluoresces, with the $|\uparrow\rangle$ state remaining dark.

Experimental Sequence A typical experimental sequence is very similar to that performed with the optical qubit, and is comprised of four main steps: (a) Doppler cooling is performed on the ion for 3 ms (b) the ion is cooled close to the ground state of the radial vibrational modes through resolved sideband cooling on the 729 nm transition (only necessary when using the counterpropagating beam geometry) (c) the qubit is initialised in the $|\downarrow\rangle = |\mathrm{S}_{1/2}, \mathrm{m_j} = -1/2\rangle$ state (d) coherent manipulations are performed using Raman transitions between the ground state sublevels (e) the population in the $|\mathrm{S}_{1/2}, \mathrm{m_j} = +1/2\rangle$ qubit level is shelved to the $|\mathrm{D}_{5/2}, \mathrm{m_j} = +5/2\rangle$ level (f) state readout is performed through laser induced fluorescence on the 397 nm $|\mathrm{S}_{1/2}, \mathrm{m_j} = -1/2\rangle$ to $|\mathrm{P}_{1/2}\rangle$ transition, where population in the $|\mathrm{S}_{1/2}, \mathrm{m_j} = -1/2\rangle$ level will scatter photons and be recorded as 'bright', while the population which has been transferred from the $|\mathrm{S}_{1/2}, \mathrm{m_j} = +1/2\rangle$ state will subsequently be dark.

8.3 Characterisation of the Raman Transitions

Having detailed the optical setup and experimental protocol, this Section will now focus on presenting results from various characterisation measurements of the Raman transition setup.

8.3.1 Beam Size

Firstly, an external measurement of the beam spot size at the position of the trap centre was measured. A beam profiler[3] was placed at a distance from the outcoupling lens equivalent to the position of the trap centre and the profile of the beam recorded. Figure 8.5 shows the results of this measurement, with the spot size of the beam found from a least squares fit to the data to be $175\,\mu\mathrm{m} \times 173\,\mu\mathrm{m}$. Here the spot size is defined to be the radial distance from the central point of maximum irradiance to the point where the beam irradiance has fallen to $1/e^2$ of its original value.

---

[3] Thorlabs Camera Beam Profiler BC106-VIS

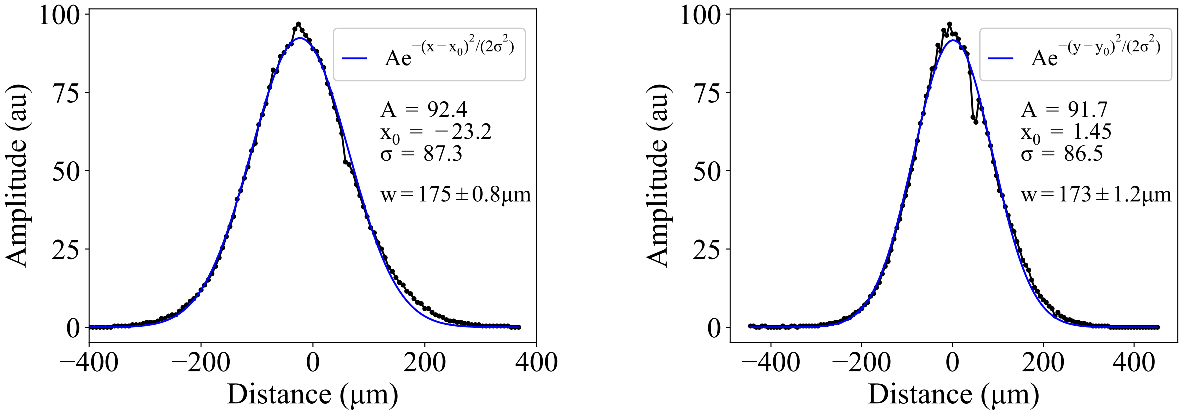

(a) Beam profile in x-direction

(b) Beam profile in y-direction

Figure 8.5: **Beam Profile measurements of the copropagating Raman beams**. The beam waist was found to be w=175±0.8 μm along x and w=173±1.2 μm along y. These values were extracted using a least-squares Gaussian fit to the data. Errors are determined from the covariance matrix of the fit.

8.3.2 Polarisation

It was previously mentioned in Section 8.1.2 that a linear polarisation for both beams would be chosen in order to minimise any differential AC-Stark shift between the two qubit levels, with the question then remaining as to which linear polarisations to use. Both a $\Delta m = 0$ and $\Delta m = \pm 1$ transition must be driven in order for a Raman transition to be achieved, and so it is necessary to use linearly polarised light which possesses both of these components.

From Equation 8.3 it can be seen that for a linear polarisation which has a polarisation vector orthogonal to the quantisation axis (for the geometry here this will correspond to vertically polarised light), no component of this polarisation will drive the $\Delta m = 0$ transition, and so all of this polarisation will be used in driving the $\Delta m = \pm 1$ transitions with equal strength. Therefore, the $|S_{1/2}, m_j = -1/2\rangle$ to $|P_{3/2}, m_j = +1/2\rangle$ transition will be driven with an intensity of 50% of the total intensity. This polarisation can then be used along with a linear polarisation which will drive the $\Delta m = 0$ transition with highest efficiency.

Equation 8.2 shows that linearly polarised light which has a polarisation vector parallel to the quantisation axis (for the geometry here corresponding to horizontally polarised light), and propagating at 60° to the trap axis (necessary due to the geometry of the vacuum chamber, see Section 3.3), will drive the $\Delta m = 0$ transition with an intensity 75% of the total incident intensity.

Therefore, the polarisations were chosen such that one beam has a polarisation vector parallel to the quantisation axis, and one with a polarisation vector orthogonal to it, so driving the Raman transition with a combined reduced intensity of 37.5%.

8.3.3 Spontaneous Emission

Spontaneous emission from the auxiliary $|P_{3/2}\rangle$ state, as mentioned in Section 8.1, can be a significant source of error during gate operations, with several possible consequences:

- Dephasing – During spontaneous emission, the qubit can return to $|S_{1/2}\rangle$ with a branching ratio of ~47% [214]. However, during this process the phase of the coherent time evolution is, in essence, 'reset' and so the coherence of the system will be lost.
- Spin flips – Spontaneous emission can also result in the qubit transitioning to another state, with branching ratio ~53% [214].

The experimental procedure for measuring the spontaneous emission rate from the auxiliary level for a standard set of experimental parameters is the following: the qubit is first prepared in $|S_{1/2}, m_j = +1/2\rangle$ and a coherent 729 nm π-pulse on the $|S_{1/2}, m_j = +1/2\rangle$ to $|D_{5/2}, m_j = +5/2\rangle$ transition is applied. This will move all the population into the excited state, and so qubit readout at this point will produce an excitation equal to 1. A single Raman beam is then applied to the qubit after state preparation but before application of the 729 nm π-pulse, and the excitation measured as a function of the length of time this beam is applied for. As no Raman transitions can occur from the presence of only one beam, any change in the observed excitation will be as a direct result of population loss due to spontaneous emission from the $|P_{3/2}\rangle$ state.

Figure 8.6 shows a measurement of this decay for five ions due to the presence of a single beam which had passed through AOM 2 (driven at a fixed frequency of 105 MHz). The rate of spontaneous emission can be extracted from fitting an exponential to the data and was found to be $R_1 = \gamma = 30.3 \pm 0.3\,\mathrm{s}^{-1}$ per ion due to this beam (assuming the rate of spontaneous emission for each ion is uncorrelated).

From Equation 2.79, the Raman Rabi frequency is given by $\Omega_R = \Omega_1\Omega_2/2\Delta$, where Ω_i is the proportional to the square-root of of the intensity of each beam, i, which *goes towards driving the transition.* Specifically, it is not equal to the total power of the beam due to the polarisations (see Section 8.3.2). In the experiment, Ω_R is maximised by adjusting the relative power in the two paths such that $\Omega_1 \simeq \Omega_2$. As such, an estimated decay rate for the second Raman beam can be calculated from R_1 to be $R_2 = R_1 \times \left(\frac{0.5}{0.75}\right) = 20.2 \pm 0.2\,\mathrm{s}^{-1}$.

Assuming that the spontaneous emission effect from both beams is additive, then the single-ion rate of decay from the auxiliary state during a two-photon Raman transition is:

$$R = 50.5 \pm 0.4\,\mathrm{s}^{-1}, \tag{8.13}$$

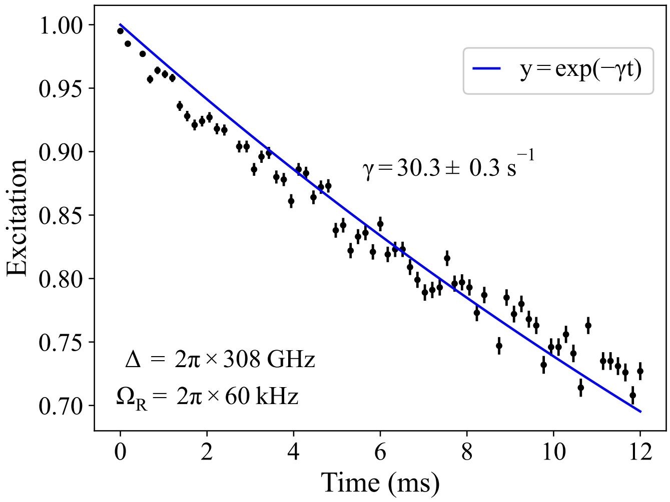

Figure 8.6: **Measured decay from the auxiliary state for 5 ions.** The resultant excitation after the application of one of the Raman beams is plotted as a function of the length of time the beam is applied (black points). A weighted least-squares exponential fit to the decay (blue line) gives a decay rate of γ = 30.3±0.3 s^{-1} per ion for a Raman Rabi frequency of $\Omega_R = 2\pi \times 60$ kHz and a detuning of $\Delta = 2\pi \times 308$ GHz. The data was taken using 200 repeats. Error bars are calculated from quantum projection noise, with the error in the decay rate extracted from the covariance matrix of the fit.

corresponding to a qubit lifetime on the order of τ = 19.8±0.2 ms. As the Raman Rabi frequency for this measurement is $\Omega_\mathrm{R} = 2\pi\times60$ kHz, this shows that a single ion will make ~1200 complete oscillations between the two states before spontaneously emitting a photon.

This value can also be compared to the theoretical decay rate expected from Equation 2.83, under the assumption that $|\Delta| \gg \Gamma, \omega_0$. This is given by:

$$R \simeq \frac{\Gamma}{4}\left(\frac{\Omega_1^2}{\Delta^2} + \frac{\Omega_2^2}{\Delta^2}\right) = \frac{\Gamma\Omega_R}{2\Delta}\left(\frac{1}{0.75} + \frac{1}{0.5}\right) = 47.1\,\mathrm{s}^{-1}, \tag{8.14}$$

which is very close to the estimate of the measured spontaneous decay rate given above. Inconsistencies between these two values is most likely due to inaccuracies in the amount of power sent into the two paths. The errors induced by spontaneous emission grow accordingly with increasing system size, with reduction of these errors only possible by increasing the detuning from the auxiliary $|\mathrm{P}_{3/2}\rangle$ state.

8.3.4 Differential AC-Stark shift

As discussed in Section 8.1.2, the AC-Stark shift experienced by the $|\mathrm{S}_{1/2}, \mathrm{m_j} = -1/2\rangle$ and $|\mathrm{S}_{1/2}, \mathrm{m_j} = +1/2\rangle$ levels may be different, which will lead to a differential shift between the

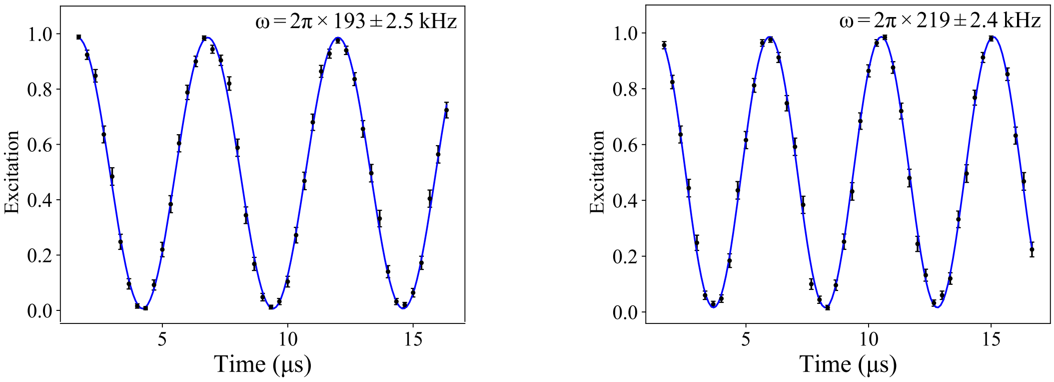

(a) AC-Stark flops on the $|\uparrow\rangle$ state from the top beam path into the vacuum vessel.

(b) AC-Stark flops on the $|\downarrow\rangle$ state from the top beam path into the vacuum vessel.

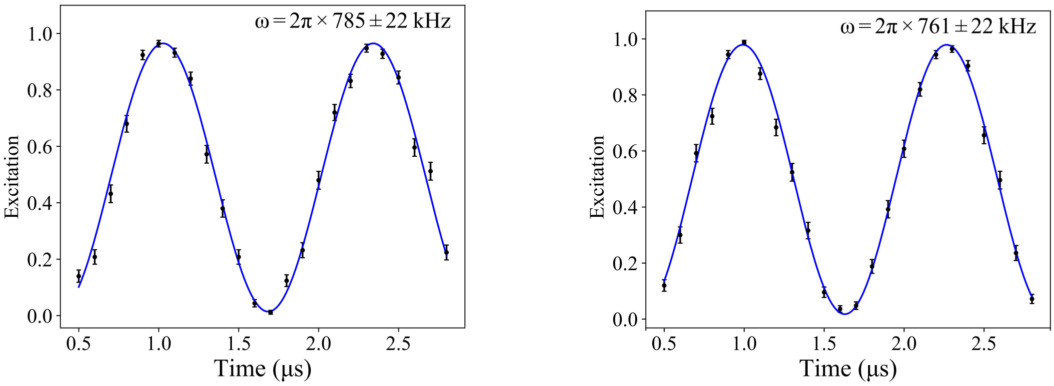

(c) AC-Stark flops on the $|\uparrow\rangle$ state from the lower path into the vacuum vessel.

(d) AC-Stark flops on the $|\downarrow\rangle$ state from the lower path into the vacuum vessel.

Figure 8.7: **AC-Stark flops**. Shown in the Figures are the Ramsey fringe signals arising from application of a single Raman beam during the wait-time of a Ramsey experiment using the 729 nm transition (see text).

two levels.

The differential AC-Stark shift between the two levels from one beam can be probed by using a Ramsey experiment on the 729 nm transition. The qubit is first optically pumped to either the $|\mathrm{S}_{1/2}, \mathrm{m_j} = -1/2\rangle$ or $|\mathrm{S}_{1/2}, \mathrm{m_j} = +1/2\rangle$ state using the 729 nm transition. It is then prepared in a superposition of either $1/\sqrt{2}(|\mathrm{S}_{1/2}, \mathrm{m_j} = -1/2\rangle + |\mathrm{D}_{5/2}, \mathrm{m_j} = +3/2\rangle)$, or $1/\sqrt{2}(|\mathrm{S}_{1/2}, \mathrm{m_j} = +1/2\rangle + |\mathrm{D}_{5/2}, \mathrm{m_j} = +5/2\rangle)$ by application of a $\pi/2$ pulse with the 729 nm laser. After a wait-time of τ, a final $\pi/2$ pulse is applied. During the wait-time τ, one of the Raman beams is applied to the ion. This leads to a Ramsey fringe signal as the duration of the wait-time is varied, called 'AC-Stark flops', shown in Figure 8.7. Figure 8.7 a) and b) shows the AC-Stark flops due to the first Raman beam (entering into the vacuum vessel from the top) on the $|\uparrow\rangle$ and $|\downarrow\rangle$ states respectively, and in c) and d) the AC-Stark flops caused by the second Raman beam (entering into the vacuum vessel from the bottom) on the $|\uparrow\rangle$ and $|\downarrow\rangle$ states respectively. The time-period of this fringe signal, τ_{AC}, gives access to the frequency shift induced by the presence of the single Raman beam through $\omega_{AC} = 2\pi/\tau_{\mathrm{AC}}$. The differential AC-Stark shift can then be calculated by determining ω_{AC} for $|\uparrow\rangle$ and $|\downarrow\rangle$, and subtracting the two values.

The measurement was performed seperately for the path entering the vacuum chamber from the top viewport, and for the path entering the chamber through the bottom viewport. For the top path, a differential AC-Stark shift of $2\pi \times 26.6 \pm 3.5\,\mathrm{kHz}$ was found, and for the bottom path a shift of $2\pi \times 23.4 \pm 31\,\mathrm{kHz}$. Given that the Raman Rabi frequency for which most measurements are performed is $\Omega_{\mathrm{R}} \simeq 2\pi \times 60\,\mathrm{kHz}$, then for the top path there is a differential shift present on the order of 30% of Ω_{R}. For the bottom path, given the error, it is difficult to conclude whether there is a statistically significant AC-Stark shift. Any shifts that do exist can be minimised by proper adjustment of the polarisation.

If there is any residual differential AC-Stark shift, then changes in the beam intensities, such as fluctuations in the output intensity of the laser or from beam pointing, can lead to phase fluctuations in the qubit, which can be a strong source of decoherence [208]. To minimise these effects, both the beam passing through AOM 1 and the one through AOM 2 have been intensity stabilised before entering the vacuum chamber using a home-built Sample and Hold intensity stabilisation circuit, as discussed in Appendix D.2. In the future, it will also be advantageous to implement an intensity stabilisation system for the beam passing through AOM 3.

8.3.5 Coherence Measurements between the two Ground States

An important quality of the ground state qubit which should be measured is that of the coherence time. The coherence time can be probed by performing Ramsey experiments on a superposition of the two states $|\mathrm{S}_{1/2}, \mathrm{m_j} = -1/2\rangle$ and $|\mathrm{S}_{1/2}, \mathrm{m_j} = +1/2\rangle$ (see Section 2.3.1). Such experiments not only allow access to the coherence time of the qubit, but can in addition provide insights into potential noise processes which can reduce the qubit coherence. As the qubit coherence can be affected by instabilities between the beam paths, the coherence of both the copropagating fields and the counterpropagating fields was probed.

Coherence Measurements for the Copropagating Fields

In order to perform these measurements, the qubit was first optically pumped into the $|\mathrm{S}_{1/2}, \mathrm{m_j} = -1/2\rangle$ state, before being prepared in a superposition of $|\mathrm{S}_{1/2}, \mathrm{m_j} = -1/2\rangle$ and $|\mathrm{S}_{1/2}, \mathrm{m_j} = +1/2\rangle$ using a global Raman $\pi/2$ pulse driven by the copropagating fields. After a wait-time of τ, a final $\pi/2$ pulse was applied, the phase of which was scanned. By fitting a least-squares sine to the phase scan, the contrast at that particular wait-time τ – given by the amplitude of the fit – can be extracted.

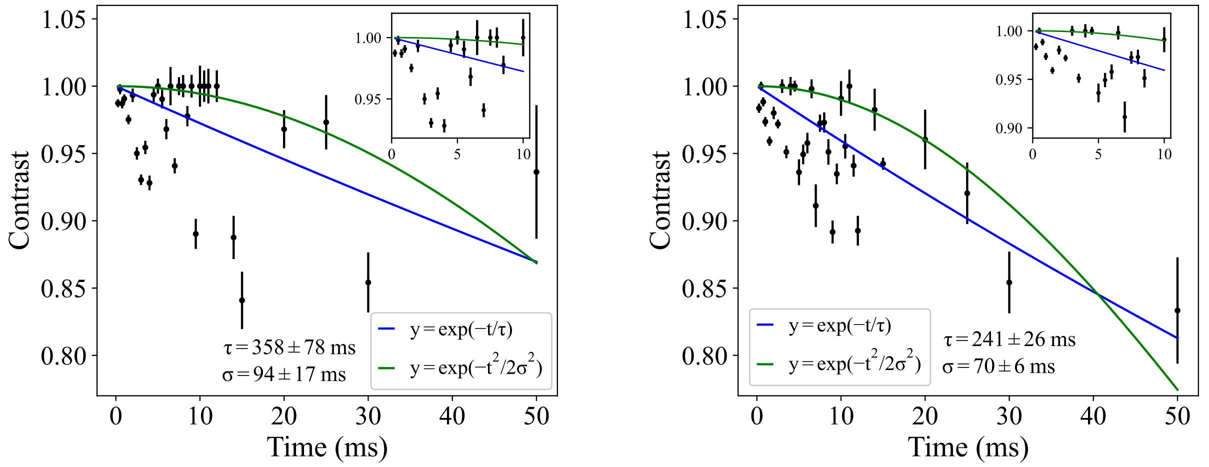

(a) Coherence measurement with copropagating fields

(b) Coherence measurement with counter-propagating fields

Figure 8.8: **Coherence time measurements on the ground state qubit using Raman transitions**. The measured contrast (black points) is fitted with a least-squares exponential decay (blue line) and least-squares Gaussian decay (green line) in order to extract estimates for the coherence time. a) Measurement using copropagating fields, with an extracted coherence time from the exponential fit of 358±78 ms and from the Gaussian fit of 94±17 ms. **Inset**: Magnified plot of the contrast at short wait-times. b) Measurement using counterpropagating fields, with a resulting coherence time from the exponential fit of 241±26 ms and from the Gaussian fit of 70±6 ms. **Inset**: Magnified plot of the contrast at short wait-times. For both data sets, 3 ions were used with 80 repeats. Errors bars are extracted from the covariance matrix of the sine fit used to extract the contrast (see text).

Figure 8.8 a) shows the extracted contrast as a function of the wait-time τ in-between $\pi/2$ pulses. Both an exponential fit and a Gaussian fit to the decay of the measured contrast have been performed in order to provide estimates for the coherence time of the system. An exponential decay is expected for high-frequency noise processes, with a Gaussian decay expected for lower-frequency noise [122]. An exponential fit to the decay of the measured contrast provided an estimated coherence time of 358±78 ms, with the Gaussian decay providing an estimated coherence time of 94±17 ms.

It is difficult to discern whether one of the decay profiles is a better fit to the data, especially as measurements at longer wait-times are susceptible to DC effects such as movements of the lift. Although not decreasing the contrast, this causes problems with performing an accurate least-squares sine fit to the phase scan. However, it can be seen that both of these estimates for the coherence time are significantly larger than the coherence of the optical qubit probed with the 729 nm transition (see Section 3.4.2). The main reason behind this increase in coherence is that the qubit used with the Raman transitions is encoded in two Zeeman levels of the same ground state through using a two-photon process. This means that the qubit is relatively insensitive to noise from the laser, and so the only major contribution to its decoherence is from magnetic field fluctuations.

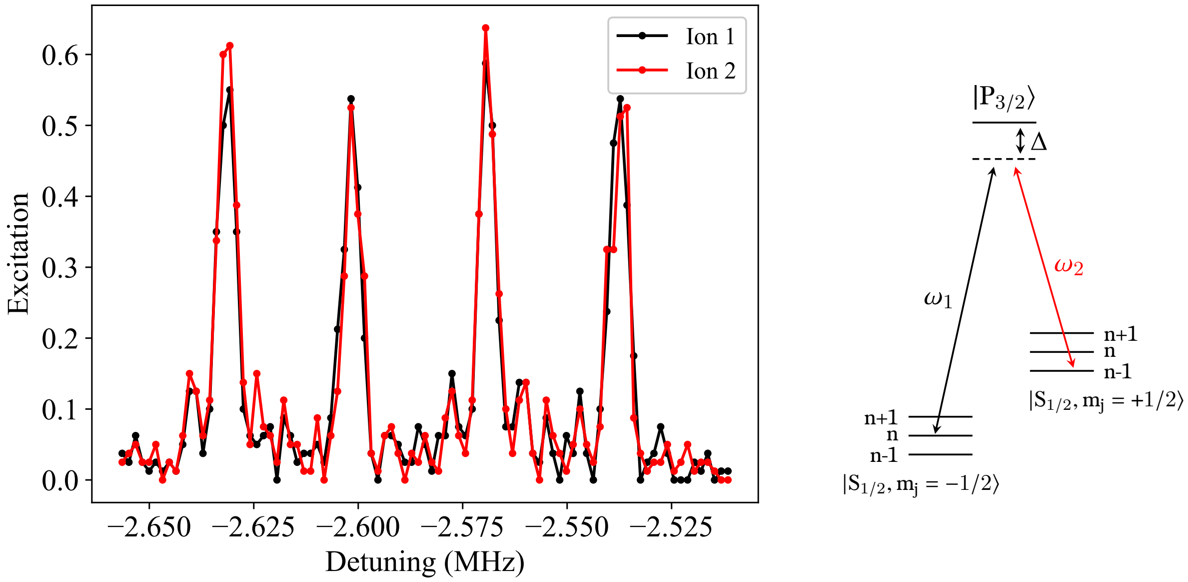

Figure 8.9: **Red-sideband spectrum**. Motional spectrum of the radial modes for two ions using the counterpropagating fields. **Left**: The measured excitation of each ion is plotted as a function of the frequency detuning of the second Raman beam, ω_2, from the resonant carrier frequency. **Right**: Schematic of a red-sideband transition as driven with the Raman beams. ω_1 is fixed, while ω_2 is free to be scanned. The measurement was performed at a detuning from the auxiliary $|P_{3/2}\rangle$ level on the order of $\Delta = 2\pi\times$ 20 GHz, with 80 repeats taken.

Coherence Measurements for the Counterpropagating Fields

The same procedure was then repeated where instead the Ramsey experiments were driven using the counterpropagating fields. For this arrrangement, an additional 6 ms of sideband cooling was performed following Doppler cooling and preceeding the Ramsey experiment. As the counterpropagating fields couple to the motion of the ion, there is the possibility for additional decoherence from motional decoherence of the qubit. In addition, the counterpropagating paths enter the chamber having traversed two different beam paths. There is therefore the potential for decoherence to occur from fluctuations in the laser phase between the two paths.

Figure 8.8 b) shows the measured contrast of the qubit, with associated exponential and Gaussian fits to the decay of this contrast. The coherence time extracted from the exponential fit was found to be 241±26 ms and from the Gaussian fit was found to be 70±6 ms. These values are, within error, reasonably consistent with the coherence times found using the copropagating fields. As such, it can be assumed that there is no significant limitation to the lifetime of the qubit from either motional decoherence, or from phase instabilities between the two beam paths.

8.3.6 Sideband spectrum of two qubits

As the counterpropagating fields couple to the radial modes of motion, it is then possible to probe the radial sidebands using this setup. To do this, the system was initialised in $|\mathrm{S}_{1/2}, \mathrm{m_j} = -1/2, n\rangle$ by Doppler cooling and optical pumping. As the ions are not expected to be in the Lamb-Dicke regime after only Doppler cooling, so the phonon number is not expected to be 0. As such, it is then possible to drive the radial sideband transition $|\mathrm{S}_{1/2}, \mathrm{m_j} = -1/2, n\rangle \rightarrow |\mathrm{S}_{1/2}, \mathrm{m_j} = +1/2, n-1\rangle$ using the counterpropagating fields.

Figure 8.9 shows a scan of the red-sideband spectrum for 2 ions as a function of the detuning of ω_2 from the carrier frequency. The motional structure of the sidebands can be clearly seen, with four radial modes visible: the first two, separated by approximately 30 kHz detuning, are the two centre-of-mass (COM) motional modes. Two COM modes are expected as these arise from the non-degeneracy of the radial modes of the trap. The second two modes are the stretch modes of motion, with again two of these arising due to the non-degenerate radial modes. Figure 8.9 demonstrates the motional control possessed over the ions by this system, a crucial feature for the following Section where such motional control will be used to engineer entangling gates between single and multiple ions.

8.4 Entangling Gates

As has been mentioned many times already, for quantum computers and simulators to demonstrate advantages over their classic counterparts, they must generate large amounts of entanglement between their respective components [29]. It is therefore of importance that the Raman setup as has been described so far in this Chapter is able to demonstrate not only the single-qubit operations described in the previous section, but also entangling operations as shall now be presented.

As discussed in Section 2.5, entangling operations require the vibrational state of the ions to be manipulated. Therefore, such operations can only be driven using the counterpropagating fields, where coupling to the motional modes is possible. One of the most well-known entangling operations is that of the MS gate (refer to Section 2.5 for a detailed theoretical description), whereby the electronic and motional states of an ion can be coupled through a bichromatic driving field [62].

In order to implement a MS gate with Raman transitions, the two Raman beams comprising the bichromatic driving field must have a difference in frequency which is close to the frequency of a radial mode (such as the COM mode), so that off-resonant transitions on the red and blue sidebands can be driven. As discussed in Section 3.3.2, such transitions are practically implemented using both a single beam passing through AOM 2 (driven at a fixed frequency of 105 MHz) in conjunction with a bichromatic light field, generated using AOM 1 driven at frequencies of $\omega_\mathrm{r} - \Delta_\mathrm{SB}$ and $\omega_\mathrm{b} + \Delta_\mathrm{SB}$. $\omega_\mathrm{r,b}$ are the frequencies of the red-

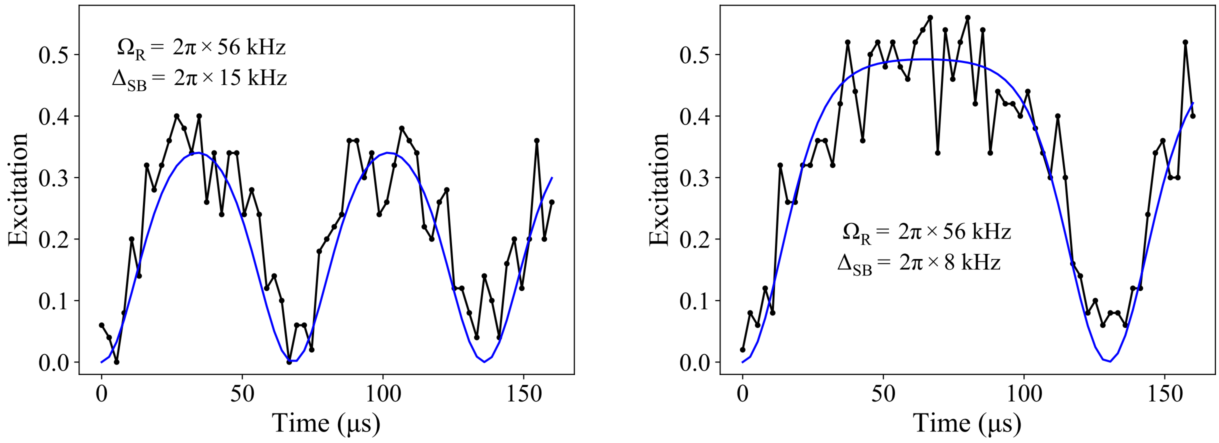

(a) $\Delta_{SB} = 2\pi \times 15\,\text{kHz}$ (b) $\Delta_{SB} = 2\pi \times 8\,\text{kHz}$

Figure 8.10: **Preparation of single-ion Cat states.** a) Measured dynamics of a single-ion Cat state (black points), created using a detuning from the sidebands of $\Delta_{SB} = 2\pi \times 15\,\text{kHz}$. The theoretical dynamic behaviour predicted from Equation 8.15 using the experimental parameters (with $\Omega = 2\pi \times 56\,\text{kHz}$) is plotted as the blue line. b) As with a), but at a smaller detuning from the sidebands of $\Delta_{SB} = 2\pi \times 8\,\text{kHz}$, where the slower dynamics allows the two ground state wavefunctions to fully separate, seen as a slight plateau at an excitation of 0.5.

and blue-sidebands respectively, and Δ_{SB} is the detuning from these sideband frequencies. The bichromatic beams are coupled into the same fibre, and enter the vacuum chamber together from the bottom viewport.

8.4.1 Single-ion Motional Cat States

The first step taken in implementing entangling interactions using such a bichromatic light field was to create a single-ion Schrödinger Cat state. A single-ion Cat state, as described in Section 2.5.1, is an entangled state of the electronic and motional degrees of freedom of a single ion. They can be created through driving a single ion with a bichromatic laser pulse, and have been demonstrated in many previous experiments [65–67], including in the QSim experiment itself on the optical qubit [49]. The bichromatic laser field couples the electronic and motional states of the ion, generating spin-motion entanglement within a single ion. This interaction is the same as can be used to engineer multiqubit quantum gates such as the MS gate, as will be experimentally demonstrated in Section 8.4.2.

As a reminder, it was previously shown in Section 2.5.1 that the probability for a single, ground-state cooled ion to be found in the $|\uparrow\rangle$ state after application of the bichromatic field is given by:

$$P_{|\uparrow\rangle} = |\langle\uparrow|\psi\rangle|^2 = \frac{1}{2} - \frac{1}{2}\exp\left(-2\left|\frac{\eta\Omega}{2\Delta_{SB}}(1 - e^{-i\Delta_{SB}t})\right|^2\right), \tag{8.15}$$

where Ω is the Raman Rabi frequency of one of the bichromat beams when tuned to be on resonance with the carrier transition (assumed to be equal for both the red- and blue-sidebands), and Δ_{SB} is the (equal) detuning of each beam from its respective sideband.

To probe such dynamics, a bichromatic light field was applied to a single ion, optically pumped and sideband cooled to the initial state $|\downarrow, 0\rangle$, in order to generate spin-motion entanglement. Figures 8.10 a) and b) show the experimentally measured, dynamic temporal behaviour of two single-ion Cat states, with a) created using a detuning from the sidebands of $\Delta_{\text{SB}} = 2\pi \times 15\,\text{kHz}$, and b) using a detuning from the sidebands of $\Delta_{\text{SB}} = 2\pi \times 8\,\text{kHz}$. The blue lines are the theoretical predictions from Equation 8.15 using the experimental parameters. At the beginning of the dynamics, the two (initially fully overlapped) ground-state wavepackets begin to move apart in phase space. At approximately $35\,\mu$s in Figure 8.10 a), the two ground-state wavepackets are almost, but not quite, maximally separated in phase space – as can be seen by the excitation reaching a maximum value of 0.4 – and the electronic and motional states are entangled at this point. The wavepackets then begin to move towards each other again, before fully recombining at approximately $70\,\mu$s. In Figure 8.10 b), the ground-state wavepackets become fully separated in phase space, as can be seen by an excitation of 0.5 being achieved.

8.4.2 Two-Ion Mølmer Sørensen Gate

Having created a single-ion Cat state, the natural progression was to implement an MS gate on a two-ion system. The theoretical background of the MS gate has been discussed in detail in Section 2.5.2, with the following section now presenting experimental results from an MS gate generated using Raman transitions on two ions.

When applied to two ions, the MS gate will generate collective spin-flips, taking an initial state $|\downarrow\downarrow\rangle$ to $|\uparrow\uparrow\rangle$ with (in the ideal case) zero population in the $|\uparrow\downarrow\rangle$ and $|\downarrow\uparrow\rangle$ states at this point. When the coupling strength and detuning are properly chosen, the MS gate will map an initial product state into a maximally entangled Bell state. High-fidelity two-qubit gates with trapped ions have been previously demonstrated in the QSim experiment with the optical qubit [59], however these gates were performed on the axial modes of motion, due to the relatively large spacing between axial modes reducing the motional excitation of non-COM modes of motion. In this work, the configuration of the counterpropagating Raman beams instead couples to the radial modes of motion, where the mode spectrum is more closely spaced than with the axial modes.

To demonstrate an MS gate, two ions were optically pumped into the ground state $|\downarrow\downarrow\rangle$ and the bichromatic light field applied. Figure 8.11 a) shows the subsequent temporal evolution of the two-qubit system. The Figure shows the evolution of the populations in the $|\downarrow\downarrow\rangle$ state (blue line), $|\uparrow\uparrow\rangle$ state (red line), and the combined populations in the $|\uparrow\downarrow\rangle$ and $|\downarrow\uparrow\rangle$ states (purple line) as a function of the length of the bichromatic pulse applied. After $75\,\mu$s, the population in the $|\uparrow\downarrow\rangle$ and $|\downarrow\uparrow\rangle$ states returns to zero as the populations

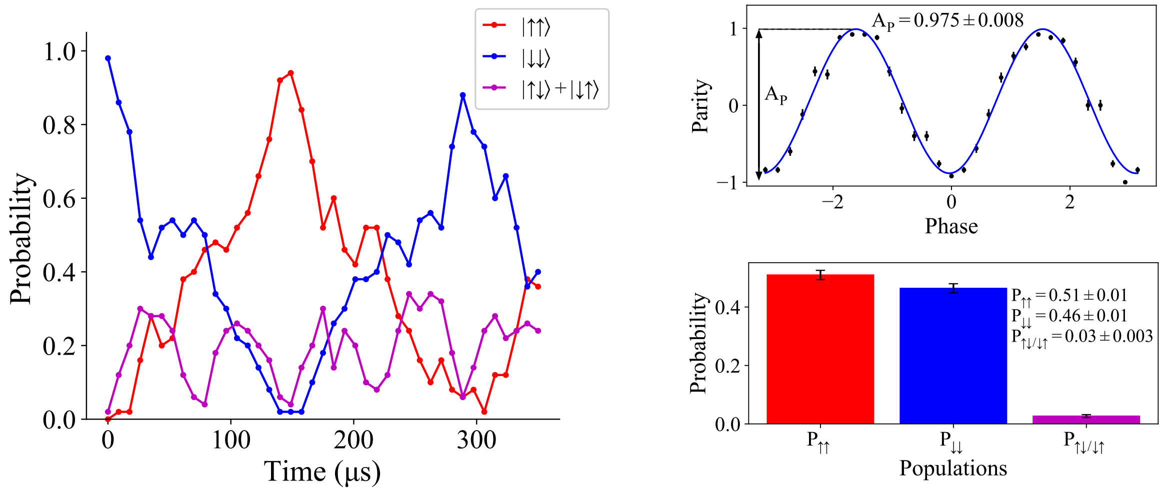

(a) Probability of state occupation as a function of the applied gate time.

(b) Evaluation of the Bell state fidelity. **Top**: Scan of the parity. **Bottom**: Relative state populations.

Figure 8.11: **Evolution of a two-ion crystal under application of a Raman MS gate.** a) Probability of state occupation as a function of the applied MS gate time. Blue is the population in the $|\downarrow\downarrow\rangle$ state, red the population in the $|\uparrow\uparrow\rangle$ state, and purple the summed population in the $|\uparrow\downarrow\rangle$ and $|\downarrow\uparrow\rangle$ states. At 75 μs, an entangled state is created. b) Evaluation of the entangled state fidelity created in a). **Top**: Plot of the parity of the entangled state as the phase of the probing $\frac{\pi}{2}\sigma_x$ pulse is scanned (black points). The blue line is a weighted least-squares sine fit to the data, with amplitude 0.975±0.008. Error bars are calculated from quantum projection noise using 50 repeat measurements. **Bottom**: Plot of the populations of the entangled state. The populations are evaluated using 1000 repeat measurements, with error bars subsequently calculated from quantum projection noise. For all measurements, the detuning of the beams was $\Delta_{SB} = 2\pi \times 13.3\,\text{kHz}$ with Raman Rabi frequency $\Omega_R = 2\pi \times 63\,\text{kHz}$ and detuning from the auxiliary state of $\Delta = 2\pi \times 308\,\text{GHz}$.

in the $|\downarrow\downarrow\rangle$ and $|\uparrow\uparrow\rangle$ states are equal at an excitation of 0.5. At this point, and under an ideal MS interaction, the maximally entangled Bell state $|\Phi^+\rangle = 1/\sqrt{2}(|00\rangle + |11\rangle)$ has been produced. After 150 μs, the population in the $|\uparrow\downarrow\rangle$ and $|\downarrow\uparrow\rangle$ states again returns to zero, with the entire population in the $|\uparrow\uparrow\rangle$ state, and so the system has returned to a product state.

It can be seen that there is an overall increase in the $|\uparrow\downarrow\rangle + |\downarrow\uparrow\rangle$ population as a function of time. This can be seen most clearly at later times as, when this population should return to zero, it does not fully do so. One possible explanation for this increase may be due to off-resonant coupling of the bichromatic beam to the other radial modes, however further work must look into the exact cause of these dynamics.

Fidelity estimation

In order to verify that the Bell state $|\Phi^+\rangle$ has indeed been produced after $75\,\mu$s, the fidelity of the state at this point can be probed. The fidelity is defined as: $\mathcal{F} = |\langle\Phi^+_{\text{prep}}|\Phi^+_{\text{ideal}}\rangle|^2$ and can be evaluated through a combination of two measurements: A measurement of the populations at the point where $|\Phi^+\rangle$ is expected, and a parity scan also at this point.

A measurement of the populations, which is essentially a measurement of the diagonal components of the density matrix, is achieved by evolving the two-qubit crystal to the point at which the state $|\Phi\rangle^+$ should be produced – in this case at $75\,\mu$s – measuring the population, and then repeating this process. Figure 8.11 b) (bottom) shows the results from such a measurement: 51±1% of the population is in the $|\uparrow\uparrow\rangle$ state, 46±1% in the $|\downarrow\downarrow\rangle$ state, and 3±0.3% in the $|\uparrow\downarrow\rangle$ and $|\downarrow\uparrow\rangle$ states. Although a useful measure, a measurement of the populations alone is not enough to characterise the fidelity of the Bell state – or even to prove that entanglement is present. For example, the fully mixed state $\frac{1}{2}(|\downarrow\downarrow\rangle\langle\downarrow\downarrow|+|\uparrow\uparrow\rangle\langle\uparrow\uparrow|)$ will produce the same values for a population measurement as the maximally entangled state $|\Phi^+\rangle$. As such, it is necessary to combine such measurements of the diagonal components with measurements of the off-diagonal terms of the density matrix. A parity scan can be used to measure these off-diagonal terms, and so provide an estimate of the fidelity when combined with population measurements, proving the existence of entanglement.

The concept behind a parity scan is as follows: The initial state, $|\downarrow\downarrow\rangle$, is once again evolved into $|\Phi^+\rangle$. After this evolution, a $\pi/2$ pulse, resonant with the carrier transition, is applied, the phase of which is scanned. For a phase of $\phi = 0$, the state $|\Phi^+\rangle$ will be rotated to $|\Psi^+\rangle = 1/\sqrt{2}(|\downarrow\uparrow\rangle + |\uparrow\downarrow\rangle)$. For a phase of $\phi = \pi/2$, the state $|\Phi^+\rangle$ will be unaltered. As such, for a perfectly prepared $|\Phi^+\rangle$ state, the parity scan samples the entire space of the two-qubit maximally entangled states, and so gives an indication of the fidelity with which a maximally entangled state has been prepared.

The parity itself is defined as $\mathrm{p} = \mathrm{P}_{\downarrow\downarrow} + \mathrm{P}_{\uparrow\uparrow} - \mathrm{P}_{\downarrow\uparrow/\uparrow\downarrow}$, where $\mathrm{P}_{\downarrow\downarrow}$ is the population in the $|\downarrow\downarrow\rangle$ state, $\mathrm{P}_{\uparrow\uparrow}$ is the population in the $|\uparrow\uparrow\rangle$ state, and $\mathrm{P}_{\downarrow\uparrow/\uparrow\downarrow}$ is the combined population from the $|\downarrow\uparrow\rangle$ and $|\uparrow\downarrow\rangle$ states. For an ideal, maximally entangled state, the parity will oscillate between -1 and 1 as the phase of the $\pi/2$ pulse is scanned. For a non-ideal Bell state preparation, these oscillations will have a smaller amplitude. As such, by fitting a sine wave to these oscillations, the amplitude, $\mathrm{A_p}$, can be extracted and used as a measurement of the state parity. Figure 8.11 b) (top) shows the parity oscillations for the Bell state prepared by the Raman transitions, with the associated weighted least-squares sine fit to the data. The amplitude of the fit is found to be 97.5±0.8%.

The fidelity for producing $|\Phi^+\rangle$ can then be calculated from the sum of these two quantities, such that:

$$\mathcal{F} = \frac{1}{2}(\mathrm{P}_{00} + \mathrm{P}_{11} + \mathrm{A_p}) = \frac{1}{2}(0.51 + 0.46 + 0.97) = 0.97 \pm 0.02. \tag{8.16}$$

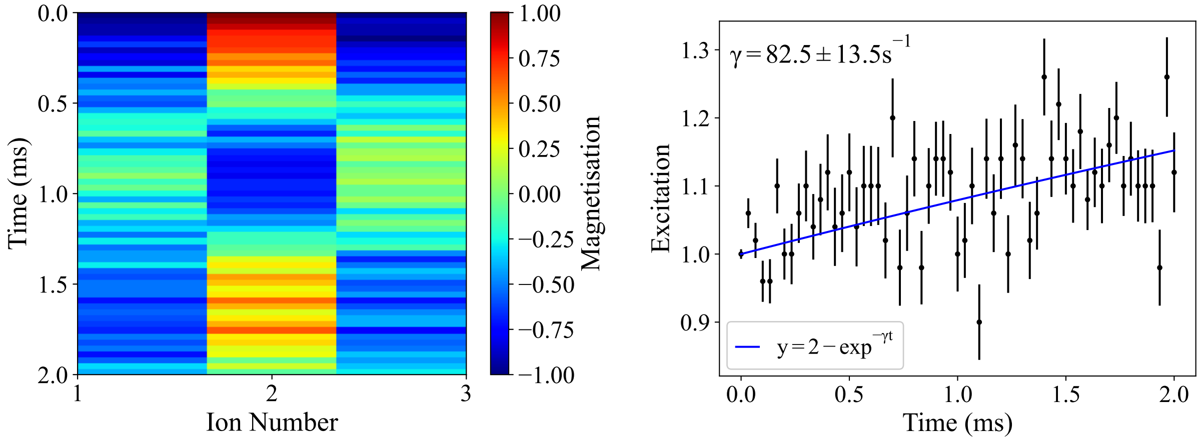

(a) Magnetisation dynamics under application of H_{XY}.

(b) Increase in excitation during evolution under H_{XY}.

Figure 8.12: **Application of the H_{XY} interaction to a three-ion state**. a) The magnetisation dynamics of the initial state $|\downarrow\uparrow\downarrow\rangle$ is shown for each ion under application of H_{XY}. It can be seen that the initial excitation hops symmetrically to the two neighbouring, outer ions, before hopping back to the middle ion. b) Increase of excitation in the system as a function of the length of time H_{XY} is applied (black points). A weighted least-squares exponential fit to the data (blue line) gives a rate of excitation increase of 82.5±13.5 s^{-1}. Error bars are calculated from quantum projection noise, with the error in the excitation increase extracted from the covariance matrix of the fit. The measurements were taken for $\Omega_R = 2\pi \times 50\,\mathrm{kHz}$, $\Delta = 2\pi \times 308\,\mathrm{GHz}$, $\Delta_{SB} = 2\pi \times 40\,\mathrm{kHz}$, $\delta = 2\pi \times 9\,\mathrm{kHz}$, and 50 repeats.

Therefore, a maximally entangled Bell state was produced with 97±2% fidelity.

As a comparison, the maximum Bell state fidelity achieved in the QSim system by implementing an MS gate on radial modes of the 729 nm transition was on the order of 96%. This fidelity is thought to be limited due to the close proximity of the radial modes to one-another, meaning it is not possible to couple purely to the COM mode (i.e. all modes will contribute in some capacity to the dynamics). Therefore, limitations to the gate fidelity do not seem to arise from properties intrinsic to the Raman setup.

8.4.3 Evolution of a 3-ion chain under H_{XY}

As a first step towards implementing multiqubit entangling operations on longer ion strings using Raman transitions, a H_{XY} model of the same type described in Section 6.1 was applied to a short ion chain of three ions. The explicit form of this Hamiltonian is given by:

$$H_{\mathrm{XY}} = \hbar \sum_{i<j} J_{ij} \left(\sigma_i^+ \sigma_j^- + \sigma_i^- \sigma_j^+ \right), \tag{8.17}$$

where σ_i^z is the spin-1/2 Pauli z-operator, $\sigma_i^+ \sigma_i^-$ the spin-raising (lowering) operators, and J_{ij} the coupling matrix.

The ion chain was prepared in the initial state $|{\downarrow}{\uparrow}{\downarrow}\rangle$, by off-resonantly addressing the middle ion using the 729 nm addressing beam [77]. The middle ion was first prepared in the $|\mathrm{D}_{3/2}, \mathrm{m_j} = +3/2\rangle$ state using this beam, before a final 729 nm global π-pulse coupling the states $|\mathrm{S}_{1/2}, \mathrm{m_j} = +1/2\rangle$ to $|\mathrm{D}_{3/2}, \mathrm{m_j} = +3/2\rangle$ prepared the ion in the $|\mathrm{S}_{1/2}, \mathrm{m_j} = +1/2\rangle$ state.

Figure 8.12 a) shows the evolution of the magnetisation for each ion under application of the H_{XY} interaction. It can be seen that the initial excitation spreads to the ions either side, before re-interfering on the middle ion once more at approximately 1.75 ms. Figure 8.12 b) shows the increase in excitation in the system as the interaction time is increased. Assuming that the increase in excitation is due solely to spontaneous emission from the $|\mathrm{P}_{3/2}\rangle$ level during the dynamics, then this increase would be expected to follow an exponential model as discussed in Section 8.3.3. Fitting an exponential model to the data gives a rate of excitation increase of $82.5 \pm 13.5\,\mathrm{s}^{-1}$. The measured rate of spontaneous emission using similar parameters was found to be $50.5 \pm 0.4\,\mathrm{s}^{-1}$ for a single-qubit Raman gate (see Section 8.3.3). However, as the H_{XY} interaction uses essentially four beams (a single Raman beam in one arm, and a trichromatic beam in the other) it should be expected that the rate of spontaneous decay will be higher during this interaction than for a single-qubit gate which uses only two beams. If a simple assumption is made that the additional two beams which comprise the trichromatic beam each add a decay rate of $R = 20.2\,\mathrm{s}^{-1}$, then the total rate of spontaneous emission should be on the order of $90\,\mathrm{s}^{-1}$. This is very close to the measured rate of excitation increase, and so it is likey that the increase in excitation can be completely explained by spontaneous emission from the $|\mathrm{P}_{3/2}\rangle$ level. However the rate of spontaneous emission due to the trichromatic beam should be explicitly measured in the future using the same technique as in Section 8.3.3 to confirm this.

By comparing the measured evolution of the magnetisation to a simulated evolution, a value for the maximum coupling strength $J_{\max} = \max|J_{ij}|$ can be extracted (see Section 6.1), and was found to be $1400\,\mathrm{s}^{-1}$. A comparison can now be made between the $J_{\max}$ achieved with the Raman transition on the ground state qubit, and the $J_{\max}$ achieved with the 729 nm transition on the optical qubit. From the results presented in Chapters 6 and 7, the maximum J_{ij} achieved with the 729 nm transition is on the order of $400\,\mathrm{s}^{-1}$. The value calculated above for the Raman transition is 3.5 times this value, and so the coupling strength is significantly stronger than that currently achievable with the optical qubit.

8.5 Conclusion

This Chapter has introduced the new experimental apparatus which enables encoding of quantum information in the ground state of $^{40}\text{Ca}^{+}$, in contrast to the optical qubit which has previously been used in this experiment. The new setup replicates the flexibility which is achievable with the optical qubit, however with several improvements.

Perhaps the most marked improvement can be seen in the coherence time of the new qubit. When probed with the copropagating fields, the coherence time extracted from an exponential decay is 358±78 ms, and with the counterpropagating fields (again extracted from an exponential decay) is 241±26 ms. This is a more than four-fold improvement in comparison to the coherence time of the optical qubit, which is on the order of 60 ms. The ground state qubit has the same sensitivity to magnetic fields fluctuations as the optical qubit, and so this marked increase in coherence shows that this qubit is extremely insensitive to laser noise.

The setup also demonstrates improvements with regards to the entangling operations which can be implemented. The fidelity of the MS gates which are implemented using Raman gates is comparable to that obtained when using the 729 nm transition, and so it is likely that this fidelity is limited through off-resonant coupling to non-COM modes during the gate dynamics. However, when implementing a H_{XY} model, the improvement in gate speed when compared to the 729 nm-driven gates is remarkable – with a factor of 3.5 improvement in the gate speed. The increase in excitation during the gate dynamics must be further investigated through a measurement of the rate of spontaneous decay from the $|\text{P}_{3/2}\rangle$ level due to application of the trichromatic beam.

Chapter 9

Outlook

The work presented in this thesis has covered both technical improvements to the existing system, as well as covering quantum simulation experiments published in three papers. The work can be divided into three major sections:

1. Noise Characterisations of the QSim System
2. Randomised Measurements on Chains of Trapped Ions
3. Implementation and Characterisation of a new Raman setup

The noise characterisations presented in Chapter 4 looked both at the quality of the single-qubit gates implemented using the 729 nm laser and the stability between two of the major 729 nm beam paths (the radial path and the single-ion addressing path). The single-qubit gates were characterised using gate set tomography (GST), with the results showing that X- and Y-rotations are implemented with very low errors, with the Z-rotations implemented with much higher errors. With regards to the beam-path stability between the radial and single-ion addressing paths, two major conclusions can be drawn: Firstly, the loss in coherence due to instabilities between these two paths is over much longer timescales than the current coherence time of the system, and so such instabilities are not (currently) a dominant source of noise in the system. This is consistent with noise produced from slow drifts. Secondly, there does not seem to be any significant contribution from high-frequency noise, such as high-frequency acoustic noise.

Following this, three theoretical protocols, which are concerned with quantum simulation, and their subsequent experimental implementation, were covered in Chapters 5, 6, and 7. All three experiments use randomised measurements to characterise systems of 10 to 20 ions.

The first of these experiments looked at the formation of entanglement in chains of 10 ions, as well as 10-ion partitions of a 20-ion chain. In moving to regimes where the system dynamics can no longer be simulated classically, protocols to characterise the dynamics of many-body quantum systems will become of increasing importance. The protocol implemented here used randomised measurements to access the Rényi entropy after evolution of the system under the XY-model of interacting bosons, H_{XY}. For the 10-ion chain, bipartite entanglement was shown to exist between all partitions of the chain. Further to this, application of the protocol to 10-ion partitions of a 20-ion chain indicated the formation of highly entangled states after several milliseconds evolution under H_{XY}. As a final investigation of the applicability of the protocol to investigating the dynamics associated with many-body localisation, the protocol was demonstrated on a 10-ion chain after evolution of the system under a disordered Hamiltonian.

The second experiment looked at scrambling in many-body quantum systems. Operator spreading under the dynamics of a transverse field Ising Hamiltonian in chains of 10-ions was probed by measuring modified out-of-time-ordered correlators (OTOCs). Of significant interest with this experiment is the application of the protocol to two different interaction ranges in the QSim system. This allowed a comparison of operator spreading for two different regimes: that of long-range interactions (showing ballistic operator spreading) and very long-range interactions (showing non-ballistic operator spreading).

The final experiment was a proof-of-principle demonstration of a cross-platform verification protocol. Currently, it is common to verify a quantum state prepared on a quantum device with a classical simulation of the state, in order to ensure the quantum device is performing as expected. However, in moving to regimes where the comparison of a prepared quantum state with a classical simulation becomes computationally infeasible, different verification procedures are required. This protocol aims to verify a quantum state by comparing it with a quantum state prepared on a separate quantum device, potentially at a very different point in time and space. The protocol uses randomised measurements in order to provide a fidelity estimate for the two prepared states. The proof-of-principle experiments presented here used the protocol to compare a state prepared using the QSim system with a state prepared using a classical simulation, as well as comparing two quantum states prepared sequentially in the QSim system.

Finally, the new Raman setup was discussed in Chapter 8, where the qubit was encoded in the ground state Zeeman levels of $^{40}\mathrm{Ca}^{+}$, as opposed to the optical qubit discussed in the previous Chapters. First characterisation measurements of this setup indicate a vastly improved coherence time in comparison to the optical qubit. Entangling operations were demonstrated using this setup, with an MS gate implemented with a fidelity comparable to that of the MS gate achieved using the optical qubit. A final demonstration of the H_{XY} Hamiltonian on 3 ions indicates the dynamics progress significantly faster with the Raman setup than with the current dynamics achieved when using the optical qubit driven with the 729 nm laser.

Looking further into the future, the ultimate aim of the QSim experiment is to perform quantum simulations on long chains of ions, ideally of at least 50 ions. This will allow complex dynamics which are computationally infeasible to simulate classically to be investigated. Such strings of ions have already been trapped and, thanks to the work of [77], single-ion addressing can now be performed on over 50 ions. However, there is clearly a large amount of work to still be done until such a regime can be reached with the QSim system. The next major steps which can be taken in order to move towards this ultimate goal will now be discussed.

The proof-of-principle demonstrations of cross-platform verification presented in this thesis already show great promise for use in verifying experimentally prepared states in systems comprised of tens of qubits. The natural next step in this matter is to apply the protocol to two independent quantum devices, separated in time and space, in order to verify the states prepared on those devices. If proved successful, this protocol will be of immense use for the future verification of experimentally prepared quantum states in regimes where comparison to classically simulated states becomes computationally infeasible.

From a technical standpoint, the Raman setup will likely be crucial in bringing the QSim experiment up to a level where it can realistically move beyond dynamics which can be classically simulated. The Raman setup has already been successfully used in further work conducted by [215]. However, there is still a large amount of work that needs to be done on the Raman setup in order to fully develop it. One of the most important quantities to be looked at next with this setup is the spontaneous decay arising from application of the trichromatic beam. This will provide an insight into whether the observed excitation increase during evolution under H_{XY} can be fully explained by this process, or whether there are additional processes such as incoherent spin-flips induced by the trichromatic beam causing an increase in excitation. In addition, a large amount of optical power is being wasted due to the polarisations used to drive the Raman transitions (see Section 8.3). Although not being used to drive the transition, this power is still contributing to spontaneous decay from the $\mathrm{P}_{3/2}$ level. A logical next step would be to optimise these polarisations further such that the amount of optical power used to drive the transitions is maximised, however whilst still ensuring that the differential AC-Stark shift between the two levels is minimised. Further, the single-qubit gates implemented by the Raman setup should be characterised using GST, as was performed in Chapter 4 with the 729 nm beam. This will allow a direct comparison between the quality of the single-qubit gates which can be performed on the optical qubit with the 729 nm beam and the ground state qubit using Raman transitions.

A major next step in upgrading the Raman setup would be to replace the current beam optics directly before the vacuum chamber with beam-shaping optics which create an elliptically shaped beam. It has already been shown in [47] that elliptical beam shaping of the radial 729 nm beam greatly increased the Rabi frequency (due to the increased amount of light which is focussed onto the ion string). It is therefore natural to assume that beam shaping optics on the two Raman paths would also provide an increase in the Raman Rabi frequency and, as such, the speed of the entangling dynamics.

With regards to entangling dynamics, a natural next step is to extend the application of H_{XY} from 3 ions to strings to 10 ions. This will allow a straightforward comparison between these dynamics to the dynamics observed with the 729 nm laser when using the optical qubit.

Appendix A

List of Publications

Publications Discussed in this Thesis

1. M. K. Joshi, A. Elben, B. Vermersch, T. Brydges, C. Maier, P. Zoller, R. Blatt, C. F. Roos,
   Quantum Information Scrambling in a Trapped-ion Quantum Simulator with Tunable Range Interactions,
   Phys. Rev. Lett., **124**(240505), pp. 1-6 (2020)

2. A. Elben, B. Vermersch, R. van Bijnen, C. Kokail, T. Brydges, C. Maier, M. K. Joshi, R. Blatt, C. F. Roos, P. Zoller,
   Cross-Platform Verification of Intermediate Scale Quantum Devices,
   Phys. Rev. Lett., **124**(010504), pp. 1-6 (2020)

3. T. Brydges, A. Elben, P. Jurcevic, B. Vermersch, C. Maier, B. P. Lanyon, P. Zoller, R. Blatt, C. F. Roos,
   Probing Rényi Entanglement Entropy via Randomized Measurements,
   Science, **364**(6437), pp.260-263 (2019)

Further Publications

4. M. K. Joshi, A. Fabre, C. Maier, T. Brydges, D. Kiesenhofer, H. Hainzer, R. Blatt, C. F. Roos,
   Polarization-gradient cooling of 1D and 2D ion Coulomb crystals,
   New J. Phys., **22**, 103013 (2020)

5. C. Kokail*, C. Maier*, R. van Bijnen*, T. Brydges, M. K. Joshi, P. Jurcevic, C. A. Muschik, P. Silvi, R. Blatt, C. F. Roos, P. Zoller,
   Self-Verifying Variational Quantum Simulation of the Lattice Schwinger Model,
   Nature, **569**, pp.355-360 (2019)

6. C. Maier, T. Brydges, P. Jurcevic, N. Trautmann, C. Hempel, B. P. Lanyon, P. Hauke, R. Blatt, C. F. Roos,
   Environment-assisted quantum transport in a 10-qubit network,
   Phys. Rev. Lett. **122**, 50501 (2019)

7. P. Jurcevic, H. Shen, P. Hauke, C. Maier, T. Brydges, C. Hempel, B. P. Lanyon, M. Heyl, R. Blatt, C. F. Roos,
   Direct observation of dynamical quantum phase transitions in an interacting many-body system,
   Phys. Rev. Lett. **119**, 80501 (2017)

Appendix B

Explicit Background Derivations

B.1 Moving to the Rotating Frame

It is often useful to consider the evolution of a system under a Hamiltonian using an approach based on transforming the problem into a *rotating frame.* This is where the system is considered in a frame such that the perturbed time-dependent evolution of the system is separated from the evolution of the unperturbed system. This can be achieved in the following way.

Consider a state $|\psi\rangle$, which can be written (completely generally) as

$$|\psi\rangle = U|\tilde{\psi}\rangle, \tag{B.1}$$

where U descibes the unitary transformation between two different bases, both of which can be used to describe the state. If the state is transformed into a new basis, then the Hamiltonian must also be transformed, something which can be achieved using the time-dependent Schrödinger equation

$$i\hbar\frac{\partial}{\partial t}|\psi\rangle = H|\psi\rangle. \tag{B.2}$$

In the newly transformed basis, Equation B.2 transforms to:

$$\begin{aligned}
i\hbar\frac{\partial}{\partial t}|\tilde{\psi}\rangle &= i\hbar\frac{\partial}{\partial t}\left(U^{\dagger}|\psi\rangle\right) && \text{(B.3)}\\
&= i\hbar\left[U^{\dagger}\frac{\partial}{\partial t}|\psi\rangle + \left(\frac{\partial U^{\dagger}}{\partial t}\right)|\psi\rangle\right] && \text{(B.4)}\\
&= \left[U^{\dagger}H + i\hbar\left(\frac{\partial U^{\dagger}}{\partial t}\right)\right]|\psi\rangle. && \text{(B.5)}
\end{aligned}$$

Substituting Equation B.1 into this, yields

$$i\hbar\frac{\partial}{\partial t}|\tilde{\psi}\rangle = \left[U^{\dagger}HU + i\hbar\left(\frac{\partial U^{\dagger}}{\partial t}\right)U\right]|\tilde{\psi}\rangle = \tilde{H}|\tilde{\psi}\rangle. \tag{B.6}$$

Therefore, the transformed Hamiltonian is given by

$$\tilde{H} = \left[U^{\dagger}HU + i\hbar\left(\frac{\partial U^{\dagger}}{\partial t}\right)U\right]. \tag{B.7}$$

This new Hamiltonian has two components to it: the first term is the straightforward transformation of H into the new basis. The second term corresponds to a fictitious energy, analogous to the fictitious forces which arise in classical mechanics when working in rotating frames [55].

B.2 Atom-Laser in the Interaction Frame

For an atom under perturbation from a laser, the Hamiltonian is given by:

$$H = \frac{\hbar\omega_0}{2}\sigma_z + \hbar\Omega\cos(\omega_{\mathrm{L}}t + \phi_{\mathrm{L}})\sigma_x. \tag{B.8}$$

In moving to the rotating frame via a transformation of $U = e^{-iH_0t}$, where $H_0 = \frac{\hbar\omega_0 t}{2}$, it is easiest to consider the transformation in two parts: firstly, the transformation of $H_0 = \frac{\hbar\omega_0\sigma_z}{2}$ and secondly the transformation of $H_1 = \cos(\omega_{\mathrm{L}}t + \phi_{\mathrm{L}})\sigma_x$.

First calculating the transformation of H_0 using $U = e^{-i\omega_0 t\sigma_z/2}$:

$$\begin{aligned}
&\tilde{H}_0 = U^{\dagger}HU + i\hbar\frac{\partial U^{\dagger}}{\partial t}U = e^{i\omega_0 t\sigma_z/2}\frac{\hbar\omega_0}{2}\sigma_z e^{-i\omega_0 t\sigma_z/2} - \frac{\hbar\omega_0}{2}\sigma_z,\\
\implies &\tilde{H}_0 = \left[\cos(\omega_0 t/2)\mathbb{I} + i\sin(\omega_0 t/2)\sigma_z\right]\frac{\hbar\omega_0}{2}\sigma_z\left[\cos(\omega_0 t/2)\mathbb{I} - i\sin(\omega_0 t/2)\sigma_z\right] - \frac{\hbar\omega_0}{2}\sigma_z,\\
\implies &\tilde{H}_0 = \frac{\hbar\omega_0}{2}\left[\cos(\omega_0 t/2)\mathbb{I} + i\sin(\omega_0 t/2)\sigma_z\right]\left[\cos(\omega_0 t/2)\sigma_z - i\sin(\omega_0 t/2)\mathbb{I}\right] - \frac{\hbar\omega_0}{2}\sigma_z,\\
\implies &\tilde{H}_0 = \frac{\hbar\omega_0}{2}\left[\cos^2(\omega_0 t/2)\sigma_z + \sin^2(\omega_0 t/2)\sigma_z\right] - \frac{\hbar\omega_0}{2}\sigma_z,\\
\implies &\tilde{H}_0 = O.
\end{aligned} \tag{B.9}$$

Secondly, calculate the quantity $U^{\dagger}H_1U$:

$$\begin{aligned}
U^{\dagger}H_1U &= \hbar\Omega\left[\cos(\omega_0 t/2)\mathbb{I} + i\sin(\omega_0 t/2)\sigma_z\right]\cos(\omega_{\mathrm{L}}t + \phi_{\mathrm{L}})\sigma_x\left[\cos(\omega_0 t/2)\mathbb{I} - i\sin(\omega_0 t/2)\sigma_z\right]\\
U^{\dagger}H_1U &= \hbar\Omega\cos(\omega_{\mathrm{L}}t + \phi_{\mathrm{L}})\left[\cos(\omega_0 t/2)\mathbb{I} + i\sin(\omega_0 t/2)\sigma_z\right]\left[\cos(\omega_0 t/2)\sigma_x - \sin(\omega_0 t/2)\sigma_y\right]\\
U^{\dagger}H_1U &= \hbar\Omega\cos(\omega_{\mathrm{L}}t + \phi_{\mathrm{L}})\left[\cos^2(\omega_0 t/2)\sigma_x - \sin^2(\omega_0 t/2)\sigma_x - \frac{1}{2}\sin(\omega_0 t)\sigma_y - \frac{1}{2}\sin(\omega_0 t)\sigma_y\right]\\
U^{\dagger}H_1U &= \hbar\Omega\cos(\omega_{\mathrm{L}}t + \phi_{\mathrm{L}})\cos(\omega_0 t)\sigma_x - \cos(\omega_{\mathrm{L}}t + \phi_{\mathrm{L}})\sin(\omega_0 t)\sigma_y. \qquad \text{(B.10)}
\end{aligned}$$

Equation B.10 can be written in a very useful manner by considering the following expansions. For for cosine:

$$\begin{aligned}
&\cos([\omega_{\mathrm{L}} - \omega_0]t + \phi_{\mathrm{L}})\sigma_x + \cos([\omega_{\mathrm{L}} + \omega_0]t + \phi_{\mathrm{L}})\sigma_x\\
&= \cos(\omega_{\mathrm{L}}t + \phi_{\mathrm{L}})\cos(\omega_0 t)\sigma_x + \sin(\omega_{\mathrm{L}}t + \phi_{\mathrm{L}})\sin(\omega_0 t)\sigma_x\\
&+ \cos(\omega_{\mathrm{L}}t + \phi_{\mathrm{L}})\cos(\omega_0 t)\sigma_x - \sin(\omega_{\mathrm{L}}t + \phi_{\mathrm{L}})\sin(\omega_0 t)\sigma_x\\
&= 2\cos(\omega_{\mathrm{L}}t + \phi_{\mathrm{L}})\cos(\omega_0 t)\sigma_x. \qquad \text{(B.11)}
\end{aligned}$$

Secondly for sine:

$$\begin{aligned}
&\sin([\omega_{\mathrm{L}} - \omega_0]t + \phi_{\mathrm{L}})\sigma_y - \sin([\omega_{\mathrm{L}} + \omega_0]t + \phi_{\mathrm{L}})\sigma_y\\
&= \sin(\omega_{\mathrm{L}}t + \phi_{\mathrm{L}})\cos(\omega_0 t)\sigma_y - \cos(\omega_{\mathrm{L}}t + \phi_{\mathrm{L}})\sin(\omega_0 t)\sigma_y\\
&- \sin(\omega_{\mathrm{L}}t + \phi_{\mathrm{L}})\cos(\omega_0 t)\sigma_y - \cos(\omega_{\mathrm{L}}t + \phi_{\mathrm{L}})\sin(\omega_0 t)\sigma_y\\
&= -2\sin(\omega_0 t)\cos(\omega_{\mathrm{L}}t + \phi_{\mathrm{L}})\sigma_y. \qquad \text{(B.12)}
\end{aligned}$$

As such, in summary:

$$\cos([\omega_{\mathrm{L}} - \omega_0]t + \phi_{\mathrm{L}})\sigma_x + \cos([\omega_{\mathrm{L}} + \omega_0]t + \phi_{\mathrm{L}})\sigma_x = 2\cos(\omega_{\mathrm{L}}t + \phi_{\mathrm{L}})\cos(\omega_0 t)\sigma_x \qquad \text{(B.13)}$$

$$\sin([\omega_{\mathrm{L}} - \omega_0]t + \phi_{\mathrm{L}})\sigma_y + \sin([\omega_{\mathrm{L}} + \omega_0]t + \phi_{\mathrm{L}})\sigma_y = -2\sin(\omega_0 t)\cos(\omega_{\mathrm{L}}t + \phi_{\mathrm{L}})\sigma_y. \qquad \text{(B.14)}$$

A rotating wave approximation can now be made where sum frequency terms of $(\omega_{\mathrm{L}}+\omega_0)t$, which rotate at much faster speeds than the time-scale of the induced dynamics, can be dropped. As such, Equations B.13 and B.14 reduce to:

$$\cos([\omega_{\mathrm{L}} - \omega_0]t + \phi_{\mathrm{L}})\sigma_x = 2\cos(\omega_{\mathrm{L}}t + \phi_{\mathrm{L}})\cos(\omega_0 t)\sigma_x \qquad \text{(B.15)}$$

$$\sin([\omega_{\mathrm{L}} - \omega_0]t + \phi_{\mathrm{L}})\sigma_y = -2\sin(\omega_0 t)\cos(\omega_{\mathrm{L}}t + \phi_{\mathrm{L}})\sigma_y. \qquad \text{(B.16)}$$

As such, Equation B.10 reduces to:

$$U^\dagger H_1 U = \frac{\hbar\Omega}{2}\left(\cos([\omega_\mathrm{L} - \omega_0]t + \phi_\mathrm{L})\sigma_x + \sin([\omega_\mathrm{L} - \omega_0]t + \phi_\mathrm{L})\sigma_y\right). \tag{B.17}$$

Finally, Equation B.8 in the rotating frame can therefore be written as:

$$\tilde{H} = \frac{\hbar\Omega}{2}\left(\cos(\delta t + \phi_\mathrm{L})\sigma_x + \sin(\delta t + \phi_\mathrm{L})\sigma_y\right). \tag{B.18}$$

where $\delta = \omega_\mathrm{L} - \omega_0$.

B.3 Explicit Calculation of Resonant Evolution

A general state evolves under the resonant Hamiltonian, $H_\mathrm{int} = \hbar\Omega/2[\cos(\phi_\mathrm{L})\sigma_x{+}\sin(\phi_\mathrm{L})\sigma_y]$, such that:

$$U = e^{-iH_\mathrm{int}t/\hbar} = e^{-i\left(\frac{\hbar\Omega}{2}[\cos(\phi_\mathrm{L})\sigma_x + \sin(\phi_\mathrm{L})\sigma_y]\right)t/\hbar}. \tag{B.19}$$

As σ_x and σ_y don't commute, so $e^{i(\sigma_x+\sigma_y)} \neq e^{i\sigma_x}e^{i\sigma_y}$. Therefore, the best approach is to expand the exponential as a Taylor series such that:

$$\begin{aligned}
U &= \mathbb{I} - \frac{i\Omega t}{2}[\cos(\phi_\mathrm{L})\sigma_x + \sin(\phi_\mathrm{L})\sigma_y] + \frac{1}{2!}\left(\frac{i\Omega t}{2}\right)^2[\cos(\phi_\mathrm{L})\sigma_x + \sin(\phi_\mathrm{L})\sigma_y]^2 \\
&- \frac{1}{3!}\left(\frac{i\Omega t}{2}\right)^3[\cos(\phi_\mathrm{L})\sigma_x + \sin(\phi_\mathrm{L})\sigma_y]^3 + \ldots \\
\implies U &= \mathbb{I} - \frac{i\Omega t}{2}[\cos(\phi_\mathrm{L})\sigma_x + \sin(\phi_\mathrm{L})\sigma_y] - \frac{1}{2!}\left(\frac{\Omega t}{2}\right)^2\mathbb{I} \\
&+ \frac{1}{3!}\left(\frac{\Omega t}{2}\right)^3 i[\cos(\phi_\mathrm{L})\sigma_x + \sin(\phi_\mathrm{L})\sigma_y] + \ldots .
\end{aligned}$$

Collecting like terms together gives:

$$U = \left(1 - \frac{1}{2!}\left(\frac{\Omega t}{2}\right)^2 + \ldots\right)\mathbb{I} - i\left(\frac{\Omega t}{2} - \frac{1}{3!}\left(\frac{\Omega t}{2}\right)^3 + \ldots\right)[\cos(\phi_\mathrm{L})\sigma_x + \sin(\phi_\mathrm{L})\sigma_y]. \tag{B.20}$$

Comparing the first and second parts of Equation B.28 to the Taylor series expansions for both sine and cosine, it can be seen that the first part can be expressed in terms of a cosine, with the second part being expressed in terms of a sine:

$$U = \cos\left(\frac{\Omega t}{2}\right)\mathbb{I} - i\sin\left(\frac{\Omega t}{2}\right)[\cos(\phi_\mathrm{L})\sigma_x + \sin(\phi_\mathrm{L})\sigma_y]. \tag{B.21}$$

As such, this simplifies to:

$$U = \begin{pmatrix} \cos(\Omega t/2) & -ie^{-i\phi_{\mathrm{L}}}\sin(\Omega t/2) \\ -ie^{i\phi_{\mathrm{L}}}\sin(\Omega t/2) & \cos(\Omega t/2) \end{pmatrix}. \tag{B.22}$$

B.4 Explicit Calculation of Off-Resonant Transitions: Frame Rotating at ω_{L}

By moving into a frame rotating at the same frequency as a component of the light field, the induced shift in the energy levels can be highlighted. First, move into the frame rotating at ω_{L} using the transformation:

$$U = e^{-iH_0 t/\hbar} = e^{-i\omega_{\mathrm{L}} t\sigma_z/2} = \cos(\omega_{\mathrm{L}} t/2)\mathbb{I} - i\sin(\omega_{\mathrm{L}} t/2)\sigma_z. \tag{B.23}$$

Assuming the general case where the incident light field is not necessarily resonant with the energy splitting between the two states, the interaction Hamiltonian associated with this is found from:

$$H_{\mathrm{int}} = U^\dagger H U + i\hbar\left(\frac{\partial U^\dagger}{\partial t}\right)U = \begin{pmatrix} -\frac{\hbar}{2}(\omega_{\mathrm{L}} - \omega_0) & \hbar\Omega\cos(\omega_{\mathrm{L}} t)e^{i\omega_{\mathrm{L}} t/2} \\ \hbar\Omega\cos(\omega_{\mathrm{L}} t)e^{-i\omega_{\mathrm{L}} t/2} & \frac{\hbar}{2}(\omega_{\mathrm{L}} - \omega_0) \end{pmatrix}, \tag{B.24}$$

where the phase ϕ_{L} has been set to zero for simplicity. A convenient way to write this is to define the detuning $\delta = \omega_{\mathrm{L}} - \omega_0$, and expand the cosine term in terms of exponentials:

$$H_{\mathrm{int}} = \begin{pmatrix} -\frac{1}{2}\hbar\delta & \frac{1}{2}\hbar\Omega\left(1 + e^{2i\omega_{\mathrm{L}} t}\right) \\ \frac{1}{2}\hbar\Omega\left(1 + e^{-2i\omega_{\mathrm{L}} t}\right) & \frac{1}{2}\hbar\delta \end{pmatrix}. \tag{B.25}$$

As the exponential terms are rotating much faster than the other terms, they can be neglected through making the rotating wave approximation. This can be understood by considering a spin in a magnetic field: the exponential term rotates so rapidly that the spin observes it as a rapidly fluctuating field. Over time, this rapidly fluctuating field effectively almost entirely cancels out. Therefore, the transformed Hamiltonian reduces to:

$$H_{\mathrm{int}} = \begin{pmatrix} -\frac{1}{2}\hbar\delta & \frac{1}{2}\hbar\Omega \\ \frac{1}{2}\hbar\Omega & \frac{1}{2}\hbar\delta \end{pmatrix} = -\frac{\hbar\delta}{2}\sigma_z + \frac{\hbar\Omega}{2}\sigma_x. \tag{B.26}$$

The propagator for this Hamiltonian is subsequently given by:

$$U = e^{-iHt/\hbar} = e^{-it(-\frac{1}{2}\delta\sigma_z + \frac{1}{2}\Omega\sigma_x)}. \tag{B.27}$$

As with the resonant case for the frame rotating at ω_0 discussed above, the best approach is to expand the exponential as a Taylor series and, using the Pauli relations $\sigma_i\sigma_i = \mathbb{I}$ and $\sigma_z\sigma_x = i\sigma_y$, $\sigma_x\sigma_z = -i\sigma_y$, this yields:

$$
\begin{aligned}
e^{-it(\frac{1}{2}\delta\sigma_z+\frac{1}{2}\Omega\sigma_x)} &= \mathbb{I} - \frac{i}{2}(-\delta\sigma_z + \Omega\sigma_x)t - \frac{1}{2!}\frac{1}{4}(\delta^2\mathbb{I} + \Omega^2\mathbb{I} + \delta\Omega\sigma_y - \delta\Omega\sigma_y)t^2 + \\
\frac{1}{3!}\frac{i}{8}(-\delta^3\sigma_z + \Omega^3\sigma_x - \delta\Omega^2\sigma_z + \Omega\delta^2\sigma_x)t^3 &+ \frac{1}{4!}\frac{1}{16}(\delta^2\mathbb{I} + \Omega^2\mathbb{I})(\delta^2\mathbb{I} + \Omega^2\mathbb{I})t^4 + \dots
\end{aligned}
$$

Collecting like terms together gives:

$$
\implies \left\{\mathbb{I} - \frac{1}{2!}\frac{\Omega_{\text{eff}}^2}{4}t^2\mathbb{I} + \frac{1}{4!}\frac{\Omega_{\text{eff}}^4}{16}t^4\mathbb{I} + \dots\right\} - i\left\{\frac{1}{2}(-\delta\sigma_z + \Omega\sigma_x)t - \frac{1}{3!}\frac{1}{8}[-\delta\Omega_{\text{eff}}^2\sigma_z + \Omega\Omega_{\text{eff}}^2\sigma_x]t^3 + \dots\right\} \tag{B.28}
$$

Where $\Omega_{\text{eff}}^2 = \delta^2 + \Omega^2$. Comparing the first and second parts of Equation B.28 to the Taylor series expansions for both sine and cosine, it can be seen that the first part can be expressed in terms of a cosine, with the second part being expressed in terms of the sum of two sine terms:

$$
\begin{aligned}
\implies \cos(\Omega_{\text{eff}}t/2)\mathbb{I} + i\left[\frac{1}{2}\delta t - \frac{1}{3!}\frac{1}{8}\delta\Omega_{\text{eff}}^2 t^3 + \dots\right]\sigma_z - i\left[\frac{1}{2}\Omega t - \frac{1}{3!}\frac{1}{8}\Omega\Omega_{\text{eff}}^2 t^3 + \dots\right]\sigma_x \\
= \cos(\Omega_{\text{eff}}t/2)\mathbb{I} + i\frac{\delta}{\Omega_{\text{eff}}}\sin(\Omega_{\text{eff}}t/2)\sigma_z - i\frac{\Omega}{\Omega_{\text{eff}}}\sin(\Omega_{\text{eff}}t/2)\sigma_x.
\end{aligned}
$$

Finally, expressing this once more in terms of a matrix:

$$
U = e^{-it(\frac{1}{2}\delta\sigma_z+\frac{1}{2}\Omega\sigma_x)} = \begin{pmatrix} \cos(\Omega_{\text{eff}}t/2) + i\frac{\delta}{\Omega_{\text{eff}}}\sin(\Omega_{\text{eff}}t/2) & -i\frac{\Omega}{\Omega_{\text{eff}}}\sin(\Omega_{\text{eff}}t/2) \\ -i\frac{\Omega}{\Omega_{\text{eff}}}\sin(\Omega_{\text{eff}}t/2) & \cos(\Omega_{\text{eff}}t/2) - i\frac{\delta}{\Omega_{\text{eff}}}\sin(\Omega_{\text{eff}}t/2) \end{pmatrix}.
$$

B.5 Explicit Calculation of the Interaction Hamiltonian for a Trapped Atom Interacting with a Laser

B.5.1 Simplification of the motional part

Separating out the motional and electronic parts of the Hamiltonian yields:

$$
H_{\text{int}} = \frac{\hbar\Omega}{2}e^{iH_{0e}^{\dagger}t/\hbar}\Big(e^{i(\omega_{\text{L}}t+\phi_{\text{L}})}e^{iH_{0m}^{\dagger}t/\hbar}e^{i\eta(a+a^{\dagger})}e^{-iH_{0m}t/\hbar} \tag{B.29}
$$

$$
+ \; e^{-i(\omega_{\text{L}}t+\phi_{\text{L}})}e^{iH_{0m}^{\dagger}t/\hbar}e^{-i\eta(a+a^{\dagger})}e^{-iH_{0m}t/\hbar}\Big)\sigma_x e^{-iH_{0e}t/\hbar}. \tag{B.30}
$$

In order to evaluate this Hamiltonian, it is best to first consider the term:

$$\begin{aligned} & e^{iH_{0m}^{\dagger}t/\hbar}e^{i\eta(a+a^{\dagger})}e^{-iH_{0m}t/\hbar} = e^{i\theta(aa^{\dagger}+1/2)}e^{i\eta(a+a^{\dagger})}e^{-i\theta(a^{\dagger}a+1/2)} \\ = \; & e^{i\theta aa^{\dagger}}e^{i\eta(a+a^{\dagger})}e^{-i\theta a^{\dagger}a} = e^{i\eta(ae^{-i\theta}+a^{\dagger}e^{i\theta})}, \end{aligned} \tag{B.31}$$

where $\theta = \omega t$, and the relations in Appendix B.6 have been used. Therefore, Equation B.29 simplifies to:

$$H_{\text{int}} = \frac{\hbar\Omega}{2}e^{iH_{0e}^{\dagger}t/\hbar}\left(e^{i(\omega_L t+\phi_{\mathrm{L}})}e^{i\eta(ae^{-i\omega t}+a^{\dagger}e^{i\omega t})} + e^{-i(\omega_L t+\phi_{\mathrm{L}})}e^{-i\eta(ae^{-i\omega t}+a^{\dagger}e^{i\omega t})}\right)\sigma_x e^{-iH_{0e}t/\hbar}. \tag{B.32}$$

B.5.2 Simplification of the electronic part

So far, the interaction Hamiltonian has been evaluated such that it takes the form:

$$H_{\text{int}} = \frac{\hbar\Omega}{2}e^{iH_{0e}^{\dagger}t/\hbar}\left(e^{i(\omega_L t+\phi_{\mathrm{L}})}e^{i\eta(ae^{-i\omega t}+a^{\dagger}e^{i\omega t})} + e^{-i(\omega_L t+\phi_{\mathrm{L}})}e^{-i\eta(ae^{-i\omega t}+a^{\dagger}e^{i\omega t})}\right)\sigma_x e^{-iH_{0e}t/\hbar}. \tag{B.33}$$

It is simplest to evaluate this Hamiltonian in two parts; evaluating the first term with $H_{0e} = \hbar\omega_0\sigma_z/2$ yields:

$$\begin{aligned} & e^{iH_{0e}^{\dagger}t/\hbar}\left(e^{i(\omega_L t+\phi_{\mathrm{L}})}e^{i\eta(ae^{-i\omega t}+a^{\dagger}e^{i\omega t})}\right)\sigma_x e^{-iH_{0e}t/\hbar} \\ \Longrightarrow\; & e^{-i\omega_0 t\sigma_z/2}\left(e^{i(\omega_L t+\phi_{\mathrm{L}})}e^{i\eta(ae^{-i\omega t}+a^{\dagger}e^{i\omega t})}\right)\sigma_x e^{i\omega_0 t\sigma_z/2} \\ \Longrightarrow\; & e^{i(\omega_{\mathrm{L}}t+\phi_{\mathrm{L}})}\left[e^{-i\omega_0 t\sigma_z/2}\sigma_x e^{i\omega_0 t\sigma_z/2}\right]e^{i\eta(ae^{-i\omega t}+a^{\dagger}e^{i\omega t})} \\ \Longrightarrow\; & e^{i(\omega_{\mathrm{L}}t+\phi_{\mathrm{L}})}[\cos(\omega_0 t/2)\mathbb{I} - i\sin(\omega_0 t/2)\sigma_z]\sigma_x[\cos(\omega_0 t/2)\mathbb{I} + i\sin(\omega_0 t/2)\sigma_z]e^{i\eta(ae^{-i\omega t}+a^{\dagger}e^{i\omega t})} \\ \Longrightarrow\; & e^{i(\omega_{\mathrm{L}}t+\phi_{\mathrm{L}})}[\cos(\omega_0 t/2)\mathbb{I} - i\sin(\omega_0 t/2)\sigma_z][\cos(\omega_0 t/2)\sigma_x + \sin(\omega_0 t/2)\sigma_y]e^{i\eta(ae^{-i\omega t}+a^{\dagger}e^{i\omega t})} \\ \Longrightarrow\; & e^{i(\omega_{\mathrm{L}}t+\phi_{\mathrm{L}})}\left[\cos^2(\omega_0 t/2)\sigma_x + \sin(\omega_0 t)\sigma_y - \sin^2(\omega_0 t/2)\sigma_x\right]e^{i\eta(ae^{-i\omega t}+a^{\dagger}e^{i\omega t})} \\ \Longrightarrow\; & e^{i(\omega_{\mathrm{L}}t+\phi_{\mathrm{L}})}[\cos(\omega_0 t)\sigma_x + \sin(\omega_0 t)\sigma_y]e^{i\eta(ae^{-i\omega t}+a^{\dagger}e^{i\omega t})} \\ \Longrightarrow\; & e^{i(\omega_{\mathrm{L}}t+\phi_{\mathrm{L}})}\begin{pmatrix} 0 & e^{-i\omega_0 t} \\ e^{i\omega_0 t} & 0 \end{pmatrix}e^{i\eta(ae^{-i\omega t}+a^{\dagger}e^{i\omega t})}. \end{aligned} \tag{B.34}$$

As before, terms which are at sum frequencies rotate much faster than those at the difference frequencies, and so once again making the rotating wave approximation, the first term of Equation B.33 is:

$$\begin{pmatrix} 0 & e^{-(i\delta t-\phi_{\mathrm{L}})} \\ 0 & 0 \end{pmatrix}e^{i\eta(ae^{-i\omega t}+a^{\dagger}e^{i\omega t})} = e^{-(i\delta t-\phi_{\mathrm{L}})}\sigma_+ e^{i\eta(ae^{-i\omega t}+a^{\dagger}e^{i\omega t})}, \tag{B.35}$$

where $\delta = \omega_\mathrm{L} - \omega_0$. Similarly, the second term in Equation B.33 simplifies to:

$$\begin{pmatrix} 0 & 0 \\ e^{(i\delta t - \phi_\mathrm{L})} & 0 \end{pmatrix} e^{-i\eta(ae^{-i\omega t} + a^\dagger e^{i\omega t})} = e^{(i\delta t - \phi_\mathrm{L})} \sigma_- e^{-i\eta(ae^{-i\omega t} + a^\dagger e^{i\omega t})}. \tag{B.36}$$

Combining these two terms, the Hamiltonian in the interaction frame is therefore given by:

$$H_\mathrm{int} = \frac{\hbar\Omega}{2}\left(e^{-(i\delta t - \phi_\mathrm{L})} \sigma_+ e^{i\eta(ae^{-i\omega t} + a^\dagger e^{i\omega t})} \;+\; h.c.\right) \tag{B.37}$$

B.6 Relations for Annihilation and Creation Operators

$$e^{i\theta a^\dagger a} a e^{-i\theta a^\dagger a} = e^{-i\theta} a \tag{B.38}$$

$$e^{i\theta a^\dagger a} a^\dagger e^{-i\theta a^\dagger a} = e^{-i\theta} a^\dagger \tag{B.39}$$

$$e^{i\eta(a + a^\dagger)} = e^{-\eta^2/2} e^{i\eta a^\dagger} e^{i\eta a} \tag{B.40}$$

$$e^{i\theta a^\dagger a} e^{i\eta(a + a^\dagger)} e^{-i\theta a^\dagger a} = e^{i\eta(ae^{-i\theta} + a^\dagger e^{i\theta})} \tag{B.41}$$

Appendix C

Generating Random Unitaries

C.1 Generation of Random Unitaries

This measurement protocol consisted of applying to each qubit a local random unitary matrix drawn from the circular unitary ensemble (CUE) [125, 126]. Random unitary matrices of dimension 2 were drawn following [131]. These unitaries act such that any state on the surface of the Bloch sphere has an equal probability of being rotated into any other state on the surface of the Bloch sphere.

Any arbitrary, local unitary operator can be written as a combination of rotations, together with global phase shifts, and so can be decomposed into rotation angles around the X, Y and Z axes of the Bloch sphere. This can be expressed in the following manner: If U is a local unitary operation, then there exist real numbers α, θ_1, θ_2 and θ_3 such that

$$U = e^{i\alpha} R_z(\theta_1) R_y(\theta_2) R_z(\theta_3), \tag{C.1}$$

where $e^{i\alpha}$ is a global phase, and $R_i(\theta) = e^{i\sigma_i\theta/2}$ where σ_i are the Pauli matrices, are rotations by θ around the $i = x, y, z$ axes. As $e^{i\alpha}$ is an arbitrary global phase it can be set equal to 1. Using the property of all unitary matrices that the rows and columns must be orthonormal, it follows there exist real numbers θ_1, θ_2, and θ_3 such that:

$$U = \begin{bmatrix} e^{-i(\theta_1/2+\theta_3/2)}\cos(\frac{\theta_2}{2}) & -e^{-i(\theta_1/2-\theta_3/2)}\sin(\frac{\theta_2}{2}) \\ e^{i(\theta_1/2-\theta_3/2)}\sin(\frac{\theta_2}{2}) & e^{i(\theta_1/2+\theta_3/2)}\cos(\frac{\theta_2}{2}) \end{bmatrix}. \tag{C.2}$$

This matrix can be represented using just two matrix elements and their complex conjugates:

$$\begin{bmatrix} U_1 & U_2 \\ -U_2^* & U_1^* \end{bmatrix}, \tag{C.3}$$

where the matrix elements U_1 and U_2 are known. Through direct comparison with (C.2), expressions for the rotation angles θ_1, θ_2 and θ_3 can be subsequently determined in terms of U_1, U_2 and their conjugates:

$$\begin{aligned}
U_1 + U_1^* &= [e^{-i(\theta_1/2+\theta_3/2)} + e^{i(\theta_1/2+\theta_3/2)}]\cos(\theta_2/2),\\
U_1 - U_1* &= [e^{-i(\theta_1/2+\theta_3/2)} - e^{i(\theta_1/2+\theta_3/2)}]\cos(\theta_2/2),\\
U_2 - U_2* &= [-e^{-i(\theta_1/2-\theta_3/2)} + e^{i(\theta_1/2-\theta_3/2)}]\sin(\theta_2/2),\\
U_2 + U_2^* &= [-e^{-i(\theta_1/2-\theta_3/2)} - e^{i(\theta_1/2-\theta_3/2)}]\sin(\theta_2/2).
\end{aligned}$$

Through use of the well-known identities $\cos(\theta) = \frac{1}{2}(e^{i\theta/2} + e^{-i\theta/2})$ and $\sin(\theta) = \frac{1}{2i}(e^{i\theta/2} - e^{-i\theta/2})$, these four equations reduce to:

$$\begin{aligned}
U_1 + U_1^* &= 2\cos(\theta_1/2 + \theta_3/2)\cos(\theta_2/2), \quad & U_1 - U_1^* &= -2i\sin(\theta_1/2 + \theta_3/2)\cos(\theta_2/2),\\
U_2 - U_2^* &= 2i\sin(\theta_1/2 - \theta_3/2)\sin(\theta_2/2), \quad & U_2 + U_2^* &= -2\cos(\theta_1/2 - \theta_3/2)\sin(\theta_2/2).
\end{aligned}$$

θ_2 can be eliminated from these expressions, yielding:

$$\begin{aligned}
i\tan(\theta_1/2 + \theta_3/2) &= \frac{U_1^* - U_1}{U_1^* + U_1} \quad \Rightarrow \quad \theta_1/2 + \theta_3/2 = \tan^{-1}\left[\frac{i(U_1 - U_1^*)}{U_1 + U_1^*}\right],\\
i\tan(\theta_1/2 - \theta_3/2) &= \frac{U_2^* - U_2}{U_2^* + U_2} \quad \Rightarrow \quad \theta_1/2 - \theta_3/2 = \tan^{-1}\left[\frac{i(U_2 - U_2^*)}{U_2 + U_2^*}\right].
\end{aligned}$$

Through addition and subtraction of these two equations, expressions for θ_1 and θ_3 are found to be:

$$\begin{aligned}
\theta_1 &= \tan^{-1}\left[\frac{-i(U_1 - U_1^*)}{U_1 + U_1^*}\right] + \tan^{-1}\left[\frac{-i(U_2 - U_2^*)}{U_2 + U_2^*}\right],\\
\text{and } \theta_3 &= \tan^{-1}\left[\frac{-i(U_1 - U_1^*)}{U_1 + U_1^*}\right] - \tan^{-1}\left[\frac{-i(U_2 - U_2^*)}{U_2 + U_2^*}\right].
\end{aligned}$$

An expression for θ_2 can be similarly found:

$$\begin{aligned}
&|U_2|^2 = \sin^2(\theta_2/2), \quad |U_1|^2 = \cos^2(\theta_2/2), \qquad (*)\\
&\tan^2(\theta_2/2) = \frac{|U_2|^2}{|U_1|^2}, \quad \Rightarrow \quad \theta_2 = 2\tan^{-1}\left[\left(\frac{|U_2|^2}{|U_1|^2}\right)^{\frac{1}{2}}\right].
\end{aligned}$$

C.2 Concatenated Unitaries

To make the drawing of random unitaries from the CUE more robust against miscalibrations or drifts of experimental control parameters, two random unitaries (assumed to be drawn from a possibly imperfect distribution) were concatanated to obtain a random unitary with a distribution that is closer to the ideal one – i.e. the applied random unitary is given by $u_i' = u_i^{(1)} u_i^{(2)}$ where $u_i^{(1)}$ and $u_i^{(2)}$ are both random unitaries drawn from the CUE. The explicit sequence of pulses this corresponds to in the QSim system is then:

$$u = R_z(\theta_6) R_y(-\pi/2) R_z(\theta_5) R_y(\pi/2)\, R_z(\theta_4)\, R_z(\theta_3)\, R_y(-\pi/2) R_z(\theta_2) R_y(\pi/2)\, R_z(\theta_1), \tag{C.4}$$

where the local rotations around the Y-axis have been replaced by a combination of a local σ_z rotation sandwiched between two global $\pi/2$ rotations around the Y-axis with opposite phase.

Appendix D

Explicit Calculation of Lamb-Dicke Parameters

D.1 Calculation of Lamb-Dicke Parameters for copropagating and counterpropagating Raman transitions

The Lamb-Dicke parameter depends on both the wavelength of the light, and the ground state wavefunction:

$$\eta = |\vec{k}|\mathrm{x}_0 \longrightarrow \eta = |\vec{k_1} - \vec{k_2}|\mathrm{x}_0.$$

Copropagating geometry For the copropagating beam geometry, both beams arrive through the same fibre, subtending an angle of 60° to the axial direction, and with 0° angle between them. As such, for a difference in wavelength between the two beams of $\sim$ 10 MHz, the Lamb-Dicke parameter is:

$$\eta = 2\pi * \sin(60^\circ) * \left(\frac{1}{29.98}\right)\sqrt{\frac{\hbar}{2\mathrm{Nm}\omega}}.$$

For a single ion (i.e. N = 1), with mass $m = 6.66 \times 10^{26}$ kg and a radial trapping frequency of $2\pi \times 2.7$ MHz, the Lamb-Dicke parameter is then found to be: $\eta = 0.12 \times 10^{-8}$.

Counterpropagating geometry For the counterpropagating beam geometry presented, both beams subtend an angle of 60° to the axial direction (i.e. 30° to the radial direction), with a 120° angle between the two beams. Therefore, the expression for the Lamb-Dicke parameter becomes:

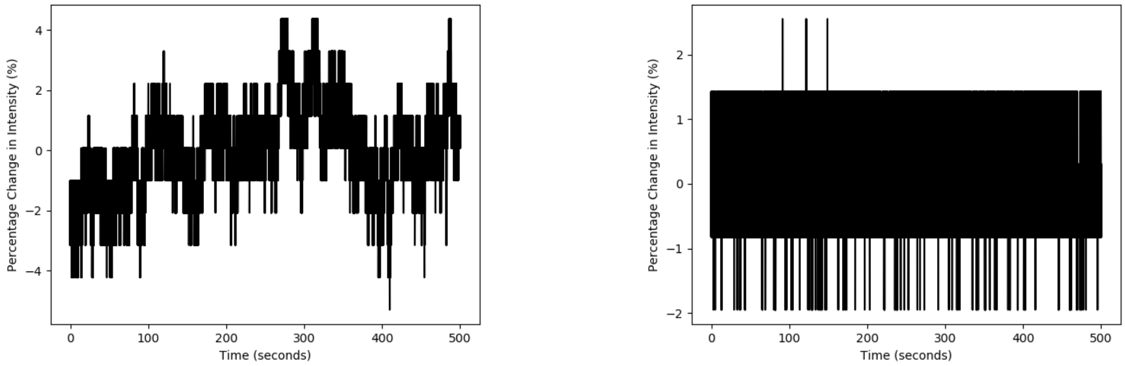

(a) Signal from unstabilised beam

(b) Signal from stabilised beam

Figure D.1: Photodiode signal showing fluctuations in the beam intensity just before entering the vacuum chamber. Plotted is the percentage change in fluctuations as a function of time, for the lower beam path using only MAC1 to drive AOM1. a) Photodiode signal from unstabilised beam. b) Photodiode signal from stabilised beam.

$$\eta = 2\pi * \left(\frac{\sin(60°)}{393.499365 * 10^{-9}} - \frac{\sin(-60°)}{393.499365 * 10^{-9}}\right)\sqrt{\frac{\hbar}{2\mathrm{N}m\omega}}.$$

For a single ion (i.e. N = 1), with mass $m = 6.66 \times 10^{26}$ kg and a radial trapping frequency of $2\pi \times 2.85$ MHz, the Lamb-Dicke parameter is: $\eta = 0.184$.

D.2 Intensity Stabilisation

There appeared to be slow drifts in the intensity of the Raman beams arriving at the trap, causing the Raman resonance to drift by several hundreds of hertzs on the order of 10 minutes. Figure D.1 shows a photodiode signal[1] recording the beam intensity for the lower beam path just before entering the vacuum chamber, where AOM1 was driven using MAC1 (see Figure 3.7). The intensity can be seen to fluctuate in magnitude by more than a few percent over a timescale of minutes, which can cause significant fluctuations in AC-Stark shifts.

These fluctuations were stabilised on both the upper and lower beam paths. For the upper beam path, residual light passes through the trap and out of the viewport opposite the incident viewport. This light is incident on a photodiode[2], whose signal is sent to a home-built sample & hold stabilisation circuit. The signal from the sample & hold circuit is sent to the amplifier supplying the signal to AOM2, which then adjusts its amplification

---

[1] Thorlabs Si Amplified Detector PDA10A-EC

[2] Home-built

depending on the signal received. A similar scheme is used for the bottom beam path, however a small portion of the beam is picked off before it enters the vacuum chamber, and is incident on a photodiode[3]. This signal is sent to the amplifier supplying the signal to AOM1, which then adjusts its amplification depending on the signal received.

---

[3] Home-built

References

[1] G. E. Moore, "Cramming more components onto integrated circuits," *Electronics*, vol. 38, pp. 114–117, April 1965.

[2] P. Benioff, "The computer as a physical system: A microscopic quantum mechanical Hamiltonian model of computers as represented by Turing machines," *J. Stat. Phys.*, vol. 22, pp. 563–591, May 1980.

[3] R. Feynman, "Simulating physics with computers," *Int. J. Theor. Phys.*, vol. 21, pp. 467–488, 1982.

[4] D. Deutsch, "Quantum theory, the Church-Turing principle and the universal quantum computer," *Proc. R. Soc. London A*, vol. 400, pp. 97–117, July 1985.

[5] D. Bouwmeester, A. Ekert, and A. Zeilinger, *The Physics of Quantum Information.* Berlin, Heidelberg: Springer-Verlag, 2000.

[6] P. W. Shor, "Algorithms for quantum computation: discrete logarithms and factoring," in *Proceedings 35th Annual Symposium on Foundations of Computer Science*, pp. 124–134, 1994.

[7] P. Shor, "Polynomial-Time Algorithms for Prime Factorization and Discrete Logarithms on a Quantum Computer," *SIAM J. Sci. Statist. Comput.*, vol. 16, pp. 1484–1509, 1997.

[8] L. M. K. Vandersypen *et al.*, "Experimental realization of Shor's quantum factoring algorithm using nuclear magnetic resonance," *Nature*, vol. 414, December 2001.

[9] B. P. Lanyon *et al.*, "Experimental Demonstration of a Compiled Version of Shor's Algorithm with Quantum Entanglement," *Phys. Rev. Lett.*, vol. 99, p. 250505, Dec 2007.

[10] A. Politi, J. C. F. Matthews, and J. L. O'Brien, "Shor's Quantum Factoring Algorithm on a Photonic Chip," *Science*, vol. 325, p. 1221, September 2009.

[11] T. Monz *et al.*, "Realization of a scalable Shor algorithm," *Science*, vol. 351, pp. 1068–1070, March 2016.

[12] M. A. Nielsen and I. L. Chuang, *Quantum Computation and Quantum Information.* Delhi, India: Cambridge University Press, 10th anniversary edition ed., 2010.

[13] A. Trabesinger, “Quantum Simulation,” *Nat. Phys.*, vol. 8, p. 263, April 2012.

[14] C. Monroe *et al.*, “Programmable quantum simulations of spin systems with trapped ions,” *Rev. Mod. Phys.*, 2020.

[15] I. Cirac, “Quantum computing and simulatino: Where we stand and what awaits us,” *Nanophotonics*, vol. 10, pp. 453–456, September 2020.

[16] R. Blatt and D. Wineland, “Entangled states of trapped atomic ions,” *Nature*, vol. 453, pp. 1008–1015, 2008.

[17] R. Blatt and C. F. Roos, “Quantum simulations with trapped ions,” *Nat. Phys.*, vol. 8, pp. 277–284, 2012.

[18] J. Preskill, “Quantum Computing in the NISQ era and Beyond,” *Quantum*, vol. 2, p. 79, August 2018.

[19] F. Arute *et al.*, “Quantum supremacy using a programmable superconducting processor,” *Nature*, vol. 574, pp. 505–510, October 2019.

[20] S. Chen, “Quantum Computing Scientists: Give Them Lemons, They’ll Make Lemonade,” *APS*, vol. 28, no. 5, 2019.

[21] S. Boixo *et al.*, “Characterising quantum supremacy in near-term devices,” *Nat. Phys.*, vol. 14, pp. 595–600, June 2018.

[22] D. Porras and J. I. Cirac, “Effective Quantum Spin Systems with Trapped Ions,” *Phys. Rev. Lett.*, vol. 92, p. 207901, May 2004.

[23] P. Jurcevic *et al.*, “Quasiparticle engineering and entanglement propagation,” *Nature*, vol. 511, pp. 202–205, July 2014.

[24] T. Brydges *et al.*, “Probing Rényi entanglement entropy via randomized measurements,” *Science*, vol. 364, pp. 260–263, 2019.

[25] M. K. Joshi *et al.*, “Quantum Information Scrambling in a Trapped-Ion Quantum Simulator with Tunable Range Interactions,” *Phys. Rev. Lett.*, vol. 124, p. 240505, June 2020.

[26] A. Elben *et al.*, “Cross-Platform Verification of Intermediate Scale Quantum Devices,” *Phys. Rev. Lett.*, vol. 124, p. 010504, Jan 2020.

[27] S. Hallgren, “Polynomial-time quantum algorithms for Pell’s equation and the principal ideal problem,” *Conference Proceedings of the Annual ACM Symposium on Theory of Computing*, pp. 653–658, May 2002.

[28] A. W. Harrow, A. Hassidim, and S. Lloyd, “Quantum algorithm for linear systems of equations,” *Phys. Rev. Lett.*, vol. 103, p. 150502, Oct 2009.

[29] G. Vidal, “Efficient classical simulation of slightly entangled quantum computations,” *Phys. Rev. Lett.*, vol. 91, p. 147902, 2003.

[30] E. Knill and R. Laflamme, "Power of One Bit of Quantum Information," *Phys. Rev. Lett.*, vol. 81, pp. 5672–5675, Dec 1998.

[31] A. Datta, A. Shaji, and C. M. Caves, "Quantum Discord and the Power of One Qubit," *Phys. Rev. Lett.*, vol. 100, p. 050502, Feb 2008.

[32] C. E. Shannon, "A Mathematical Theory of Communication," *The Bell System Technical Journal*, vol. 27, pp. 379–423, 623–656, July,October 1948.

[33] R. Dorner and V. Vedral, "Correlations in Quantum Physics," *International Journal of Modern Physics B*, vol. 27, p. 1345017, January 2013.

[34] J. von Neumann, *Mathematische Grundlagen der Quantenmechanik.* Berlin, Germany: Springer, 1932.

[35] R. F. Werner, "Quantum states with Einstein-Podolsky-Rosen correlations admitting a hidden-variable model," *Phys. Rev. A*, vol. 40, pp. 4277–4281, Oct 1989.

[36] R. Horodecki *et al.*, "Quantum Entanglement," *Phys. Mod. Phys.*, vol. 81, p. 865, June 2009.

[37] D. Greenbaum and Z. Dutton, "Modeling coherent errors in quantum error correction," *Quantum Sci. Technol.*, vol. 3, p. 015007, December 2018.

[38] D. Greenbaum, "Introduction to Quantum Gate Set Tomography," *arXiv:1509.02921v1*, 2015.

[39] D.J. Wineland *et al.*, "Experimental Issues in Coherent Quantum-State Manipulation of Trapped Atomic Ions," *J. Res. Natl. Inst. Stand. Technol.*, vol. 103, no. 3, pp. 259–328, 1998.

[40] H. Dehmelt, "Radiofrequency spectroscopy of stored ions I: Storage," *Adv. At. Mol. Phys.*, vol. 3, pp. 53–72, 1968.

[41] W. Paul, O. Osberghaus, and E. Fischer, "Ein Ionenkäfig," *Forschungsberichte des Wirtschafts- und Verkehrsministeriums Nordrhein-Westfalen*, vol. 415, pp. 1–67, 1958.

[42] W. Paul, "Electromagnetic traps for charged and neutral particles," *Rev. Mod. Phys.*, vol. 62, pp. 531–542, July 1990.

[43] D. Leibfried *et al.*, "Quantum dynamics of single trapped ions," *Rev. Mod. Phys.*, vol. 75, pp. 281–324, March 2003.

[44] M. Knoop, "Radiofrequency Traps," in *Trapped Charged Particles: A Graduate Textbook with Problems and Solutions* (M. Knoop, N. Madsen, and R. C. Thompson, eds.), ch. 2, pp. 35–54, 57 Shelton Street, Covent Garden, London: World Scientific Publishing Europe Ltd., 2016.

[45] C. F. Roos, *Controlling the quantum state of trapped ions.* PhD thesis, University of Innsbruck, 2000.

[46] E. Mathieu, "Le mouvement vibratoire d'une membrane de forme elliptique," *J. Math. Pures Appl.*, vol. 13, pp. 137–203, 1868.

[47] P. Jurcevic, *Quantum Computation and Many-Body Physics with Trapped Ions.* PhD thesis, University of Innsbruck, January 2017.

[48] J. Eschner *et al.*, "Laser cooling of trapped ions," *Journal of the Optical Society of America B*, vol. 20, pp. 1003–1015, May 2003.

[49] C. Hempel, *Digital quantum simulation, Schrödinger cat state spectroscopy and setting up a linear ion trap.* PhD thesis, University of Innsbruck, August 2014.

[50] R. J. Glauber, "Coherent and Incoherent States of the Radiation Field," *Phys. Rev.*, vol. 131, pp. 2766–2788, Sep 1963.

[51] F. Schmidt-Kaler *et al.*, "The coherence of qubits based on single Ca^+ ions," *Journal of Physics B: Atomic, Molecular and Optical Physics*, vol. 36, pp. 623–636, January 2003.

[52] H. Häffner, C. F. Roos, and R. Blatt, "Quantum computing with trapped ions," *Physics Reports*, vol. 469, pp. 155–203, September 2008.

[53] M. Chwalla, *Precision spectroscopy with $^{40}Ca^+$ ions in a Paul trap.* PhD thesis, University of Innsbruck, April 2009.

[54] P. Schindler *et al.*, "A quantum information processor with trapped ions," *New J. Phys.*, vol. 15, p. 123012, December 2013.

[55] J. A. Jones and D. Jaksch, *Quantum Information, Computation and Communication.* Cambridge University Press, 10th anniversary edition ed., 2012.

[56] N. F. Ramsey, "Experiments with separated oscillatory fields and hydrogen masers," *Rev. Mod. Phys.*, vol. 62, pp. 541–552, Jul 1990.

[57] R. Han, H. K. Ng, and B. Englert, "Raman transitions without adiabatic elimination: a simple and accurate treatment," *Journal of Modern Optics*, vol. 60, pp. 255 – 265, 2013.

[58] G. Kirchmair, "Frequency stabilization of a Titanium-Sapphire laser for precision spectroscopy on Calcium ions," Master's thesis, University of Innsbruck, November 2006.

[59] J. Benhelm *et al.*, "Towards fault-tolerant quantum computing with trapped ions," *Nat. Phys.*, vol. 4, pp. 463–466, April 2008.

[60] D. P. DiVincenzo, "The Physical Implementation of Quantum Computation," *Fortschritte der Physik*, vol. 48, pp. 771–783, 2000.

[61] A. Barenco *et al.*, "Elementary gates for quantum computation," *Phys. Rev. A*, vol. 52, pp. 3457–3467, Nov 1995.

[62] K. Mølmer and A. Sørensen, "Multiparticle Entanglement of Hot Trapped Ions," *Phys. Rev. Lett.*, vol. 82, pp. 1835–1838, March 1999.

[63] C. A. Sackett *et al.*, "Experimental entanglement of four particles," *Nature*, vol. 404, pp. 256–259, March 2000.

[64] E. Schrödinger, "Die gegenwärtige Situation in der Quantenmechanik," *Die Naturwissenschaften*, vol. 23, pp. 807–812, 1935.

[65] C. Monroe *et al.*, "A "Schrödinger Cat" Superposition State of an Atom," *Science*, vol. 272, pp. 1131–1136, May 1996.

[66] S.-B. Zheng, "Preparation of motional macroscopic quantum-interference states of a trapped ion," *Phys. Rev. A.*, vol. 58, pp. 761–763, 1998.

[67] K. Lake *et al.*, "Generation of spin-motion entanglement in a trapped ion using long-wavelength radiation," *Phys. Rev. A*, vol. 91, p. 012319, Jan 2015.

[68] C. F. Roos, "Ion trap quantum gates with amplitude-modulated laser beams," *New J. Phys.*, vol. 10, p. 013002, 2008.

[69] T. Monz *et al.*, "14-Qubit Entanglement: Creation and Coherence," *Phys. Rev. Lett.*, vol. 106, p. 130506, Mar 2011.

[70] X.-L. Deng, D. Porras, and J. I. Cirac, "Effective spin quantum phases in systems of trapped ions," *Phys. Rev. A*, vol. 72, p. 063407, Dec 2005.

[71] K. Kim *et al.*, "Quantum simulation of the transverse Ising model with trapped ions," *New Journal of Physics*, vol. 13, p. 105003, October 2011.

[72] C. Schneider, D. Porras, and T. Schaetz, "Experimental quantum simulations of many-body physics with trapped ions," *Rep. Prog. Phys.*, vol. 75, p. 024401, January 2012.

[73] J. Benhelm, *Precision Spectroscopy and Quantum Information Processing with Trapped Calcium Ions.* PhD thesis, University of Innsbruck, May 2008.

[74] G. Kirchmair, *Quantum non-demolition measurements and quantum simulation.* PhD thesis, University of Innsbruck, July 2010.

[75] R. Stricker, "Gatteroperationen hoher Güte in einem optischen Quantenbit," Master's thesis, University of Innsbruck, March 2017.

[76] S. T. Gulde, *Experimental Realization of Quantum Gates and the Deutsch-Jozsa Algorithm with Trapped* $^{40}Ca^{+}$ *Ions.* PhD thesis, University of Innsbruck, March 2003.

[77] L. F. Pernthaler, "Single ion Addressing of up to 50 Ions," Master's thesis, University of Innsbruck, August 2020.

[78] M. S. L. Ltd, *SolsTiS Narrow Linewidth, Tunable CW Ti:Sapphire Laser User Manual v10.3.* M Squared Laser Ltd.

[79] R. L. Barger, M. S. Sorem, and J. L. Hall, “Frequency stabilization of a CW dye laser,” *App. Phys. Lett.*, vol. 22, no. 11, pp. 573–575, 1973.

[80] R. W. Fox, C. W. Oates, and L. W. Hollberg, “Stabilizing Diode Lasers to High-Finesse Cavities,” in *Cavity-Enhanced Spectroscopies* (R. D. van Zee and J. P. Looney, eds.), vol. 40 of *Experimental methods in the physical sciences*, pp. 1–46, Academic Press, 2003.

[81] T. Hänsch and B. Couillaud, “Laser Frequency Stabilization by Polarization Spectroscopy of a Reflecting Reference Cavity,” *Opt. Commun.*, vol. 35, pp. 441–444, December 1980.

[82] M. Vainio, J. E. Bernard, and L. Marmet, “Cavity-enhanced optical frequency doubler based on transmission-mode Hänsch-Couillaud locking,” *Appl. Phys. B*, vol. 104, pp. 897–908, February 2010.

[83] L. G. Gouy, “Sur une propriété nouvelle des ondes lumineuses,” *C. R. Acad. Sci. Paris*, vol. 110, no. 1251, 1890.

[84] J. Nothhelfer, “Optikaufbau zum Treiben stimulierter Ramanübergänge,” Master’s thesis, Johannes Gutenberg Universität Mainz, April 2017.

[85] P. Schindler, “Frequency synthesis and pulse shaping for quantum information processing with trapped ions,” Master’s thesis, Leopold-Franzens University of Innsbruck, September 2008.

[86] T. Ruster *et al.*, “A long-lived Zeeman trapped-ion qubit,” *Appl. Phys. B*, vol. 122, pp. 1–7, October 2016.

[87] K. H. Knuth, “Optimal Data-Based Binning for Histograms,” *arXiv:physics/0605197v2*, 2006.

[88] E. Nielsen *et al.*, “Gate Set Tomography,” *arXiv:2009.07301v1*, 2020.

[89] R. Blume-Kohout and K. Young, “A volumetric framework for quantum computer benchmarks,” *Quantum*, vol. 4, p. 362, 2020.

[90] A. W. Cross *et al.*, “Validating quantum computers using randomized model circuits,” *Phys. Rev. A*, vol. 100, p. 032328, Sep 2019.

[91] J. Emerson *et al.*, “Symmetrized Characterization of Noisy Quantum Processes,” *Science*, vol. 317, pp. 1893–1896, September 2007.

[92] E. Knill *et al.*, “Randomized benchmarking of quantum gates,” *Phys. Rev. A.*, vol. 77, p. 012307, Jan 2008.

[93] J. J. Wallman and S. T. Flammia, “Randomized benchmarking with confidence,” *New J. Phys.*, vol. 16, p. 36, October 2014.

[94] J. F. Poyatos, J. I. Cirac, and P. Zoller, "Complete Characterization of a Quantum Process: The Two-Bit Quantum Gate," *Phys. Rev. Lett.*, vol. 78, pp. 390–393, January 1997.

[95] H. Häffner *et al.*, "Scalable multiparticle entanglement of trapped ions," *Nature*, vol. 438, pp. 643–646, December 2005.

[96] D. Kim *et al.*, "Microwave-drive coherent operation of a semiconductor quantum dot charge qubit," *Nat. Nanotechnol.*, vol. 10, pp. 243–247, March 2015.

[97] R. Blume-Kohout *et al.*, "Demonstration of qubit operations below a rigorous fault tolerance threshold with gate set tomography," *Nat. Comms.*, vol. 8, pp. 1–14, 2017.

[98] R. Blume-Kohout *et al.*, "Robust, self-consistent, closed-form tomography of quantum logic gates on a trapped ion qubit," *arXiv:1310.4492v1*, 2013.

[99] A. J. Scott, "Tight informationally complete quantum measurements," *Journal of Physics A*, vol. 39, pp. 13507–13530, 2006.

[100] I. L. Chuang and M. A. Nielsen, "Prescription for experimental determination of the dynamics of a quantum black box," *Journal of Modern Optics*, vol. 44, pp. 2455–2467, 1997.

[101] E. Magesan, J. M. Gambetta, and J. Emerson, "Characterizing quantum gates via randomized benchmarking," *Phys. Rev. A*, vol. 85, p. 042311, Apr 2012.

[102] T. Xia *et al.*, "Randomized Benchmarking of Single-Qubit Gates in a 2D Array of Neutral-Atom Qubits," *Phys. Rev. Lett.*, vol. 114, p. 100503, Mar 2015.

[103] T. Proctor *et al.*, "What Randomized Benchmarking Actually Measures," *Phys. Rev. Lett.*, vol. 119, p. 130502, Sep 2017.

[104] D. C. McKay *et al.*, "Three-Qubit Randomized Benchmarking," *Phys. Rev. Lett.*, vol. 122, p. 200502, May 2019.

[105] K. Wright *et al.*, "Benchmarking an 11-qubit quantum computer," *Nat. Comms.*, vol. 10, pp. 1–6, 2019.

[106] A. Erhard *et al.*, "Characterizing large-scale quantum computers via cycle benchmarking," *Nat. Commun.*, vol. 10, November 2019.

[107] E. Derbyshire *et al.*, "Randomized benchmarking in the analogue setting," *Quantum Sci. Technol.*, vol. 5, July 2020.

[108] E. Magesan, "Gaining Information About a Quantum Channel Via Twirling," Master's thesis, University of Waterloo, 2008.

[109] K. M. Rudinger and E. Nielsen, "Quantum Characterization Verification & Validation (QCVV) Tutorial: Calibration-free Characterization (invited)." APS March Meeting, 2016.

[110] J. P. Dehollain *et al.*, “Optimization of a solid-state electron spin qubit using gate set tomography,” *New J. Phys.*, vol. 18, p. 103018, 2016.

[111] T. Proctor *et al.*, “Detecting and tracking drift in quantum information processors,” *Nat. Comms.*, vol. 11, p. 5396, 2020.

[112] O. D. Matteo, G. J., C. Granade, K. Rudinger, and N. Wiebe, “Operational, gauge-free quantum tomography,” *Quantum*, vol. 4, p. 364, November 2020.

[113] E. Nielsen *et al.*, “Probing quantum processor performance with pyGSTi,” *Quantum Sci. Technol.*, vol. 5, p. 044002, July 2020.

[114] J. Qi and H. K. Ng, “Comparing the randomized benchmarking figure with the average infidelity of a quantum gate-set,” *International Journal of Quantum Information*, vol. 17, p. 1950031, 2019.

[115] J. Wallman, “Error rates in quantum circuits,” *arXiv:1511.00727v2*, 2016.

[116] M. D. Bowdrey *et al.*, “Fidelity of single qubit maps,” *Physics Letters A*, vol. 294, pp. 258–260, March 2002.

[117] R. Blume-Kohout, “Robust error bars for quantum tomography,” *arXiv:1202.5270v1*, 2012.

[118] S. S. Wilks, “The Large-Sample Distribution of the Likelihood Ratio for Testing Composite Hypotheses,” *Ann. Math. Statist.*, vol. 9, no. 1, pp. 60–62, 1938.

[119] T. L. Scholten and R. Blume-Kohout, “Behaviour of the maximum likelihood in quantum state tomography,” *New J. Phys.*, vol. 20, February 2018.

[120] R. L. Wasserstein and N. A. Lazar, “ASA Statement on p-Values: Context, Process, and Purpose,” *The American Statistician*, vol. 70, pp. 129–133, June 2016.

[121] R. Hubbard *et al.*, “Confusion over Measures of Evidence (p’s) versus Errors (α’s) in Classical Statistical Testing,” *The American Statistician*, vol. 57, pp. 171–178, August 2003.

[122] J. Home, *Entanglement of Two Trapped-Ion Spin Qubits.* PhD thesis, University of Oxford, Linacre College, Hilary Term 2006.

[123] D. Leibfried *et al.*, “Experimental Determination of the Motion Quantum State of a Trapped Atom,” *Phys. Rev. Lett.*, vol. 77, pp. 4281–4285, November 1996.

[124] N. Friis *et al.*, “Observation of Entangled States of a Fully Controlled 20-Qubit System,” *Phys. Rev. X*, vol. 8, p. 021012, Apr 2018.

[125] A. Elben *et al.*, “Rényi Entropies from Random Quenches in Atomic Hubbard and Spin Models,” *Phys. Rev. Lett.*, vol. 120, p. 050406, Feb 2018.

[126] B. Vermersch *et al.*, "Unitary n-designs via random quenches in atomic Hubbard and spin models: Application to the measurement of Rényi entropies," *Phys. Rev. A*, vol. 97, p. 023604, Feb 2018.

[127] A. Elben *et al.*, "Statistical correlations between locally randomized measurements: A toolbox for probing entanglement in many-body quantum states," *Phys. Rev. A*, vol. 99, p. 052323, May 2019.

[128] A. Ketterer, N. Wyderka, and O. Gühne, "Characterizing Multipartite Entanglement with Moments of Random Correlations," *Phys. Rev. Lett.*, vol. 122, p. 120505, Mar 2019.

[129] B. Vermersch *et al.*, "Probing Scrambling Using Statistical Correlations between Randomized Measurements," *Phys. Rev. X*, vol. 9, p. 021061, Jun 2019.

[130] L. Knips *et al.*, "Multipartite entanglement analysis from random correlations," *npj Quantum Information*, vol. 6, June 2020.

[131] F. Mezzadri, "How to generate random matrices from the classical compact groups," *Notices of the AMS*, vol. 54, pp. 592–604, 2007.

[132] F. J. Dyson, "Statistical Theory of the Energy Levels of Complex Systems. I," *J. Math. Phys.*, vol. 3, no. 1, pp. 140–156, 1962.

[133] R. Killip and I. Nenciu, "Matrix Models for Circular Ensembles," *International Mathematics Research Notices*, vol. 2004, pp. 2665–2701, January 2004.

[134] B. P. Lanyon *et al.*, "Efficient tomography of a quantum many-body system," *Nat. Phys.*, vol. 13, pp. 1158–1162, 2017.

[135] G. Torlai *et al.*, "Neural-network quantum state tomography," *Nat. Phys.*, vol. 14, pp. 447–450, May 2018.

[136] A. Rényi, "On the Foundations of Information Theory," *Review of the International Statistical Institute*, vol. 33, no. 1, pp. 1–14, 1965.

[137] A. K. Ekert *et al.*, "Direct Estimations of Linear and Nonlinear Functionals of a Quantum State," *Phys. Rev. Lett.*, vol. 88, p. 217901, May 2002.

[138] R. Islam *et al.*, "Measuring entanglement entropy in a quantum many-body system," *Nature*, vol. 528, pp. 77–83, December 2015.

[139] A. M. Kaufman *et al.*, "Quantum thermalization through entanglement in an isolated many-body system," *Science*, vol. 353, pp. 794–800, August 2016.

[140] N. M. Linke *et al.*, "Measuring the Rényi entropy of a two-site Fermi-Hubbard model on a trapped ion quantum computer," *Phys. Rev. A*, vol. 98, p. 052334, August 2018.

[141] S. J. van Enk and C. W. J. Beenakker, "Measuring $\mathrm{Tr}(\rho)^n$ on Single Copies of ρ Using Random Measurements," *Phys. Rev. Lett.*, vol. 108, p. 110503, March 2012.

[142] D. Gross *et al.*, “Quantum State Tomography via Compressed Sensing,” *Phys. Rev. Lett.*, vol. 105, p. 150401, Oct 2010.

[143] A. Bohrdt *et al.*, “Scrambling and thermalization in a diffusive quantum many-body system,” *New J. Phys.*, vol. 19, p. 063001, June 2017.

[144] P. Hosur *et al.*, “Chaos in quantum channels,” *J. High Energ. Phys.*, vol. 2016, February 2016.

[145] B. Swingle, “Unscrambling the physics of out-of-time-order correlators,” *Nat. Phys.*, vol. 14, pp. 988–990, October 2018.

[146] K. A. Landsman *et al.*, “Verified quantum information scrambling,” *Nature*, vol. 567, pp. 61–65, March 2019.

[147] S. H. Shenker and D. Stanford, “Black holes and the butterfly effect,” *J. High Energ. Phys.*, vol. 2014, March 2014.

[148] P. Hayden and J. Preskill, “Black holes as mirrors: quantum information in random subsystems,” *J. High Energ. Phys.*, vol. 2007, p. 21, September 2007.

[149] R. Fan *et al.*, “Out-of-time-order correlation for many-body localization,” *Sci. Bull.*, vol. 62, pp. 707–711, May 2017.

[150] Y. Huang, Y.-L. Zhang, and X. Chen, “Out-of-time-ordered correlators in many-body localized systems,” *Ann. Phys.*, vol. 529, p. 1600318, December 2016.

[151] X. Chen *et al.*, “Out-of-time-ordered correlators in many-body localized and thermal phases,” *Ann. Phys.*, vol. 529, p. 1600332, December 2016.

[152] B. Sundar, “Proposal to measure out-of-time-ordered correlations using Bell states,” *arXiv:2006.15093v1*, 2020.

[153] B. Swingle *et al.*, “Measuring the scrambling of quantum information,” *Phys. Rev. A*, vol. 94, p. 040302, Oct 2016.

[154] G. Zhu, M. Hafezi, and T. Grover, “Measurement of many-body chaos using a quantum clock,” *Phys. Rev. A*, vol. 94, p. 062329, Dec 2016.

[155] N. Y. Yao *et al.*, “Interferometric Approach to Probing Fast Scrambling,” *arXiv:1607.01801*, 2016.

[156] M. P. da Silva, O. Landon-Cardinal, and D. Poulin, “Practical Characterization of Quantum Devices without Tomography,” *Phys. Rev. Lett.*, vol. 107, p. 210404, Nov 2011.

[157] J. Emerson, R. Alicki, and K. Zyczkowski, “Scalable Noise Estimation with Random Unitary Operators,” *J. Opt. B*, vol. 7, pp. S347–S352, September 2005.

[158] D. Lu *et al.*, “Experimental Estimation of Average Fidelity of a Clifford Gate on a 7-Qubit Quantum Processor,” *Phys. Rev. Lett.*, vol. 114, p. 140505, Apr 2015.

[159] Y.-C. Liang *et al.*, “Quantum fidelity measures for mixed states,” *Rep. Prog. Phys.*, vol. 82, p. 076001, June 2019.

[160] R. Jozsa, “Fidelity for Mixed Quantum States,” *Journal of Modern Optics*, vol. 41, no. 12, pp. 2315–2323, 1994.

[161] H. F. Trotter, “On the Product of Semi-Groups of Operators,” *Proc. Am. Math. Soc.*, vol. 10, pp. 545–551, August 1959.

[162] A. Elben *et al.*, “Mixed-state entanglement from local randomized measurements,” *arXiv:2007.06305v1*, 2020.

[163] S. Barz, “Quantum computing with photons: introduction to the circuit mode, the one-way quantum computer, and the fundamental principles of photonic experiments,” *Journal of Physics B: Atomic, Molecular and Optical Physics*, vol. 48, p. 083001, March 2015.

[164] M. Erhard *et al.*, “Experimental Greenberger-Horne-Zeilinger entanglement beyond qubits,” *Nature Photonics*, vol. 12, pp. 759–764, December 2018.

[165] S. Slussarenko and G. J. Pryde, “Photonic quantum information processing: A concise review,” *Applied Physics Reviews*, vol. 6, no. 4, p. 041303, 2019.

[166] G. Wendin, “Quantum information processing with superconducting circuits: a review,” *Rep. Prog. Phys.*, vol. 80, p. 106001, September 2017.

[167] M. Kjaergaard *et al.*, “Superconducting Qubits: Current State of Play,” *Annual Review of Condensed Matter Physics*, vol. 11, no. 1, pp. 369–395, 2020.

[168] C. Gross and I. Bloch, “Quantum simulations with ultracold atoms in optical lattices,” *Science*, vol. 357, pp. 995–1001, 2017.

[169] F. Schäfer *et al.*, “Tools for quantum simulation with ultracold atoms in optical lattices,” *Nature Reviews Physics*, vol. 2, pp. 411–425, August 2020.

[170] C. D. Bruzewicz *et al.*, “Trapped-ion quantum computing: Progress and challenges,” *Applied Physics Reviews*, vol. 6, no. 2, p. 021314, 2019.

[171] J. M. Pino *et al.*, “Demonstration of the trapped-ion quantum CCD computer architecture,” *Nature*, vol. 592, pp. 209–213, April 2021.

[172] A. Cho, “IBM casts doubt on Google’s claims of quantum supremacy,” *Science*, 2019.

[173] K. Svozil, “Comment on “Quantum supremacy using a programmable superconducting processor",” *arXiv:1911.00577v1*, 2019.

[174] E. Gibney, “Underdog Tech Makes Gains in Quantum Computer Race,” *Nature*, vol. 587, pp. 342–343, November 2020.

[175] P. Jurcevic *et al.*, “Spectroscopy of Interacting Quasiparticles in Trapped Ions,” *Phys. Rev. Lett.*, vol. 115, p. 100501, Sep 2015.

[176] P. Hauke and L. Tagliacozzo, “Spread of Correlations in Long-Range Interacting Quantum Systems,” *Phys. Rev. Lett.*, vol. 111, p. 207202, Nov 2013.

[177] E. Altman, “Many-body localization and quantum thermalization,” *Nat. Phys.*, vol. 14, pp. 979–983, October 2018.

[178] D. M. Basko, I. L. Aleiner, and B. L. Altshuler, “Metal-insulator transition in a weakly interacting many-electron system with localized single-particle states,” *Ann. Phys. (N. Y).*, vol. 321, no. 5, pp. 1126–1205, 2006.

[179] A. L. Burin, “Localization in a random XY model with long-range interactions: Intermediate case between single-particle and many-body problems,” *Phys. Rev. B*, vol. 92, p. 104428, 2015.

[180] R. Nandkishore and D. A. Huse, “Many-Body Localization and Thermalization in Quantum Statistical Mechanics,” *Annu. Rev. Condens. Matter Phys.*, vol. 6, pp. 15–38, March 2015.

[181] P. W. Anderson, “Absence of Diffusion in Certain Random Lattices,” *Phys. Rev.*, vol. 109, pp. 1492–1505, Mar 1958.

[182] M. Schreiber *et al.*, “Observation of many-body localization of interacting fermions in a quasirandom optical lattice,” *Science*, vol. 349, no. 6250, pp. 842–845, 2015.

[183] P. Calabrese and J. Cardy, “Evolution of entanglement entropy in one-dimensional systems,” *Journal of Statistical Mechanics: Theory and Experiment*, vol. 2005, no. 04, p. P04010, 2005.

[184] J. H. Bardarson, F. Pollmann, and J. E. Moore, “Unbounded growth of entanglement in models of many-body localization,” *Phys. Rev. Lett.*, vol. 109, p. 017202, 2012.

[185] M. Serbyn, Z. Papić, and D. A. Abanin, “Universal Slow Growth of Entanglement in Interacting Strongly Disordered Systems,” *Phys. Rev. Lett.*, vol. 110, p. 260601, June 2013.

[186] K. Xu *et al.*, “Emulating many-body localization with a superconducting quantum processor,” *Phys. Rev. Lett.*, vol. 120, p. 050507, 2018.

[187] A. Lukin *et al.*, “Probing Entanglement in a Many-Body-Localized Dystem,” *Science*, vol. 364, pp. 256–260, April 2019.

[188] A. Safavi-Naini *et al.*, “Quantum dynamics of disordered spin chains with power-law interactions,” *Phys. Rev. A.*, vol. 99, p. 033610, March 2019.

[189] J. Smith *et al.*, “Many-body localization in a quantum simulator with programmable random disorder,” *Nat. Phys.*, vol. 12, pp. 907–911, 2016.

[190] B. Efron and G. Gong, “A Leisurely Look at the Bootstrap, the Jackknife, and Cross-Validation,” *Am. Stat.*, vol. 37, pp. 36–48, February 1983.

[191] C. Maier *et al.*, “Environment-assisted quantum transport in a 10-qubit network,” *Phys. Rev. Lett.*, vol. 122, p. 050501, Feb 2019.

[192] J. Schachenmayer *et al.*, “Entanglement growth in quench dynamics with variable range interactions,” *Phys. Rev. X*, vol. 3, p. 031015, Sep 2013.

[193] M. Foss-Feig *et al.*, “Nearly linear light cones in long-range interacting quantum systems,” *Phys. Rev. Lett.*, vol. 114, p. 157201, Apr 2015.

[194] T. Matsuta, T. Koma, and S. Nakamura, “Improving the Lieb-Robinson Bound for Long-Range Interactions,” *Ann. Henri Poincaré*, vol. 18, pp. 519–528, February 2017.

[195] M. C. Tran *et al.*, “Locality and digital quantum simulation of power-law interactions,” *Phys. Rev. X*, vol. 9, p. 031006, Jul 2019.

[196] D. V. Else *et al.*, “Improved Lieb-Robinson bound for many-body Hamiltonians with power-law interactions,” *Phys. Rev. A*, vol. 101, p. 022333, Feb 2020.

[197] D. J. Luitz and Y. Bar Lev, “Emergent locality in systems with power-law interactions,” *Phys. Rev. A*, vol. 99, p. 010105, Jan 2019.

[198] T. Zhou *et al.*, “Operator Lévy Flight: Light Cones in Chaotic Long-Range Interacting Systems,” *Phys. Rev. Lett.*, vol. 124, p. 180601, May 2020.

[199] X.-L. Qi *et al.*, “Measuring operator size growth in quantum quench experiments,” *arXiv:1906.00524*, 2019.

[200] K. R. Brown, J. Kim, and C. Monroe, “Co-designing a scalable quantum computer with trapped atomic ions,” *npj Quantum Information*, vol. 2, November 2016.

[201] A. Bautista-Salvador *et al.*, “Multilayer ion trap technology for scalable quantum computing and quantum simulation,” *New J. Phys.*, vol. 21, p. 043011, April 2019.

[202] J. Preskill, “Quantum computing and the entanglement frontier,” *arXiv:1203.5813v3*, 2012.

[203] J. G. Bohnet *et al.*, “Quantum spin dynamics and entanglement generation with hundreds of trapped ions,” *Science*, vol. 352, pp. 1297–1301, 2016.

[204] M. K. Ivory *et al.*, “A Paul trap with sectored ring electrodes for experiments with two-dimensional ion crystals,” *Review of Scientific Instruments*, vol. 91, May 2020.

[205] M. Johanning *et al.*, “Individual Addressing of Trapped Ions and Coupling of Motional and Spin States Using rf Radiation,” *Phys. Rev. Lett.*, vol. 102, p. 073004, Feb 2009.

[206] U. Warring *et al.*, “Individual-Ion Addressing with Microwave Field Gradients,” *Phys. Rev. Lett.*, vol. 110, p. 173002, Apr 2013.

[207] C. Piltz *et al.*, “A trapped-ion-based quantum byte with 10^{-5} next-neighbour cross-talk,” *Nat. Commun.*, vol. 5, August 2014.

[208] U. G. Poschinger *et al.*, “Coherent Manipulation of a ^{40}Ca^{+} Spin Qubit in a Micro Ion Trap,” *Journal of Physics B: Atomic, Molecular and Optical Physics*, vol. 42, July 2009.

[209] U. G. Poschinger, *Quantum Optics Experiments in Microstructured Ion Trap.* PhD thesis, Universität Ulm, 2010.

[210] P. J. Lee, *Quantum Information Processing with Two Trapped Cadmium Ions.* PhD thesis, University of Michigan, 2006.

[211] S. Webster, *Raman Sideband Cooling and Coherent Manipulation of Trapped Ions.* PhD thesis, St John’s College, University of Oxford, Hilary Term 2005.

[212] C. J. Foot, *Atomic Physics.* Oxford, United Kingdom: Oxford University Press, 2005.

[213] M. Hettrich, *Measurement of Reduced Dipole Matrix Elements in ^{40}Ca^{+} and Construction of a Scalable Light-Ion Interface.* PhD thesis, Universität Ulm, May 2016.

[214] R. Gerritsma *et al.*, “Precision measurement of the branching fractions of the 4p ^{2}P$_{3/2}$ decay of Ca II,” *Eur. Phys, J. D*, vol. 50, pp. 13–19, October 2008.

[215] J. Franke, “Magnetic field noise cancellation for quantum simulation experiment with trapped ions,” Master’s thesis, University of Innsbruck, 2021.